PRINT ISSN : 2395-6011
ONLINE ISSN : 2395-602X
ISBN 978-81-951171-5-4

TECHNO SCIENCE ACADEMY
THE INTERNATIONAL OPEN ACCESS PUBLISHER

EAST POINT
COLLEGE OF ENGINEERING AND TECHNOLOGY

IJSRST

Conference Proceedings
Abstracts Book

National Conference on Applied Sciences Synergising The Engineering And Technology ASSET-2021

Organised by
Department Basic Sciences
East Point College of Engineering And Technology,
Avalahalli, Bengaluru, Karnataka, India

VOLUME 8, ISSUE 2, JANUARY-FEBRUARY-2021

INTERNATIONAL JOURNAL OF SCIENTIFIC RESEARCH IN SCIENCE & TECHNOLOGY

Publisher : Technoscience Academy
(The International Open Access Publisher)

Email : editor@ijsrst.com Website : http://ijsrst.com

Conference Proceedings and Abstracts Book

National Conference
on
Applied Sciences Synergising The Engineering and Technology

ASSET-2021

18th - 19th January 2021

Organised by

Department Basic Sciences, East Point College of Engineering and Technology, Avalahalli, Bengaluru, Karnataka, India

In Association With

International Journal of Scientific Research in Science and Technology

[Peer-Reviewed International Scientific Refereed Journal]

Online ISSN : 2395-602X | Print ISSN : 2395-6011

Volume 8, Issue 2, January-February-2021

Published By

(The International open Access Publisher)

[www.technoscienceacademy.com]

ISBN 978-81-951171-5-4

EAST POINT COLLEGE OF ENGINEERING & TECHNOLOGY

(Affiliated by VTU Belagavi, Approved by AICTE- New Delhi & Government of Karnataka)

Jnana Prabha, East Point Campus, Virgo Nagar Post, Avalahalli, Bengaluru-560049 Karnataka India

Smt. B L Ramadevi Venkatapathi

Chairperson,

East Point Group of Institutions, Bengaluru, Karnataka, India

MESSAGE

It is indeed our pleasure & privilege to host ***National Conference on Applied Sciences Synergising the Engineering and Technology*** **(ASSET-2021),** which will be held through digital mode during January 18th-19th, 2021 at EPCET, Bengaluru

This conference provides a platform which brings Researchers, Scientists, Engineers, and Academicians & Research Scholars from across the country under one platform to discuss their views, ideas and experience related to Applied Sciences.

I extend my best wishes to entire organizing team and committee members in bringing out this proceeding on the occasion of the National Conference. I extend my greetings and best wishes to all the participants and wish this conference a grand success.

B L Ramadevi Venkatapathi

EAST POINT COLLEGE OF ENGINEERING & TECHNOLOGY

(Affiliated by VTU Belagavi, Approved by AICTE- New Delhi & Government of Karnataka) Jnana Prabha, East Point Campus, Virgo Nagar Post, Avalahalli, Bengaluru-560049 Karnataka | India

Sri S V Pramod Gowda

CEO,

East Point Group of Institutions, Bengaluru,
Karnataka, India

MESSAGE

It is a great pride to host the **National Conference on Applied Sciences Synergising the Engineering and Technology (ASSET-2021),** which will be held through digital mode during January 18th-19th, 2021 at EPCET, Bengaluru. I am sure that this occasion will provide an affable environment for the researchers and academicians to freely exchange the views and ideas in the related field.

I wish the participants of this conference to come out with new inventions and innovative ideas which will contribute for the advancement of global technology.

I convey my warm greetings and felicitations to the organizing committee and the participants and extend my best wishes for the success of the conference.

S V Pramod Gowda

EAST POINT COLLEGE OF ENGINEERING & TECHNOLOGY

(Affiliated by VTU Belagavi, Approved by AICTE- New Delhi & Government of Karnataka) Jnana Prabha, East Point Campus, Virgo Nagar Post, Avalahalli, Bengaluru-560049 Karnataka | India

Sri S V Rajiv Gowda

CEO,

East Point Group of Institutions, Bengaluru,
Karnataka, India

MESSAGE

It is a great honour and privilege to host **National Conference on Applied Sciences Synergising the Engineering and Technology (ASSET-2021),** which will be held through digital mode during January 18th-19th, 2021 at EPCET, Bengaluru.

This conference provides a forum for industry professionals and researchers to deliberate and state a wide range of practices, trends, research findings, discuss the latest advancements & explore the future in emerging industrial technologies.

A great amount of planning and organizing is required to hold a successful conference and I appreciate the efforts of all the people who were involved in making the conference a success.

Our Management is ever ready to extend constant support for all the activities undertaken and we look forward to have more conferences in the days to come.

I wish this conference to be a grand success.

S V Rajiv Gowda

EAST POINT COLLEGE OF ENGINEERING & TECHNOLOGY

(Affiliated by VTU Belagavi, Approved by AICTE- New Delhi & Government of Karnataka) Jnana Prabha, East Point Campus, Virgo Nagar Post, Avalahalli, Bengaluru-560049 Karnataka | India

Dr. Prakash S

Principal

East Point College of Engineering and Technology, Bengaluru

On behalf of whole ASSET- 2021 team, I take this opportunity to welcome all the dignitaries, delegates and participants to the **National Conference on Applied Sciences Synergising the Engineering and Technology (ASSET-2021)** which will be held through digital mode during January 18th-19th, 2021 at EPCET, Bengaluru. It has been a real honour and privilege to serve as the General Chair of the conference.

The conference will span over two days and the conference will provide ample opportunities for Academicians, Researchers, Scientists, Industry Practitioners to exchange their views, ideas and experience related to Applied Sciences and their applications in Engineering & Technology.

We would like to express our appreciation to the organizing committee and all the colleagues for their enthusiastic and hard work in organising this conference.

We greatly appreciate the authors for their outstanding paper contributions and we thank them in advance for their participation. We also value the time spent by the expert reviewers for paper evaluation efforts. We are fortunate to have leading eminent speakers at our conference to share their experience and views in the related field.

I am sure that you will have a great time at this conference, and find it a stimulating and informative meeting. I wish the conference a great success.

Dr. Prakash S

OUR INSPIRATION AND PATRONS

INSPIRATION

Late Dr. S. M. Venkatpathi, Founder Chairman, EPGI.

CHIEF PATRON

Smt. B.L. Ramadevi Venkatpathi, Chairperson, EPGI

PATRONS

Shri S.V. Pramod Gowda, CEO, EPGI

Shri S.V. Rajiv Gowda, CEO, EPGI

Shri Peter Francis, Secretary, EPGI

GENERAL CHAIR

Dr. Prakash S, Principal, EPCET

CONVENER

Dr. G. Maruthi, Prof., HOD-Physics, EPCET

PUBLICITY CHAIR

Dr. Doreswamy. H.S, Prof., HOD-Maths, EPCET

ORGANISING CHAIR

Dr. A. K. Shukla, Prof., Chem., EPCET

CO-ORGANISING CHAIR

Dr. Rangaraju, Assoc. Prof., Maths, EPCET

ACADEMIC ADVISORY COMMITTEE

Dr. RMVGK Rao, FNAE, DVP (AICTE-INAE), Former Sci. G -CSIR-NAL

Dr. Sreenivasa Rao, Assoc.Prof. Chem, DSU

Shri S. Sridhar, Former Addl Director, CPRI

Dr. S. Adimurthy, Sr. Prin. Sci., CSIR-CSMCRI, Bhavnagar

Dr. Jayaram Naidu, National Consultant, UNIDO, Fmr. Joint Dir.-CPRI

Dr. Ashok Kr, Assoc Prof. Chem, VIT, TN
Dr. PV Reddy, Former Joint Dir., CPRI
Dr. Srilakshmi C, Assoc. Prof., Geetam Univ
Dr. Shailly K. Rajusth, Qual. Services, Merck
Dr. T.K. Sateesh, Prof., HOD, CSE, EPCET
Dr. Yogesh, Prof., HOD, ECE, EPCET
Prof. Kemparaju, HOD, ISE, EPCET
Dr. Nagaraj Sitaram, Prof., HOD, CIV, EPCET
Dr. Harishanand K.S., Prof., HOD, ME, EPCET
Dr. Sivadasan M., Prof, Head-IQAC, EPCET
Dr. G. Sahadeva, Prof., ME, EPCET

ORGANISING COMMITTEE

Mr. Srinivas Gowda, Asst Prof, Phys, EPCET
Mrs. Rekha C, Asst. Prof., Chem, EPCET
Ms. Sumitha, Asst Prof., Phys, EPCET
Dr. I. Manimozhi, Assoc. Prof, CSE, EPCET
Ms. Gayathri, Asst Prof, Maths, EPCET
Dr. Jayanti Mishra, Asst. Prof., Chem, EPCET
Mrs. Shilpa Patil, Asst. Prof., CSE, EPCET
Mr. Ravindra, Asst Prof, Maths, EPCET
Dr. Chaithra, Asst Prof., Maths, EPCET
Mrs. Gowthami, Asst Prof., Maths, EPCET
Mr. Dhananjay Kr., Head, Placement, EPCET

ABOUT THE INSTITUTE

East Point College of Engineering and Technology (EPCET) established in the year 1999, functions under the aegis of M G Charitable Trust Located in sprawling campus of 90 acres in the eastern suburb of Bangalore. The college is affiliated to VTU Belgaum. Currently, East Point College of Engineering and Technology offers several UG courses in different Branches of engineering in addition, the college also offers PG courses in the emerging fields of Engineering. Presently over 3500 students are pursuing their Technical education in various streams of BE, M.T ech. and PhD. Along with Integrated Learning Program from various domains such as: Salesforce, AWS, UiPath, VMware, Robotics, Automation, Machine Learning, Deep Learning, IOT, aerospace, 3-D printing etc.

ABOUT THE CONFERENCE

National Conference on Applied Sciences Synergising the Engineering and Technology (ASSET-2021) will be held online during January 18th-19th, 2021 and is organised by the EPCET Bangalore. It will bring distinguished Academicians, Scientists/Engineers, R&D and Industry professionals and Research Scholars on to a common platform for sharing their views, ideas and experience related to Applied Sciences and their applications in Engineering & Technology through Invited lectures, Paper presentations, interactions and discussions during the conference.

CONFERENCE THEME & SCOPE

Conference Theme & Scope National Conference on Applied Sciences Synergising the Engineering and Technology (ASSET-2021) will be held online during January 18th -19th, 2021 and is organised by the EPCET Bangalore. It will bring distinguished Academicians, Scientists/Engineers, R&D and Industry professionals and Research Scholars on to a common platform for sharing their views, ideas and experience related to Applied Sciences and their applications in Engineering & Technology through Invited lectures, Paper presentations, interactions and discussions during the conference.

CHEMISTRY (ALL BRANCHES)

- ✓ Materials Science
- ✓ Environmental Science
- ✓ Biomaterials and Composites
- ✓ Materials' Characterization
- ✓ Nanoscience & applications
- ✓ Energy conversion/Storage systems

PHYSICS (ALL BRANCHES)

- ✓ Nanomaterials & thin films
- ✓ Non-linear optical materials
- ✓ Semiconductors & Dielectrics
- ✓ Photonic materials & Plasma physics
- ✓ Superconducting materials
- ✓ Crystallography & Ferroelectricity

MATHEMATICS (ALL BRANCHES)

- ✓ Fluid Dynamics
- ✓ Graph Theory
- ✓ Operation Research
- ✓ Differential Equations
- ✓ Algebra
- ✓ Complex Analysis

CONTENTS

National Conference on Applied Sciences Synergising the Engineering and Technology
Print ISSN: 2395-6011 | Online ISSN: 2395-602X (www.ijsrst.com)
© 2021 IJSRST | Volume 8 | Issue 2

Innovation, Science & Technology : Factors to Society and Economy

V. Krishna Murthy
Research Professor, Department of Chemistry, Dayananda Sagar University, Innovation Campus, Hosur Main Road, Kudlu Gate, Bengaluru, Karnataka, India

ABSTRACT

Innovation, engineering, science and technology are the terms that are closely related. The discussion deliberated in the article relates know how these are linked and how they are ultimately related to economy and industrial progress. Innovation is a means to changes that are induced and triggers engineering and technology. Science initiates the chain of the events and a synergy evolves in the process. The science and technology, although do possess certain differences, very are closely related. They go hand in hand and both play a vital role in our lives. It is important to do a foresight exercise as a plan to delineate short, mid and long term ramifications for an enterprise that is an eventual entity with synergistic contribution of science and technology. overt indulgence to technology have a few negative influences and hence being aware and cautious is essential. Robust science and technology policy has a potential to influence economic development. Governmental fostering technology by prioritizing fund allocation on all possible levels is conducive to overall development. Science, engineering and technology and synergism with this admixture is therefore vital. They are integral and significant to factors to the economic development and society.
Keywords : Society, Economy, Robust science and technology policy

I. INTRODUCTION

Innovation, engineering, science and technology are the buzz words that are in vogue at present times. The students, parents and youth get into an atmosphere of excitement and activity when the will have to choose an option to pursue their higher education. It is however, important to know the real meaning and right perspectives of these words. What is good about these words, how they are related, is it close or distant, how they contribute to industry, economy, society are a few common questions that is worth contemplating

It has been a changing world, ever. The change inducing agents are generally subtle and not highly linked to related fields. In this aspect, innovation, engineering, science and technology are in fact closely operating and inter-related so much that often one means the other. The foregoing discussion relate to a better understanding of these in correct perspective as well as pave way to appreciate their inevitability to the service of social, economic and industrial developments. The technology has made everyone more productive and science has enabled technology. If one plus one is two, it could be eleven, thus there is an emergence of synergism.

II. METHODS AND MATERIAL

Innovation:

Inventing something that is novel, new for the first time and making things or even a new practice or process for release of new things is referred to as innovation. The thing per say could be a new product, a new way of doing something or a new way of even thinking. It is most commonly associated with business and technology. It could be any field where people introduce change, including the arts, medicine, politics, cooking, language—even philosophy and religion. For example, the internet - that has *changed* the society.

History:

Looking at the past, the actual science policy came into real terms and existence during imminent close of the World War II (1939-1945). There was so much of loss of all sorts, all round and the necessity to come out of the low economy, poverty as well as unemployment the industrial revolution very obviously originated and emerged into an intensive activity. The late 1960s saw the technology driven galore of industrial activities which are always associated with inventions, discoveries, technology, production on a mass scale and consequent developments in the sphere of economy. Making new tools for the first time of a purpose, for example converting a mass of granite piece to a shrapnel dates stone-age history. There was a dire need for governance of these surge of activities and the governments focus therefore had to be the establishment of an innovation policy. The private sector followed the suit and complied to these innovation policies.

Differences between Science and Technology:

Although closely related the science and technology has a few differences worth reckoning. They are distinct in connotation and they blend so well that synergy springs when the scientific theories invented are put to practice by technology. The following table presents a few notable differences between science and technology. However, it is not an exhaustive list of differences.

Table-1: Principal Differences Between Science & Technology

SCIENCE	TECHNOLOGY
'Scientia' (Latin): Knowledge Leads to the establishment of a hard fact	Techne' (Latin): Craft; logia:Study generated with both science and engineering
Involves observation and experimentation	Involves invention and production
Observing natural world , building up theories	Putting such theories into practice
About ideas, human intellectual creations	Uses concrete materials to build the product
Reasons 'why'	Answers 'how'
Is about reductionism→ isolation and then defining the distinct concepts	Deals with the integration of demands, theories, ideas, and data
Searches and theorizes the causes	Searching and theorizing new processes
Draws accurate conclusions from good theories and precise data	Takes good decisions from incomplete data and approximate models.

Science & Technology – Closely Related:

The technology development and consequent outcomes are spinoff results of knowledge and methods derived from science, and hence they are chief inputs. Science is useful in the establishment of explanations of why technological interventions succeeded or failed in the past. The explanations for the obvious questions such as why and why not is addressed and provided by the science. Both the scientific studies as well as the related technology thrive in a natural manner. Solar panels which is responsible for the generation of electrical energy and power paved way for a new technology. Thus, Science and technology are closely related, they go hand in hand and both play a vital role in our lives.

Prudence – The Approach:

Strategizing to have visualization and understanding of future of science, technology, economy and society is a significant and an essential exercise. Having an idea of emerging generic as well as technology is disruptive in nature facilitates preparedness. In all the probabilities this *foresight* results in an exponential economic and societal implications that are highly beneficial (Irvine and Martin, 1984)

Time Horizon of Foresight:

A new enterprise in the business space can and should never be static in both size and reach. It has to evolve into bigger and better and the foresight exercise for this has to commence well before the business in actual initiates. This foresight exercise preferable delineate short, mid and long term ramifications so that the time of horizon for the enterprise is visualized well. The new enterprise shall be subjected to extrapolation in the short-term and the strategic planning in the mid-term leading to foresight planning to continually grow and perform. In all the stages the economy will also commensurately progress and thus resulting in a planned, stage or phase-wise overall development. The associated fact in such a foresight exercise is the ever changing technology that metamorphoses with the undercurrent and reliance on science. Dennis Gabor, a Dutch scientist believed that "The future cannot be predicted, but it can be invented".

Characteristics of Foresight: Following are the few points that are the characteristics of a foresight exercise.

- Well defined technology is a consideration for foresight exercise;
- Projections of probable advances in the technology;
- The speed of the occurrence these advances;
- Definition of potential follow-on technologies;
- Projections of how large the market for the emerging technology will be and how that market will develop.

Science – to - Business Lag Time:

Ideation, problem statement, hypothesis, objectives, experiments, results, findings, facts and theories are the principal stages to establish objective facts following strict regimen of research methodology in science. To evolve at theory and or a principle, it takes time and rigorous analytical as well as synthetic thinking. Obviously, the emergence of theory takes substantial time. This is the true nature of fundamental research.

Based on the principles bestowed by science and scientists, engineers build and create, construct structures. Engineers build models and prototypes, provide proofs of concepts and make the principles a reality in applications that are useful to society. Thus they are the architects of applied science and engineering. It is now the time for technology to intervene and scale up, productize, gadgetries and make ready to manufacturing production in industries. Thus science has now become an industrial product. Once product emerges, it gets into the rigmarole of marketing which is a notion of business enterprise.

If one estimates the time for all these to happen, by and large, the science consumes about 5 to 20 years, engineering & technology take about 3-6 years an industrial product comes out in about 1 to 3 years.

Technology Foresight Process:

The logical flow of steps in the technology foresight process are - Define The Question, do an analysis of global trend of the technology that includes science-technology and market dynamisms, growth opportunities relying on national capacity and technology interactions and finally the emergence of growth platforms.

Technological innovations advanced swiftly sustained by the huge amount of resources. No one can deny to the fact that the technological advancement has been accelerating. The most celebrated discoveries in technology sphere as of now are the computers, entertainment, nanotechnology, materials science, renewable energy, space travel, and medicine. Currently, abundant discoveries in mobile media and technology are, creating a new world of possibilities. Technology is rather associated with *speed*, hence *disruptive technology* is rather *predatory* in nature. The latest or advanced version of technology decimates its own previous version. This extinction rate upsets in a spiral of changes that are often difficult to cope. The only way is to adapt, *change* swiftly and rapidly by *foresight and strategy*.

III. RESULTS AND DISCUSSION

ECONOMIC DEVELOPMENT:

Innovation & technology are key drivers of the economic development. Innovation includes creating new products and services or new or improved processes; new delivery or distribution methods; new industries and new management. practices or organizational structure.

The Technology for Development:

This refers to the use of tools, machines, materials, techniques and sources of power to make work easier and more productive. The synergy emerging from science-technology and economic development focuses on making things happen.

S&T POLICY:

It is essential that the Science and Technology policy of any entity or a geographical country shall promote economy, else there is seldom any utility of S&T. In fact the development of economy is very synonymous to the growth and development of science and technology.

S&T policy is to be designed to resolve the existing disconnect between sociopolitical and economic planning and science and technology in tandem with the objectives of development plans. Building a large, strong, diversified, sustainable and competitive economy is the essence of evolution of S& T policy., that guarantees a high standard of living and quality of life. The policy specifically provide a strong platform for science, technology and innovation commitment with the economic transformation that is people centered. The government has to encourage the establishment and strengthening of organizations, institutions and structures for science and technology development facilitate the acquisition of knowledge to adapt, utilize, replicate and diffuse technologies for the growth of Small and Medium Enterprises (SMEs), agricultural development, food security, power generation and poverty alleviation.

Negative Aspects Associated With Technology:

The technology, while inherently possess benefits as a key promoter of economy has a tinge of hazard and risk, too. Since majority of technologies ultimately solves problems and makes life easy in society, the extended use of these technologies promotes a more sedentary lifestyle, which is known to have negative health effects, such as contributing to: 1. obesity 2. cardiovascular disease 3. Type 2 diabetes 4. premature death Prolonged computer usage and digital work : Eyestrain, sleep problems, reduced physical activity; In children – lack of concentration, lack of creative activity, aggressive behavior, addiction to technology.

There is a link between social media and mental health: Psychological and physical issues, such as eyestrain and difficulty focusing on important tasks. More serious mental problem like depression could result from profuse use of social media for such a facility often do not consider individual end-user susceptibility or vulnerability. Isolation and remaining in virtual world more than physical world is yet another negative effect of overt usage and reliance of technology. The technologies, such as social media, are designed to bring people together, yet they may have the opposite effect in some cases. Technological revolutions such as the industrial revolution and the agricultural revolution cannot be ignored either. Probably the worst use of technology — and the science which informs its development — has been weapons of mass destruction. The ability to create materials that we use in our everyday life, the ability to feed a massive amount of people are due to the development of technological innovations.

IV. CONCLUSION

The Future of Science, Technology & Society:

By any measure, basic scientific research has made monumental contributions to technology and national priorities. There is an inherent strong association between new technology and science. Science informs technological advancements. We rely on theories on physics, material science, electricity, chemistry, etc to develop new technologies.

The economic benefits coming from technologies, governments supports research, supported with public funds for societal priorities. There should be no doubt that science and society will continue to co-evolve. The government should affix adequate and right funding priority so that this evolution is not lead to adverse effects.

V. REFERENCES

[1]. Mohammadreza Abdolmaleki1, Shahram Yazdani, Sedigheh Momeni, Nader Momtazmanesh. A Social Accountable Model for Medical Education System in Iran: A Grounded-Theory, Journal of Medical Education, 2017; 16(2):55-70.
[2]. https://www.differencebetween.com/difference-between-science-and-technology-2/
[3]. https://stemsynergy.org/innovation-technology/
[4]. https://www.researchgate.net/publication/319456206_The_Role_of_Science_and_Technology_in_Development
[5]. https://www.sciencedirect.com/science/article/abs/pii/S0040162510001307
[6]. https://en.wikipedia.org/wiki/Dennis_Gabor

National Conference on Applied Sciences Synergising the Engineering and Technology
Print ISSN: 2395-6011 | Online ISSN: 2395-602X (www.ijsrst.com)

Corrosion Inhibition of Carbon Steel by Using Rhoeo Discolor Leaves Extract in Acid Media

Netravati Gayakwad*[1], Vittalgouda Patil[1], B. Muralidhara Rao[2]

*[1]Department of Engineering chemistry, Rural Engineering College, Hulkoti, India

[2]Department of Chemistry, Govinda Dasa college, Surathkal, Karnataka, India

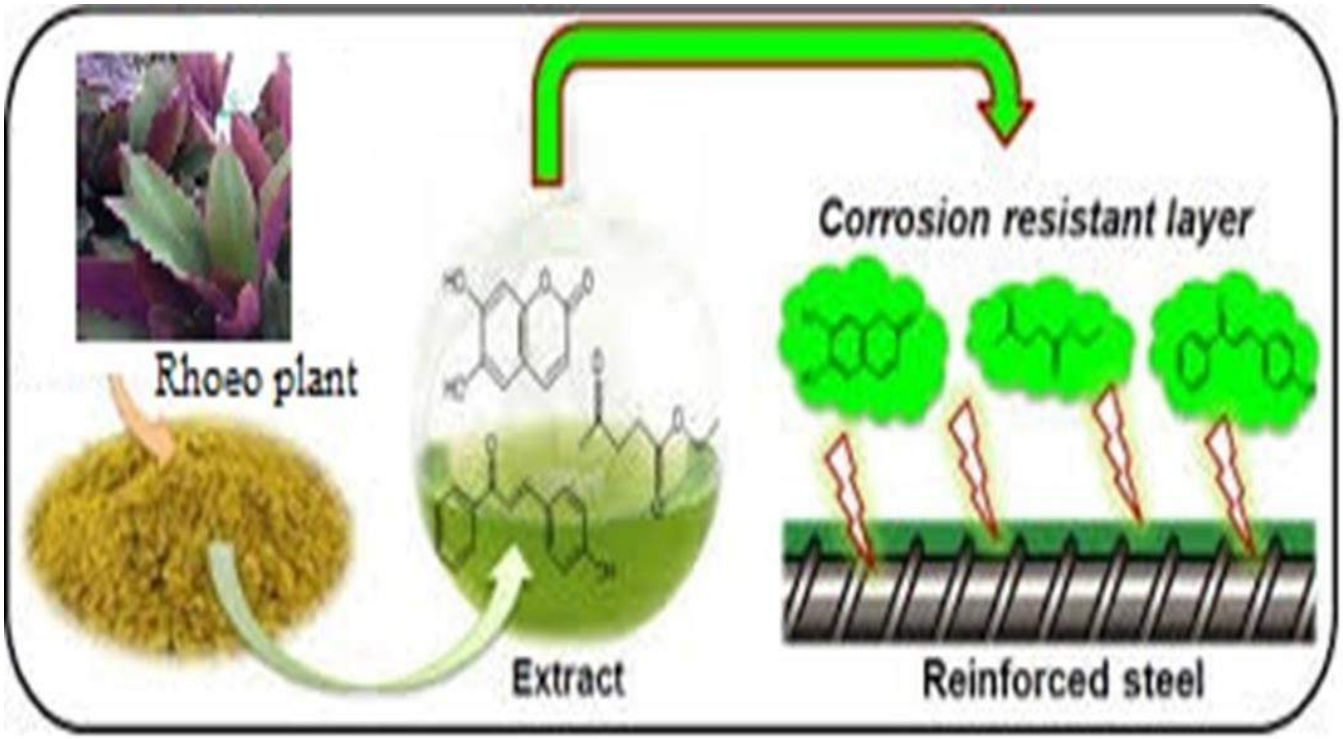

ABSTRACT

Green corrosion inhibitors are biodegradable and do not contain heavy metals or other toxic compounds. These inhibitors are easily available in nature, cheap and do not contain toxic compounds. The inhibition efficiency of aqueous extract rhoeo leaves extract on the corrosion of carbon steel in 0.1g/L-0.5g/L was investigated by potentio-dynamic polarization and electrochemical impedance measurements. The corrosion rate of carbon steel and inhibition efficiency of the rhoeo leaves extract were calculated. The results obtained showed that rhoeo leaves extract could serve as an effective inhibitor for the corrosion of carbon steel in acid media. Inhibition was found to increase with increasing concentration of the extract. Potentio-dynamic polarization curves revealed that this extract acts as a mixed type inhibitor and the inhibition efficiency of up to 66% and impedance 86% can be obtained.

Keywords: Corrosion, Corrosion Inhibition, Carbon steel, Rhoeo discolor, HCl

I. INTRODUCTION

Carbon steel is one of the most important alloys which frequently used in wide industrial applications in partially [1]. It is used in manufacture of petroleum pipelines, pumping and stations for agricultural water irrigation. A less severe treatment than pickling like acid cleaning is used for final finish of metal surface before painting, plating or storage. Iron and iron based alloys of different grades are extensively used in numerous industrial and engineering applications, including construction and design [2,3]. Where they are developed in various service environment containing acids, alkaline, and salt solutions. The extract of leaves, peels, seeds, fruits and roots have been reported as effective corrosion inhibitor in different aggressive environment [4]. One promising strategy for minimizing the steel inhibitors to the corrosive media. Inhibitors are two types synthetic and natural. Synthetic inhibitor which consisting of chromates and dichromate's based inhibitors such as zinc chromates are reported to have inhibition efficiency however, they are toxic to human and environment because of which their use has been restricted or banned [5,6]. Most other synthetic inhibitors are toxic, expensive and pose a hazard to environment ,this has prompted research to find non toxic, biodegradable, cheap and effective green alternatives apart from various characteristics of plant extract [7,8] (containing N S & O heteroatom's) and complex organic species include tannin, alkaloid and N-based carbohydrates and proteins as well as hydrolysis products. In recent work [9-16] synergetic inhibition of carbon steel has been reported.

We propose to work on the inhibition of corrosion in carbon steel both in presence and absence of HCl (from 0.1M to 0.5M) along with addition of extract of Rhoeo discolor plant at dosage of 0.1g/L to 0.5 g/L at 30ºC

II. METHODS AND MATERIAL

2.1 Experimental Procedure

2.1.1 Preparation of Rhoeo discolor leaves extract

The plant belongs to kingdom plantae, family commelinaceae with popular name boat lilly or garden plant [17]. The leaves of rhoeo discolor plant were collected around 4-5 kg squeezed and then treated with ethanol. Later this layer is separated in funnel the aqueous layer is treated with ether to separate chlorophyll. The aqueous extract is allowed to settle down for a day. The extract is then washed with acetone and dried in air. The whitish green solid extract is now ready as the inhibitor of corrosion.

2.1.2 Specimen Preparation

The carbon steel test specimen of size 1.06 cm^2 exposed part bar composition (weight %) C = 0.3%, Si= 0.08%, S = 0.025%, Mn = 0.13% and rest Fe were used for electrochemical studies. The carbon steel were polished successively using different grade of sand paper i.e 100,150,300,320,400,600,1000,1200 and 1500.It was then degreased with acetone, rinsed with double distilled water and finally dried before each experiment.

2.1.3 Electrolyte Preparation

Hydrochloric 1M concentration of acid was prepared using double distilled water. Then HCl is standardized by standardized sodium hydroxide solution required lower standard HCl solutions 0.1M,

0.2M, 0.3M, 0.4M and 0.5M are prepared from standardized HCl with proper addition of double distilled water.

2.2 Methods

2.2.1 Electrochemical Measurements

Potentiodynanic polarization studies and electrochemical impedance measurements were carried out using Gill AC (ACM Instrument) version 5.14 software. A conventional three electrode arrangement was used where carbon steel embedded in araldite served as the working electrode with an exposure area of 1.06 Cm^2.The saturated calomel electrode coupled with platinum electrode functioned as the reference & auxiliary electrode respectively. The potential of the working electrode in 0.1M to 0.5M HCl was measured against secondary calomel electrode in presence and absence of various concentration of inhibitor at 30ºC. Prior to each experiment, the working electrode was immersed in the test solution for a period of 45 minutes to achieve stable corrosion potential values, thereafter measurements of potential is made always with respect to reference electrode. Polarization and electrochemical impedance is performed immediately after electrochemical impedance spectroscopy (EIS) and studies is made on the same specimen without any further surface treatment in the same medium.

2.2.2 Surface Analysis

The surface of mild steel is analyzed by JEOL JSM6380LA using analytical scanning electron microscope. Steel specimen of size 1cm x 1 cm x 0.5 cm is immersed in 0.1M HCl for 24 hrs in presence and absence of inhibitor. Further, the specimens is removed, cleaned with double distilled water, rinsed with acetone, dried and analyzed by SEM.

III. RESULTS AND DISCUSSION

3.1.1 Potentiodynamic polarization studies

The effect of different concentration of rhoeo leaves extract on anodic and cathodic behavior of carbon steel in 0.1M to 0.5M at 30ºC was studies and resulting tafel plots are shown in fig-1. Values of corrosion parameters like corrosion current density (I_{corr}), corrosion potential (E_{corr}), anodic tafel slope (b_a) and cathodic tafel slope (b_c) and inhibition efficiency (IE%) are tabulated in table 1.corrosion current density (I_{corr}) value are evaluated by using tafel extrapolation.

Table-1.Polarization parameters for carbon steel in 0.1-0.5M HCl at 30ºC with Rhoeodiscolor extract of polarization method

Con of acid	Dosage	I_{corr}	Tafel		Corrosion rate	surface coverage	I.E(%)
			b_a	b_c			
0.1M	BLANK	0.21	238.93	286.16	1.67		
	0.1	0.14	237.61	275.83	1.46	0.03333	33.33

	0.2	0.12	225.47	270.74	1.41	0.04585	45.85
	0.3	0.11	221.47	255.97	1.09	0.04761	47.61
	0.4	0.09	217.15	243.03	0.85	0.05714	57.14
	0.5	0.07	213.9	218.44	0.77	0.06666	66.66
0.2M	BLANK	1.42	263.84	277.35	4.13		
	0.1	1.39	219.03	260.36	2.86	0.0021	2.11
	0.2	1.24	215.77	259.72	2.17	0.01267	12.67
	0.3	1.11	207.55	247.83	1.56	0.021.83	21.83
	0.4	0.98	198.61	245.85	1.51	0.03098	30.98
	0.5	0.71	182.94	217.83	1.37	0.05	50
0.3M	BLANK	3.1	158.86	223.58	11.71		
	0.1	2.89	132.26	143.93	9.62	0.00677	6.77
	0.2	2.71	117.29	127.96	4.46	0.01258	12.58
	0.3	2.57	113.78	126.91	4.33	0.01709	17.09
	0.4	2.18	108.64	123.31	3.36	0.02967	29.67
	0.5	1.56	107.36	121.99	3.18	0.04967	49.67
0.4M	BLANK	3.52	192.74	164.2	20.13		
	0.1	2.91	117.29	134.65	13.99	0.01732	17.32
	0.2	2.63	117.39	122.27	12.75	0.02528	25.28
	0.3	2.21	113.06	120.77	11.86	0.03721	37.21
	0.4	1.89	109.66	119.14	10.61	0.0463	46.3
	0.5	1.84	108.59	117.8	9.03	0.04772	47.72
0.5M	BLANK	3.77	204.82	228.45	22.58		
	0.1	3.63	204.21	203.69	15.28	0.00371	3.71
	0.2	3.45	213.82	195.2	12.18	0.00848	8.48
	0.3	3.41	195.02	163.11	11.16	0.00954	9.54
	0.4	3.17	119.19	107.82	10.53	0.01591	15.91
	0.5	2.26	114.45	105.09	9.4	0.0405	40.05

The inhibition efficiency was calculated from the measured corrosion current density values using the following expression

$$IE\ \% = \frac{I_{corr} - I^{*}_{corr}}{I_{corr}} \times 100$$

Where icorr and i*corr are corrosion current in the absence and presence of plant extract.

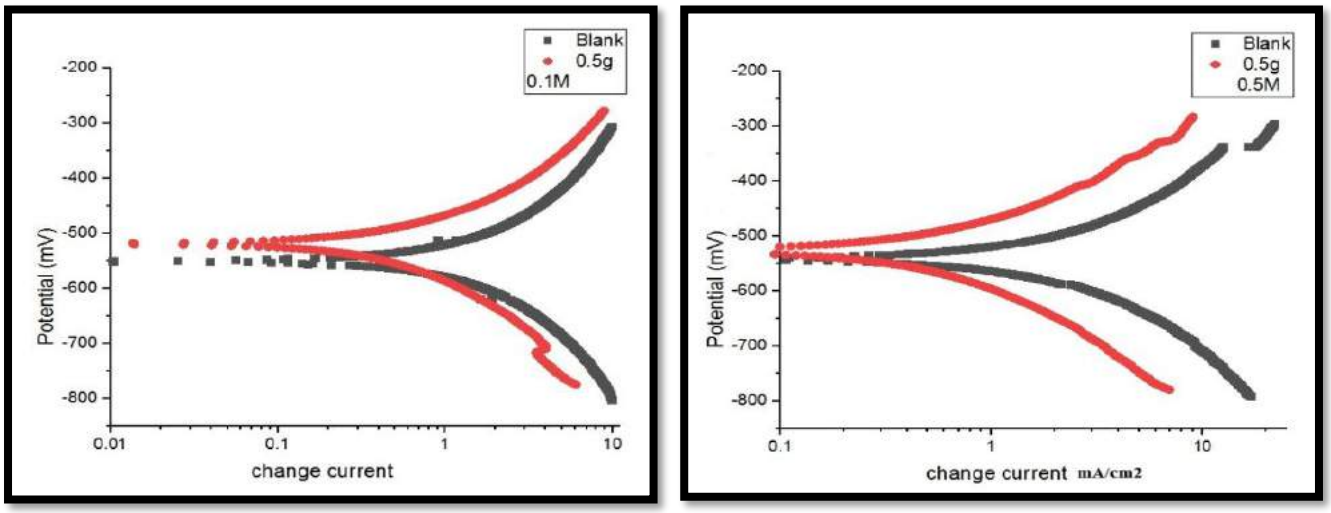

Figure-1 Potentiodynamic polarization curves of carbon steel in 0.1M & 0.5M HCl with 0.5g/L inhibitor and without inhibitor.

All polarization curves were taken at end of the exposure time to avoid alteration of the surface, from the polarization curves, corrosion current densities were obtained by tafel extrapolation. If the shift in Ecorr value is greater than 85 mV in either anodic or cathodic direction, the inhibitor can be classified as anodic or cathodic type respectively. However if the shifts in Ecorr values is less than 85mV, the inhibitor suppress the reactions occurring at both anodic and cathode there by behaving as mixed type inhibitor. It can be observed in table-1, Ecorr value shifts only slightly in both anodic and cathodic diections, which is less than 85 mV, therefore rhoeo extract can be classified as mixed type inhibitor [18,19].Change of ba and bc values supports modification in anodic and cathodic reactions due to adsorption phenomenon, which is due the involvement of different type of mechanism.[20,21]

3.1.2 Electrochemical impedance spectroscopy (EIS)studies

Elcctrochemical impedance spectroscopy measurements for carbon steel in 0.1M - 0.5M HCl in the absence and presence of inhibitor concentrations were carried out at 30ºC. The data obtained is represented as nyquist plots in figure 2. These plots were used to obtained charge transfer resistance (R_{ct}) values which were further used to calculate inhibition efficiency value by the following formula.

$$IE = \frac{R^*_{ct} - R_{ct}}{R^*_{ct}} \times 100$$

Where R*ct and Rct represent the charge transfer resistances in the presence and absence of the inhibitor respectively.

Table-2 AC impedance parameters for carbon steel in 0.1 to 0.5M HCl at 30ºC with Rhoeo discolor extract.

Con of acid	Dosage	R_{ct}	C_{dl}	I.E(%)
0.1M	BLANK	$5.56x10^{1}$	$2.97x10^{-4}$	
	0.1	$1.26x10^{2}$	$1.96x10^{-4}$	55.87
	0.2	$1.44x10^{2}$	$1.95x10^{-4}$	61.38
	0.3	$2.46x10^{2}$	$1.075x10^{-4}$	77.39

	0.4	$2.51x10^{2}$	$1.408x10^{-5}$	77.8
	0.5	$4.15x10^{2}$	$4.94x10^{-5}$	86.6
0.2M	BLANK	$2.87x10^{1}$	$4.69x10^{-4}$	
	0.1	$4.75x10^{1}$	$4.40x10^{-4}$	39.57
	0.2	$5.77x10^{1}$	$3.90x10^{-4}$	50.25
	0.3	$5.82x10^{1}$	$3.65x10^{-4}$	50.68
	0.4	$7.18x10^{1}$	$3.50x10^{-4}$	60.02
	0.5	$1.15x10^{2}$	$3.04x10^{-4}$	75.04
0.3M	BLANK	$4.09x10^{1}$	$4.68x10^{-4}$	
	0.1	$4.92x10^{1}$	$4.03x10^{-4}$	16.86
	0.2	$5.09x10^{1}$	3.75x10-4	19.64
	0.3	$6.33x10^{1}$	$3.14x10^{-4}$	35.38
	0.4	$8.07x10^{1}$	$2.92x10^{-4}$	49.31
	0.5	$1.43x10^{2}$	$2.09x10^{-4}$	71.39
0.4M	BLANK	$6.05x10^{1}$	$1.025x10^{-3}$	
	0.1	$6.85x10^{1}$	$5.32x10^{-4}$	11.67
	0.2	$6.97x10^{1}$	$3.48x10^{-4}$	13.19
	0.3	$7.64x10^{1}$	$2.2x10^{-4}$	20.81
	0.4	$1.007x10^{2}$	$1.66x10^{-4}$	39.92
	0.5	$1.83x10^{2}$	$1.51x10^{-4}$	66.93
0.5M	BLANK	$2.07x10^{2}$	$1.99x10^{-4}$	
	0.1	$2.47x10^{2}$	$1.78x10^{-4}$	16.19
	0.2	$2.79x10^{2}$	$1.61x10^{-4}$	25.8
	0.3	$2.93x10^{2}$	$1.47x10^{-4}$	29.35
	0.4	$3.46x10^{2}$	$1.27x10^{-4}$	40.17
	0.5	$3.88x10^{2}$	$1.14x10^{-4}$	46.64

The impedance response of carbon has significantly changed on addition of this inhibitor. For the analysis of impedance spectra contain a single capacitive semi circle, a polarization resistance component /charge transfer component (Rct) and capacitance component (Cdl). A corresponding increase in Rct value and decrease in Cdl with increase in the concentration of rhoeo leaves extract is depicted in table-2.this is attributed to increase in chamber of adsorption molecule of leaves extract forming a barrier between carbon steel surface and aggressive acid environment inhibiting the corrosion process[22,23]. As we observed the rate of corrosion decrease with increasing the inhibitor concentration up to certain limit, beyond that concentration the corrosion rate again increases .It seems that at high inhibitor concentration beyond a limit, the inhibitor substances can no more gets adsorbed on the metal substrate, rather dissolves in acid solution and increase the acid concentration.

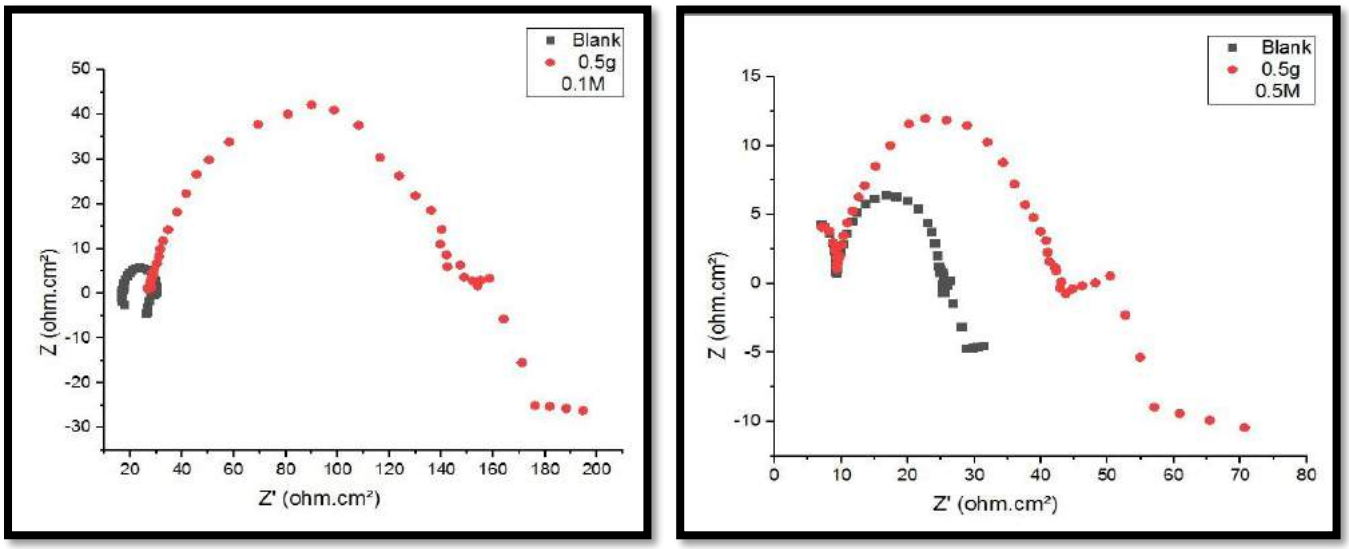

Figure-2 AC imprdance spectroscopy of carbon steel in 0.1M & 0.5M HCl with 0.5g/L inhibitor and without inhibitor.

3.2 Surface Analysis

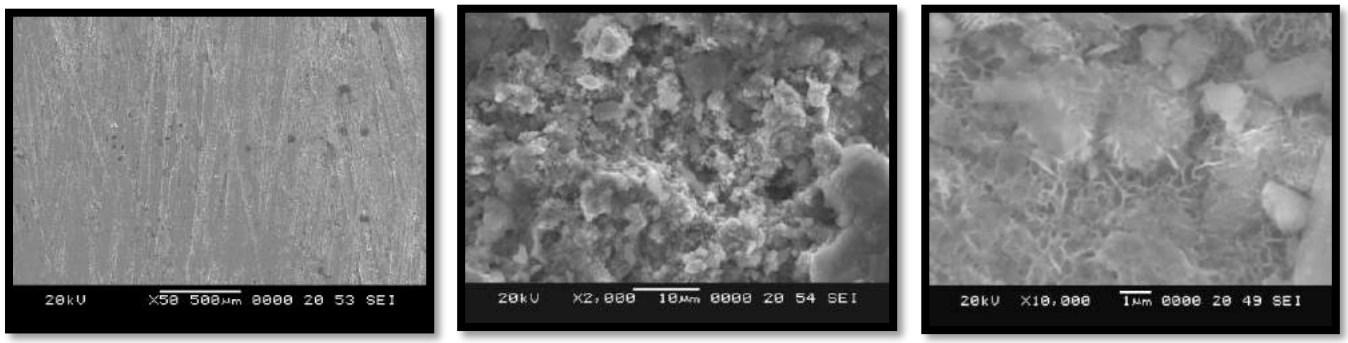

Polished specimen **Absence of inhibitor** **Presence of inhibitor**

Figure-3 SEM Results of carbon steel with or without inhibitor.

Fig.3exhibits the morphological features of specimens before and after soaking in an acidic aggressive environment for 30 minutes. By contrast the surface of C-steel is comparatively smooth and the corrosion grooves are apparently minor compared with blank solution in the presence of corrosion inhibitor. A barrier layer is developed between the metal and the acid medium as corrosion inhibitor becomes adsorbed on the C-steel surface, which effectively suppresses the dissolution reaction. These observations are in excellent agreement with the electrochemical data.

3.3 Mechanism of inhibition

The adsorption of inhibitor on metal surface is mainly due to these metabolites such as flavonoids, saponins, carotenoids, anthocyanins, terpenoids, ferulic acid, chloregenic acid, vanillic acid, p-coumaric acid and steroidal compounds. A weak wander wall forces exist between nuclei of inhibitor to the metal surface to make bond and formation of protective layer on the metal surface to inhibit the rate of anodic and cathodic reactions.[24,25,26]

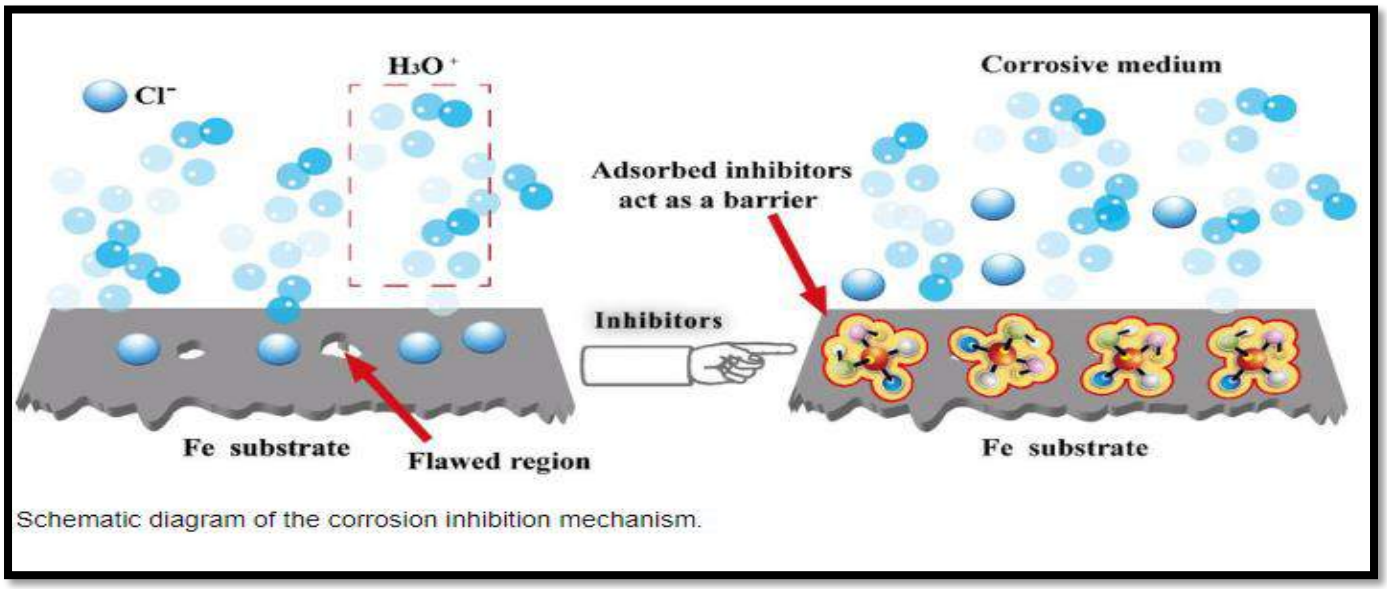

Figure-4 Mechanism of rhoeo leaves extract on surface of C-steel.

IV. CONCLUSION

1. The corrosion rate decreases with increase in concentration of inhibitor and inhibition efficiency also increases with increase in inhibitor concentration of Carbon steel in acidic media. The maximum Efficiency in 0.1M HCl of 0.5g/L dosage inhibitor measured by electrochemical polarization is 66.66% and by impedance is 86.6%.
2. The potentiodynamic polarization studies conclude that rhoeo discolor plant extract controls both anodic and cathodic reactions.
3. EIS studies reveal increase in resistance (Rct) and decreases in double layer capacitance (Cdl) with Respect to increase in the concentration of extract. This behavior is found to be due to the formation of dense protective layer on the surface of mild steel.
4. The surface morphology studies of the mild steel substrate by SEM conclude the formation of protective layer.

V. ACKNOWLEDGEMENT

I express a deep sense of gratitude to Department of chemistry NITK surathkal for providing Lab facilities. I express a deep sense of gratitude to Dr.Geeta Nazareth ,Department of Chemistry St Aloysius College Mangalore and Prof Krishna Gurulhosur and S.S.Sadamal Department of Engineering Science, Rural Engineering College Hulkoti, for their kind support and guidance which have been great value in this study.

VI. REFERENCES

[1]. Kenneth Kanayo ALANEME and Sunday Joseph OLUSEGUN "Corrosion Inhibition Performance of Lignin Extract of Sun Flower (Tithonia Diversifolia) on Medium Carbon Low Alloy Steel Immersed in H2SO4 Solution" Leonardo Journal of Sciences ISSN 1583-0233,Issue 20, January-June 2012 p. 59-70.

[2]. K. K. Alaneme1, Y. S. Daramola1, S. J. Olusegun1, A. S. Afolabi, "Corrosion Inhibition and Adsorption Characteristics of Rice Husk Extracts on Mild Steel Immersed in 1M H2SO4 and HCl Solutions" Int. J. Electrochem. Sci., 10 (2015) 3553 – 3567

[3]. Kenneth Kanayo ALANEME*, Adetomilola Victoria FAJEMISIN, Sunday Joseph OLUSEGUN, Joseph Olatunde BORODE "Corrosion inhibition and adsorption characteristics of Tridax Procumbens L leaves extract on mild steel immersed in 1M HCl solution" Leonardo Electronic Journal of Practices and Technologies ISSN 1583-1078,Issue 29, July-December 2016 p. 43-60

[4]. Mujeeb ur Rahman, Shereen Gul, Mohammad Umair, Adeela Anwar, A. K. K. Achakzai, "Anticorrosive Activity of Rosemarinus officinalis L. Leaves Extract Against Mild Steel in Dilute Hydrochloric Acid" International Journal of Innovative Research in Advanced Engineering (IJIRAE) Issue 03, Volume 3 (March 2016).

[5]. Anjali Peter, I. B. Obot, Sanjay K. Sharma, "Use of natural gums as green corrosion inhibitors: an overview" Int J Ind Chem (2015) 6:153–164 DOI 10.1007/s40090-015-0040-1.

[6]. J. Buchweishaija,G.S. Mhinzi "Natural Products as a Source of Environmentally Friendly Corrosion Inhibitors: The Case of Gum Exudate from Acacia seyal var. seyal" Portugaliae Electrochimica Acta 26 (2008) 257-265

[7]. C.O. Akalezi, C.E. Ogukwe, E.A. Ejele and E.E. Oguzie, "Mild steel protection in acidic media using Mucuna pruriens seed extract" Int. J. Corros. Scale Inhib., 2016, 5, no. 2, 132–146.

[8]. P. muthukrishnan, K. saravana kumar, B. jeyaprabha, and P. prakash "Anticorrosive Activity of Kigelia pinnata Leaves Extract on Mild Steel in Acidic Media" DOI: 10.1007/s11661-014-2366-2

[9]. B.E.AmithaRaniandBharathiBaiJ.Basu "Green Inhibitors for Corrosion Protection of Metals and Alloys: AnOverview" Hindawi Publishing Corporation International Journal of Corrosion Volume 2012, Article ID 380217, 15 pages doi:10.1155/2012/380217.

[10]. N.Karthiga a], S.Rajendran b], P.Prabhakar c], R.Joseph Rathish "Corrosion inhibition by plant extracts-An overview" Int. J. Nano. Corr. Sci. Engg. 2(4) (2015)31-49.

[11]. M.H. Mahross*, M.A. Taher and M.A. Mostafa "Some Natural Product Extracts As Eco-Friendly Inhibitors On The Corrosion Behavior Of Mild Steel Exposed To 1.0m Sulphuric Acid" IJAPBC – Vol. 4(4), Oct - Dec, 2015,ISSN: 2277 – 4688

[12]. L. Li Liao, S. Mo, H. Qun Luo, N. Bing Li, "Corrosion protection for mild steel by extract from the waste of lychee fruit in HCl solution: experimental and theoretical studies", Journal of Colloid and Interface Science (2018), doi: https://doi.org/10.1016/j.jcis.2018.02.071

[13]. M. Mobin, M. Basik, J. Aslam, Pineapple stem extract (Bromelain) as an environmental friendly novel corrosion inhibitor for low carbon steel in 1M HCl, Measurement (2018), doi: https://doi.org/10.1016/j.measurement.2018.11.003

[14]. Manpreet Kaur Bagga,Ranu Gadi,Ompal Singh Yadav,Investigation of phytochemical components and corrosion inhibition property of ficus racemosa stem extract on mild steel in H2SO4 medium,Journal of environmental chemical engineering, http://dx.doi.org/10.1016/jece.2016.10.022.

[15]. Nurudeen A. Odewunmi, Saviour A. Umoren, Zuhair M. Gasema, Saheed. A. Ganiyu, Qamaruddin Muhamma "l-Citrulline: An active corrosion inhibitor component of watermelon rind extract for mild steel in HCl medium" Journal of the Taiwan institute of chemical engineerings 000(2015) 1-9.

[16]. Palanisamy, G. Maheswaran, A. Geetha Selvarani, C. Kamal and G. Venkatesh, Ricinus communis – A green extract for the improvement of anti-corrosion and mechanical properties of reinforcing steel in concrete in chloride media, Journal of Building Engineering, https://doi.org/10.1016/j.jobe.2018.05.020

[17]. http//google.com

[18]. B Muralidhar Rao*, Gopal M. Gokhale, Ishwar Bhat and S. Rashmi "Study of Adathoda vasica as corrosion inhibitor on mild steel" Der Pharma Chemica, 2015, 7(9):153-160.

[19]. M.A.Quraishi, A.Singh ,V K Singh, D K Yadav, "Green approach to corrosion inhibition of mild steel in hydrochloric acid and sulphuric acid solutions by the extract of murraya koenigii leaves, Mat.Chem.Phy.122(2010)114-122.

[20]. M H Hussin, M J Kassim,The corrosion inhibition and adsorption behavior of Uncaria gambir extract on mild steel in 1M HCl,Mat.Chem,Phy.125(2011)461-468.

[21]. L .Lingjie,Z Xueping ,L Jinglei,H Jianxin, Adsorption and corrosion inhibition of Osmanthus fragran leaves extract on carbon steel Corros.Sci.63(2012)82-90.

[22]. Y.Li, P.Zhao, Q.Liang, B.Ho,Berberine as a natural sources inhibitor for mild steel in 1M H2SO4,App.Surf.Sci.252(2005)1245-1253.

[23]. M.A.V.Gonzalez,J G G. Rodriguez,M G V,Cisneros, I A H Diaz, Use of Rosmarinus officinal is as green corrosion inhibitor for carbon steel in acid medium,Am J.of Analyt.Chem.5(2014)55-64.

[24]. Saviour.A, Umoren (2016) Biomaterials for Corrosionprotection: Evaluation of musterd Seed Extract as ecofriendly corrosion inhibition for X60 steel in acid media Journal of Adhesion Science and Technology (Taylor &Fr)Vol.30(17),1858-1879.

[25]. Parekh.J and Chands.S (2008) Phytochemical screening ofsome plants from Western regions of India, Plant Arch, 8: 657 – 662.

[26]. Rebeca García-Varela 1,2, Rebeca M. García-García 1, Bertha A. Barba-Dávila "Antimicrobial Activity of Rhoeo discolor Phenolic Rich Extracts Determined by Flow Cytometry" Molecules 2015, 20, 18685-18703; doi:10.3390/molecules201018685

National Conference on Applied Sciences Synergising the Engineering and Technology
Print ISSN: 2395-6011 | Online ISSN: 2395-602X (www.ijsrst.com)
© 2021 IJSRST | Volume 8 | Issue 2

Kinetic Spectrophotometric Method for The Determination of Ir(III) by Its Catalytic Effect on The Oxidation of Sulphur Containing Amino Acid by HCF(III) in Aqueous Alkaline Medium

Dr. Anjali Goel[1*], Dr. Savita Garg[2]

[1]Deparment of Chemistry, Kanya Gurukul Mahavidyalaya, Gurukul Kangri University Haridwar, Uttarakhand, India

[2]Deparment of Chemistry, SEA college of Arts, Science and Commerce, K.R.Puram, Bangalore, Karnataka, India

ABSTRACT

A simple kinetic spectrophotometric method has been developed for the determination of ultra trace amount of Ir(III).The method is based on the Ir(III) catalysed oxidation of sulphur containing amino acid by HCF(III) in aqueous alkaline medium. Under the optimum experimental conditions Ir (III) can be determined in the range 0.258 -8.37µg ml^{-1} for cystine and methionine with an maximum average error of 99.5% and maximum relative standard deviation of 1.702%.The effect of few interfering ions have been worked out .For developing the calibration curves in terms of absorbance or reaction rate or pseudo first order rate constant vs. [Ir (III)] plot, absorbance was noted at λmax of 420 nm. The molar absorptivity and sandell's sensitivity are found for cystine 2.83 x 10^3 – 4.11 x 10^3 l mol^{-1} cm^{-1} & 0.0680 – 0.0467µgcm^{-2} and for methoinine 2.31 x 10^3 – 3.27 x10^3 l $mol^{-1}cm^{-1}$ & 0.0834 – 0.0588µgcm^{-2} respectively. The results show that the present method is more simple and sensitive than the reported methods and especially useful in absence of expected interfering ions.

Keywords - Microgram determination, Ir (III), Hexacyanoferrate (III), Oxidation, Cystine and Methoinine

I. INTRODUCTION

In recent year with the increasing interst in the geochemistry of iridium and other platinum group eles. ments higher sensitivity and precision for the analysis of these elements have been required. Iridium is a minor constituent of most platinum metal deposits.Therefore high selective sensitivity, rapid ,economical methods are needed for its trace determination. Some instrumental methods are reported for this purpose[1-5]. However the necessary instruments are expensive day to day and maintenance costs are high and the methods are not from various types of interferences.[6-10]. Anjali et al also reported the kinetic spectrometry methods for the determination of trace iridium based on the catalytic effect of the iridium in the oxidation reaction of alanine[11], Cystine [12] & Isoleucine[13].

Thus in the present study an attempt has been made to determine Ir (III) concentration in micrograms in aqueous alkaline medium by kinetic – spectrophotometric method. The method is based on the oxidation of amino acids like cystine, methionine by hexacyanoferrate (III) catalyzed by Ir (III) in aqueous alkaline medium.

II. METHODS AND MATERIAL

All chemical used were of A.R. grade. HCF (III) was used after recrystallisation. All the solution and reaction mixtures were prepared by using double distilled water. Absorbance was recorded on Sys. UV-Vis spectrophotometer -117, λmax for the reaction mixture observed was 420nm.$IrCl_3 10H_2O$ (SRL) was prepared by dissolving the sample in dil HCl[14]. In order to optimize the variable effect of concentration of each reagent, the rate of reaction was studied.

The condition worked out for estimation of Ir(III)

Following are the finally worked out conditions for running the kinetic sets for the purpose of determination of [Ir(III)] in aqueous alkaline medium based upon the hexacyanoferrate(III) oxidation of amino acids.

[Cystine & Methionine] = 3.00 x 10^{-3} mol dm^{-3}, HCF (III) = 3.00 x 10^{-3} mol dm^{-3}, NaOH = 0.4 mol dm^{-3} Temp. = 35 ± 0.1•C, λmax = 420nm, μ = 0.5 mol dm^{-3}

Preparation of calibration curve

A definite volume of stock solution of HCF (III) was mixed with calculated volume of a stock solution of Ir(III) ,Sodium hydroxide, Potassium chloride and water and stirred a little with the help of pipette. The reaction mixture and stock solution of amino acids like cystine and methionine were then clamped in a thermostat at 35 ± 0.1•C. After 30 min. a required amount of amino acid solution was added to the reaction mixture and stirred to start the reaction. Aliquots were withdrawn from the reaction mixture after repeated intervals of 5 min and the absorbance was recorded on systronic UV- Vis. Spectrophotometer 117. The absorbance of reaction mixture goes on decreasing with the passage of time. Absorbances vs. time plots were made for all the sets. Initial rates $(dA / dt)_i$ were evaluated after 5 min. from the start of the reaction by using plane mirror method. The first order rate constant (K_1) were calculated by Guggenheim's method. Different sets were prepared in a similar manner varying the [Ir(III)] between 0.258 – 8.37 $\mu g ml^{-1}$ for cystine and methionine. All the additions were made in amounts calculated for maintaining the concentration of different reagents as mentioned above.

The stoichiometry of the reaction was studied by estimating the standard solution of ceric(IV)sulphate using ferrion as redox indicator. The studies shows that eight moles of hexacyanoferrate (III) are used for the oxidation of one mole of cystine and four moles of hexacyanoferrate (III) are used for the oxidation of one mole of methionine. Based on the experimental results, it can be proposed that reaction proceeds through complex formation between anion of (cystine and methionine) and Ir(III) which slowly disproportionate into Ir(I) and intermediate product. Ir(I) deoxidized by two moles of HCF(III) ions to Ir(III) through electron transfer mechanism and the intermediate product decomposes to final product [15 – 17].

III. RESULTS AND DISCUSSION

The proposed method was tested for many reaction mixture containing known amounts of [Ir(III)] in the range of the detection limits. The results were found to be reproducible with reasonable standard deviation and low range of errors as calculated from six determinations. **(Table – 1)**

Validity of Beer's law and other characteristics of the method

The range of Ir(III) in which the Beer's law is obeyed, Molar absorptivity, Sandell's sensitivity, Correlation coefficient and coefficient of determination, relative standard deviation and % error for the estimation of[Ir(III)] in μgml^{-1} by using oxidation of cystine and methionine is given in **Table -1** for HCF(III) in alkaline medium.

The amounts of Ir(III) in the range of the detection limit were tested for the above proposed method. The results were found to be reproducible with reasonable standard deviation and low range of errors as calculated from six determinations. A comparison of the data presented in **Table -1** reveals that the Beer's law limit for the estimation of [Ir(III)] using amino acids- cystine and methionine are the same i.e. 0.258 – 8.37μgml^{-1}. The value of slope of the calibration curves, molar absorptivity and sandell's sensitivity indicated that the sensitivity of the method is good. A change in absorbance by 0.001 unit is expected on changing the concentration of [Ir(III)] by 0.0345 – 0.0983$\mu g\ cm^{-3}$. The detection limits are also good for the trace determination of [Ir(III)]. The correlation coefficient (r) is in the range 0.9996 – 0.9866 which indicate the high precision involved in the determination and almost perfect correlation of the data. The negative sign shows decrease in absorbance with time. The value of coefficient of determination (r^2) suggests that 0.9994 – 0.9734 change in the value of A_5 or A_{10} or A_{15} or A_{20} or $(dA/dt)_i$ or K_1 is caused by Ir(III). The standard deviation is within reasonable limits. Percentage recovery on the basis of six parallel determinations is 98.8 – 95.5. The values of the molar absorptivity and sandell's sensitivity calculated from the graph lies in the range of 2.83×10^3 – 3.27×10^3 $l\ mol^{-1}cm^{-1}$ and 0.0680– 0.0588μgcm^{-2} respectively.

Procedure for estimation of [Ir(III)] curves

For the estimation of [Ir(III)], the calibration curves should be prepared first as described above in the range of 0.258 – 8.37μgml^{-1} concentration of[Ir(III)] . Then [Ir(III)] may be determined in aqueous calculated quantity of HCF(III) and starting the reaction by adding amino acid solution followed by noting the absorbance of reaction mixture at different desired time as described above or evaluating initial rate in terms of $(dA/dt)_i$ after 5 min. or evaluating (K_1) by the methods discussed above. Then by using these different calibration curves [Ir(III)] in μgml^{-1} may be determined. **(fig 1-4)**

Interference Effect of Cations and Anions

The effect of various ions on the determination of [Ir(III)] By this method has also been studied. It has been observed that the presence of cations like Na^+, K^+, NH_4^+,AS_3^+,Mn_2^+,Ca_2^+,Cr_3^+,Li^+,Sr^{2+} and anions like CO_3^{2-} PO_4^{3-} ,F^-,Cl^-,Tartrate ion, Citrate ion,NO_3^-,SCN^-,EDTA,Oxide,$C_2O_4^{2-}$,IO_4^- do not interfere in the estimation of [Ir(III)] . The metals like Ag, Al, Co, Cd, Bi, Cu, Mo, Ni, Pb, Sb and Zn interfere in this method. Therefore a pretreatment is required for separation/ precipitating/masking these ions before undertaking the proposed method for this purpose, H_2S may be passed in presence of 0.3 MH^+ solutions, followed by filtration and boiling of H_2S. After it a dilute alkaline solution of α – nitroso – β – naphthol is added and precipitates are filtered[17]. Thereafter the solution is neutralized and the present method is applied. In absence of the above given

interferrants, the proposed method is applied. In absence of the above given interferrants, the proposed method may successfully be used for the determination of microgram quantities of[Ir(III)] in aqueous media.

Comparison with other methods

The result of the present method is compared with other reported spectrophotometric methods in **Table -2**. From the data it can be revealed that the reported methods are consuming, occurs at very high temperature and in the organic solvents like chloroform, ether etc. As compared with these methods, the present method is considerably less complicated occurs at room temperature and in aqueous alkaline medium. The method is also sensitive and requires low reagent concentration. The linear range of detection for the present method is quite good i.e.0.258 – 8.37μgml^{-1} as compared to reported methods. The absorptivity value ranges from 2.37 x 10^3 – 3.27 x 10^3 lmol^{-1}cm^{-1} which lies in the range of reported methods in ethyl acetate medium. But the absorptivity value is lower than the reported in chloroform medium.

IV. CONCLUSION

Thus from the above results it can be concluded that the proposed method is relatively simple, inexpensive and sensitivity which require low reagent concentration and can be used at room temperature without heating in aqueous alkaline medium. In the present work a simple, sensitive, selective and inexpensive method with sulphur containing amino acid like cystine and methionine, HCF (III) redox system has been developed for the determination of iridium. The method avoids the use of hazardous solvent as the reaction occurs in aqueous medium. The method requires low reagent concentration and can be used at room temperature without heating. Thus the present method is simple, sensitive cost effective and more environments friendly.

Table -1

Characteristics of various types of calibration curves for the proposed method

[HCF (III)] = 3.00 X 10 $^{-4}$ mol dm^{-3}, [Cystine] or [Methionine] = 3.00 X 10 $^{-4}$ mol dm^{-3}

[NaOH] = 0.4 mol dm^{-3}, μ =0.5 mol dm^{-3}, Temp. =35 ± 0.1•C, λmax = 420nm

Parameters	Cystine	Methionine
Beer's law limit	0.258 -8.37	0.258 – 8.37
Molar absorptivity x 10^{-3} (lmol^{-1}cm^{-1})	2.83 – 4.11	2.31 – 3.27
Sandell's sensitivity (μgcm^{-2})	0.0680 – 0.0467	0.0834 – 0.0588
Slope x 10^2 Absorbance unit(μg^{-1}cm^3)	(-) 1.47 – 0.0254	(-) 0.120 – 0.003
Intercept (Absorbance unit)(μg^{-1}cm^3)	0.3388 – 0.00008	0.3810 – 0.00025
Correlation coefficient(r)	(-) 0.9996 – 0.9995	(-) 0.9994 – 0.9866
Coefficient of determination(r^2)	0.9994 – 0.9989	0.9988 – 0.9734
Standard Deviation (%) (From six determination)	0.0406 – 6.786	0.0318 – 1.702
Recovery	98.8 – 96.2	99.5 – 95.5

Coefficient of variance	0.121 – 2.52	0.0681 – 0.8895

Table -2

Comparison of the present method for iridium determination with some of methods reported in literature

Reagent	Medium	Heating T®C (T/min.) No heating	Molar absorptivity	Linear range (μg cm^{-3})	Reference
Difurfuryl – thiocarbohydrazone (DCE)	Ethyleacetate	No heating	4.15 x 10^4	0.93 – 3.73 [Ir(III)]	18
1phenyl -4,4 -6 – trimethyl – (1H,4H)-Pyrimidine -2 – Thiolate(PTPT)	$CHCl_3$	60®C 5 min.	3.38 x 10^3	3.8 – 42.0 [Ir(III)]	19
2 –Mercapto -4,methyl – 5-phenylazopyrimidine(MFAP)	$CHCl_3$	No heating	9.5 x 10^3	0.6 – 9.0 [Ir(III)]	20
Bis(thiopheno -2 –aldehydo)-thiocarbohydarzone (BTATCH)	Ethyleacetate	100®C 30 min.	3.2 x 10^4	1.2 -4.2 [Ir(III)]	21
Present Method	**Aqueous alkaline**	**35®C**	**2.37 X 10^3 – 3.27 X 10^3**	**0.258 – 8.37 [Ir(III)]**	--

V. REFERENCES

[1]. Y.Wanq, J.Wanq, F.Yanq & X.Yanq (2010) Spectrophotometric Determination of cysteine with gold nanoparticles stabilized with single – stranded oligonucleotides, Vol 26,(5),545 -549,Anal.Sci.

[2]. Nivedita Agnihotri & Rajesh Agnihotri (2012) Extractive Spectrophotometric Determination of Nibodium(V) using 3 – Hydroxyl -2-(4 –Methoxyphenyl) – 4 oxo – 4H -1 –Benzopyran as a complexing Agent, 6, 39 – 44,The open Analytic Chemistry J..

[3]. Yusof,Nor Azah & Omar Zainab (2009) Spectrophotometric determination of trace Arsenic(III) ion based on complex formation with gallocyanine, 17(1), 53 -59,Petanika J. Sci. and Tech.

[4]. Hassan Golmohammadi, Abbas Rashidi and Seyed Jaber Safdari (2012) Simple and rapid Spectrophotometric method for determination of uranium(VI) in low grade uranium ores using Arsenazo(III), Vol.6, No.3,Chemistry and Chemical Tech.

[5]. Anand Kumar, S.Gupta & V.D.Barhate (2012) Extractive Spectrophotometric method for determination of Rhodium(III) using[N-(O –Hydroxy benzylidene) pyridine – 2 – amine] (NOHBPA) as an analytical reagent . Vol 14, No.1, 35 – 40,International J. of Chemical and Technical Research.

[6]. V. Druskovic, V.Vojkovic & S. Miko (2004) Spectrofluorimetric determination of iridium (IV)traces using 4 – pyridine derivatives, 62(3), 489 -495,Talanta.

[7]. G.G. Tertipis & F.E.Beamish (1962) Solvent Extraction separation & spectrophotometric determination of rhodium and iridium, 34, 623, Anal.Chem..

[8]. Li Zhenya (1993) Simultaneous determination of Iridium and Rhodium in precious metal sample by dual wavelength spectrophotometry, 21,(2), 224 -227,Chinese J. Of Anal. Chem.

[9]. E.G.Khomutova, V.A.Zagorodnikova, S.A.Zagorodnikova & O.I.Ostanina (2013) Individual Catalytic determination of Iridium and Rhodium using the oxidation of sulfarsazene by potassium periodate as an indicator reaction in a flow – injection system, Vol 68, Issue 7, 611 -615, J. of Anal. Chem.

[10]. Zhang Ning, Kong, Qing- Chen, Zhen, Xu, Ke –Hua & Tang Bo (2007) Determination of trace rhodium by supramolecular catalytic kinetic spectrofluorimetry of β – CD – Rhodium –KBrO3 - Vanillin Salicylhydrazone, Vol 158, No.1-2, 165 – 171,Microchimica Acta.

[11]. Anjali Goel & Shankunj (2012) Microgram Determination of iridium(III) by Kinetic spectrophotometric Method, Vol 2, No – 5, Discovery.

[12]. Anjali Goel, Savita devi & Shailija (2007) Spectrophotometric determination of Ir(III) with cystine in aqueous alkaline medium, Vol.21, (1 -2), 27 – 35, J. of Natural and Physical sciences.

[13]. Anjali Goel, Savita Gupta & Sonia Sharma (2009) Kinetic – catalytic – spectrophotometric Determination of Ir(III) by its catalytical effect in the oxidation of isoleucine by hexacyanoferrate(III) ions, Vol.1, No.4, 559 -556, International Transactions in Applied Sciences.

[14]. K.Sharanabasamma & Suresh M. tuwar (2010) Kinetics and mechanism of oxidation of DL – methionine by HCF(III) in aqueous alkaline medium. Vol.31, issue 3, page 177 – 187, J. of sulfur chemistry.

[15]. Anita Slavica,Iskandar Dib & Bernd Nidetzky (2005) Single – site oxidation,Cysteine 108 to cysteine sulfinic,in D-amino acid oxidase from trigonopsis variabilis and its structural and functional consequences, Vol 71, No.2, 8061 -8068. Appl.Environ.Microbiology,

[16]. T.Sumathi,P.Shanmugasundaram,G.Chandramohan (2011) A Kinetic and mechanistic study on the oxidation of L-methionine and N-acetyl L- methionine by cerium (IV) in sulfuric acid medium. Arbanian j.chem..

[17]. L. Meites (1963) Handbook of Analytical Chemistry. McGraw Hill Book Co., Inc., New York,3-4.

[18]. A.Chaudhari, S.C.Shome, & H.R.Das, (1996) Extraction of sodium & iridium with polyurethane foam, 73,549, J. Indian Chem. Soc.,

[19]. A.Wasey, R.K.Bansal & B.K.Puri (1984) Spectrophotometer Determination of Iridium(III) and Osmium (VIII) with phenanthrenequinine monoxime after extraction into molten Naphthalene,211,Microchim. Acta[Wein]

[20]. A. Kumar, (1985) Spectrophotometric determination of palladium,tellurium and iridium after extraction with 2 – mercapto – 4 – methyl – 5 – phenyazopyrimidine, 11, 281, Anal.Sci.,

[21]. S.P.Chaudhury, & S.C.Shome, (1991) Spectrofluorimetric determination of Iridium (IV) traces using 4 – pyridine derivative, 68, 430, J. Indian Chem. Soc.

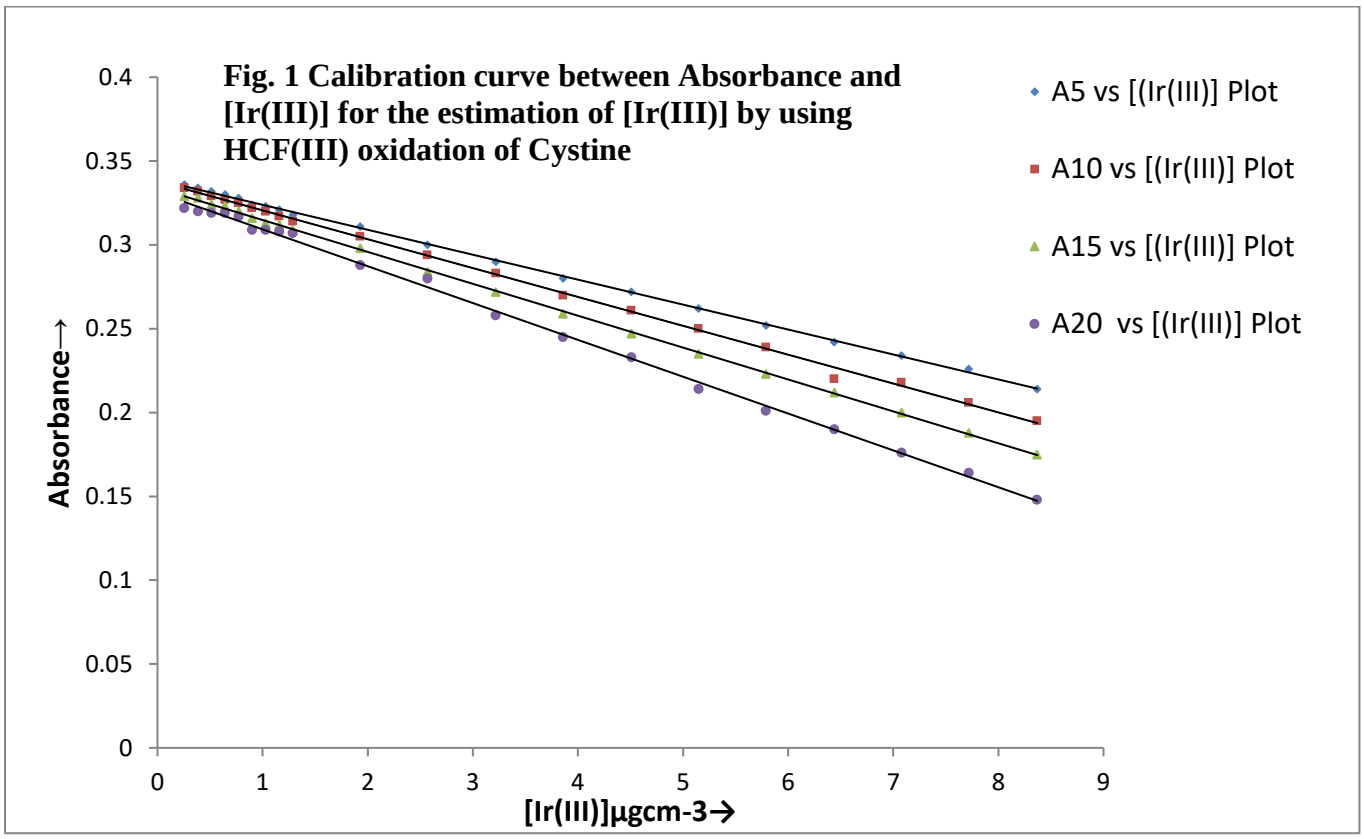
Fig. 1 Calibration curve between Absorbance and [Ir(III)] for the estimation of [Ir(III)] by using HCF(III) oxidation of Cystine
A5 vs [(Ir(III)] Plot
A10 vs [(Ir(III)] Plot
A15 vs [(Ir(III)] Plot
A20 vs [(Ir(III)] Plot
Absorbance→
[Ir(III)]µgcm-3→
0.4
0.35
0.3
0.25
0.2
0.15
0.1
0.05
0
0 1 2 3 4 5 6 7 8 9

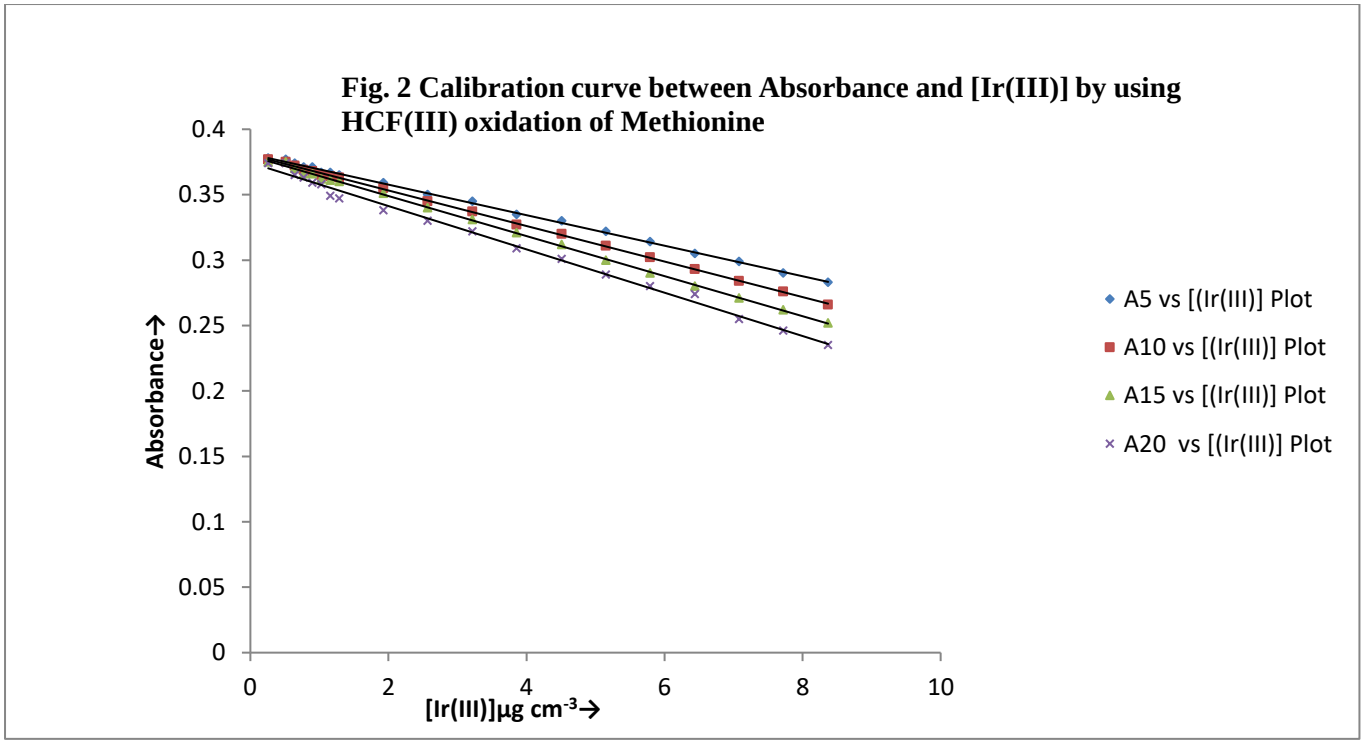
Fig. 2 Calibration curve between Absorbance and [Ir(III)] by using HCF(III) oxidation of Methionine
A5 vs [(Ir(III)] Plot
A10 vs [(Ir(III)] Plot
A15 vs [(Ir(III)] Plot
A20 vs [(Ir(III)] Plot
Absorbance→
[Ir(III)]µg cm-3→
0.4
0.35
0.3
0.25
0.2
0.15
0.1
0.05
0
0 2 4 6 8 10

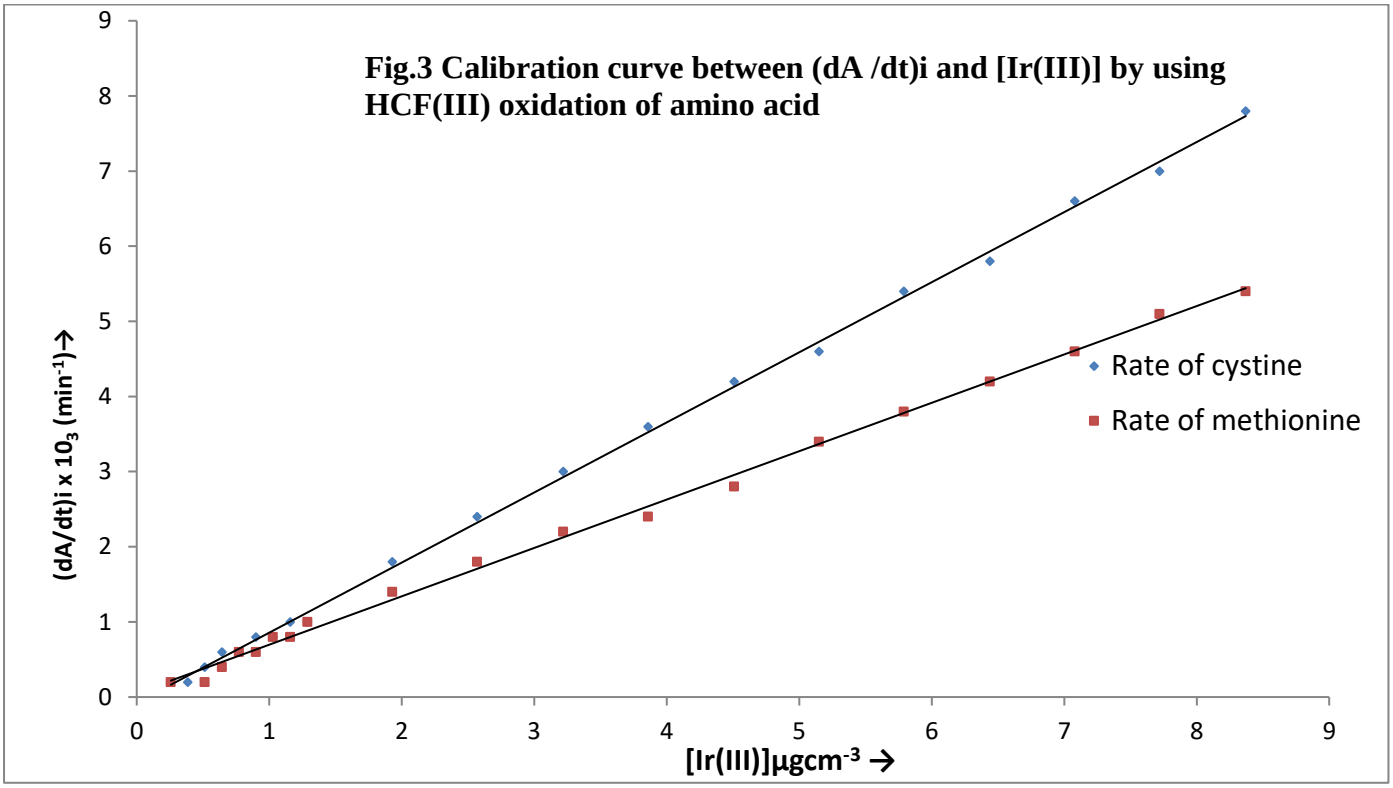
Fig.3 Calibration curve between (dA /dt)i and [Ir(III)] by using HCF(III) oxidation of amino acid
(dA/dt)i x 10₃ (min⁻¹)→
[Ir(III)]µgcm⁻³ →
Rate of cystine
Rate of methionine

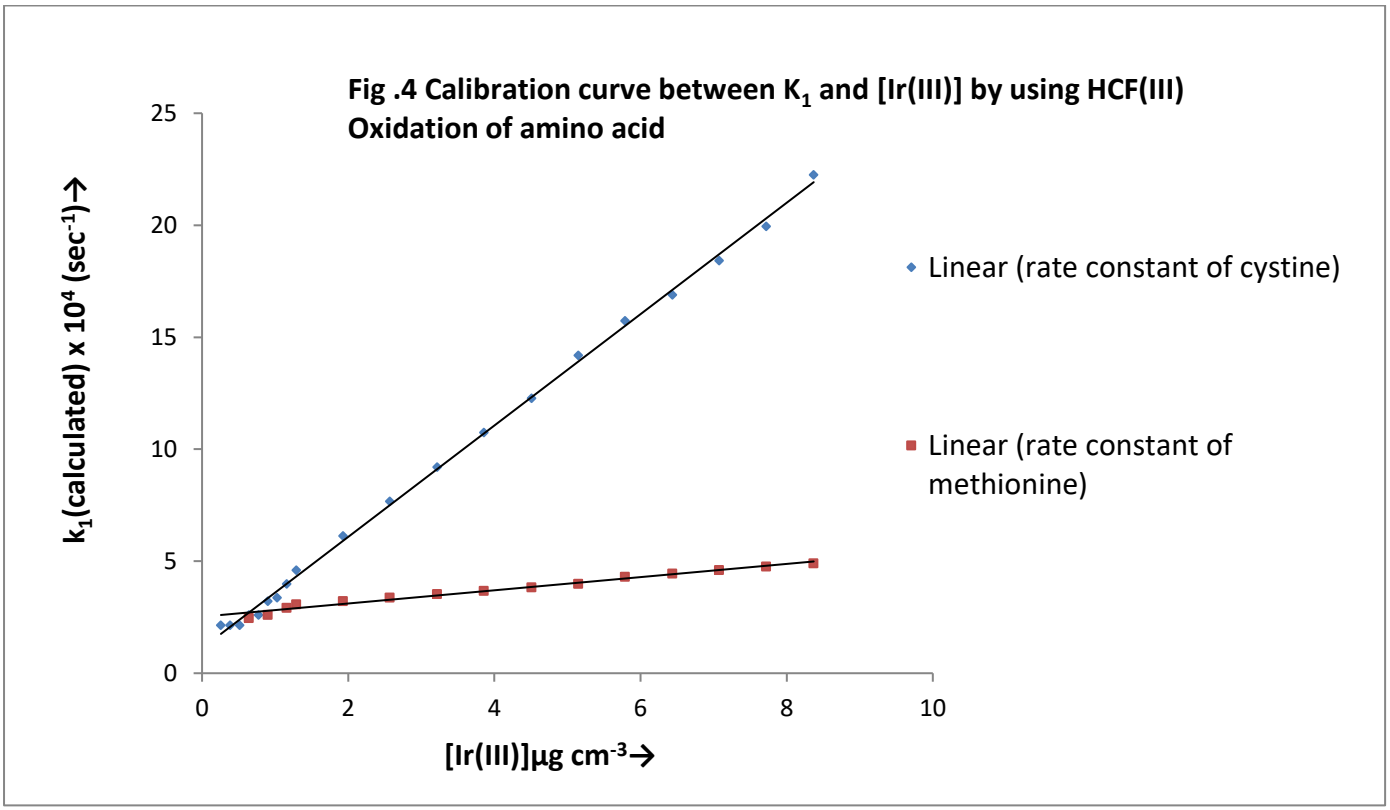
Fig .4 Calibration curve between K1 and [Ir(III)] by using HCF(III) Oxidation of amino acid
k1(calculated) x 10⁴ (sec⁻¹)→
[Ir(III)]µg cm⁻³→
Linear (rate constant of cystine)
Linear (rate constant of methionine)

National Conference on Applied Sciences Synergising the Engineering and Technology
Print ISSN: 2395-6011 | Online ISSN: 2395-602X (www.ijsrst.com)
© 2021 IJSRST | Volume 8 | Issue 2

Comparative Study of Electrodeposition Processes for Polymer Composites for Technological Applications – An Overview

Ashok Kumar Shukla
Chemistry Department, East Point College of Engineering & Technology, Bangalore, India

ABSTRACT

The paper presents an overview of electro-deposition (ED) processes used for preparation of polymer composite (micro- and nano-) coatings for application in engineering and technology. Broadly classified into three types namely, electrolytic deposition (ELD) [1], electrophoretic deposition (EPD) [2] and electrostatic deposition (ESD) [3] processes, that have been compared for their principle, processing conditions and characterisation of the deposited coating. Limitation and difficulties observed in cationic and anionic electrophoretic deposition processes for preparation of polymer micro-composites (PMCs) and nano-composites (PNCs), have been discussed and recommendations to alleviate some of them are proposed.

Emphasis is placed on electrophoretic deposition, one of the advanced and versatile techniques to produce Polymer micro- and nano-composites for engineering and bio-medical applications. Author highlighted the process parameters and characterisation data of deposited composites and attempted to compare the available data from the three techniques, including the author's own results pertaining to electro-phoretically deposited epoxy nano-clay composites. Advantages of the EPD process included a significant improvement (nearly two-fold or more) in dielectric and corrosion protective properties, as compared to their conventional micro-composites, besides having the tailorability of composition suiting to a particular application. Extension of EPD technique to fabricate Polymer micro- and nano-composites with suitable polymer and filler combinations for strategic applications, e. g. electromagnetic interference (EMI) shielding and stealth, required in aerospace and defence equipment, is a distinct possibility and is recommended for further studies.

Keywords : Electrode Position, Electrophoretic, Electrostatic, Micro-Composites, Nano-Composites

I. INTRODUCTION

Selection of materials and designing of the mechanical components and structures for specific applications are the essential requirements in the manufacturing industry. However, every material possesses certain constraints in their functional properties e. g. mechanical strength, thermal stability, wear resistance, corrosion resistance etc. limiting their applications. To mitigate these challenges and to improve the material properties for a particular application, various methods are employed like, heat-treatment, alloying and processing, applying surface protective coatings etc. Among these methods, surface coating processes are most commonly used due to their simplicity and cost-effectiveness. Surface coatings offer specific advantages like, corrosion

resistance, wear resistance, enhanced surface hardness, electrical and thermal insulation, enhanced hydrophobicity etc. [4]

Wide range of coating techniques are in practice due to extensive diversity of applications and requirements in various industries. Most of the properties are degraded due to the natural phenomenon of corrosion resulting in corrosion products that in-turn lead to more intense corrosive environment and degradation in many applications [5,6]. Most effective deposition methods include, Physical vapor deposition (PVD), Chemical vapor deposition (CVD), Polymer coating deposition (PVD), Sol-gel, and thermal spray methods and are suitable for different application. Besides being effective and beneficial, these methods do suffer from certain limitations that adversely affect their reliability. These degrading effects include, distortion, delamination, crack formation, impurity contamination in substrate, etc, are needed to be considered while exploiting the other properties of the coating materials.

Various materials including metals, ceramics, polymers and composites can be employed to deposit a protective coating [7], by taking into account the diversity of the material characteristics and the coating techniques that may cause difficulties in selecting the right composition of the deposited coating. The present article covers the common electrocoating processes, materials and the surface characteristics of the deposited coatings.

II. METHODS AND MATERIAL

ELECTRODEPOSITION PROCESSES

Electro-deposition (ED) Processes are basically classified as Electrolytic (ELD), Electro-phoretic (EPD) and Electrostatic Deposition (ESD) processes, based on a seemingly common principle of charging and discharging of the coating material of interest, yet distinguishable as depicted in the Flow chart below in Fig.1.

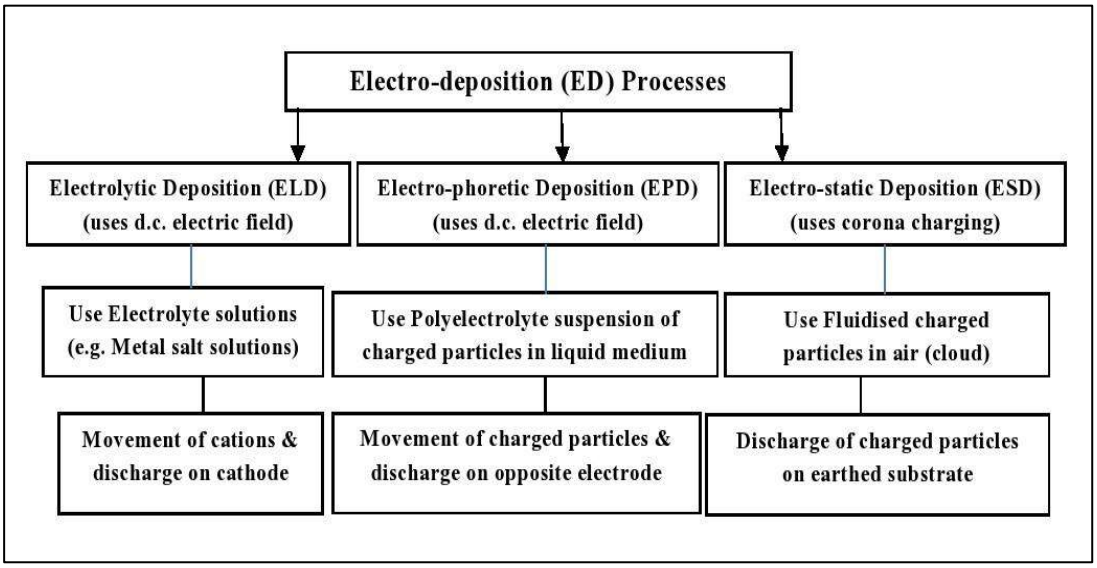

Fig.1: Distinction of principles of the three ED processes

Electro-deposition is a process that facilitates movement of ions in a liquid medium (solution or suspension) or of clouds of charged particles, under the influence of an applied direct current (DC) electric field, towards an oppositely charged electrode and their discharge and deposition onto its surface, as a film or coating.

The ELD and the EPD processes can be construed as falling under one class (only differing in the dispersion media). On the contrary, the ESD process involves electro-statically charging fine powders of organic (typically polymeric) and inorganic materials, exposing them to a high voltage corona field to convert them into clouds of charged particles suspended in air and finally directing them on to an earthed surface of a preheated metal or a non-conducting composite or ceramic substrate, resulting in their discharge and deposition, as a thin adherent coating. A general schematic representation of an ED process is shown in the Fig.2.

The ED processes have their own inherent characteristic merits and limitations, and need to be understood for proper choice and use, as dictated by the scope and scale of end use and the material to be deposited ultimately. Several researchers have reported on the use of these processes in the past decades, and yet leaving considerable scope for refined or novel approaches, when it comes to highly demanding requirements of several advanced engineering and strategic applications.

This scenario motivated the authors to take up this study, supplementing it with the novelty and merits of their recently developed EPD technique that clearly reveals its versatility (simplicity, economy and adaptability) to any sort and scale of application, through innovative modifications and upgrades, as outlined further.

Electrodeposition of materials, an electrochemical process, is essentially an ionic or atomic deposition process that can be used to synthesise nanomaterial or nanocomposite films /coatings and has been under intensive study in recent years. In this process, a potential difference between cathode and anode causes the migration of ions in the electrolytic cell under DC electric field. A coating layer is deposited on the substrate (one of the electrodes) by receiving ions from the other electrode submerged in the electrolyte.

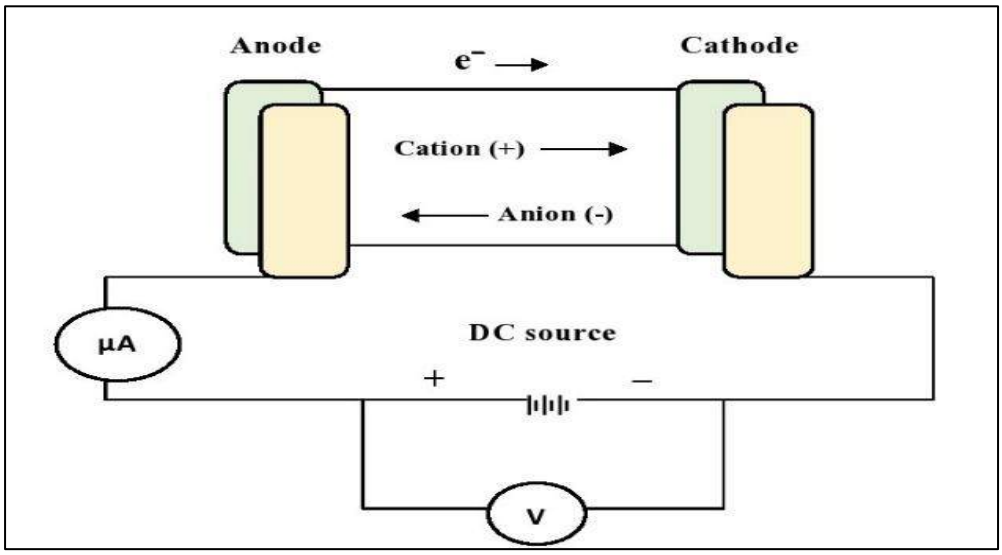

Fig.2: General schematic of ED process

Several studies [8, 9] are reported about electrodeposition of composite coatings that enhance the corrosion resistance of the substrate material. All the three types of ED processes are discussed below:

A. Electrolytic Deposition (ELD) process:

It is an electrochemical process, also known as electroplating, used for deposition of an uniform and dense metallic layer on conductive objects made of different metal or alloys.

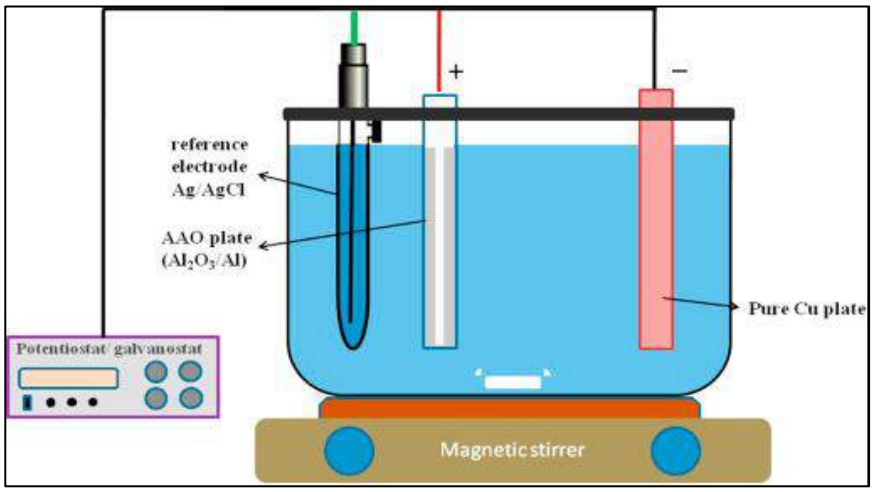

Fig.3: A schematic of Electrolytic deposition [10].

The ELD process is carried out in an electrochemical cell comprising of two electrodes, anode and cathode, immersed in the electrolyte and a DC power source. The electrolyte contains the metal salt solutions with certain additives and buffer to maintain pH and is agitated using a magnetic stirrer at a very low speed.

Under the influence of DC electric field, the metal ions from the electrolyte solution migrate towards the cathode substrate and get discharged on the cathode surface and get deposited. Concentration of metal ions in the bath is generally maintained constant [10] by replenishing periodically the salt solution during the electroplating process. The ELD process, besides being used for anti-corrosion, decorative and anti-wear applications, it's applications are also reported in the fields of electronics, optics, biomedical high temperature and fuel cells [11-12]. There are reports of electrodepositing the alloy coatings [13] such as Ni-Co-Al_2O_3 and Ni-Co-SiC [14] on carbon steel pipes for enhanced corrosion resistance against oil-sand based slurries. A schematic representation of electrolytic deposition process (ELD) is illustrated in Fig.3 [10].

B. Electrophoretic Deposition (EPD) process:

The EPD process works on the same principle as in the ELD process, however, EPD involves the movement of charged colloidal particles of larger size and/or polymeric ions or inorganic particles dispersed in aqueous or non-aqueous medium towards one electrode under the influence of external direct current electric field (electrophoresis) [15, 16].

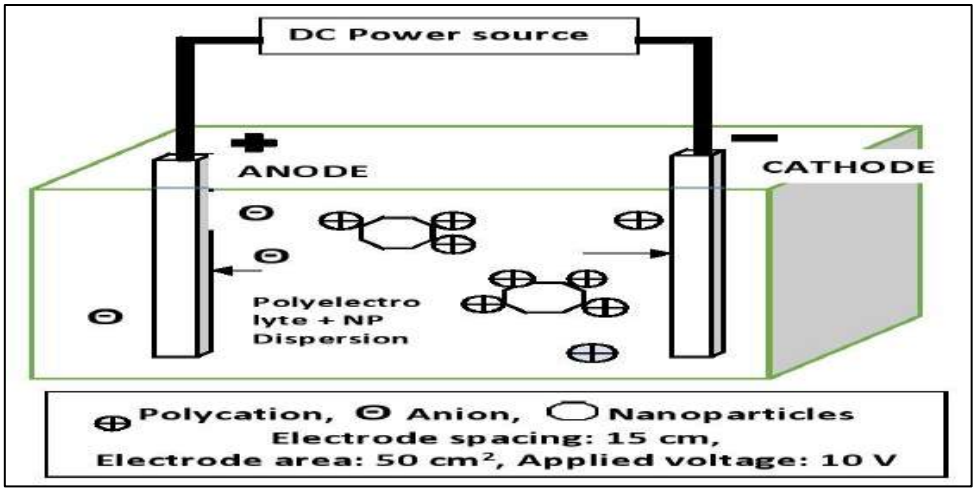

Fig.4: Mechanism of Electrophoretic deposition [17]

The moving charged particles discharge and get deposited on the surface of the opposite electrode forming a thick layer of coagulated particles with the polymer. A schematic of the EPD process and it's working mechanism is illustrated in the fig.4 [17].

The electrodeposited thick coating is subsequently subjected to drying, curing or densification processes like, oven curing, light/radiation curing or sintering etc, depending upon the nature of deposited materials.

Electrophoretic Deposition (EPD) process is carried out in two ways, namely (i) anodic deposition that involves the movement of negatively charged particles or/and polymeric anions towards anode of the EPD cell under the DC electric field and get discharge on the anode surface resulting in deposition, and the other (ii) cathodic deposition which is based on the movement of positively charged particles or/and polymeric cations to cathode resulting in discharge and deposit formation on the cathode surface, under the applied DC voltage. Cathodic EPD method is preferred due to formation of neat coating free from any contamination due to absence of any side reactions on the cathode surface except the gas formation at higher applied voltages. On the other hand, the anodic EPD process has been reported in very limited and specific applications, viz. EPD of mica in electrical industry [18, 19] due to contamination in the deposit by anodic oxidation products, as well as the bath contamination.

Several applications of EPD process have been reported such as corrosion protection, electrical insulation, various engineering fields including the biomedical applications. Engineering materials commonly deposited by the EPD process include oxides, phosphates, carbides, borides etc, [20].

C. Electrostatic Deposition process (ESD):

The ESD process is based on the principle of charging the polymer powder particles, moving them towards a grounded (earthed) object or substrate on which the charged polymer particles get discharged and deposited due to electrostatic attraction, refer the Fig.5 below.

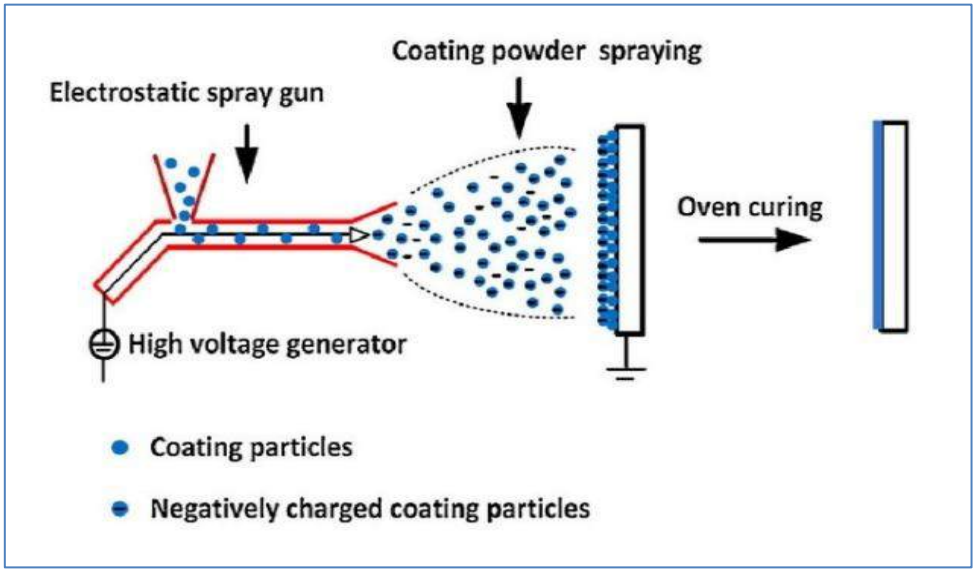

Fig.5: Corona charging of powder particles and electrostatic deposition [21].

Generally, the workpiece or substrate is kept at elevated temperature that helps the instant melting and adhesion of the powder particles on to the substrate surface. This is followed by curing in an electric oven at higher temperature to obtain uniform and adherent polymer coating on the substrate.

Table 1 compares the broad characteristics of the above three Electrodeposition (ED) processes.

D. State-of-the art

One of the recent developments in electro-deposition technique is the application of modulated electric fields, such as alternating current (AC) and pulsed direct current (PDC) as a substitute to the conventional use of continuous direct current (CDC) [22, 23]. Several advantages have been reported in the new methods. Use of alternating current electric field in aqueous medium, results in the superior quality of deposited coatings associated with enhanced deposition rate with respect to polarisation time and the amplitude.

Table 1: Characteristics of Electrodeposition processes

Characteristics	Electrolytic deposition (ELD)	Electrophoretic deposition (EPD)	Electrostatic deposition (ESD)
Bath content	Solution	Suspension	Suspension in air
Moving species	Ions	Solid particles/polymers	Solid particles
Surface charge	Medium	High	High
Charging mechanism	Dissociation	Dissociation	Corona/Triboelectric
Preferred medium	Water	Organic or mixed water + organic	Air
Ionic electrolytic strength	High	Low	Not applicable
Electrolytic conductivity	High	Low	Not applicable
Deposition rate	10^{-3} – 1 μm/min	1 – 10^{3} μm/min	1 – 10^{3} μm/min
Coating thickness	10^{-3} – 10 μm	1 – 10^{3} μm	1 – 10^{3} μm
Coating uniformity	On nm scale	Limited by particle size	Limited by particle size

Use of pulsed direct current supresses the water electrolysis giving the advantage of less gas bubbles formation thereby, leading to uniform and smooth deposited coatings. Use of PDC also helps in deagglomeration of nanoparticles leading to homogeneous and uniform coatings, besides permitting negligible variation of pH near the surface of electrodes, an advantage in depositing the biochemical and biological species. The new methods utilizing PDC and AC electric fields hold great promise for future application in biotechnology [23], especially in the fields of biosensors, bioreactors and bio-fuel cells.

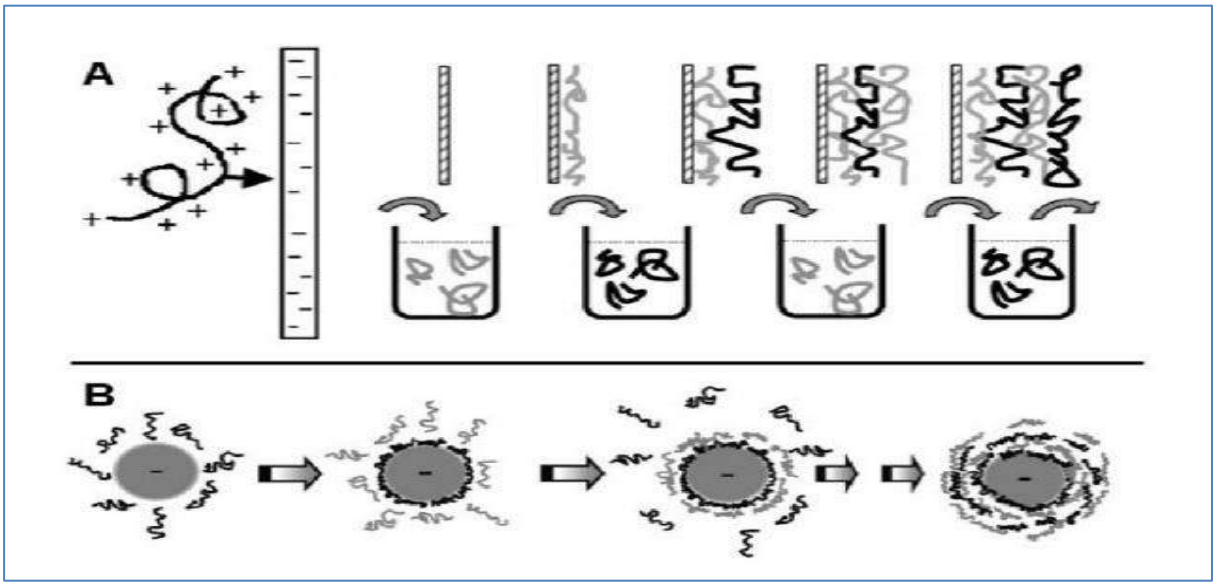

Fig.6. Schematic of LbL-ESD process on charged substrate surface. (A) Planar (B) Colloidal particle. [27]

Another latest development in the ESD is the LbL technique which involves the deposition of a polyelectrolyte layer on to an oppositely charged surface by adding one or more oppositely charged polymers. The charged polyelectrolyte molecules move from the solution to the oppositely charged surface due to strong electrostatic attraction arising as a consequence of the coulombic forces [24, 25]. The adsorption of large number of polyelectrolyte molecules on the substrate surface results in the reversal of the net charge on the substrate surface from negative to positive or from positive to negative. Repetition of the process leads to the formation of a double layer or secondary layer, that may be followed by the triple layered derivative of the base structure and may continue the repetition up to 5 or 6 multilayers, refer thefig.6. The net electrical charge of the deposited multilayer structure is determined by the charge of the outer layer [25].

EXPERIMENTAL

A. Materials used:

Diglycidyl ether of bisphenol-A (DGEBA) based Bifunctional Epoxy resin with epoxy value in the range 1.1-1.2 eq./kg available commercially and without further purification was used for conversion into a water dispersible emulsion form. Proprietary solvents like the mixture of ethylene glycol mono butyl ether, Methanol, Xylene in different proportions and reagents such as primary and secondary amines and surfactant Triton X-100 of L.R. grade was procured locally. Sodium Montmorillonite (MMT) nano-clay Cloisite Na+ from m/s Southern Clay Products, USA, was used as nano-clay particles. SI-304 grade stainless steel sheets of 1.75 mm thickness cut to size 100 x 50 mm with edges rounded off, were used to make the cathode and anode with a DC power source.

B. Methods used:

Determination of epoxy equivalent weight using the standard volumetric method ISO 3001:1997(E) was used to monitor the extent of epoxy-amine adduct formation. FTIR spectroscopic method was used to monitor the reduction in the absorption band intensity of the epoxy group. Progress of electrodeposition of polymer nano-composite (PNCs) coating was monitored by drop in the current density and also by deposition-yield through weight and thickness measurements. Nanostructure of the deposited film was established using analytical techniques such as Scanning Electron Microscopy (SEM) and X-ray Diffractometry. Dielectric characterisation of electrodeposited PNCs was carried out by measuring the Breakdown voltage (BDV) using the Dielectric strength tester and Volume resistivity using Million Megohm meter.

C. Electrophoretic deposition (EPD) process

Electrophoretic deposition (EPD) was carried out using an in-house fabricated cell, represented in fig.4, containing the aqueous cationic epoxy emulsion containing the dispersion of MMT or BNT nano-clays. EPD cell is equipped with two electrodes made from SS plates, a DC power supply and a magnetic stirrer to stir slowly the contents of the bath. Epoxy Nano-composite (ENC) coating was electrodeposited on cathode by subjecting to DC electric field. Epoxy polycations together with MMT or BNT nanoparticles move towards the cathode plate and discharge on the metal surface forming the adherent layer of Epoxy nanocomposite (ENC) coating. Electrodeposited metal plate is removed from the bath, dried in air and cured at 150°C for 2 hrs in hot-air electric oven and subjected to characterisation.

D. Process Monitoring:

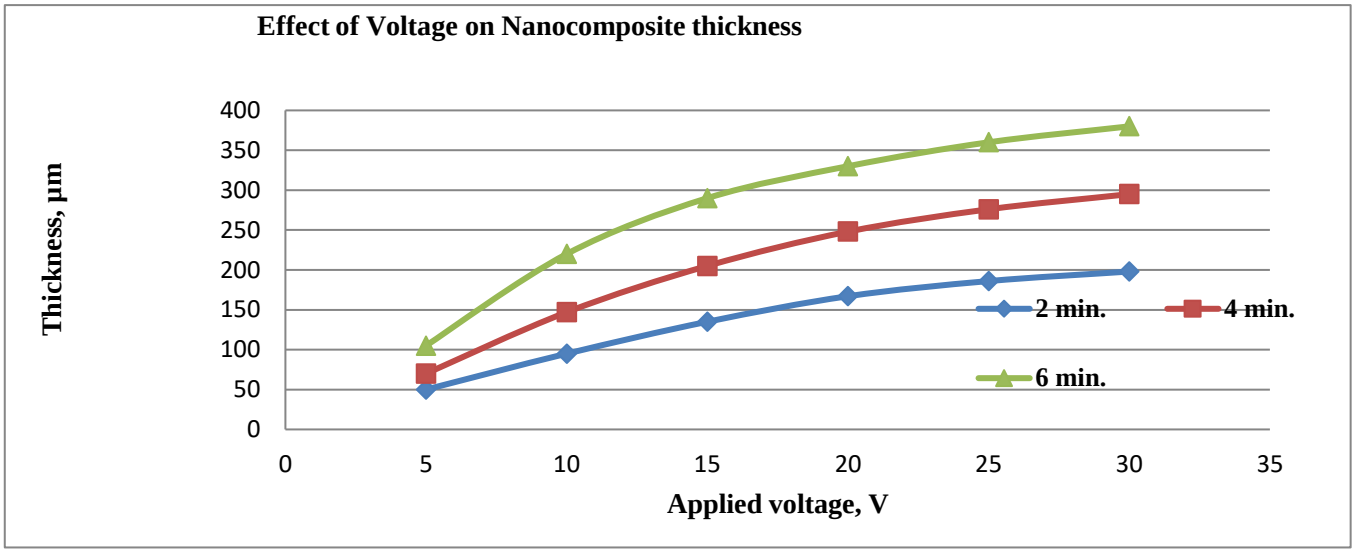

Fig.7: Thickness vs. Applied voltage [26]

The important process parameters that influence the quality of the electrodeposited coating have been briefed below with salient features [26]:

The deposition yield and the coating thickness is directly influenced by applied voltage as depicted in the fig.7. Increase in EPD coating thickness is observed with increase in applied voltage in steps from 5V to 30V for the duration of 2, 4, and 6 minutes. Current density was monitored during the electro-deposition process. Fig.8 shows the drop in the current density with time indicating the rise in the resistance of the deposited coating.

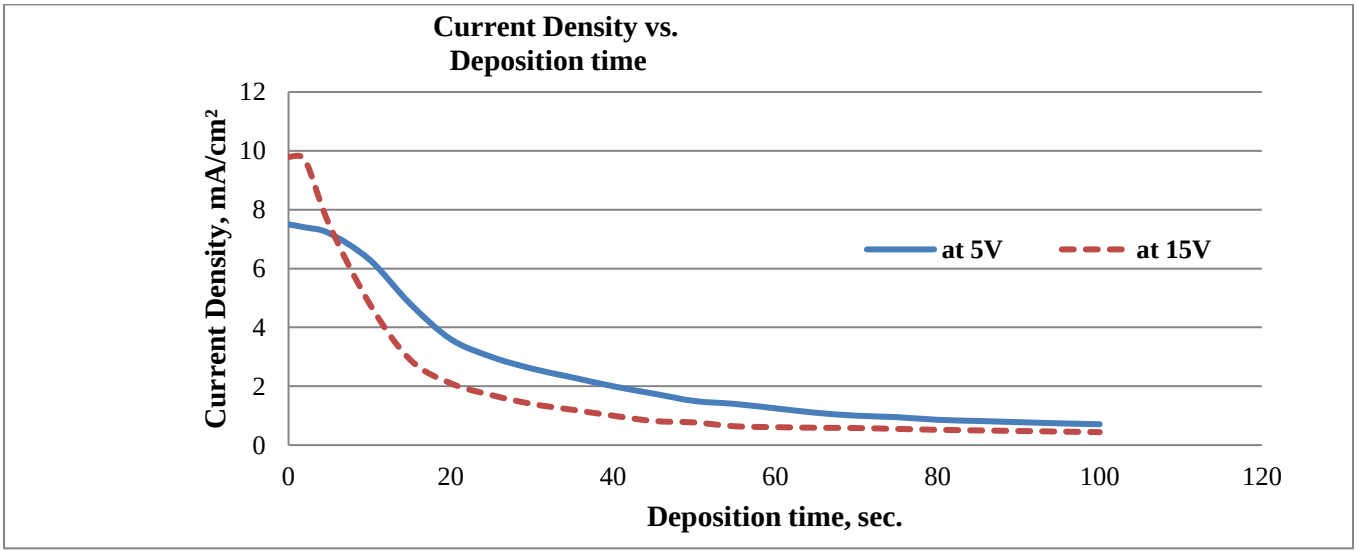

Fig.8: Drop in Current Density [26]

Significant increase in the Dielectric strength of the cured EPD nanocomposite coatings is observed with increase in the nano-clay content as shown in fig.9.

III. RESULTS AND DISCUSSION

EPD of Polymer nanocomposite coatings has shown significant enhancement in dielectric and corrosion resistance properties and has established the simplicity, versatility and many advantages.

Property enhancement is explained as a consequence of good intercalation of polycations into the layered structure of the MMT nano platelets. This phenomenon also explains the significant rise in the dielectric strength of the PNCs, almost 2-fold at the nanoclay loading levels of about 8-10 % b/w of the polymer matrix as depicted in the Fig.8. It indicates great scope for insulation application in HV electrical machines.

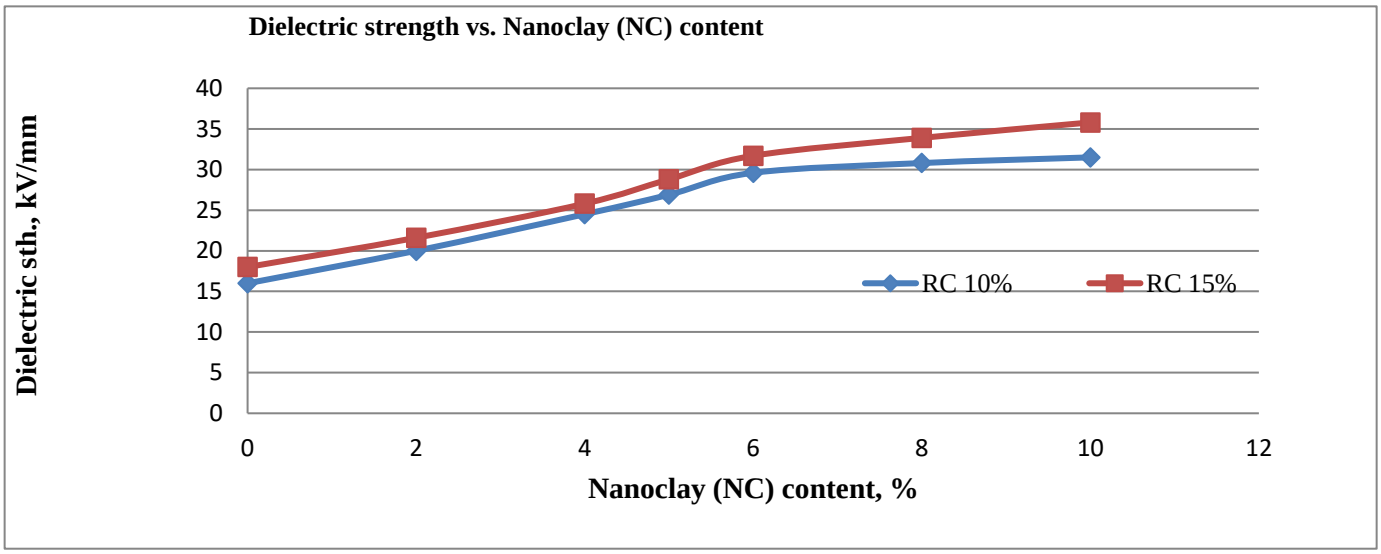

Fig.9: Dielectric strength vs. NC content [26]

Corrosion resistance, a significant property of the EPD PNCs has been studied with respect to resin content of the deposition bath by measuring the electrical volume resistivity (considered as indicative of chemical resistance and structural integrity of the PNC coating) of the cured PNCs after prolonged exposure to the salt fog spray (at 3.5% salt concentration) for 1, 3 and 5 days duration, as shown by a plot of logarithm of electrical resistivity (Logρ_e, Ωcm) under above conditions versus resin content in Fig.10.

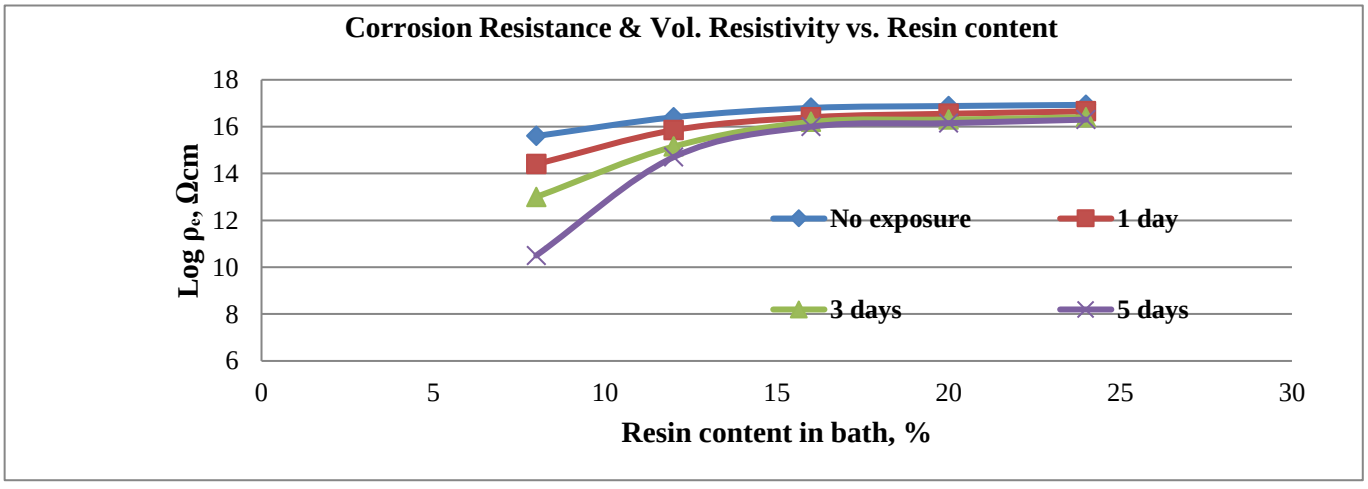

Fig.10: Corrosion resistance vs. Resin content [26]

FUTURE POTENTIAL OF EPD PROCESS

The EPD process for fabricating the polymer nano-composites (PNCs) has the specific advantage of preparing water-based formulations derived from any polymer matrix and any dispersed phase, besides permitting the deposition on to the conducting or non-conducting surfaces. This is an important feature of this technique that

opens great scope of extension to PNCs containing the functionalised nano-fillers such as carbon nanotubes (CNT), single-walled (SWCNT) and multi-walled (MWCNT) types, ferrites, ceramics and perovskites etc. [20]. Currently, such PNCs are prepared by conventional methods for EMI shielding application in electronic equipment but to a limited success due to constraints of loading the CNTs resulting in high viscosity build-up. An electro activated polymer based aqueous formulation and electrodeposition process may hold the key to overcome the above constraints in the technology of Polymer nanocomposite coatings.

IV. CONCLUSION

Electrodeposition processes are broadly classified into three major categories, namely, electrolytic, electrophoretic and electrostatic deposition methods. Their principles, processes, characteristics, applications and state-of-the art in these techniques, have been discussed. The most versatile EPD process has the capability of creating the films and coatings based on polymers, composites, nano-composites, ceramics, dielectrics, semiconducting materials with tailored properties for specific applications. EPD process can provide uniform coatings with high throwing power on the substrates of any nature and geometry, besides being easy, economical and eco-friendly. Salient results of electrophoretically deposited polymer nanocomposite coatings possessing enhanced dielectric and corrosion resistance from the author's own work, have been discussed.

V. ACKNOWLEDGEMENT

The author expresses thanks to the EPCET management to permit the presentation of this work at the ASSET-2021, and to DRDO-EMR, New Delhi for the research grant to develop the EPD process.

VI. REFERENCES

[1]. C. Kerr, et.al., (2017) 67-72 (Published online) https://doi.org/10.1080/00202967.2002.11871436.
[2]. O. Omer, Van der Biest, Luc J. Vadeperre, Annu. Rev. Mat. Sci., 29 (1999), 327-52.
[3]. M. Barletta, V. Tagliaferri,; Surface & Coatings Technology, 200 (2006), 4282– 4290.
[4]. Bhushan B., Gupta B.K.,Handbook of Tribology: Materials, Coatings, and Surf. Treatments; Krieger Pub Co,: (1991) Malabar, FL, USA
[5]. Klaassen, C.D., Casarett and Doull's Toxicol., Bas.. Sci. Pois. McGraw-Hill: (1996); V5; NY.
[6]. Dehghanghadikolaei, A.; et.al. Abrasive Machining Techn. for Biomed. Dev. Applns; J. Mater. Sci. 5, (2018), 1–11.
[7]. DeMasi-Marcin, et.al.; Protective coatings in gas turb. engine.; Surf. Coat. Tech. 68, (1994), 1–9.
[8]. Radwan, A.B.; et. al., Properties Enhancement of Ni-P ED Coatings by Incorpn. of Nano Y2O3 Particles.; Appl. Surf. Sci. 2018, 457, 956–967.
[9]. Zhou, H.-H.; et.al., Pulse electroplating of Ni-WP coating and its anti-corrosion performance. Trans. Nonferrous Met. Soc. China 2018, 28, 88–95.
[10]. Bindra, P.; et. al., Electrolytic deposition of thin metal films on semiconductor substrates. J. Electrochem. Soc. 1977, 124, 1012–1018.

[11]. Kyerematenng, N.A.; et.al., Micro supercapacitors as miniaturized energy-storage components for on-chip electronics.; Nat. Nanotechnol. 2017, 12, 7.
[12]. Minh, N.Q. Solid oxide fuel cell technology—features and applications. Solid State Ion. 2004, 174, 271–277.
[13]. Tian, B.; Cheng, Y. Electrolytic deposition of Ni–Co–Al2O3 composite coating on pipe steel … sand slurry; Electrochim. Acta 2007, 53, 511–517.
[14]. Yang, Y.; et.al. Electrolytic dep. of Ni–Co–SiC nano-coating for erosion-enhanced … sand slurry., Surf. Coat. Technol. 2011, 205, 3198–3204.
[15]. I. Zhitomirsky, "Cathodic electroph. deposition of ceramic and organo-ceramic materials", Adv Coll. Inter. Sci,, 2002, vol. 97, pp 279–317.
[16]. M.V. Pavan Raja, et.al., "Impact of Viscosity … using a Novel Electrophoretic Deposition Setup", (2012), Jl. of Biotech. and Biomatls., USA.
[17]. A.K. Shukla, "EPD of Polymer nanocomp. for engg. applns - a green process", Proc. of Internl. conf. ICMTCI4.0, Bangalore, 27-28 Aug, 2020.
[18]. A.K. Shukla, S. Sridhar, et.al., "A new composite insulation based on electrodeposited mica", Proc. of 3rd Intl. Seminar on Elec. & Electronic Insul. Matls. & Syst. (INSULEC-88), (1988), IEEMA, Bombay.
[19]. H. W. Rotter, "Electrophoretic method of applying high grade insulation coatings", Siemens Review, XXXVII (1970), No.9, p. 496-498.
[20]. Boccaccini, A.R.; et.al., Electrophoretic deposition of CNTs.; Carbon 2006, 44, 3149–3160.
[21]. Bailley A.G., "The Sci. and Tech. of electroststic powder spraying, transport and coating", 1998, Journal of Electrostatics, 85-120.
[22]. M. Ammam, "Electrophoretic deposition under modulated electric fields", J. RSC Advances, no. 20, Sep. 2012.
[23]. S.A. Yavari, "Electrophoretic deposition – A versatile tool against biomaterials associated infections", J. Mat. Chem. B, vol. 6, 1128-1148, Feb 2018.
[24]. L. Yan, et.al.; ACS Appl. Matl. Interfaces, vol. 9, pp 5023-5030, 2017.
[25]. Caruso, F.; Trau, D.; M€ohwald, H.; Renneberg, R. Langmuir 2000, 16, 1485.
[26]. A. K. Shukla, and RMVGK Rao, "A Novel; Electro-Cathodic Deposition Process". Jl. Electrochem. Soc. Ind., IISc, ISSN: 0013-466X ,Vol.67, No.1, 2018.
[27]. B. Fotovvati, el.al., "On coating technique for Surf. Prot.: A review", J. Manuf. Mat. Proc., 2019, 3, 28,; doi:10.3390/jmmp3010028.

National Conference on Applied Sciences Synergising the Engineering and Technology
Print ISSN: 2395-6011 | Online ISSN: 2395-602X (www.ijsrst.com)
© 2021 IJSRST | Volume 8 | Issue 2

Preparation, Characterization and Visible light Photocatalytic Activity of Rare earth doped Zinc Oxide Nanoparticles

M. Prathap Kumar[1,2], G. A. Suganya Josephine[3], A. Sivasamy[1*]

[1]Chemical Engineering area, CSIR-Central Leather Research Institute, Adyar, Chennai, Tamil Nadu, India

[2]Department of Chemistry, MVJ College of Engineering, Bangalore, Karnataka, India

[3]AVIT, Vinayaka Mission's Research Foundation, (Deemed to be University) Paiyanoor, Tamil Nadu, India

ABSTRACT

The present study focused on synthesis, characterization and photocatalytic activity of Rare earth doped ZnO nanoparticles for the degradation of Malachite green dye from aqueous phase under visible light irradiation. The concentration of dopant was varied from 3 - 10 wt% and thoroughly characterized by XRD, FT-IR, UV-Vis-DRS, FE-SEM, EDAX and EPR techniques. The band gap energy of (DZ (1:9)) was found to be 3.07 eV, as determined from UV-Vis-DRS analysis. Particle size of the material was in the nano regime (38 to 47 nm) with a hexagonal morphology which is confirmed from FE-SEM analysis. In-situ generation of $OH^{\bullet}$ radicals by light irradiation was confirmed from EPR analysis. The synthesized rare earth doped photocatalyst was investigated under Visible light irradiation for the photocatalytic degradation of non azo dye (MG). At neutral pH (7.10) the photocatalyst displayed 92% degradation of MG dye under both Visible light irradiations. As the substrate concentration increased from 5 ppm to 25 ppm the rate constant showed a decreased trend. The R^2 values clearly indicated that the reaction follows a pseudo-first order kinetics and found to possess enhanced photocatalytic activities under Visible light irradiation. The efficiency and cost effectiveness of DZ (1:9) nanomaterial was determined from reusability studies for the photocatalytic degradation of MG dye and it exhibited better photocatalytic activity even after three cycles of reuse under Visible light irradiation.

Keywords: Rare Earth Doped, Nanoparticles, MG, Visible Light

I. INTRODUCTION

Effluents from various industries such as pharmaceutical, textile, tanneries, paper mills, food, cosmetic industries etc., has been expelled into water bodies thereby contaminating the nature, colour and odour of water. It also affects the natural ecosystem present in water. As the toxic substances exceeds the permissible level it can be harmful and causes serious health disorders to both flora and fauna. The major constituents of effluents includes organic and inorganic compounds, pesticides, heavy metals etc., Several research groups around the world have employed physical and chemical methods for detoxification of pollutants present in waste water. Due to generation and discharge of secondary metabolites and use of solvents etc., (1, 2) the methods were not practised. In order to overcome the disadvantages of these methods Advanced Oxidation Processes (AOP) was employed which has attracted many researchers globally for degradation of organics and

inorganics present in the waste water in the presence of semiconductor photocatalyst. Semiconductor metal oxides are suitable candidates for light induced photocatalytic processes (3, 4). Metal oxides such as TiO2, ZnO, Bi2O3, WO3, CeO2 etc., exhibits excellent photocatalytic activity in degradation of organic and inorganic molecules (5, 6, 7, 8). Since UV light is energy intensive and the availability is less, hence we focused on synthesis of visible light active photocatalyst by modification of band gap. This is achieved by doping of metals, non-metals, rare earth metals etc., (9, 10, 11, 12, 13, 14).

In the present work we focused on visible light active Dy doped ZnO by co-precipitation technique. The prepared material was characterised by FT-IR, XRD, UV-Vis-DRS, FE-SEM, EDAX and EPR techniques. Evaluation of the photocatalyst was investigated by degradation of MG dye under Visible light irradiation.

II. METHODS AND MATERIAL

2.1 Materials

Dysprosium Nitrate hexahydrate (99.9%, Dy(NO3).6H2O), Zinc nitrate hexahydrate (98%, Zn(NO3)2•6H2O) and DMPO (5,5-Dimethyl-1-pyrroline-N-Oxide) were purchased from Sigma-Aldrich, India. Na2CO3, Orange G dye (90%, 7-hydroxy-8-phenlyazo-1,3-naphthalenedisulfonic acid disodium salt) and Malachite green dye (90%, 4-{[4-(Dimethylamino) phenyl] (phenyl) methylidene}-N,N-dimethylcyclohexa-2,5-dien-1-iminium chloride) were supplied by S.D. Fine Chem., Mumbai, India.

2.2 Preparation of Dy3+ doped ZnO (DZ)

The rare earth doped ZnO used in this study was prepared by a simple co-precipitation technique as reported elsewhere (15). A typical procedure involves ZnNO3.6H2O and DyNO3.6H2O mixed in the required molar ratio in double distilled water and Na2CO3 was prepared in a 1:1 ratio with respect to the nitrates. The salt solution was vigorously stirred followed by dropwise addition of Na2CO3 which resulted in the formation of white precipitate. After successful addition of Na2CO3, the obtained precipitate was allowed to stir for 15 min, filtered, washed thrice with water and then with ethanol. The obtained precipitate was dried at 100°C in an oven overnight and then calcined at 700°C for 2 h. The various doping ratios prepared were: 0:100, 3:97, 5:95, 7:93, 10:90, 100:0 of dysprosium nitrate : zinc nitrate and named as PZ (pristine ZnO), 3DZ, 5DZ, 7DZ, 10DZ, PD (pristine Dy2O3).

2.3 Instrumental Analysis

The instrumental techniques such as X-ray diffraction (XRD) analysis, Fourier transform-infra red (FT-IR), ultra-violet diffuse reflectance spectroscopy (UV-DRS), field emission scanning electron microscope (FE-SEM), energy dispersive X-ray diffraction (EDAX) and (EPR) spectroscopy were employed for characterization of prepared semiconductor material. The bond stretching vibrational frequencies of metal oxides were determined by FT-IR analysis in a Perkin Elmer instrument. Crystallinity and phase analysis was determined from X-ray diffraction by PAN analytical X-ray diffractometer, Germany, with scanning angle 2θ in the scan range between 10◦ and 70◦ with Cu Kα radiation. In order to determine the surface morphology and particle size of the synthesized material FE-SEM (Model Supra 55 - Carl Zeiss, Germany) was carried out. EDAX analysis was

carried out to determine the percentage of dopant concentration in the synthesized material. UV-Diffuse Reflectance Spectroscopy (UV 2600, Shimadzu spectrometer; Japan) was employed to calculate the band-gap energy of the nanomaterial with a scan speed of 200 nm/min in the UV-Visible range (200-800nm). EPR spectrometer (Model - Bruker EMX X Band) was employed to determine the generation of OH• radicals in the in-situ process of Visible irradiation.

2.4 Photocatalytic degradation studies

Malachite Green (MG) dye was employed as model pollutant for the photocatalytic degradation Visible light irradiations. The photocatalytic degradation was performed in an annular type photoreactor (Heber Scientific Company Ltd., Chennai, India) with an irradiation source of 500 W tungsten halogen lamp. The irradiation source was surrounded by a water jacketed tube which was cooled continuously with water circulation to reduce the heat. Preliminary experimental parameters like effect of pH, catalyst dosage and substrate concentration were performed to determine the optimal dopant concentration that exhibits enhanced photocatalytic activity with respect to the undoped material. The reaction tubes containing the aqueous dye solution and photocatalyst were irradiated for a specific time and kinetic analysis was conducted by withdrawing aliquots of the samples at prescribed time intervals to assess the extent of degradation process by UV-visible absorption measurements. The substrate concentration before and after photocatalytic degradation was computed from a calibration curve and the percentage degradation of MG was calculated using equation (1).

degradation efficiency (%) = (C0-Ce/ C0) * 100 (1)

where, C0 and Ce are the initial and final MG dye concentrations in the aqueous phase, respectively.

III. RESULTS AND DISCUSSION

3.1 FT-IR analysis

The FT-IR spectra of synthesized (DZ) material is shown in Fig. 1(a). The bond stretching frequencies of metal to oxygen bond i.e., Dy-O and Zn-O was observed at 481 and 533 cm^{-1} respectively of the photocatalyst confirming the composition of the prepared material [16, 17].

3.2 X-Ray Diffraction Pattern

The XRD patterns of DZ photocatalyst is shown in **Fig. 1(b).** The material exhibited crystalline nature which is confirmed from clear and sharp peaks and the patterns obtained were matched with zinc oxide and dysprosium oxide JCPDS data (ZnO-JCPDS No. 36-1451 and Dy2O3-JCPDS 01-079-1722) (18). The as-prepared DZ photocatalyst exhibited (222) reflection which is a characteristic of Dy_2O_3 confirming the presence of Dy^{3+} in the photocatalyst. The average crystallite size of the prepared material was calculated using Scherer equation eq (2).

$$D = k\lambda / (B \cos \theta) \quad (2)$$

where, k is 0.94 (spherical nanoparticles), λ the wavelength of radiation (0.154 nm) and B is the full width at half maximum (FWHM) and θ half the diffraction angle. The average crystallite size of DZ photocatalyst was found to be 36.36 nm. 10DZ exhibited diffraction planes at (222), (100), (400), (002), (101), (102), (110), (103), (004), (112) and (201). The lattice parameters 'a' and cell volume 'c' of DZ photocatalyst was found to be 1.0625 and 1.1935 nm respectively.

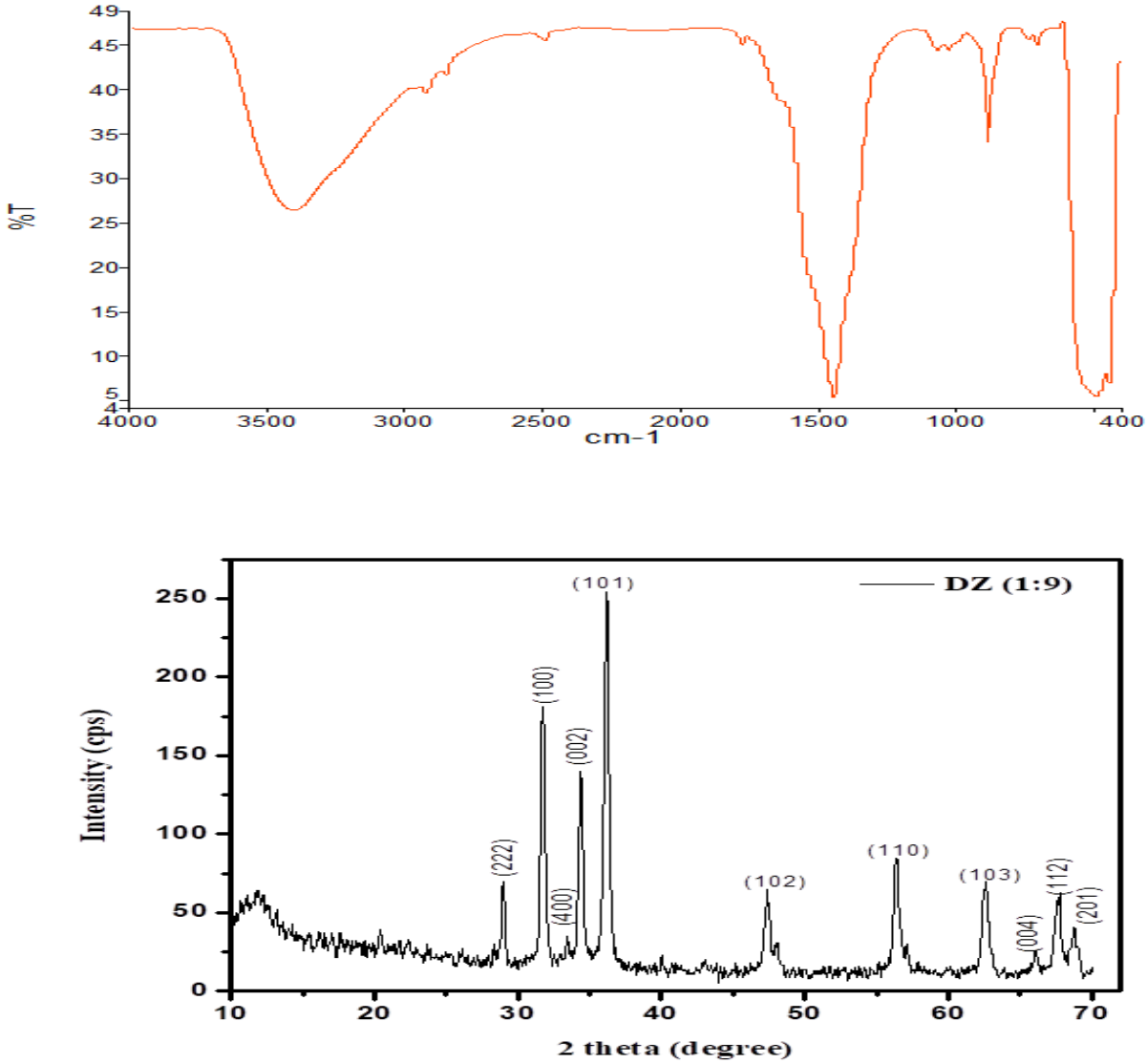

Fig. 1. (a) FT-IR spectrum and; (b) X-ray Diffraction pattern of DZ (1:9) photocatalyst

3.3 UV- Vis Diffuse Reflectance Spectrum

The band gap energy (E_g) of prepared nanomaterial was determined by UV- Vis DRS spectrometer and the spectrum was recorded for PZ, 3 DZ, 5 DZ, 7 DZ and 10 DZ and is shown in **Fig. 2(a) and (b).** As the doping concentration of Dy^{3+} increases from 0-10% a shift towards the visible region was observed. The absorption bands of lanthanide elements was observed above 700 nm and is due to f-f transitions. A plot of $(Ahv)^2$ *vs* hv gives the band gap energy (Eg) of the prepared photocatalyst and is found to be 3.16 eV for PZ and 3.07 eV for 10 DZ respectively.

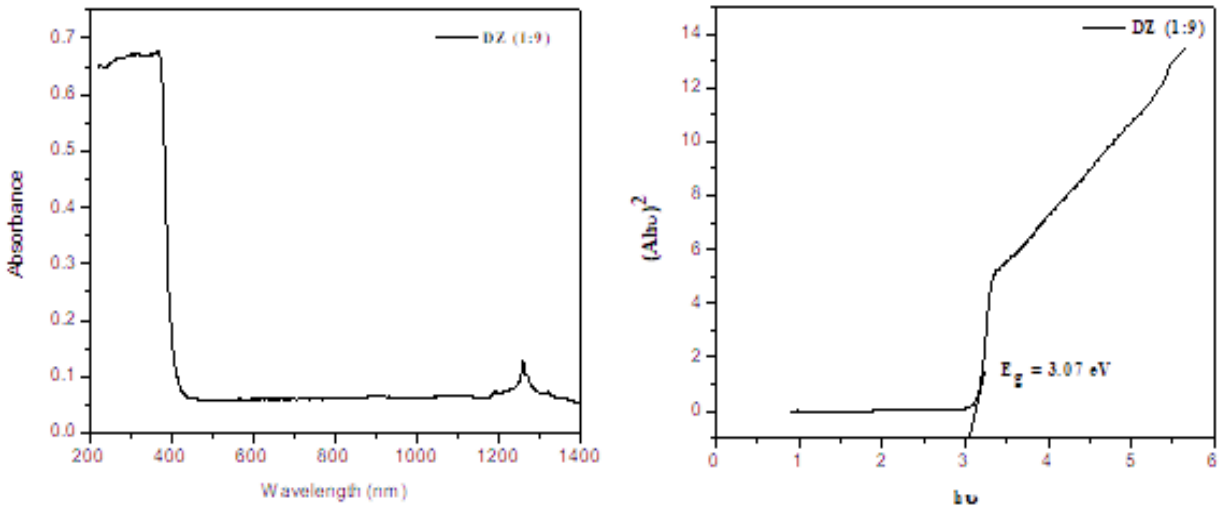

Fig. 2. (a) UV-Vis DRS pattern and; (b) Band gap energy of DZ (1:9) photocatalyst

3.4 Morphology and surface roughness

Surface morphology and particle size of the as-prepared material was determined by FE-SEM analyses and the results are displayed in **Fig. 3.** It exhibits hexagonal morphology with particle size ranging from 38 - 47 nm as shown in **Fig. 3(a)**. EDAX analysis was carried out to determine the elemental composition of the prepared material and confirms the presence of Zn, Dy and O elements and is shown in **Fig. 3(b)**.

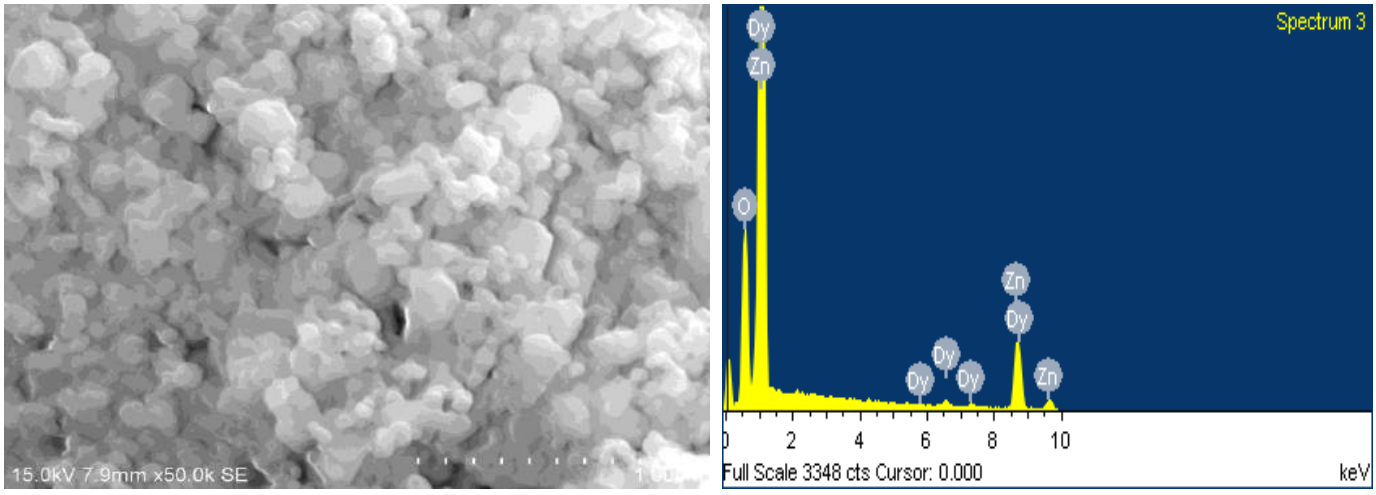

Fig. 3. Morphological and Elemental composition by (a) FESEM; (b) EDAX; and (c) HRTEM analysis

3.5 EPR studies

EPR spin trap technique was employed to probe the reactive oxygen species generated on the surface of DZ photocatalyst upon Visible light irradiation. The spin trapping agent employed was DMPO. As shown in Fig.4 four characteristic peaks in the ratio of 1:2:2:1 was observed indicating the spin trapped DMPO-OH•. This clearly shows that OH• radicals were generated on the surface of DZ photocatalyst.

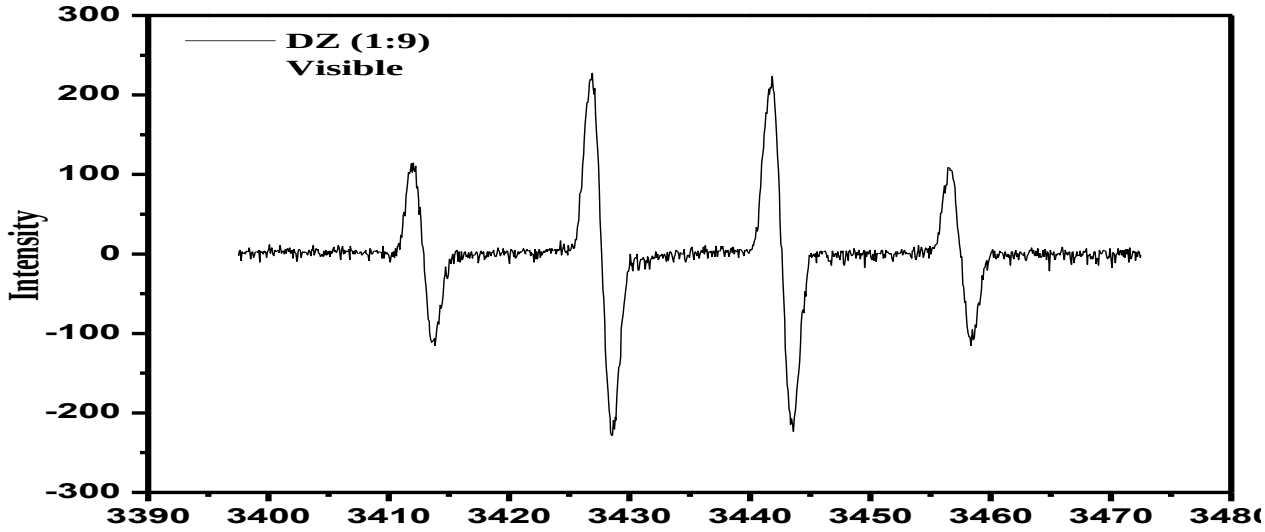

Fig. 4. EPR spectrum of the DMPO spin trapped •OH radical generated *in-situ* under (a) visible irradiation.

3.6 Preliminary experimental parameters for photocatalytic degradation of Malachite Green dye molecules under Visible light irradiation

3.6.1 Effect of aqueous phase pH

Effect of aqueous phase pH on photocatalytic degradation of MG dye by DZ photocatalyst under Visible light irradiation was performed. A series of aqueous phase pH of the dye solutions varying from 2 - 11 were prepared and irradiated. 10 mg of DZ photocatalyst in 10 ppm/10 ml of MG dye concentration exhibited more than 90% of degradation under Visible light irradiation at neutral pH and the result is shown in Fig. 5 (a).

3.6.2 Effect of catalyst dosage

To determine the optimum dosage of catalyst required for photocatalytic reaction, studies on varying catalyst dosage were carried out and the results are shown in Fig. 5 (b). The catalyst dosage was varied from 5 - 25 mg/ 10 ml of 10 ppm MG dye concentration. It was observed that 10 mg of DZ photocatalyst exhibited 97% degradation under Visible light irradiation. The percentage of degradation decreased on increasing the dosage of catalyst. This is due to large amount of catalyst present in the system and causing more turbidity and that obstructs the photons entering onto the surface of the catalyst thereby reduces the photocatalytic activity of the catalysts.

3.6.3 Effect of substrate concentration

The effect of varying initial dye concentration on photocatalytic degradation of MG dye molecules DZ photocatalyst under Visible light irradiations was investigated to determine the optimum concentration of MG dye molecules required for further photocatalytic reaction. The substrate concentration was varied from 5 to 25 mg/l for 10 ml of test solutions. 10 mg of DZ photocatalyst exhibited above 98% of degradation for 10 ppm of MG dye molecules under Visible light irradiations at neutral pH. The percentage degradation decreased from 96% (5 ppm) to 95% (25 ppm) was observed for MG dye and the obtained results were shown in Fig. 5 (c). As the substrate concentration increased decrease in percentage of degradation was observed and is due to

reduction in number of photons reaching the surface of catalyst which further results in lack of hydroxyl radicals.

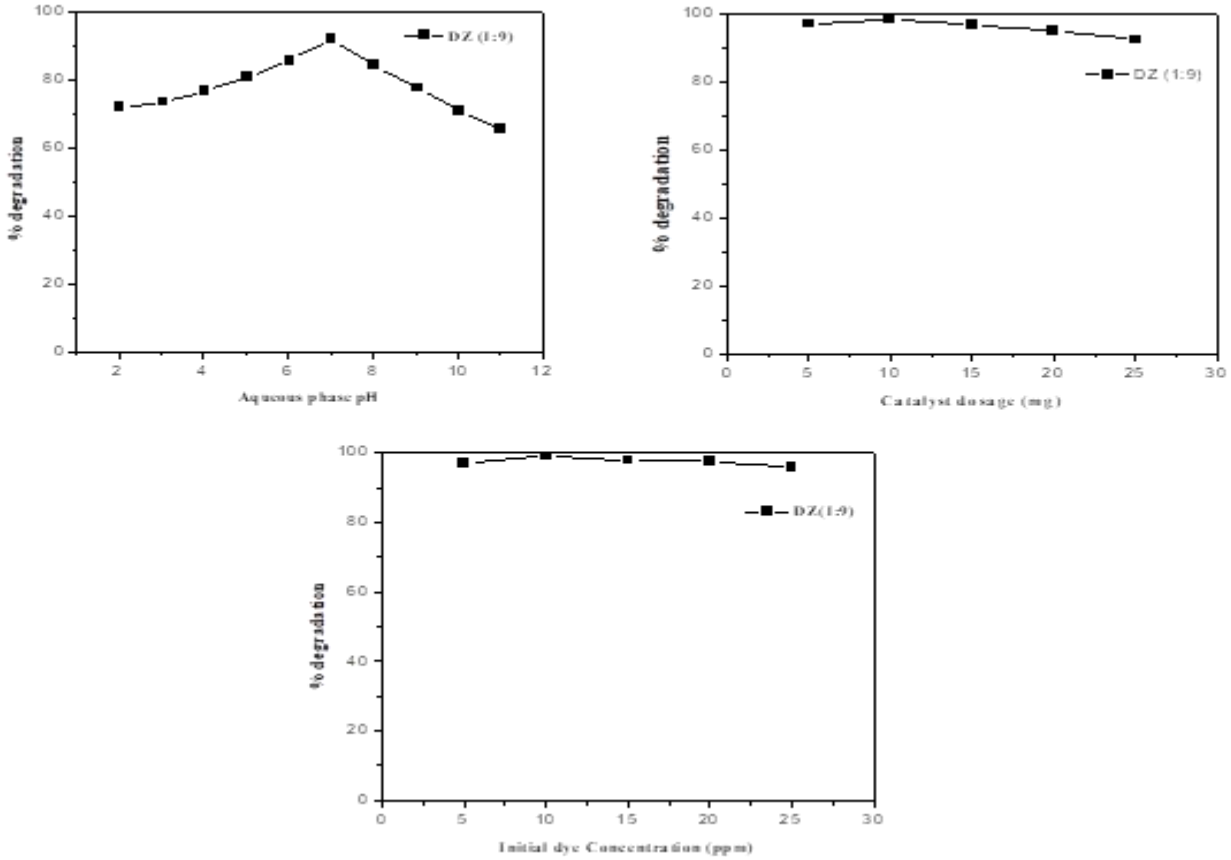

Fig. 5 Preliminary photocatalytic studies of the prepared 10 DZ photocatalyst under Visible light irradiation (a) Effect of pH, (b) Variation of photocatalyst mass and (c) Variation of substrate concentration

3.6.4 Kinetics

The kinetics of photodegradation of MG dye molecules by DZ photocatalyst was monitored by time dependence studies. The kinetic experiments were performed for various initial substrate concentrations such as 5, 10, 15, 20 and 25 ppm with catalyst dosage of 100 mg of DZ photocatalyst in 100ml of preferred dye concentration. Samples were withdrawn at regular intervals of time during the photocatalytic experiments and absorbance were measured at respective λmax of the dye molecule. The residual concentrations were computed from the calibration graph and COD levels were analyzed. DZ photocatalyst exhibited 89% of degradation at 240 min under Visible light irradiation. The obtained results were tabulated in Table 1 and Fig. 6 (a). The pseudo-first order rate constant were calculated and the values were found to decrease as shown in Table 1. The R2 values clearly indicated that the reaction follows pseudo-first order kinetics for photocatalytic degradation of MG dye molecules which is shown Fig. 6 (b). A decrease in COD level from 584 mg/L to 14.4 mg/L was observed for MG dye degradation under Visible light irradiation and results are shown in Fig. 6(c).

Table 1.

Malachite green (Visible light irradiation)					
Catalyst	DZ				
Concentration of the organic molecule (ppm)	5	10	15	20	25
Rate Constant x 10^{-3} min^{-1}	12.71	9.68	6.97	5.70	5.41
R^2	0.9875	0.9811	0.9822	0.9931	0.9885
% COD removal	95.00	97.53	93.85	74.59	72.39

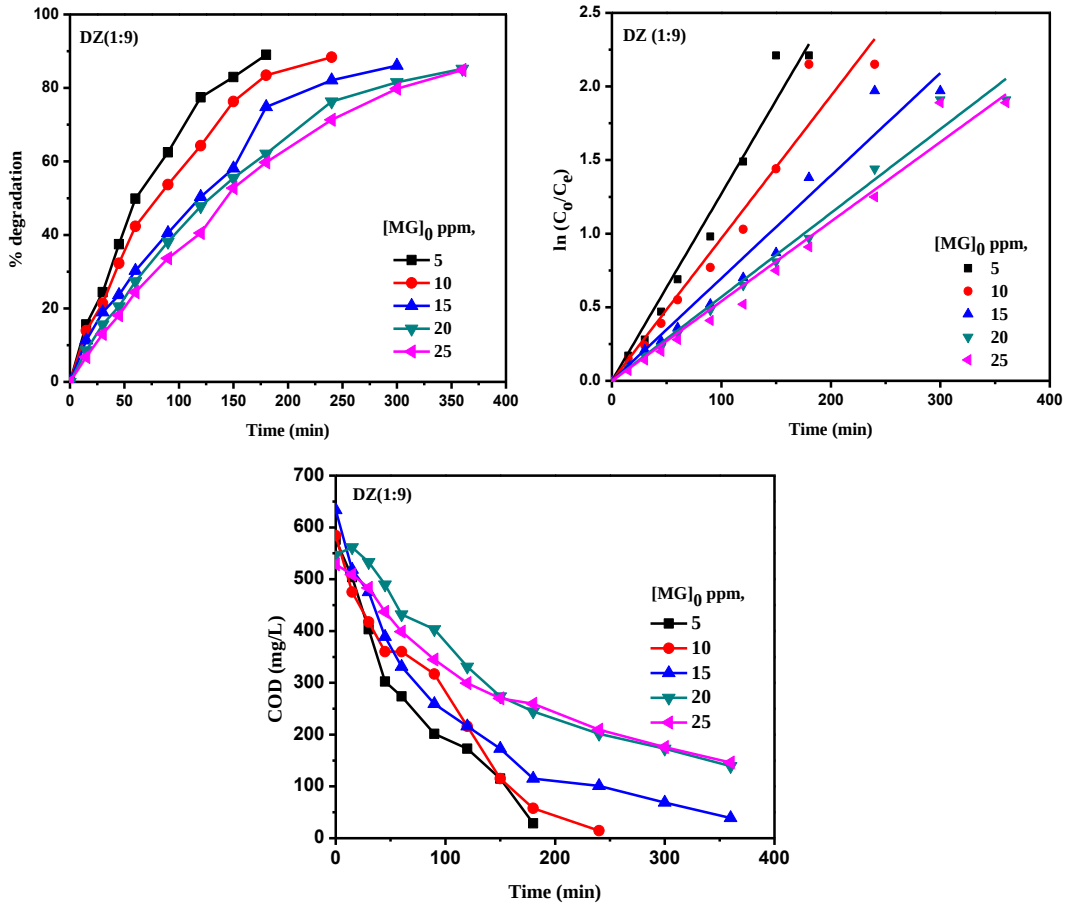

Fig. 6. (i) Kinetics of photo degradation of MG dye molecule (ii) Pseudo- first order kinetic plots for photo degradation of MG dye molecule (iii) COD removal under Visible light irradiation.

3.6.5 Effect of Electrolytes

The interference of inorganic anions present in the industrial waste water on photocatalytic degradation of MG dye molecules by DZ (1:9) photocatalyst under Visible light irradiation was investigated. The electrolytes employed were KCl, $MgSO_4$, Na_2CO_3 and $NaHCO_3$. The electrolyte concentrations were varied from 1 to 7 wt% for dye molecules. The obtained results were shown in Fig. 10. As the concentration of KCl is increased, the percentage of degradation of MG dye molecules decreases and is due to chloride ions that acts as radical scavengers (19). It is confirmed that carbonates and bicarbonates has no effect on the activity. Similarly,

increasing the concentration of sulphate up to 1.5% showed an increase in photocatalytic degradation and is due to generation of sulphate radicals in the photocatalytic system. Further increasing the concentration of sulphate beyond 1.5% leads to decreased photocatalytic degradation of MG dye molecules. This phenomena may be due to adsorption of sulphate radicals on the surface of the catalyst which competes with the substrate molecules (20).

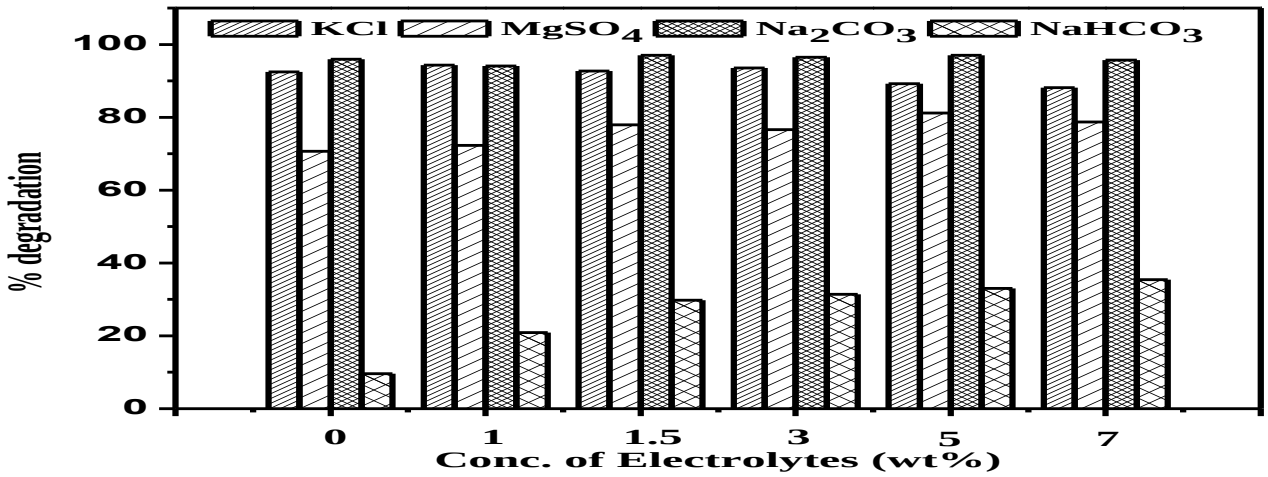

Fig. 8. Effect of electrolytes on the photocatalytic degradation MG dye molecule by 10DZ under Visible light irradiation

3.6.6 Reusability Studies

The efficiency of the DZ photocatalyst was determined from reusability studies in photocatalytic degradation of MG dye molecule under Visible light irradiation and the results were shown in Fig. 11. DZ (1:9) photocatalyst shows decrease in percentage of degradation from 93% to 88% under Visible light irradiation indicating that the catalyst retains its photocatalytic activity even after three cycles of regeneration.

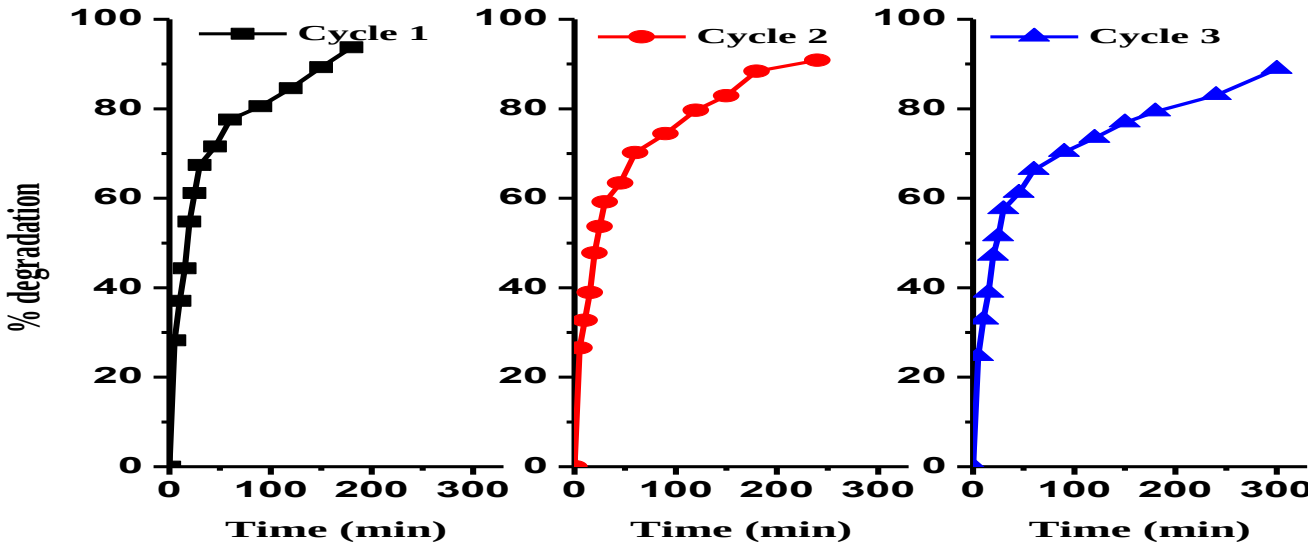

Fig. 9 Reusability studies of 10DZ in photocatalytic degradation of MG dye molecule under (i) Visible light irradiation.

3.6.7 By- Product analysis

The UV-Visible absorbance spectrum further supports that the MG dye molecule has completely degraded and no peaks corresponding to UV-Visible active by-products are present from 200 - 800 nm in the spectrum. Hence, the prepared photocatalyst completely degrades the MG dye molecule effectively under Visible light irradiation. The Fig. shows the change in colour on irradiation of MG dye molecule in the presence of the 10 DZ photocatalyst.

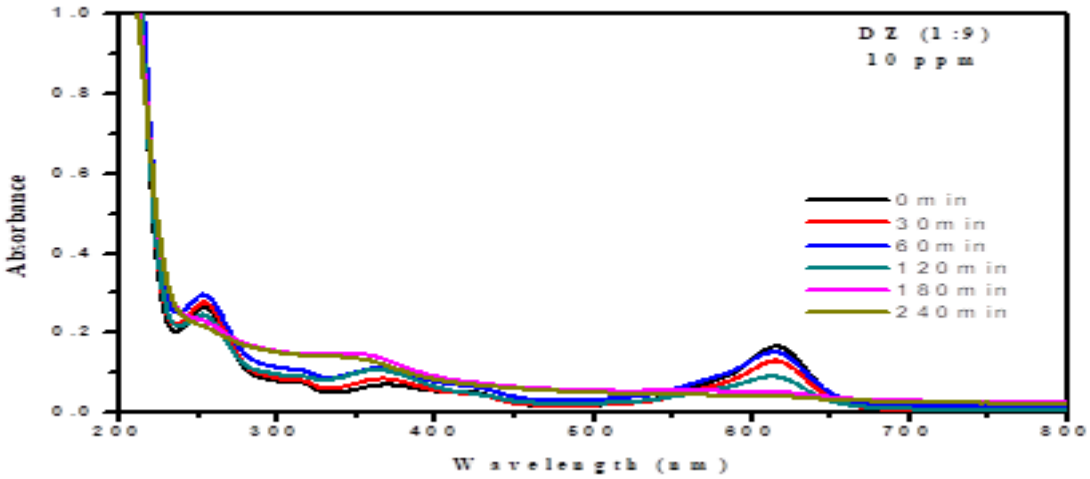

Fig. 10 UV- Visible absorbance spectrum of MG dye molecule under Visible light irradiation

IV. CONCLUSION

Nanocrystalline dysprosium modified ZnO (DZ) photocatalyst prepared by co-precipitation method and characterized by FT-IR, XRD, UV-Vis-DRS, FE-SEM, EDAX & EPR techniques. The characterization results of the synthesized photocatalyst clearly confirms the presence of elements, band gap, crystallinity, morphology & EPR analysis confirms the generation of ·OH radicals in photocatalytic system. The synthesized photocatalyst was evaluated for its photocatalytic activity in degradation of Malachite Green dye molecules in aqueous phase under Visible light Irradiations. Preliminary studies like effect of pH, varying catalyst dosage and variation of initial substrate concentration were studied in detail. Kinetics studies were investigated and the reaction followed pseudo-first order relationship. The progress of the reaction was also monitored by COD analysis. The efficiency of the photocatalyst was determined from reusability studies. Rare earth doped metal oxides exhibited better photocatalytic activity than Pristine metal oxides.

V. REFERENCES

[1]. C. Philippe, B. Vandevivere, V. Willy, J. Chem. Technol. Biotechnol. 72 (1998) 289,
[2]. Y.M. Slokar, M.A. Le Marechal, Dyes Pigm. 37 (1998) 335
[3]. Hoffmann, M. R.; Martin, S. T.; Choi, W. Y.; Bahnemann, D. W. Environmental Applications of Semiconductor Photocatalysis. Chem. Rev. 1995, 95, 69–96,

[4]. Teoh, W. Y.; Scott, J. A.; Amal, R. Progress in Heterogeneous Photocatalysis: From Classical Radical Chemistry to Engineering Nanomaterials and Solar Reactors. J. Phys. Chem. Lett. 2012, 3, 629–639
[5]. D. Devilliers, Energeia 17 (2006) 1–6,
[6]. M.M. Khan, S.A. Ansari, D. Pradhan, M.O. Ansari, D.H. Han, J. Lee, M.H. Cho, J. Mater. Chem. A 2 (2014) 637–644,
[7]. S.A. Ansari, M.M. Khan, M.O. Ansari, J. Lee, M.H. Cho, New J. Chem. 38 (2014) 2462–2469,
[8]. S. Anandan, M. Miyauchi, Chem. Commun. 48 (2012) 4323–4325
[9]. S.A. Ansari, M.M. Khan, S. Kalathil, A.N. Khan, J. Lee, M.H. Cho, Nanoscale 5 (2013) 9238–9246,
[10]. Z. Ambrus, N. Balazs, T. Alapi, G. Wittmann, P. Sipos, A. Dombi, K. Mogyorosi, Appl. Catal. B: Environ. 81 (2008) 27–37,
[11]. S.A. Ansari, M.M. Khan, J. Lee, M.H. Cho, J. Ind. Eng. Chem. 20 (2014) 1602–1607,
[12]. T.A. Egerton, J.A. Mattinson, J. Photochem. Photobiol. A: Chem. 194 (2008) 283–289,
[13]. S.A. Ansari, M.M. Khan, M.O. Ansari, J. Lee, M.H. Cho, J. Phys. Chem. C 117 (2013) 27023–27030,
[14]. K.G. Kanade, B.B. Kale, J.O. Baeg, S.M. Lee, C.W. Lee, S.J. Moon, H. Chang, Mater. Chem. Phys. 102 (2007) 98–104
[15]. Anandana, S., Vinua, A., Mori, T., Gokulakrishnan, N., Srinivasu, P., Murugesan, V., Ariga, K., 2007. Photocatalytic degradation of 2,4,6-trichlorophenol using lanthanum doped ZnO in aqueous suspension. Catal. Commun.: 8, 1377-1382
[16]. R.Y. Hong, J.H. Li, L.L. Chen, D.Q. Liu, H.Z. Li, Y. Zheng, J. Ding, Synthesis, surface modification and photocatalytic property of ZnO nanoparticles, Powder Technol. 189 (2009) 426-432,
[17]. Y. Zhang, K.L. Zhang, M.K. Jia, H. Tang, J.T. Sun, L.J. Yuan, Synthesis, Characterization of a Novel Compound SnEr2O4, Chin. Chem. Lett. 13 (2002) 587-589
[18]. B. Karthikeyan, C.S. Suchand Sandeep, T. Pandiyarajan, P. Venkatesan, P. Reji, Spectrally broadened excitonic absorption and enhanced optical nonlinearities in Dy3+-doped ZnO nanoparticles, Appl. Phys. A: Mater. Sci. Process. 102 (2011) 115-120
[19]. Trabelsi, H.; Atheba, P.; Gbassi, G. K.; Ksibi, M.; Drogui, P. Int. J. Hazard. Mater. 2012, 1, 6-10
[20]. Sakthivel, S.; Neppolian, B.; Shankar, M. V.; Arabindoo, B.; Palanichamy, M.; Murugesan, V. Sol. Energy Mater. Sol. Cells 2003, 77, 65–82

National Conference on Applied Sciences Synergising the Engineering and Technology
Print ISSN: 2395-6011 | Online ISSN: 2395-602X (www.ijsrst.com)
© 2021 IJSRST | Volume 8 | Issue 2

Utilization of Nano Oxide on Adsorption of Hexavalent Chromium: A Kinetic and Isotherm Study

Sushma[1], Susmita Kamila[2*]

[1]East Point College of Engineering, Bangalore-560049(VTU), Karnataka, India

[2]M.S. Engineering College, Bangalore-562110, Karnataka, India

ABSTRACT

Zinc oxide nanoparticles were successfully employed for the mitigation of hexavalent chromium [Cr (VI)] from synthetic water Sample by Batch Adsorption Technique. Parameters like adsorbent dose and contact time were studied in this process. The experimental data were examined for their kinetic studies using Lagergren's First Order and Pseudo second order kinetics. Furthermore, the data were fit to both Langmuir and Tempkin isotherms, where they fit to Tempkin isotherm with high correlation coefficients (R^2 = 0.998). The maximum adsorption was found at adsorbent dose 0.1g and contact time of 40mins. In kinetics, the data were best fitted to pseudo second order kinetics indicating that the adsorption is chemical in nature.

Keywords : Zinc Oxide Nanoparticles, Batch Adsorption, Correlation Coefficients

I. INTRODUCTION

Nanotechnology, is one of the finest technology gaining interest of many researchers in different areas of science. One of the major application of Nanotechnology is in the field of water treatment. Various types of Nano materials are being developed to study their application in water treatment. Due to their extraordinary properties such as surface area, particle size, pores and stability, they can be easily transported through a water body by pedesis without the external force [1]. Several Attempts have been made by the researchers to utilize these smart materials in the removal of Chromium in water. The metal Chromium has Atomic no.24 and density of 7.19 $g.cm^{-3}$, and exists in two forms in nature i.e. hexavalent chromium [Cr (VI)] and trivalent Chromium [Cr (III)].The Cr (VI) is toxic to flora and fauna whereas Cr (III) is micronutrient required for the growth of plants. The major accumulation of Cr (VI) in water takes place due to the release of waste from electroplating industries, batteries, Potteries etc. [2].

The methods like ion exchange, phyto-remediation, photo catalysis, membrane filtration, reverse osmosis, electro dialysis, Adsorption [3-9] are frequently used for dechlorination of water samples. Among these, Adsorption is found to be simple, cost effective and easy to operate. Various Nano adsorbents such as Metal nanoparticles, metal oxide nanoparticles such as zinc oxide, copper oxide, magnetic nanoparticles such as ferric oxide, carbon based nanoparticles etc. are used by many researchers [10-12].

In the present investigation, Zinc oxide nanoparticles have been used to remove Cr (VI) from synthetic water sample.

II. METHODS AND MATERIAL

A. Materials and Methods

The chemicals are used were of analytical grade and used as received. A Synthetic water sample was prepared by dissolving 2.489g of $K_2Cr_2O_7$ in 1000ml of deionized water. The Nano sorbent was prepared by Precipitation Method [13].These nanoparticles were then utilized for batch adsorption study.

B. Batch Adsorption Experiment and Analysis of Cr (VI)

The Effect of adsorbent dose and contact time has been carried out. In a 50ml conical flask, 25ml of synthetic water sample was taken and stirred with known amount of Zinc Oxide for 60mins at 30^0C. After stirring, the solutions were filtered using Whatmann 41filter paper and the filtrate was taken to determine the Cr (VI) using Diphenyl- Carbazide method from UV-Visible Spectrophotometer (Elico, SL-159) [14].The percentage removal of Cr after adsorption is calculated using the relation.1

$$\% \text{ Removal} = \frac{C_O - C_e}{C_O} \times 100 \qquad (1)$$

Where, C_o is initial concentration, C_e is Final concentration [9].

III. RESULTS AND DISCUSSION

A. Effect of Reaction Time

The Impact of reaction time for Chromium adsorption was carried out in the range of 30min to 70min at 30^0C.The Graph of percentage removal of hexavalent chromium vs. Contact Time is shown in the fig.1. The adsorption is found to be rapid in the first 40mins due to the availability of free vacant sites on the surface of the Adsorbent. After 40mins, the adsorption slowly decreases because the vacant sites becomes saturated with the time.

B. Effect of Adsorbent Dose

It is clear from the fig.2.that the adsorption Increases with increase in the dosage (from 0.02g to 0.1g).This is due to the availability of lager surface area and vacant sites.

C. Adsorption Isotherm Model

1. Langmuir Adsorption Isotherm

It is two parameter isotherm, and The Equilibrium adsorption data for the concentration of Cr (VI) was fitted to the linear form of the Langmuir isotherm. The isotherm constants are calculated from the linear plot of $1/q_e$ v/s $1/c_e$ as shown in fig.3.

The linear form of the Langmuir isotherm model is given by

$$\frac{1}{q_e} = \frac{1}{Q_o} + \frac{1}{Q_o K_{LC_e}} \quad (2)$$

Where, q_e is amount of metal adsorbed (mg/g), Ce is concentration after adsorption (ppm), Q_0 is maximum monolayer coverage capacity (mg/g) and KL is Langmuir constant (L/mg).

2. Tempkin Adsorption Isotherm

It is also a two parameter isotherm, which takes into account the interactions between adsorbate and adsorbent. It is also assumed that the heat of adsorption of all the molecules in all the layers decreases linearly as the result of increase in surface coverage. The Tempkin isotherm is valid for the intermediate range of concentration of ions. The above equation is written linearly as follows:

$q_e = B \ln A + B \ln C_e$ (3)

Where B is constant related to heat of sorption (J/mol), A is the Tempkin isotherm constant (L/g), The constants A and B are calculated from the intercept and slope of the linear plot of the isotherm. [15].A plot of q_e v/s ln C_e is shown in fig.4 and constants are reported in Table.1.

D. Adsorption kinetics

The adsorption kinetics and constants were determined by Lagergren's first order and pseudo second order model using equation 4 and 5.

$$\log(q_e - q_t) = log q_e - \frac{k_1}{2.303} t \quad (4)$$

$$\frac{t}{q_1} = \frac{1}{k_2 q_e^2} + \left(\frac{1}{q_t}\right) t \quad (5)$$

Where, q_e is the amount of hexavalent Chromium adsorbed at equilibrium time, q_t is the amount of Cr (VI) adsorbed at time t, k_1 and k_2 are the rate constants of first order and second order kinetics respectively .Lagergren's first order model is obtained by the plot of log (qe- qt) v/s time and pseudo second order model is obtained by plotting t/q v/s time. The correlation coefficients (R^2) Value for the second order kinetics was found to be greater than Lagergren's first order model indicating that the adsorption is chemical in Nature[16].The Kinetic plots are given in fig.5 and fig.6 constants are tabulated in Table.2.

Table.1. Adsorption isotherm constants

Langmuir isotherm			**Tempkin isotherm**		
Q_O	K_L	R^2	A_T	B	R^2
0.00165	-76.313	0.9381	3.162	85.106	0.998

Table.2.Kinetic Parameters for Cr (VI) adsorption on ZnO Nanoparticles

Lagergren's first order kinetics			**Pseudo second order kinetics**		
q_e	K_1	R^2	q_e	K_2	R^2
18.96	0.002	0.694	21.5	0.004	0.971

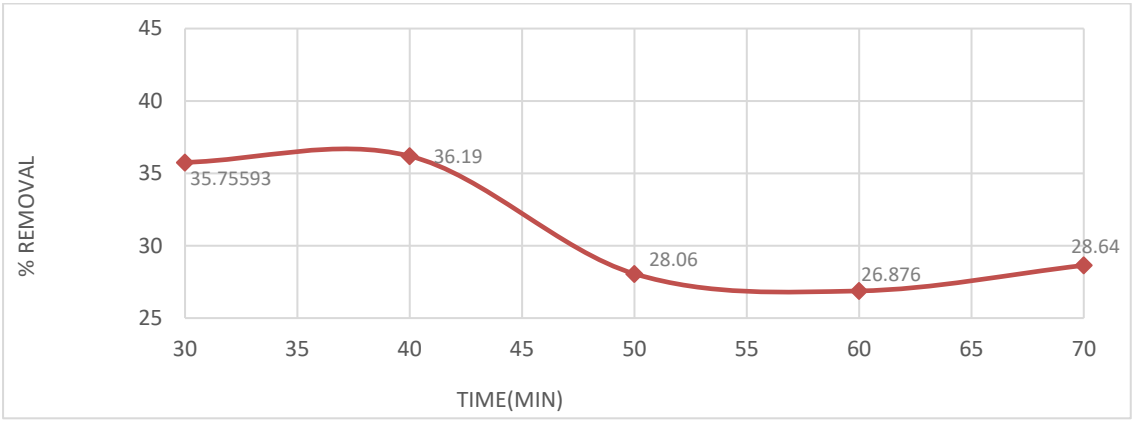

Fig.1.Effect of Reaction Time

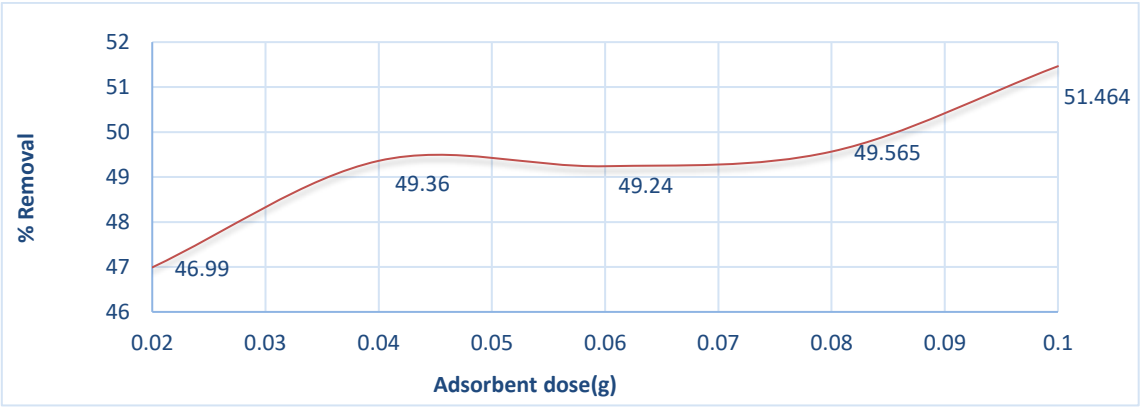

Fig.2.Effect of Adsorbent dose

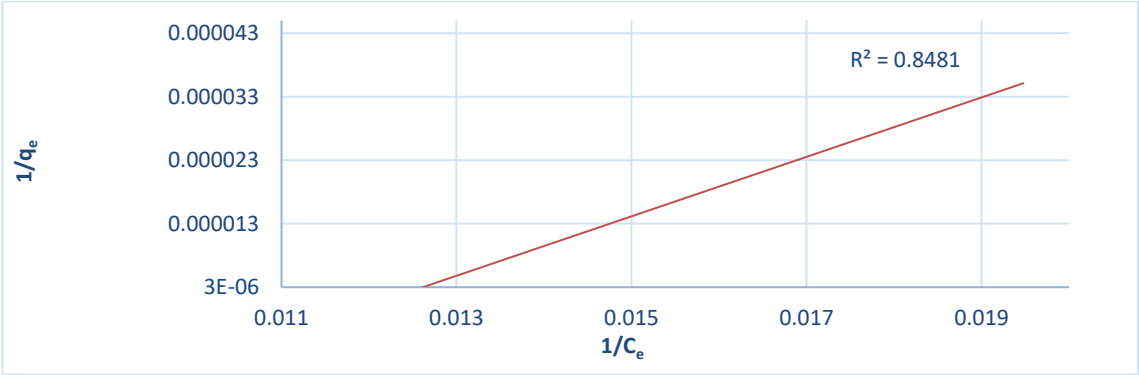

Fig.3.Langmuir Adsorption Isotherm

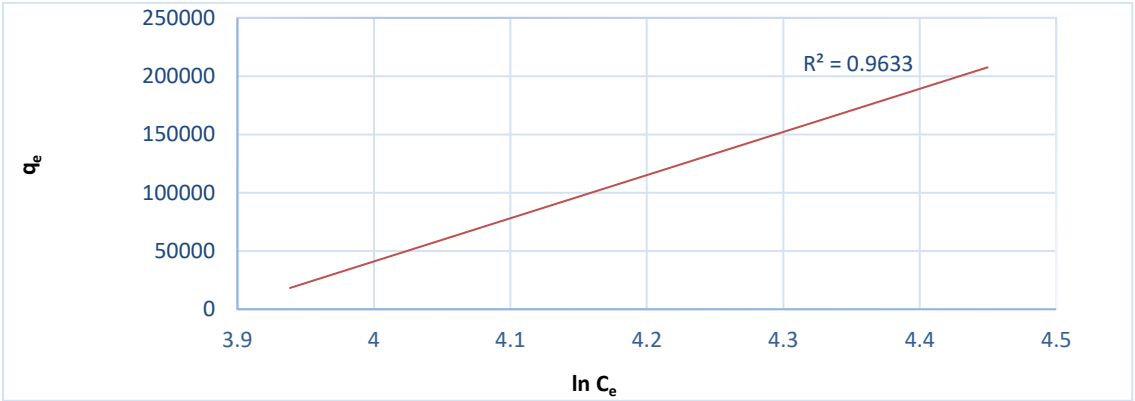

Fig.4.Tempkin Adsorption

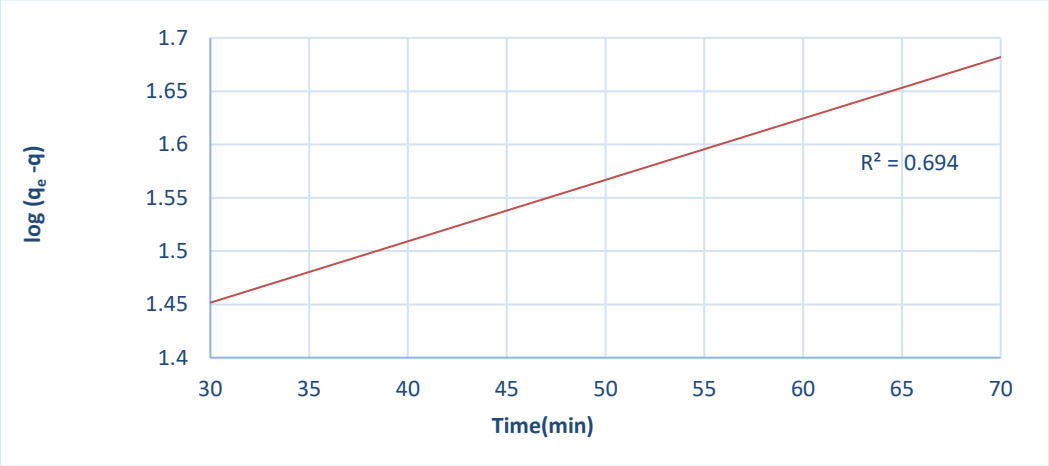

Fig.5.Lagergren's first order kinetics

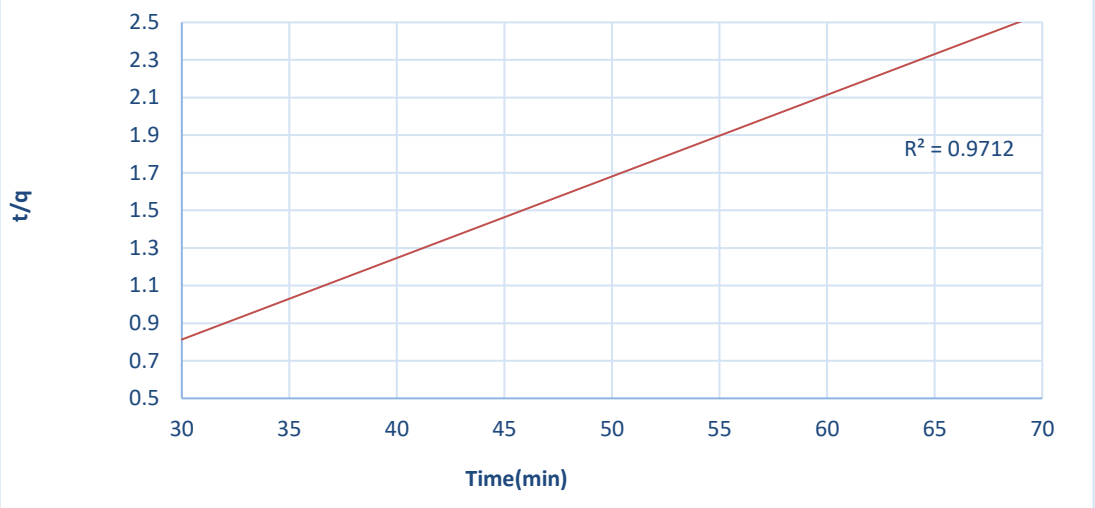

Fig.6.Pseudo second order kinetics

IV. CONCLUSION

This Paper reports the utilization of Zinc oxide nanoparticles for the removal of hexavalent Chromium from water sample. It was found that the adsorption is maximum at 40mins and dosage of 0.1g. The data was analysed using Langmuir isotherm and Tempkin isotherm. However, there is good fit for tempkin isotherm than that of Langmuir isotherm. The kinetic model reveals that pseudo second order kinetics is best followed than pseudo first order indicating that
the system follows the chemical Adsorption.

V. ACKNOWLEDGMENT

The authors are thankful to East Point College of Engineering, Bangalore for Infrastructural facilities.

VI. REFERENCES

[1]. X.Qu, P.J.J.Alvarez and Q.Li,"Applications of nanotechnology in water and wastewater treatment," Water Research, vol.47, pp.3931-3946, Aug 2013.

[2]. V.E.Pakade, N.T.Tavengwa and L.M.Madikizela, "Recent advances in hexavalent chromium removal from aqueous solutions by adsorptive methods," RSC Adv., vol.45, pp.26142-26164, Aug 2019.

[3]. S.Rengaraj, K.H.Yeon, S.H.Moon," Removal of Chromium from water and waste water by ion exchange resins," Hazardous Materials,vol.87,pp.273-287,Oct 2001.

[4]. G.Kassaye, N.Gabbiye and A.Alemu,"Phytoremediation of Chromium from tannery wastewater using local plant species,"Water practice & Technology, vol.12, pp.894-901, Dec 2017.

[5]. K.M.Joshi, V.S.Shrivastava," Photo catalytic degradation of Chromium (VI) from wastewater using Nano materials like TiO2, ZnO and CdS," Appl. Nanosciecne, pp.145-155, Sept 2011.

[6]. G.Zolfaghari, M.Kargar,"Nano filtration and Microfiltration for the removal of Chromium, Total dissolved Solids, Sulfates from water," MethodsX, pp.549-557, Mar 2019.

[7]. A.Cimen,"Removal of Chromium from wastewater by Reverse Osmosis,"Russian J. Phy.Chem., vol.89, pp.1238-1243, July 2015.

[8]. R.C.A.Moura, D. A. Bertuol, C. A. Ferreira, and F.D. R. Amado," Study of Chromium removal by the Electro dialysis of Tannery and Metal Finishing Effluents, "International Journal Of Chemical Engineering,2012.

[9]. T.Dula, K.Siraj and S.A.Kitte,"Adsorption of hexavalent Chromium from Aqueous solution using Chemically Activated Carbon Prepared from Locally Available Waste of Bamboo (Oxytenanthera abyssinica),"International Scholarly Research Notices, 2014.

[10]. V.K.Guptha, R.Chandra, I.Tyagi and M.Verma," Removal Of hexavalent chromium ions using CuO nanoparticles for water purification applications," J.Colloid interface sci., vol.478, pp.54-62, Sept 2016.

[11]. H.Kumar, S.K.Sinha, V.V.Goud andS.Das, "Removal Of Cr(VI) by magnetic iron oxide nanoparticles synthesized from extracellular polymeric substances of chromium resistant acid-tolerant bacterium Lysinibacillus sphacericus RTA-01,"J.Environ. Health sci. Engg., vol.17, pp.1001-1016, Nov 2019.

[12]. R.Baby, B.Saifullah and M.Z.Hussein," Carbon Nano materials for the treatment of heavy metal-contaminated water and environmental Remediation," Nano scale Res.Lett. vol.14, Nov.2019.

[13]. V.R.Venugopal and S.Kamila,"Effect of temperature on the morphology of ZnO nanoparticles: A comparative study," Appl. Nanosci., vol.7, pp.75-82, Mar 2017.

[14]. A.Lace, D.Ryan, M.Bowkett and J.Cleary, "Chromium monitoring in water by colorimetry using optimised 1,5-DPC method,"Int.J.Environ.Res.Public Health,vol.16,May 2019.

[15]. J.Bayuo, K.B.P.Ba and M.A.Abukari," Adsorptive removal of chromium (VI) from aqueous solution into groundnut shell," Appl.Water sci., vol.9, May 2019.

[16]. K.Mulani, S.Daniels, K.Rajdeo, S.Tambe and N.Charan,"Adsorption of Chromium (VI) from aqueous solution by coffee polyphenol-Formaldehyde/Acetaldehyde resins," Journal of polymers, vol.2013, Dec 2013.

National Conference on Applied Sciences Synergising the Engineering and Technology
Print ISSN: 2395-6011 | Online ISSN: 2395-602X (www.ijsrst.com)
© 2021 IJSRST | Volume 8 | Issue 2

Urea Based Tripodal Nano receptors and Their Application in Chemo sensing For Cr (III) And HSO4 (I)

Dr. Jayanti Mishra[1,2], Ashok K. Ganguli*[3], Navneet Kaur*[4]

[1]Centre for Nanoscience and Nanotechnology (UIEAST), Panjab University, Chandigarh-160014, India.

[2]Department of Chemistry, East Point College of Engineering and Technology, Virgo Nagar Post, Avalahalli, Bengaluru-560049, Karnataka, India

[3]Department of Chemistry, Indian Institute of Technology, Hauz Khas, New Delhi-110016, India

[4]Department of Chemistry, Panjab University, Chandigarh-160014, India

ABSTRACT

Two urea based tripodal ligands X i.e. 1,1',1''-(2,2',2''-nitrilotris (ethane-2,1-diyl))tris(3-(4-nitrophenyl)urea) and Y i.e. 1,1',1''-(2,2',2''-nitrilotris(ethane-2,1-diyl))tris(3-(naphthalen-1-yl)urea) are synthesised which differ in the terms of their pods. The ligands are characterised by NMR, IR and mass spectroscopic methods. Their organic nanoparticles (ONPs) i.e. X-ONP and Y-ONP are generated by reprecipitation method and analysed by TEM, DLS, UV-Vis and fluorescence spectroscopic methods. Both of X-ONP and Y-ONP are of nanospherical morphology of diameter ~30-35 nm and ~15-20 nm respectively. The chemosensing study of X-ONP showed its fluorescent recognition behaviour towards HSO4(I) with limit of detection as 1.026 micromolar and Y-ONP showed its recognition towards Cr(III) with limit of detection as 1.3 micromolar. The binding of HSO4(I) and Cr(III) with X-ONP and Y-ONP follows continuous pattern by PET-on mechanism with decrease in the fluorescent emission intensity as the function of analyte concentration.

Keywords : Urea, Tripodal, HSO4(I), Cr(III), Fluorescence, PET-on

I. INTRODUCTION

Urea group is very beneficial for sensing because it can alter organic transformations by its hydrogen bonding interactions which is directional in nature and make it favourable for analyte binding with increase in sensitivity “reference [1-3]”. Along with hydrogen atoms, it also possesses electronegative oxygen atom as well as two electron rich nitrogen atoms [1,2] which provide multiple ways and possibilities for host-guest interaction. In organic molecules, electron confinement is not necessary because electrons are localised either in chemical bonds or on any molecule but optical responses are affected by the size variation [3]. Reprecipitation method is opted to prepare organic nanoparticles (ONPs) in this manuscript because of being simple, economic and fast in action [4]. The aqueous dispersion of organic molecule restricts their bond rotation and increase the rigidity which results in specific recognition properties. A sensor detects an input parameter and converts it into an output signal. A good sensor should be economic, stable, selective and sensitive. Fluorescence based sensors are very popular because of being highly selective and sensitive. The

recognition site in the fluorometric sensor identifies the analyte while the fluorophore converts this behaviour into detectable and readable signal [5-9].

Zhou *et al.* prepared a fluorescent sensor for Cr(III) based on rhodamine with detection limit of 0.023 μM applicable in aqueous media [10]. Wu *et al.* detected Cr(III) and Fe(III) in aqueous medium with limit of detection as 25 μM and 2 μM respectively using ratiometric fluorescent sensor bearing two benzimidazole groups [11]. Karak *et al.* developed a fluorescent sensor for Cr(III) using 9-Acridone-4-carboxylic acid based upon chelation assisted fluorescence quenching in DMF-water system [12]. Bhardwaj *et al.* prepared benzthiazole based chemosensor having siderophores like binding sites for detection of HSO_4(I) and Fe(III) by UV-Vis bathochromic shift and fluorescence enhancement respectively [13]. Sain *et al.* developed naked eye chemosensor of CN(I) and HSO_4(I) ions based upon indole [14]. Erdemir *et al.* reported calix[4]arene appended benzothiazole units based fluorescent sensor for HSO_4(I) [15]. Zhang *et al.* prepared a fluorophore based on acridine having benzimidazolium and urea groups for chemosensing of H_2PO_4(I) and HSO_4(I) by fluorescent bathochromic-shift and fluorescence quenching respectively [16]. Tayade *et al.* developed fluorescent turn-on chemosensor based on isonicotiamide for chemosensing of Zn(II) and HSO_4(I) with limit of detection upto nanomolar level [17]. Gunnlaugsson *et al.* prepared fluorescent selective chemosensor for dicarboxylates and pyrophosphate based on thiourea in DMSO [18]. Saluja *et al.* developed a benzimidazole based receptor for Cr(III) detection and the resultant complex proved to be fluorescent chemosensor for HSO_4(I) and F(I) also [19].

From above manuscripts, it can be observed that (–NH), (–CO–) and ($–NO_2$) groups are very popular among the molecules designed for sensing because of their specific binding affinities. By combining these groups with perfect cavity size, we can get ideal chemosensor molecule. Most of the reported sensor molecules are functional in organic solvents. There is need of sensors which can be applicable in aqueous medium to get wider area for sensing because most of the biological fluids and environmental sample exist in aqueous medium only.

Taking inspiration from above manuscripts, we have synthesised two urea based tripodal compounds (X and Y) by simple one step synthesis and employed their organic nanoparticles (ONP) for chemosensing studies. X-ONP and Y-ONP showed chemosensing towards HSO_4(I) and Cr(III) respectively among the pool of cations and anions. 4-nitrophenyl pods of X-ONP and 1-naphthyl pods of Y-ONP formed cavity of perfect space and affinity to fit their respective cation/anion.

II. METHODS AND MATERIAL

A. General information (materials and instruments)

Tris (2-aminoethyl) amine, 4-nitrophenyl isocyanate and 1-naphthyl isocyanate are purchased from Sigma-Aldrich company and used without further purification. Chloroform is purified by simple distillation over K_2CO_3. Reactions are monitored over TLC plates which are prepared by silica gel (Kieselgel 60 PF254, Merck) coated glass sheets. Cation sources are metal nitrates while anion sources are tertrabutylammonium anions, used for recognition studies.

The products are characterised by NMR, Mass and IR spectroscopic techniques. NMR of compounds is performed by BRUKER SPECTROSPIN at 300 MHz. FT-IR studies are done by Thermo Fisher Scientific NICOLET iS50 FT-IR machine. Mass spectroscopic studies are done by BRUKER MICROTOF-QII machine. Elements of products are estimated by elemental analysis performed by FLASH 2000 Organic Elemental

Analyzer by Thermo Fisher Scientific instrument. The optical properties of products are studied by UV-Vis and Fluorescence spectrophotometer on Shimadzu UV-2450 spectrometer (double distilled water as the absorption standard) and SHIMADZU RF-5301PC spectrofluorophotometer.

Reprecipitation method is used to prepare organic nanoparticles (ONPs) which are characterised by transmission electron microscope (TEM) technique, scanning electron microscope (SEM) technique and dynamic light scattering spectroscopy (DLS) as wll as UV-Visible and fluorescence spectroscopic techniques. The particle size and distribution of organic nanoparticles (ONPs) are determined with Dynamic Light Scattering (DLS) using the Malvern ZETASIZER NANO ZSP instrument. TEM images studies are performed on JEM-2100 JEOL machine which is operated at an accelerating voltage of 200 kV. A copper grid of 300-mesh is used as substrate and mounted with 2-3 drops of ONPs for analysis. JSM-IT300 JEOL scanning electron microscope (SEM) is operated at 20kV voltage to get particle morphology. For this, silicon wafers are used as substrate to coat the samples which are further coated with gold coating (to make the samples conducting) for SEM analysis. Absorption studies are performed by SHIMADZU 2600 UV spectrophotometer.

Recognition studies are done on SHIMADZU RF-5301 PC spectrofluorophotometer which have xenon lamp as excitation source using quartz cells (1 cm path length) to fill solutions. The fluorescence emission spectra of the solutions are observed to investigate the chemosensing properties.

B. Synthesis of ligands X and Y

X and Y are tripodal receptors having three urea arms.

X: Tris (2-aminoethyl) amine (2 mM, 300 µl) is mixed with 4- nitrophenyl isocyanate (3 equivalents) and refluxed for overnight at 60-70^{0}C in dry chloroform. The precipitate is filtered and dried to get **X** [Scheme 1].

Y: Tris (2-aminoethyl) amine (1.37 mM, 205 µl) is mixed with 1-naphthyl isocyanate (3 equivalents) and refluxed at 60-70 ^{0}C in dry chloroform for overnight. White precipitate obtained which is filtered and dried to get **Y** [Scheme 1].

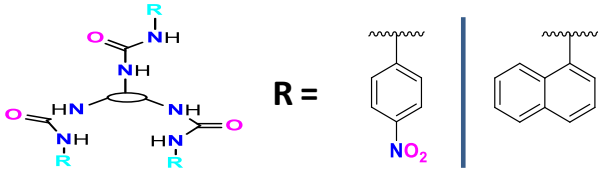

Figure 1.Tripodal receptor molecule

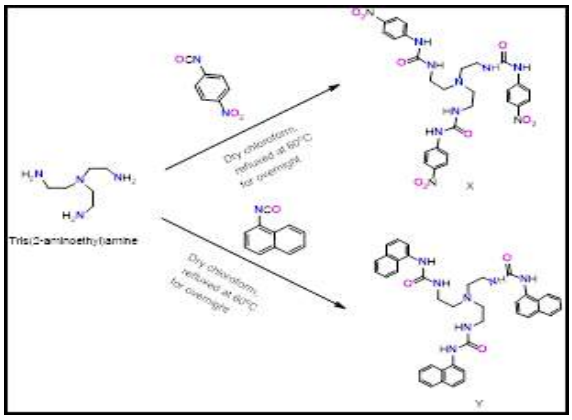

Scheme 1.Synthesis procedure for ligands **X** i.e. 1,1',1''-(2,2',2''-nitrilotris (ethane-2,1-diyl))tris(3-(4-nitrophenyl)urea) and **Y** i.e. 1,1',1''-(2,2',2''-nitrilotris(ethane-2,1-diyl))tris(3-(naphthalen-1-yl)urea)

C. Preparation of organic nanoparticles of ligands

Organic ligands are dissolved in organic solvent i.e. N, N-dimethylformamide (DMF) and injected in small amount into double distilled water while sonication followed by 5-10 min more sonication to get uniform ONP solution. The polarity difference in solvents segregates the tiny ONP particles and facilitates uniform dispersion.

X-ONP: Ligand X (7 mg) is dissolved in N, N-dimethylformamide (DMF) (5 ml) and 1 ml of this solution (2 mM) is injected slowly into 200 ml double distilled water under ultrasonic waves which is sonicated for 5-10 minutes further to get uniform X-ONP solution (0.01 mM).

Y-ONP: Ligand Y (4 mg) is dissolved in N, N-dimethylformamide (DMF) (5 ml). 1 ml of this solution (1.22 mM) is slowly injected into 150 ml of double distilled water under ultrasonic waves which is sonicated for 5-10 minutes more to get uniform Y-ONP solution (0.0080 mM).

III. RESULTS AND DISCUSSION

A. Characterisation of the ligands

In the ^{1}H NMR spectrum of **X**, the chemical shift (values at 3.22 and 2.63 ppm showed the presence of aliphatic protons while the doublets at 8.07 and 7.58 ppm represented two kinds of aromatic protons [Figure 1S]. In the ^{13}C NMR spectrum of **X**, the chemical shift (values at 53.96 and 38.07 ppm confirmed the presence of two types of aliphatic carbon atoms while chemical shifts (at 147.76 and 140.78 ppm showed the aromatic carbon atom attached to (–NH) group and ($–NO_2$) group respectively of the substituted p-nitrophenyl ring. The other two chemical shift (values at 125.46 and 117.24 ppm represented two aromatic carbon atoms attached to hydrogen atoms of the substituted p-nitrophenyl ring. The chemical shift (value at 154.94 ppm represented the carbon of carbonyl group of ligand **X** [Figure 2S]. The $[M-H]^+$ and $[M-Na]^+$ peaks at m/z value of 639.5 and 661.5 confirmed ligand **X** synthesis [Figure 3S]. In FT-IR spectrum of ligand **X**, the reflectance peaks at 1495.13 cm^{-1} and 1230.54 cm^{-1} represented aromatic nitro group. The peaks at 3338.15 cm^{-1} and 3092.98 cm^{-1} confirmed the presence of (–NH) group of ligand **X** while 1655.65 cm^{-1} marked the presence of carbonyl group [Figure 4S]. The elemental analysis of **X** shows the carbon, hydrogen, nitrogen and oxygen atoms as 50.12%, 5.17%, 22.08% and 22.63% respectively which is close to the theoretical outcome i.e. C: 50.78%; H: 4.74%; N: 21.93% and O: 22.55%.

^{1}H NMR (300 MHz, DMSO-d_6, 25°C) peaks of **X**: δ = 9.35 (s, 3H, –NH), 8.07 (d, 6H, ArH), 7.58 (d, 6H, ArH), 6.46 (t, 3H, –NH), 3.22 (m, 6H, $–CH_2$) and 2.63 (t, 6H, $–CH_2$) ppm [Figure 1S]. ^{13}C NMR (300 MHz, DMSO-d_6, 25°C) peaks of **X**: δ = 154.94 (3C, –CO), 147.76 (3C, ArCNHCS), 140.78 (3C, ArC-NO_2), 125.46 (6C, ArC), 117.24 (6C, ArC), 53.96 (3C, $–CH_2$) and 38.07 (3C, $–CH_2$) ppm [Figure 2S]. ESI-MS m/z = 639.5 $[M-H]^+$, ESI-MS m/z = 661.5 $[M-Na]^+$ [Figure 3S]. FTIR peaks at 3338.15 cm^{-1} (–NH stretching), 3092.98 cm^{-1} (–NH stretching), 2941.79 cm^{-1} (–CH– stretching of CH_2 group), 2864.15 cm^{-1} (–CH– stretching of CH_2 group), 1655.65 cm^{-1} (–C=O stretching), 1573.62 cm^{-1} (aromatic –C=C– bending), 1495.13 cm^{-1} (Ar-NO_2 stretching), 1414.79 cm^{-1}(NCN stretching), 1230.54 cm^{-1}(Ar-NO_2 stretching), 841.03 cm^{-1} (parasubstituted benzene bending) [Figure 4S]. Elemental analysis: C= 50.12%, H= 5.17%, N=22.08% and O=22.63%.

In the ^{1}H NMR spectrum of ligand **Y**, the chemical shift (values at 3.34 and 2.7 ppm showed the presence of two types of aliphatic protons while chemical shift (values at 8.08, 7.94, 7.87, 7.51, 7.43, 7.35 and 6.75 ppm

represented the aromatic protons of naphthyl group [Figure 5S]. In the ^{13}C NMR spectrum of ligand **Y**, the chemical shift (□□□values at 54.74 and 38.25 ppm represented the presence of two kinds of aliphatic carbon atoms while the chemical shift (□□□values at 135.55, 134.15, 128.68, 126.29, 126.25, 126.10, 125.76, 122.64, 121.99 and 117.45 ppm confirmed 10 aromatic carbon atoms of naphthyl group among which 135.55 ppm represented the aromatic carbon atom of naphthyl ring which is attached to (–NH) group. The chemical shift (□□□at 156.32 ppm represented carbon of (–C=O) group [Figure 6S]. In the mass spectrum, $[M-H]^+$ peak at m/z value of 654.3298 confirmed the formation of ligand **Y** [Figure 7S]. In the FT-IR spectrum of ligand **Y**, the peaks at 1622.65 cm^{-1} and 1501.01 cm^{-1} marked the presence of (–C=O) group and (aromatic –C=C–) group respectively. The peaks at 3297.29 cm^{-1}, 3043.95 cm^{-1} and 1563.41 cm^{-1} represented the (–NH) group [Figure 8S]. The elemental analysis study of ligand **Y** estimates the carbon, hydrogen, nitrogen and oxygen atoms as 68.37%, 5.82%, 13.87% and 11.94% respectively which resembles with the theoretical outcome i.e. C: 71.65%; H: 6.01%; N: 15.00% and O: 7.34%.

^1H NMR (300 MHz, DMSO-d_6, 25°C) peaks of **Y**: δ = 8.63 (s, 3H, –NH), 8.08 (d, 3H, ArH), 7.94 (d, 3H, ArH), 7.87 (d, 3H, ArH), 7.51 (m, 3H, ArH), 7.43 (m, 3H, ArH), 7.35 (m, 3H, ArH), 6.75 (t, 3H, ArH), 3.34 (m, 6H, –CH_2) and 2.7 (t, 6H, –CH_2) ppm [Figure 5S]. ^{13}C NMR (300 MHz, DMSO-d_6, 25°C) peaks of **Y**: δ = 156.32 (3C, –CO), 135.55 (3C, ArC-NH), 134.15 (3C, ArC), 128.68 (3C, ArC), 126.29 (3C, ArC), 126.25 (3C, ArC), 126.10 (3C, ArC), 125.76 (3C, ArC), 122.64 (3C, ArC), 121.99 (3C, ArC), 117.45 (3C, ArC), 54.74 (3C, –CH_2 -N) and 38.25 (3C, –CH_2 -NH) ppm [Figure 6S]. ESI-MS m/z = 654.3298 $[M-H]^+$ [Figure 7S]. FTIR peaks at 3297.29 cm^{-1} (–NH stretching), 3043.95 cm^{-1} (–NH stretching), 2933.62 cm^{-1} (–CH– stretching of CH_2 group), 2827.38 cm^{-1} (–CH– stretching of CH_2 group), 1622.65 cm^{-1} (–C=O stretching), 1563.41 cm^{-1} (–NH bending) and 1501.01 cm^{-1} (aromatic –C=C– bending) [Figure 8S]. Elemental analysis: C= 68.37%, H= 5.82%, N=13.87% and O=11.94%.

B. Characterisation of ONPs

Charactersation of X-ONP

Ligand X absorbed at 348 nm and X-ONP absorbed at 334 nm exhibiting a blue shift with lowered intensity. In fluorescence study, X-ONP emitted at two wavelengths i.e. 372 nm and 410 nm when excited at 270 nm, with increase in intensity as compared to ligand X which emitted at 468 nm [Figure 2(A) and 2(B)].

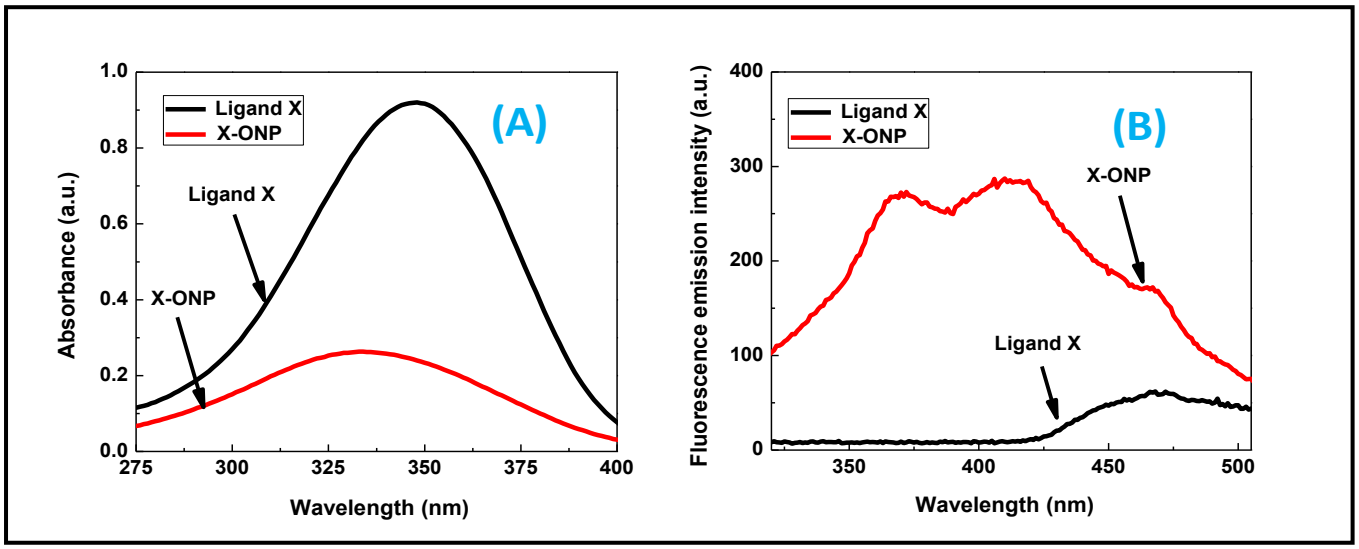

Figure 2.Comparison of ligand X and X-ONP by (A) UV-Vis and (B) Fluorescence emission spectroscopy

TEM image revealed the spherical morphology of X-ONP of diameter ~30-35 nm [Figure 3].

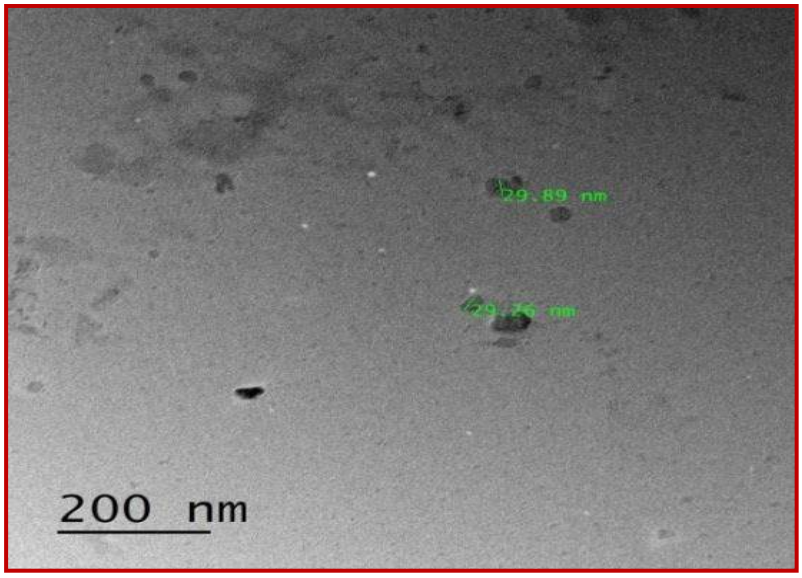

Figure 3.TEM image of **X**-ONP

The EDX spectrum of X-ONP confirmed the presence of C, N and O atoms in it [Figure 9S(A)]. DLS study showed its hydrodynamic diameter as 133.6 nm [Figure 9S(B)].

Characterisation of Y-ONP

Ligand Y and Y-ONP absorbed at 292 nm and 232 nm respectively while emitted at 372 nm and 383 nm respectively, when excited at 250 nm. In its absorption spectrum, Y-ONP showed a distinct blue shift while in the emission spectrum it showed a distinct red shift with higher intensity than that of ligand Y [Figure 4(A) and 4(B)].

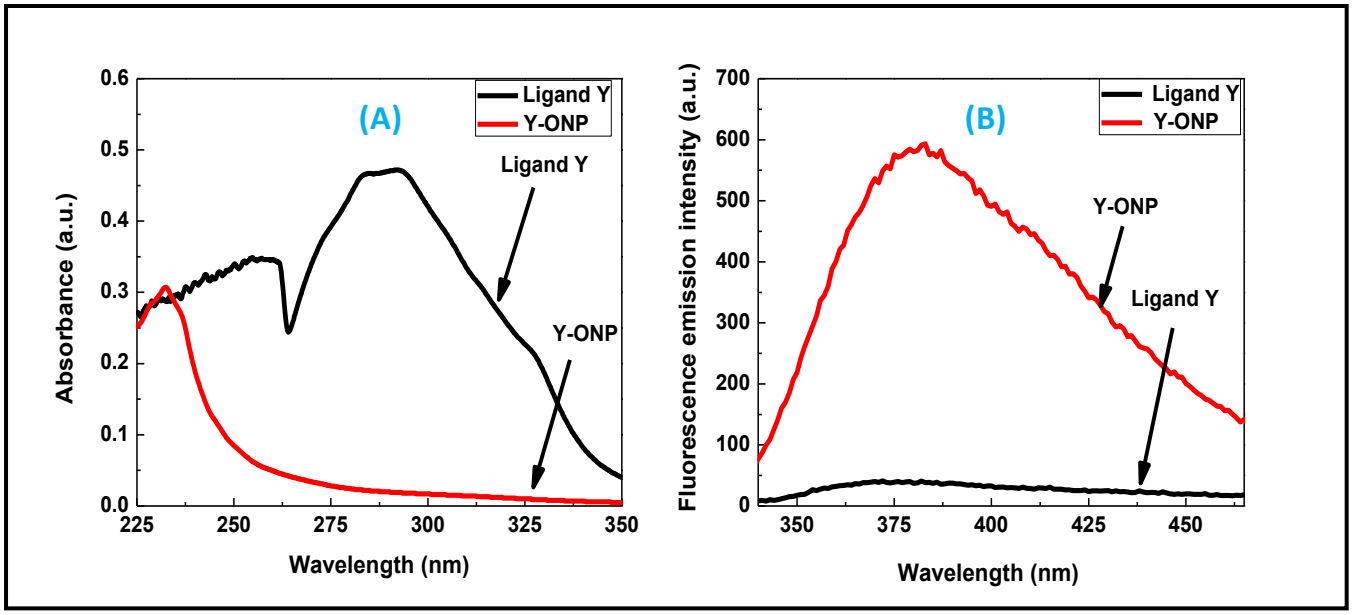

Figure 4.Comparison of ligand **Y** and **Y**-ONP by (A) UV-Vis and (B) Fluorescence emission spectroscopy

The SEM image of Y-ONP showed small spherical structures along with big aggregates which is supported by TEM image also [Figure 5 and Figure 10S(A)].

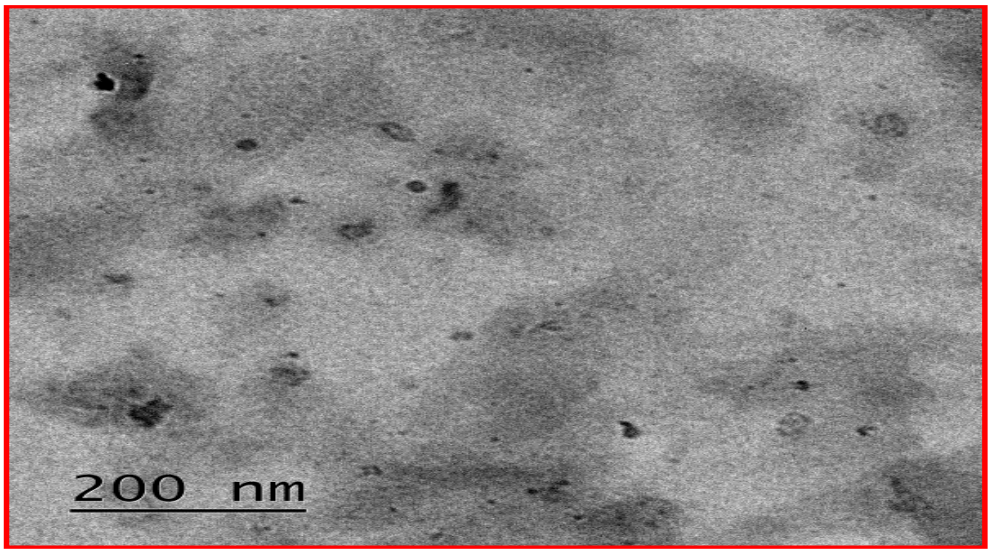

Figure 5.TEM image of **Y**-ONP

The EDX spectrum of Y-ONP confirmed the presence of C, N and O atoms in it [Figure 10S(B)]. DLS study showed its hydrodynamic diameter as 139.8 nm [Figure 10S(C)]. TEM image showed the spherical morphology of Y-ONP having diameter ~15-20 nm [Figure 5].

C. Photophysical or chemosensing study of ONPs:

Recognition studies are carried out by adding aqueous cationic solutions (5 mM, 50 µl) i.e. Li(I), Na(I), K(I), Cs(I), Ag(I), Mg(II), Co(II), Ba(II), Ca(II), Sr(II), Cu(II), Zn(II), Fe(III), Cr(III), Hg(II), Al(III), Pb(II), Ni(II), Mn(II) and Cd(II) or anionic solutions (5 mM, 50 µl) i.e. CH_3COO(I), F(I), Cl(I), CN(I), HSO_4(I), Br(I), I(I), NO_3(I), ClO_4(I) and HPO_4(II) into 5 ml ONP solution. The mixture of solutions are shaken vigorously and left still for complexation. The emission spectra of resultant solutions are recorded by spectrofluorophotometer having xenon lamp source, using their maximum absorption wavelength as excitation wavelength.

Any distinct anomalous behaviour in the fluorescence emission spectra of any ONP-analyte complex give rise to chemosensing behaviour towards that analyte which is confirmed by fluorometric titration as the function of concentration of analyte. The fluorescence emission intensity maxima at each concentration is joined and fitted in straight line to get the detection limit which is calculated by following equation [20],

$$\text{Limit of Detection} = \frac{3 \text{ X Standard deviation of the intercept}}{\text{Slope of the intercept}}$$

Some additional studies are also performed like competitive binding or interference studies to investigate the interference of other cations/ anions with the host-cation/ anion complex.

For this, at first ONP-analyte (cation/ anion) complex is formed after which other cationic/ anionic solutions are added and shaken vigorously to allow to displace the earlier cation/ anion from the complex which is tracked by their fluorescence emission spectra. Any change or distortion in the fluorescence emission spectra of new solution is indication of interference by that cation/anion. The stability ONPs under various pH values and high ionic strength are also investigated. Tetrabutylammonium perchlorate salt is used to create high ionic

strength environment. Response time studies are also done to investigate the ONP- analyte complex stability as the function of time at various concentrations for recording of at least 5 spectra.

Chemosensing study of X-ONP:

The fluorescence spectra of X-ONP complexes with various cations/anions are investigated at 270 nm to observe the difference in X-ONP profile after complexation. It is observed that few metal ions have lowered the fluorescence intensity of X-ONP after complexation like Hg(II), Al(III), Cr(III) and Fe(III) but since selectivity is absent so it cannot be a good sensor for any particular metal ion among Hg(II), Al(III), Cr(III) and Fe(III) [Figure 6(A)].

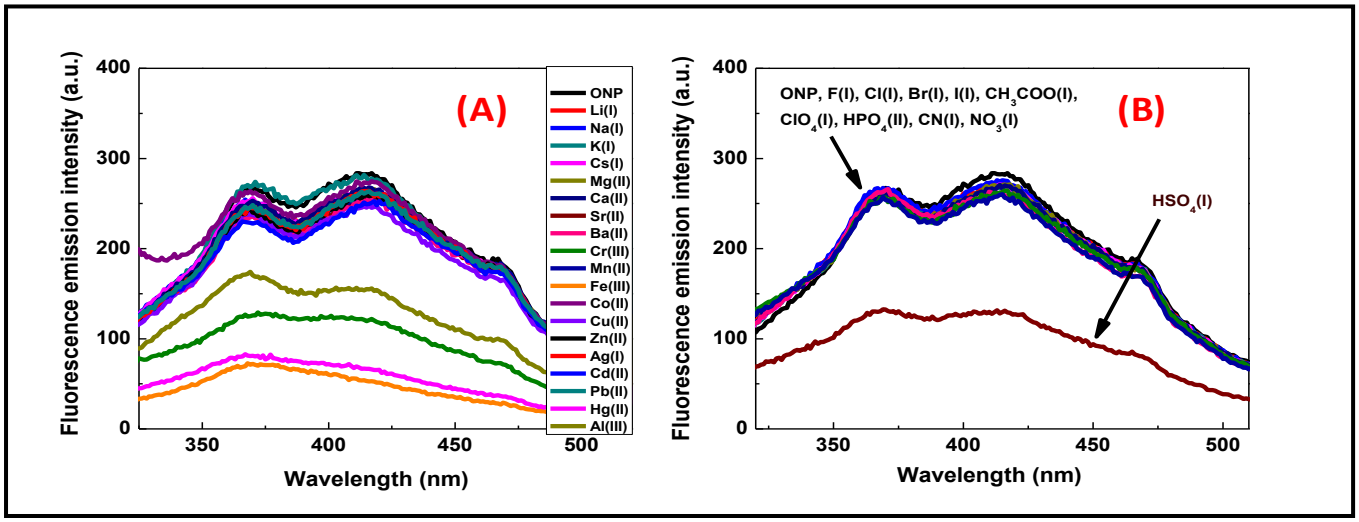

Figure 6.Chemosensing study of **X**-ONP; (A) Recognition study of **X**- ONP towards various cations; (B) Recognition study of **X**-ONP towards various anions

In case of anions, X-ONP exhibited anomalous behaviour towards $HSO_4(I)$ by showing a significant drop in fluorescence emission intensity of X-ONP- $HSO_4(I)$. So, X-ONP proved to be a selective sensor for $HSO_4(I)$ [Figure 6(B)] which is further confirmed by fluorometric titration.

In fluorometric titration, the emission profile of X-ONP is observed as a function of $HSO_4(I)$ concentration. The fluorescence emission intensity of X-ONP-$HSO_4(I)$ complex decreases with increase in $HSO_4(I)$ concentration. After 80 μM concentration of $HSO_4(I)$, further decrease in emission intensity is not observed [Figure 7(A)]. The maxima obtained at each concentration during titration is joined and fitted in straight line which showed good linearity (adjusted R^2 value = 0.9845) with negative slope [Figure 7(B)]. The limit of detection calculated from this fit is calculated as 1.026 μM. The chemosensing of $HSO_4(I)$ by X-ONP follows photoinduced electron transfer (PET)-on mechanism. The electron transferred from the HOMO of receptor to the HOMO of fluorophore instead of the LUMO of fluorophore to the HOMO of fluorophore, after complexation of X-ONP and $HSO_4(I)$ which quenched its fluorescence emission intensity. In the response time study, stability of X-ONP-$HSO_4(I)$ complex is observed with respect to time at various concentrations of $HSO_4(I)$ (i.e. 10, 30, 50, 90 μM). At each concentration, the fluorescence emission spectra is observed for at least 5 measurements. The emission profile of X-ONP-$HSO_4(I)$ complex remained unaffected which shows that it is stable with time and radiation source of spectrophotometer. At higher concentrations i.e. 50 and 90 μM, the graphs are very similar because of saturation attainment of $HSO_4(I)$ [Figure 7(C)].

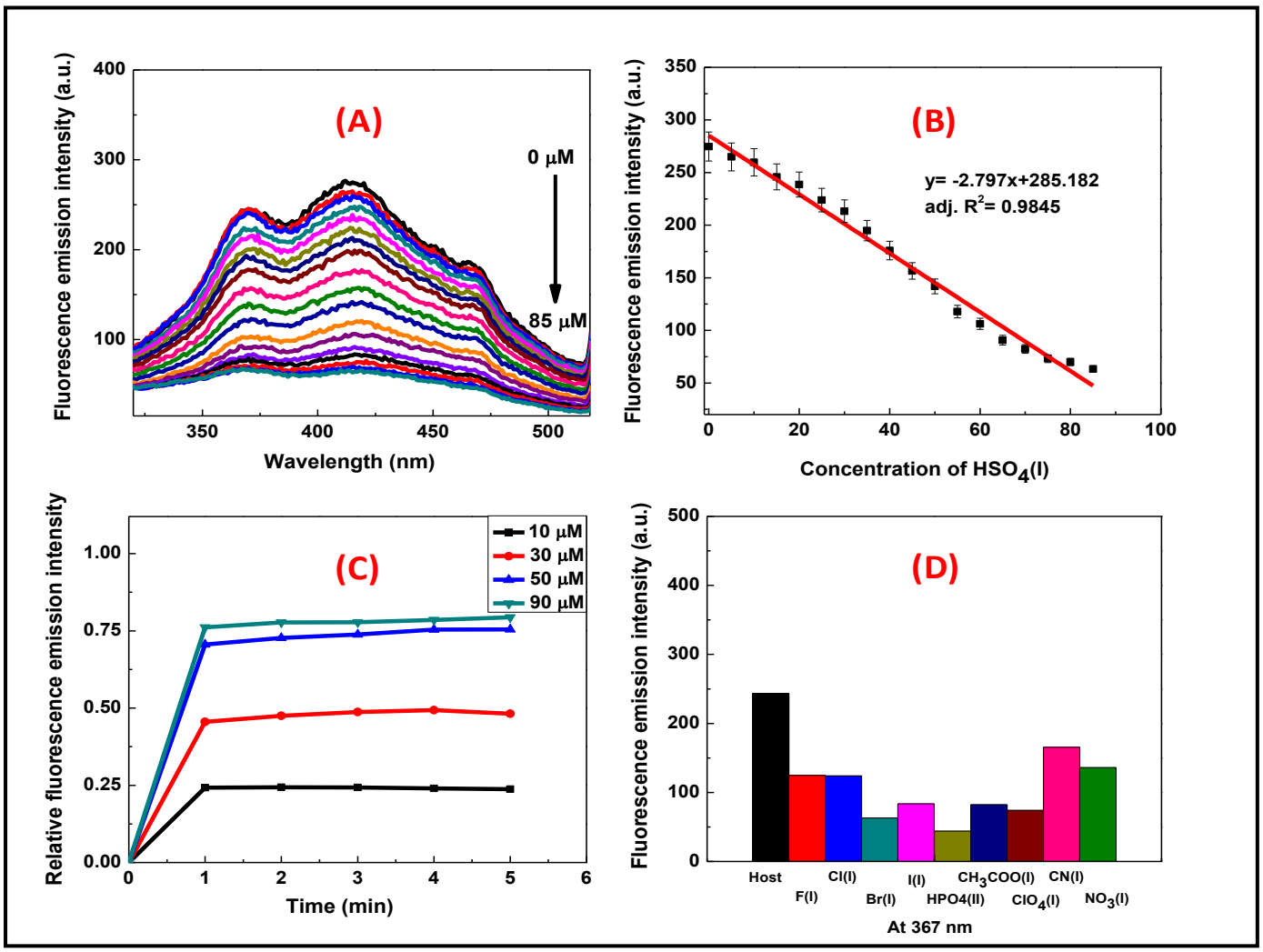

Figure 7.(A) Fluorometric titration of **X**-ONP with increasing concentration of $HSO_4(I)$; (B) Linear fit of fluorescence emission maxima of **X**-ONP-$HSO_4(I)$ complex with increasing concentration of $HSO_4(I)$; (C) Response time study of **X**-ONP-$HSO_4(I)$ complex at various concentration of $HSO_4(I)$ ions; (D) Interference of other anions on **X**-ONP- $HSO_4(I)$ complex

For interference studies, at first, $HSO_4(I)$ solution is added to X-ONP solution, shaken vigorously and allowed to form complex followed by addition of solutions of other anions. The resulting solutions are observed under spectrophotometer which revealed that Br(I) and $HPO_4(II)$ interfere with X-ONP-$HSO_4(I)$ complex i.e. more than 50 a.u. while other anions did not influence it to any significant extent [Figure 7(D)].

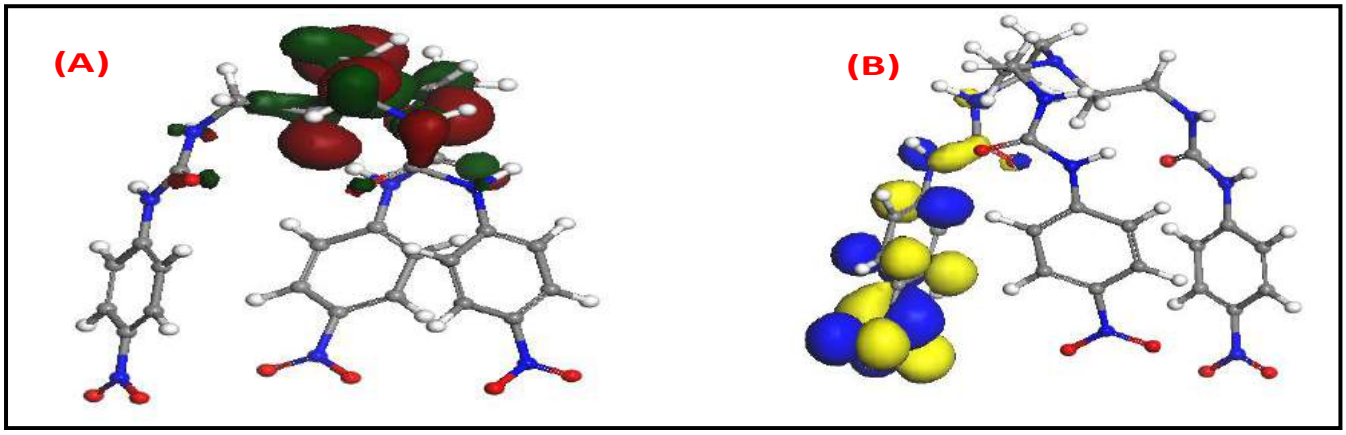

Figure 8.The DFT optimised structure of X; (A) HOMO of X, (B) LUMO of X (red and green colour for the HOMO, blue and yellow colour for the LUMO).

In the pH studies, it is observed that the emission profile of X-ONP is applicable in the pH range of 5.3 to 10.45 [Figure 11S(A)]. In the salt effect study, it is observed that X-ONP can withstand the heavy salt addition till 300 μM after which some change in its fluorescence emission spectra is observed [Figure 11S(B)]. The density functional theory (DFT) calculations [21, 22] showed that HOMO and LUMO orbitals of ligand X are located on 167th and 168th orbital with energy as -5.257eV and -4.778eV respectively [Figure 8(A) and 8(B)].

Chemosensing study of Y-ONP

The recognition behaviour of Y-ONP towards various cations is investigated by observing their fluorescence emission spectra by exciting them at 250 nm. Among cations, Y-ONP showed a selective chemosensing towards Cr(III) by PET-on mechanism with a significant quenching in its fluorescence emission intensity. Y-ONP-Cr(III) complex showed two peaks with lowered emission intensity after complexation with Y-ONP. After binding of Cr(III) with Y-ONP, the peak at 376 nm showed a blue shift along with quenching of ~334.6 a.u. in its emission intensity with arise of a new peak at 417 nm while before complexation Y-ONP emitted at 383 nm with 593.40 a.u. emission intensity. Though some of other cations have also shown lowering in their emission intensity after complexation like Ag(I), Cu(II), Mn(II), Hg(II), Fe(III) and Al(III) but not so distinct as Cr(III) [Figure 9(A)]. The binding of Y-ONP with Cr(III) is confirmed further by fluorometric titration of Y-ONP with increasing concentration of Cr(III). Initially, 10 μM addition of Cr(III) solution led to decrease in fluorescence emission intensity of 27.62 a.u. along with blue shift of 3 nm.

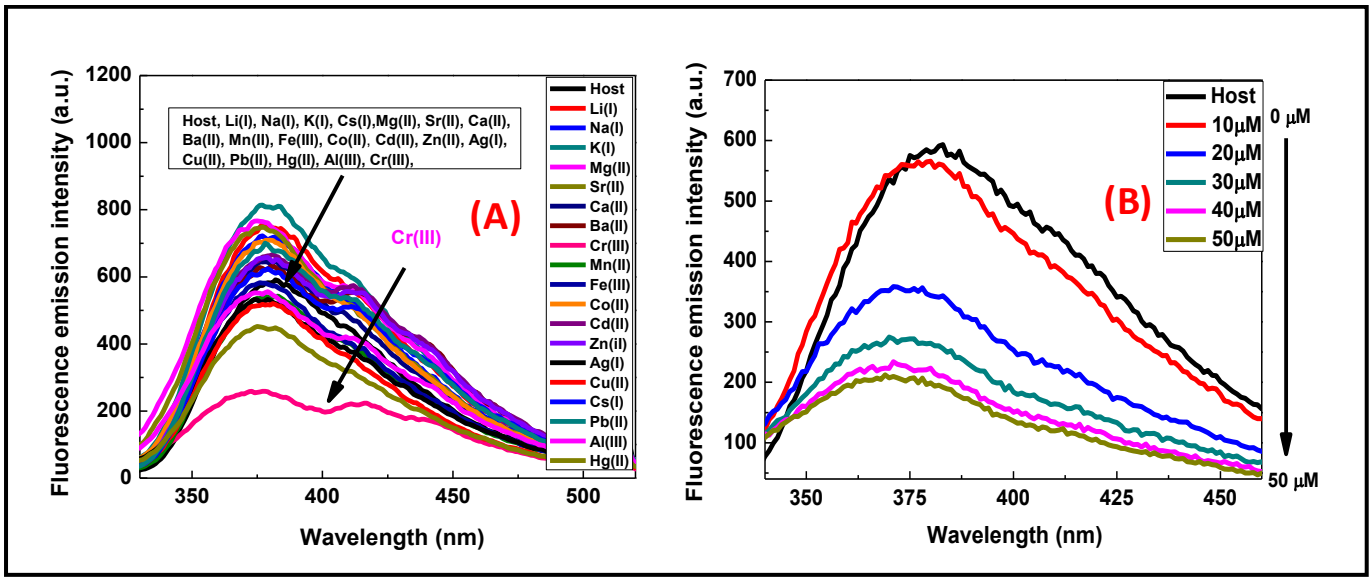

Figure 9.(A) Photophysical study of **Y**-ONP towards recognition of various cations; (B) Fluorometric emission titration of **Y**-ONP with increasing concentration of Cr (III)

After 20 μM addition of Cr(III) solution, an abrupt quenching in fluorescence emission intensity i.e. 207.45 a.u. with blue shift of 9 nm, is observed which continued further till addition of 50 μM of Cr(III) [Figure 9(B)]. The emission spectrum maxima at every concentration is joined and fitted into a straight line (Adjacent R^2 value = 0.8716) to get the detection limit i.e. 1.3 μM [Figure 10(A)]. The complexation of Y-ONP with Cr(III) occurred

by photoinduced electron transfer (PET)-on mechanism in which after binding, the electron from receptor HOMO transferred to fluorophore HOMO instead of fluorophore LUMO to fluorophore HOMO of Y molecule. It caused in quenching of fluorescence emission intensity of Y-ONP-Cr(III) complex. In the response time studies, the fluorescence emission spectra of Y-ONP-Cr(III) complex is observed at various concentrations of Cr(III) i.e. 20, 40 and 80 μM for at least 3 measurements which showed that the complex is stable till at least 3 measurements [Figure 10(B)]. The interference studies shows the interference of Zn(II) with the complex to some extent [Figure 10(C)].

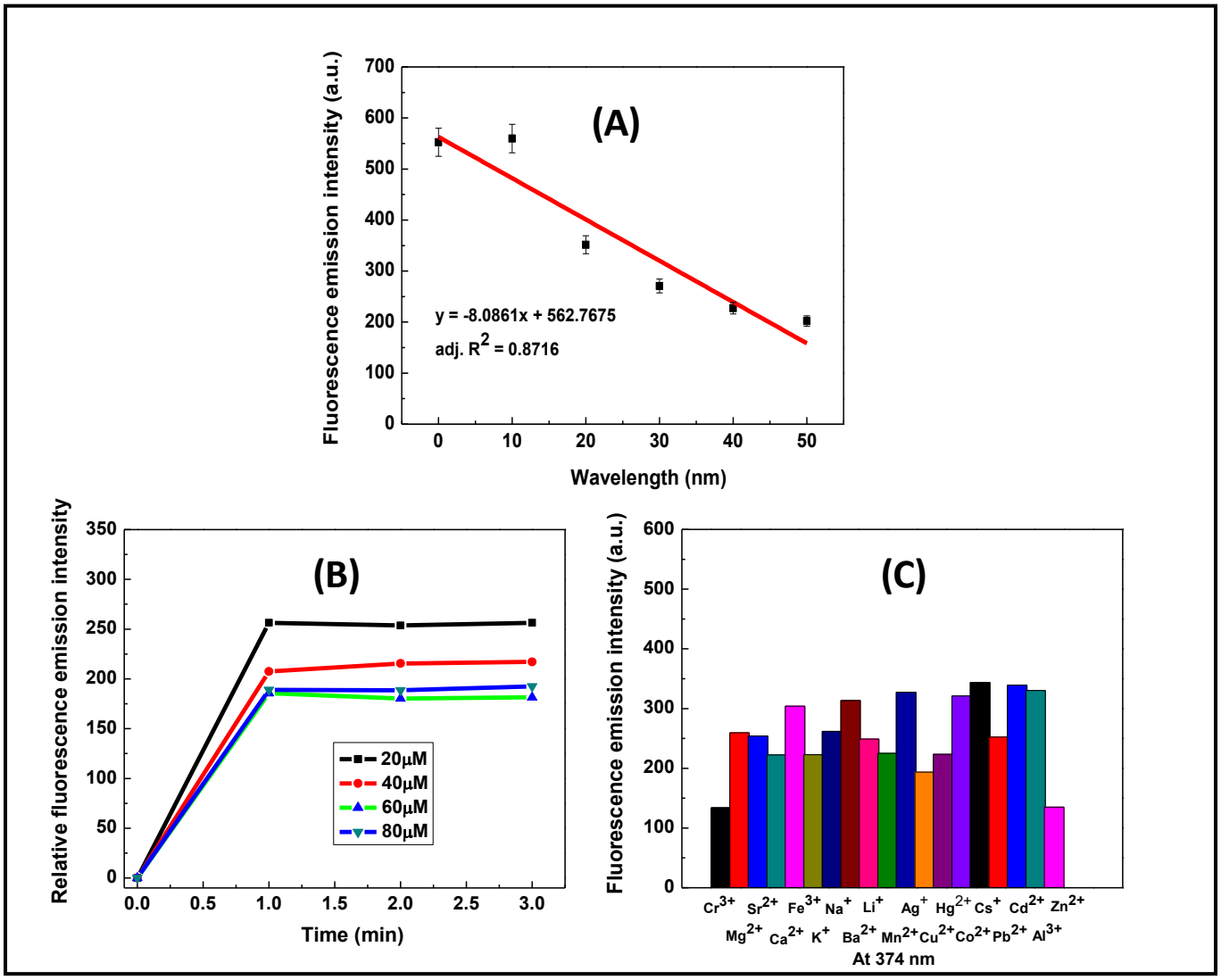

Figure 10.(A) Linear fit of fluorescence emission maxima of **Y**-ONP-Cr(III) complex with increasing concentrations of Cr(III); (B) Response time study of **Y**-ONP-Cr(III) complex at various concentrations of Cr(III); (C) Interference of other cations with **Y**-ONP-Cr(III) complex

pH studies of Y-ONP says that it is applicable under neutral or slight basic environment [Figure 12S(A)]. The salt effect studies showed the stability of Y-ONP till 700 μM addition of tetrabutylammonium perchlorate salt [Figure 12S(B)].

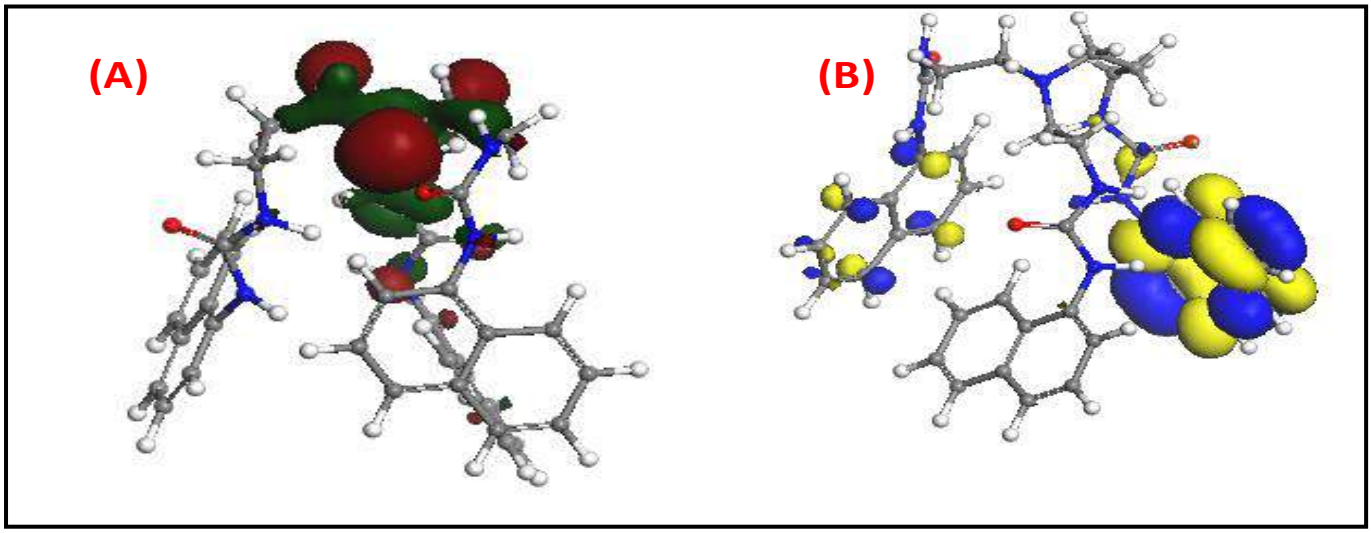

Figure 11.DFT optimised pictorial representation of **Y**; (A) HOMO of **Y**; (B) LUMO of **Y** (red and green colour for the HOMO, blue and yellow colour for the LUMO).

The density functional theory (DFT) calculation [21,22] of molecule Y showed that its HOMO is located on 177th orbital with energy as -5.035 eV while its LUMO is located on 178th orbital with energy as -3.080 eV [Figure 11(A) and 11(B)].

IV. CONCLUSION

Two urea based tripodal ligands X and Y are synthesised and characterised by NMR, IR and mass spectroscopic techniques. All of three pods of X constitute 4-nitrophenyl group while all of three pods of Y constitute 1-naphthyl group. Spherical organic nanoparticles (ONPs) of X and Y are prepared as X-ONP (diameter ~30-35 nm) and Y-ONP (diameter ~15-20 nm) respectively by reprecipitation method. ONPs are characterised by DLS, SEM, TEM as well as absorption and emission spectroscopic methods. The chemosensing studies of X-ONP and Y-ONP revealed that former has shown chemosensing behaviour towards HSO_4(I) while latter towards Cr(III). Both have followed photoinduced electron transfer (PET)-on mechanism of sensing with limit of detection as 1.026 μM and 1.3 μM for X-ONP and Y-ONP respectively. Both of ONPs are applicable under high ionic strength. The difference in pods resulted into difference in cavity size and affinity because of which X-ONP recognises HSO_4(I) while Y-ONP recognises Cr(III). This manuscript discusses the role of ONPs of urea based tripodal ligands in the chemosensing studies.

Corresponding Authors:
*E-mail:navneetkaur@pu.ac.in, ashok@chemistry.iitd.ac.in.

V. Acknowledgment

Authors are thankful to Department of Science and Technology (DST), Government of India for financial support. JM thanks Sophisticated Analytical Instrumentation Facility (SAIF), Panjab University, Chandigarh, Indian Institute of Technology (I.I.T.), Delhi and Institute of Nano Science and Technology (INST), Mohali for instrumentation support.

VI. REFERENCES

[1]. C. Perez-Casas and A. K. Yatsimirsky, "Detailing hydrogen bonding and deprotonation equilibria between anions and urea/thiourea derivatives," J. Org. Chem., vol. 73, 2008, pp. 2275–2284.

[2]. (A) H. Miyaji and J. L. Sessler, "Off-the-shelf colorimetric anion sensors," Angew. Chem., vol. 113, 2001, pp. 158-161.; (B) M. Cametti and K. Rissanen, "Recognition and sensing of fluoride anion," Chem. Commun., vol. 0, 2009, pp. 2809-2829.

[3]. B. Valeur, Molecular Fluorescence: Principles and applications, Wiley-VCH Weinheim, 2001, Print ISBN: 9783527299195, Online ISBN: 9783527600243, DOI: 10.1002/3527600248.

[4]. (A) H. Kasai, H. S. Nalwa, H. Oikawa, S. Okada, H. Matsuda, N. Minami, A. Kakuta, K. Ono, A. Mukoh and H. Nakanishi, " A novel preparation method of organic microcrystals," Jpn. J. Appl. Phys., vol. 31, 1992, pp. L 1132-L 1134.

[5]. W. Gopel, J. Hesse, J. N. Zemel, T. Grandke and W. H. Ko, Sensors, A Comprehensive Survey, Fundamentals and General Aspects, Volume 1, Wiley-VCH Weinheim, 2008, Print ISBN: 9783527267675, DOI: 10.1002/9783527620128.

[6]. G. Aragay, F. Pino and A. Merkoci, "Nanomaterials for sensing and destroying pesticides ," Chem. Rev., vol. 112, 2012, pp. 5317–5338.

[7]. X. Luo, A. Morrin, A. J. Killard and M. R. Smyth, "Application of nanoparticles in electrochemical sensors and biosensors," Electroanalysis, vol. 18, 2006, pp. 319–326; (B) J. M. Garcia, F. C. Garcia, F. Serna and J. L. de la Pena, "Fluorogenic and chromogenic polymer chemosensors," Polym. Rev., vol. 51, 2011, pp. 341–390.

[8]. (A) A. S. Klymchenko and A. P. Demchenko, "Electrochromic modulation of excited-state intramolecular proton transfer: The New principle in design of fluorescence sensors," J. Am. Chem. Soc., vol. 124, 2002, pp. 12372–12379; (B) A. P. Demchenko, Introduction to fluorescence sensing Second Edition, Springer International Pulishing Switzerland, 2015, Print ISBN: 978-3-319-20779-7, DOI 10.1007/978-3-319-20780-3.

[9]. D. Wu, A. C. Sedgwick, T. Gunnlaugsson, E. U. Akkaya, J. Yoon and T. D. James, "Fluorescent chemosensors: the past, present and future ," Chem. Soc. Rev., vol. 46, 2017, pp. 7105-7123.

[10]. Y. Zhou, J. Zhang, L. Zhang, Q. Zhang, T. Ma and J. Niu, "A rhodamine-based fluorescent enhancement chemosensor for the detection of Cr3+ in aqueous media," Dyes Pigm., vol. 97, 2013, pp. 148-154.

[11]. M. Wang, J. Wang, W. Xue and A. Wu, "A benzimidazole-based ratiometric fluorescent sensor for Cr3+ and Fe3+ in aqueous solution," Dyes Pigm., vol. 97, 2013, pp. 475–480.

[12]. D. Karak, A. Banerjee, A. Sahana, S. Guha, S. Lohar, S. S. Adhikari and D. Das, "9-Acridone-4-carboxylic acid as an efficient Cr(III) fluorescent sensor: Trace level detection, estimation and speciation studies," J. Hazard. Mater., vol. 188, 2011, pp. 274–280.

[13]. V. K. Bhardwaj, P. Saluja, G. Hundal, M. S. Hundal, N. Singh and D. O. Jang, "Benzthiazole-based multifunctional chemosensor: fluorescent recognition of Fe3þ and chromogenic recognition of HSO4-," Tetrahedron, vol. 69, 2013, pp. 1606–1610.

[14]. D. Sain, C. Kumari, A. Kumar and S. Dey, "Indole-based distinctive chemosensors for 'naked- eye' detection of CN and HSO4-, associated with hydrogen-bonded complex and their DFT study," Supramol. Chem., vol. 28, 2016, pp. 239-248.

[15]. S. Erdemir, B. Tabakci and M. Tabakci, Sens. Actuators B Chem., "A highly selective fluorescent sensor based on calix4]arene appended benzothiazole units for Cu2+, S2– and HSO4– ions in aqueous solution," vol. 228, 2016, pp. 109–116.

[16]. D. Zhang, X. Jiang, Z. Dong, H. Yang, A. Martinez and G. Gao, "A bifunctional acridine-based fluorescent sensor: ratiometric sensing of H2PO4- and obvious fluorescence quenching towards HSO4- through a synergistic binding effect of benzimidazolium and urea moieties," Tetrahedron, vol. 69, 2013, pp. 10457–10462.

[17]. K. Tayade, B. Bondhopadhyay, K. Keshav, S. K. Sahoo, A. Basu, J. Singh, N. Singh, D. T. Nehete and A. Kuwar, "A novel zinc(II) and hydrogen sulphate selective fluorescent "turn-on" chemosensor based on isonicotiamide: INHIBIT type's logic gate and application in cancer cell imaging," Analyst, vol. 141, 2016, 1814–1821.

[18]. T. Gunnlaugsson, A. P. Davis, J. E. O'Brien and M. Glynn, "Fluorescent sensing of pyrophosphate and bis-carboxylates with charge neutral PET chemosensors," Org. Lett., vol. 4, 2002, pp. 2449-2452.

[19]. P. Saluja, N. Kaur, N. Singh and D. O. Jang, "Benzimidazole-based fluorescent sensors for Cr3+ and their resultant complexes for sensing HSO4- and F-," Tetrahedron, vol. 68, 2012, pp. 8551–8556.

[20]. A. Shrivastava, V. Gupta, "Methods for the determination of limit of detection and limit of quantitation of the analytical methods," Chron Young Sci., vol. 2, 2011, pp. 21-25.

[21]. (A) J.P. Perdew, Y. Wang, "Accurate and simple analytic representation of the electron-gas correlation energy," Phys. Rev. B, vol. 45, 1992, pp. 13 244-13 249; (B) Accelrys, Materials Studio Release Notes, Release 4.4, Accelrys Software Inc, 2008.

[22]. R.D.L. Johnstone, A.R. Lennie, S.F. Parker, S. Parsons, E. Pidcock, P.R. Richardson, J.E. Warren, P.A. Wood, "High-pressure polymorphism in salicylamide", CrystEngComm, vol. 12, 2010, pp. 1065-1078.

National Conference on Applied Sciences Synergising the Engineering and Technology
Print ISSN: 2395-6011 | Online ISSN: 2395-602X (www.ijsrst.com)
© 2021 IJSRST | Volume 8 | Issue 2

Studies on Thermal Conductivity and Zeta Potential of Cuo-Nanofluids at Different Temperatures

V. R. Venu Gopal, Susmita Kamila*
East Point College of Engineering and Technology, Bangalore, Karnataka, India

ABSTRACT

The purpose of the present investigation is to study the effect of adding copper oxide nano powder to the conventional heat transfer fluids for their comparative thermal conductivity properties. CuO nano powder was synthesized and subsequently different nanofluids were prepared in two base fluids such as water and tri-ethylene glycol by ultrasonication technique. Synthesized CuO nano powder was characterized for its shape and size from XRD, EDX and SEM analysis. Thermal properties of prepared nanofluids have been studied from thermal conductivity at different temperature. In addition, particle size analysis, zeta potential studies, viscosity and density of the nanofluids were carried out. The thermal conductivities of all nanofluids were found to be enhanced, whereas the density and viscosities of nanofluids were less in comparison to their base fluids.

Keywords : CuO Nanofluids, Thermal Conductivity, Tri-Ethylene Glycol

I. INTRODUCTION

In industries Heat management and automobile sectors is becoming a challenging process. Heat transfer fluids have been an integral part of this process for many years. Enhancement of heat transfer capacity of a fluid can be expected by increasing the thermal conductivity.Varieties of heat transfer fluids both Aqueous and organic were being used to meet the operating needs of various applications. Other than water, ethylene glycol has better capacity of heat transfer properties including high density and low viscosity in comparison to many other fluids. However, TEG is non-toxic and more eco-friendly to be used as heat transfer fluid [1]. Study is being carried out by using nano particles in heat transfer fluids, where these nano particles found to boost the heat transfer capacity of basefluids [2]. Review of literature shows that metals and metallic oxides in their nano scale are utilized for the preparation of nanofluids [3-5]. Based on their physical, chemical, thermal and structural properties from bulk materials, these nanoparticles have plenty of applications in various frontier areas like optoelectronics [6,7], sensing [8], catalysis [9], solarcells etc,. In the area of nano research, investigations on nanofluids are quite demanding field apart from nanoparticles. These are the most modern class of fluids engineered by Choi et al [10].

Out of different metal oxides nano particles, CuO nanoparticles are the promising materials due to their applications in various technologies both as solid form as well as in fluids. CuO nanoparticles dispersed with fluids have many applications in the industries and instruments especially with heat transfer systems.

In present work, CuO nano particles were synthesized and different nanofluids were prepared with base fluids such as water and TEG to study different thermo and rheological parameters. All these parameters shed light on the molecular environment as well as the dispersed phase of the nanofluids with respect to the temperature.

II. MATERIALS AND METHODS

The reagents used for the synthesis and preparation were of AR grade and procured from Merck, India. These reagents were used as it is without further purification. Deionized double distilled water was used throughout the experiment.

A. Synthesis of CuO Nano Particles and Preparation of Nanofluids

Copper oxide nanoparticles are prepared from copper chloride dihydrated and sodium hydroxide pellets as precursors in aqueous media maintaining pH of the solution from 4 to 11 and temperature 60-70^{0}C [11]. A brownish-black precipitation of copper hydroxide was obtained after stirring continuously for one hour to complete the precipitation reaction. Hydrochloric acid was used to neutralize the solution. The precipitate was centrifuged and washed with deionized water and was dried in oven at 90^{0}C for 4hour to get Copper Oxide nanoparticles. The synthesized nanoparticles were then characterized for their properties using XRD, EDX and SEM.

B. Preparation of Nanofluids

Nanofluids have been prepared by using the synthesized CuO nano particles in water and Triethylene glycol [0.005% (w/V)]. These two different solutions were properly stirred for 30mins by a magnetic stirrer before subjecting to ultra-sonication for 2 hr using Ultrasonic Processor. After dispersing, the nanofluids were carried out for Zeta potential, electrical conductivity, thermal conductivity along with rheological properties studies.

C. Characterization of CuO Nanoparticles and Nanofluids

The prepared nanoparticles have been characterized for structural determination from XRD by using X-ray Diffractometer with CuK alpha radiation (λ= 1.5405 Å). Both, the elemental composition (EDX analysis) and the particle shapes (SEM morphology) of CuO nanoparticles and nanofluids have been carried out. In addition, zeta potentials and particle size of nanofluids were determined.

D. Rheological Properties of Nanofluids

In the present study, the kinematic viscosities of the solutions were measured with a calibrated Ostwald viscometer immersed in a constant temperature water bath maintained within ±0.01K. It was followed by determine the time of flow at three different temperatures. Apart from this, the thermal conductivity of all the fluid samples were measured experimentally using KD-2 Pro KS-1 sensor instrument, where it uses transient hot wire source method for the conductivity measurement.

III. RESULTS AND DISCUSSIONS

From XRD diffractogram, it is observed that the intensity and position of peaks are indicative of the presence of copper oxide in the sample and the particles are of monoclinic crystal system (literature: JCPDS, File No 01-

080-1916). The average crystallite size (D) has been calculated from the line broadening using the following Debye-Scherrer's relation [12] and the average crystal size is found to be 11.23nm

$$D=\frac{K\lambda}{\beta\cos\theta} \quad (1)$$

where K is the crystallite shape factor and a good approximation is 0.9, λ is the wavelength of X-ray, β is full width at half the maximum (FWHM) in radians of the X-ray diffraction peak and θ is the Braggs angle.

The images of EDX analysis for the samples show the presence of copper and oxygen elements in the prepared nano powder with the % weight composition of copper and oxygen are 67.73 and 25.60, respectively. The SEM images are the evidence for the nanoscale sizes of CuO particles in range of 43 to 73nm. It also reveals that, the shapes of copper oxide particles were found to be spherical.

Zeta potential is an important property and it shows the difference between the dispersion medium and the stationary layer of fluid attached to the dispersed particle. Larger the values of zeta potential better will be the dispersion. pH of a colloidal solution is found to be one of the main parameters influencing the particle aggregation and the stability of the suspension. In the present investigation, zeta potential has been studied with the variation of pH of the nanofluids and it has been observed that the potentials of all the nanofluids increase with pH values. However, it decreases after pH 8 in most of the fluids with negative mV. This variation may be due to more anionic dispersant [13]. In the present study, there is increment of thermal conductivity for all the nanofluids from their respective base fluids. It increases with temperatures appreciably for the CuO nanofluids in water, though there is not any remarkable change in TEG. Electrical conductivity is another parameter that is related to the ability of charged particles or ions in the suspension to carry the charges towards respective electrodes when an electric potential is applied [14]. There is no such appreciable variation in electrical conductivity with pH except for the nanofluid with water, where the conductivity shows maxima at pH 4. This enhanced conductivity is assumed to be presence of more charged particles at this range.

Viscosity is an essential parameter that describes the internal resistance of a fluid to flow and, in case of a nanofluids, it depends on the morphology and size of nanoparticles. The kinematic viscosities of nanofluids are more than that of their base fluids and it decreases with temperature (Table1). This might be due to the increased disturbance in particles with temperature that makes the fluids to move fast. The enhanced viscosity is indicative of increased particulate-solvent association in fluids. It also shed light on better dispersion of CuO nanoparticles [15].

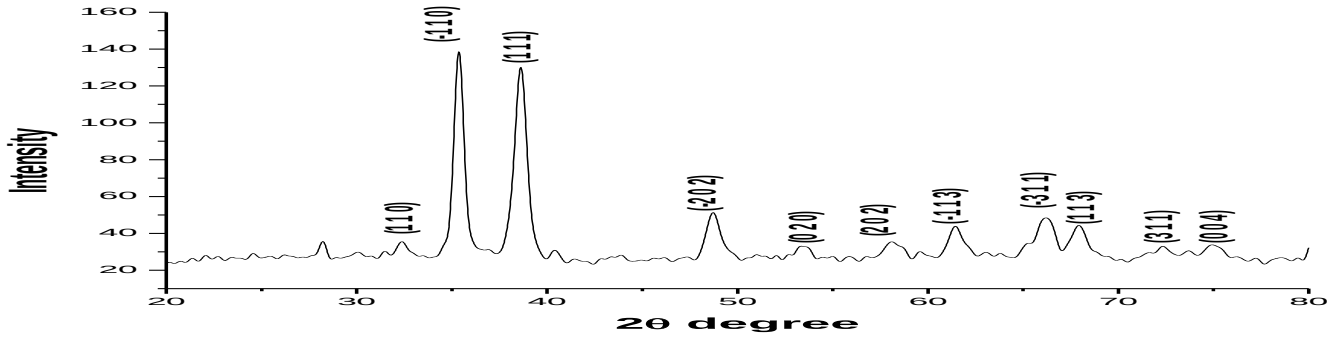

Fig.1. X-ray diffractograms of CuO Nanoparticles

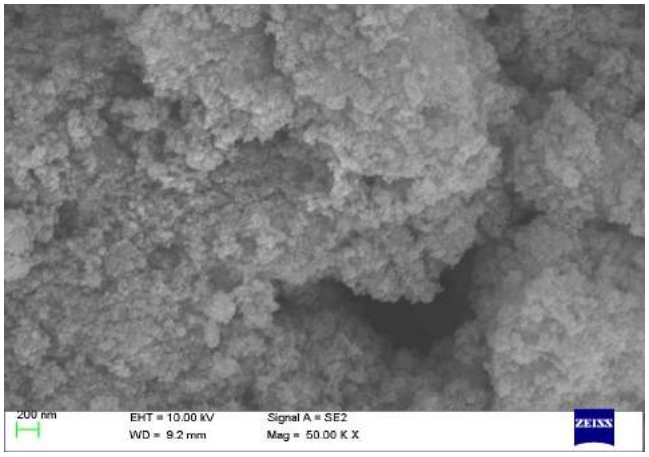

Fig.2. SEM Morphologies of CuO Nanoparticles

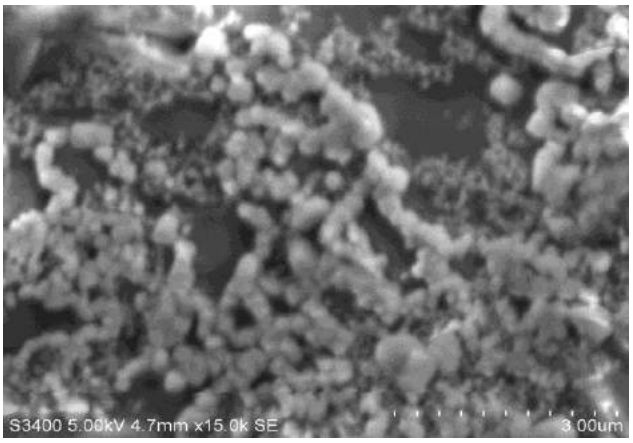

Fig.3. SEM Morphologies of CuO Nanofluid in Water

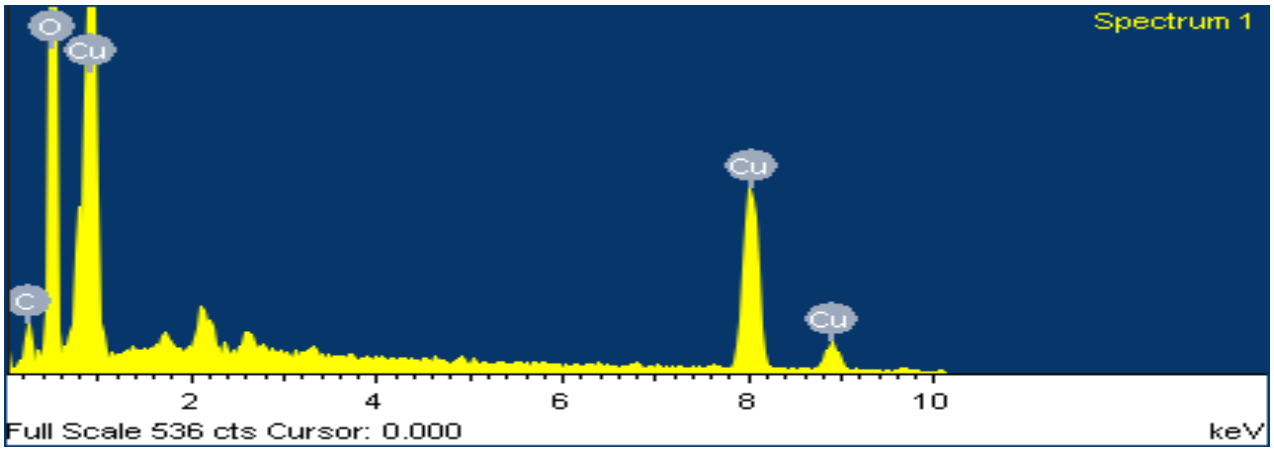

Fig. 4. EDAX images of CuO Nanoparticles

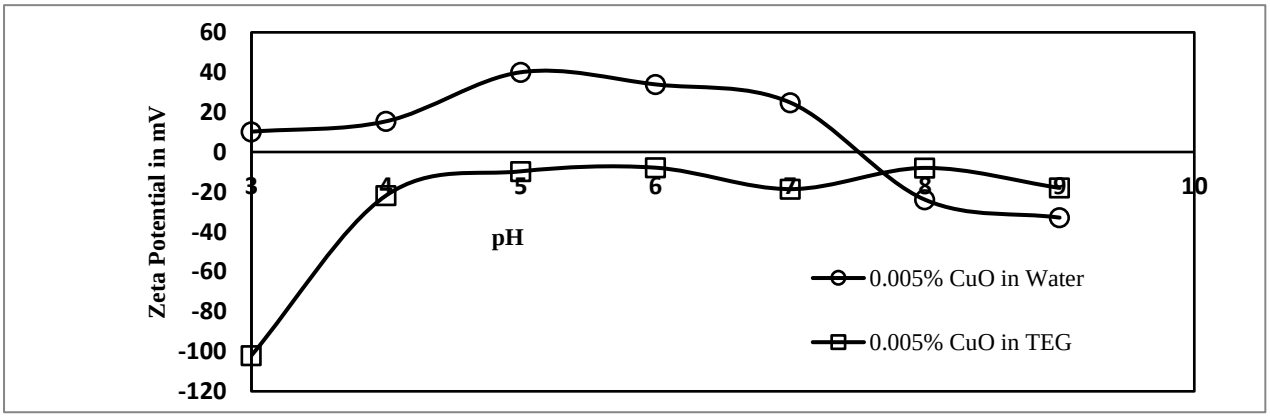

Fig.5. Plot of Zeta Potential of CuO Nanofluids in Water and TEG

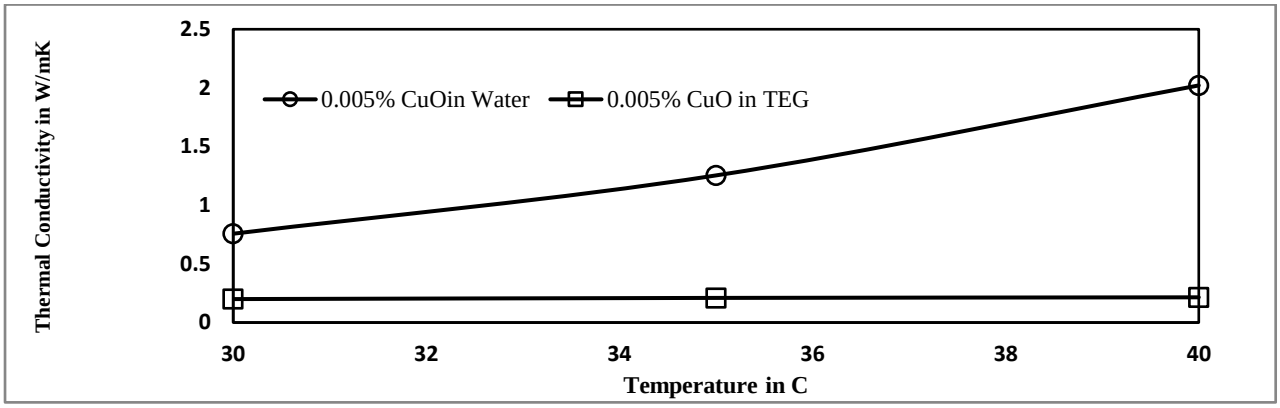

Fig.6. Plot of Thermal Conductivity of CuO Nanofluids in Water and TEG

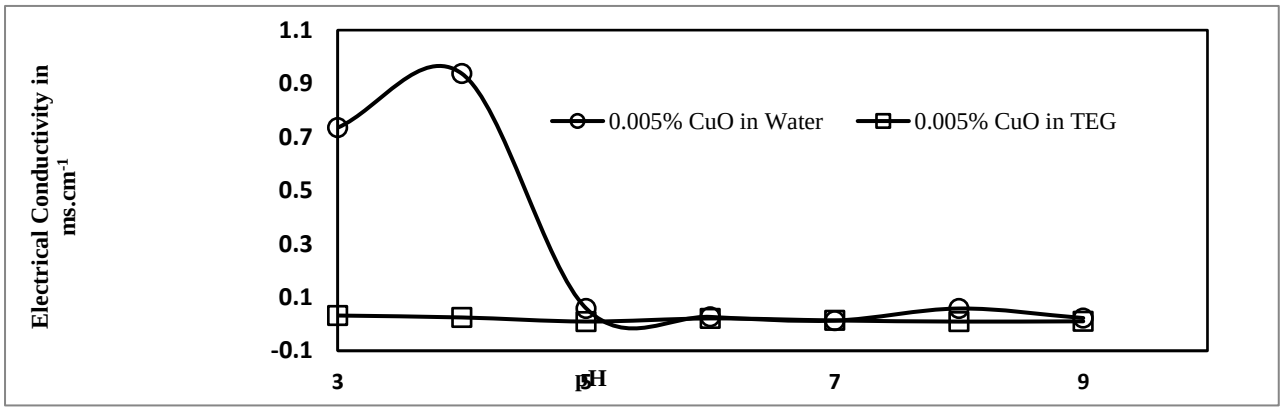

Fig.7. Plot of Electrical Conductivity of CuO Nanofluids in Water and TEG

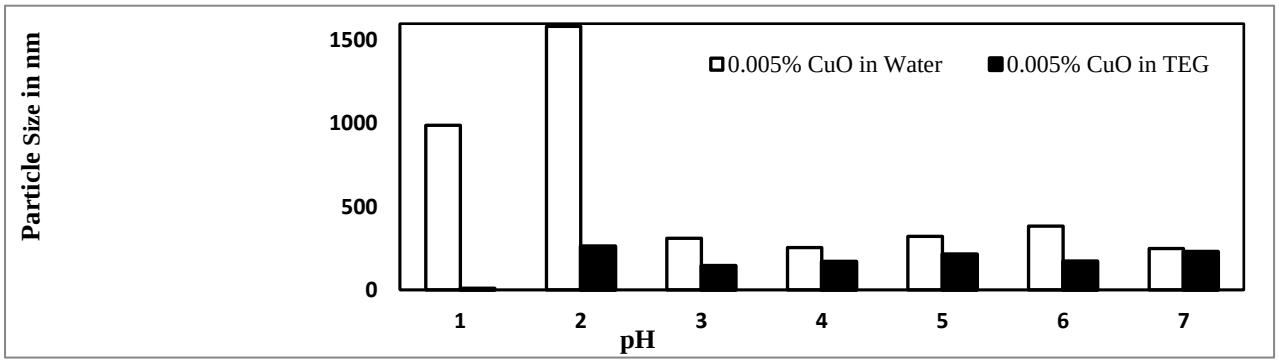

Fig.8. Particle sizes for 0.005% CuO nanofluid in Water and TEG at different pH

Table 1: Experimentally determined density, ρ and viscosity, η of Water, TEG (basefluid) & 0.005% CuO nanofluids in Water and TEG at 303.15K, 308.15K and 313.15K

Solvents	ρ x 10^{-3} kg.m^{-3}			η x 10^{3} kg.$m^{-1}s^{-1}$		
Basefluids						
	303.15K	**308.15K**	**313.15K**	**303.15K**	**308.15K**	**313.15K**
Water	0.9945	0.9943	0.9931	0.7877	0.7112	0.6531
TEG	1.1121	1.1091	1.1071	21.1615	18.0889	13.6685
0.005% CuO in different basefluids						
Water	0.9953	0.9942	0.993	0.7952	0.726	0.6603
TEG	1.1135	1.1133	1.1125	29.6908	21.8496	18.8393

IV. CONCLUSION

From the present investigation, the following conclusions have been drawn:

- Copper oxide nanoparticles have been successfully prepared by chemical precipitation technique and stable CuO nanofluids have been prepared by taking base fluids such as water and TEG.
- Noticeable changes that, there was enhancement in thermal conductivity for the nanofluids from their respective base fluids.
- The studies of zeta potential, which is the important parameter for the stability and dispersibility also shows enhancement even with the variation of pH

V. Acknowledgement

The author (VG) is grateful to Visvesvaraya Technological University, Belagavi, Karnataka for his Ph.D program.

VI. REFERENCES

[1]. N. Canter, "Heat Transfer Fluids: Selection, maintenance and new applications," Tribology and Lubricant Technology, 2009, pp. 28-35.

[2]. N. Canter, "Improving Refrigeration with nanoparticles," Tribology and Lubricant Technology vol. 64(11), 2008, pp. 14-15.

[3]. B. Yang and Z. H. Han, "Thermal conductivity enhancement in water-in-FC72 nano emulsion fluids," Appl. Phys Lett vol. 88, 2006, 261914.

[4]. Z.H. Han, B. Yang, S. H. Kim and M. R. Zachariah, "Application of hybrid sphere/carbon nanotube particles in nanofluids," Nanotechnology, vol. 18(10), 2007, pp. 105701.

[5]. C. H. Li and G. P. Peterson, "Experimental investigation of temperature and volume fraction variations on the effective thermal conductivity of nanoparticles suspensions (nanofluids)," J. Appl. Phys. vol. 99(8), 2006, pp. 084314.

[6]. S.Y. Lee, E.S. Shim, H.S. Kang and S.S. Pang, "Fabrication of ZnO Thin FilmDiode Using Laser Annealing," Thin Solid Films, vol. 473(1), 2005, pp. 31-34.

[7]. Z. L. Wang, X.Y. Kong, Y. Ding, P. Gao, W.L. Hughes, et al, "emicon-ducting and Piezoelectric oxides nanostructures induced by polar sur- faces," Adv. Funct. Mater. vol. 14(10), 2004, pp. 943-956.

[8]. X. L. Cheng, H. Zhao, L. H. Huo, S. Gao and J. G. Zhao, "ZnO nanoparticu- late thin film: preparation, characterization and gas-sensing property," Sensors and Actuators B, vol. 102(2), 2004, pp. 248-252.

[9]. S. S. Joshi, P. R. Patil, M. S. Nimase and P. P. Bakare, "Role of ligands in the formation, phase stabilization, structural and magnetic properties of α-Fe2O3nanoparticles," J. Nanopart. Res. vol. 8(5), 2006, pp. 635-643.

[10]. S. U. S. Choi and J. A. Eastman, "Enhancing thermal conductivity of fluids with nanoparticles," International Mechnical Engineering Congress and Exihibition, 1995.

[11]. R. Manimaran, K. Palaniradja, N. Alagumurthi, S. Sedhilnathan and J. Hussain, "Preparation and characterization of copper oxide nanofluid for heat transfer applications," Applied Nano Science, vol. 4(2), 2014, pp. 163-167.

[12]. U. Holzwarth and N. Gibson, "The Scherrer equation versus the Debye–Scherrer equation," Nat. Nanotechnology, vol. 6,2011, pp. 534-534.

[13]. K.. G. K. Sarojini, S. V. Manoj, P. K. Singh, T. Pradeep and S. K. Das, “Electricalconductivity of ceramic and metallic nanofluids," Colloids and Surfaces a: Physicochem. Eng Aspects, vol. 417, 2013, pp. 39-46.
[14]. R. R. Yadav, G. Mishra, P. K. Yadawa, S. K. Kor, A. K. Gupta and et al, "Ultrasonic properties of nanoparticles-liquid suspensions,” Ultrasonics, vol. 48(6-7), 2008, pp. 591-593.
[15]. K. S. Suganthi, V. L. Vinodhan and K. S. Rajan, “Heat transfer performance and transport properties of ZnO-ethylene glycol and ZnO-ethylene glycol-water nanofluid coolants,” Appl. Energy. vol. 135(15), 2014, pp. 548-559.

National Conference on Applied Sciences Synergising the Engineering and Technology
Print ISSN: 2395-6011 | Online ISSN: 2395-602X (www.ijsrst.com)
© 2021 IJSRST | Volume 8 | Issue 2

Synthesis and Characterization of Spiro Indoline and Indene Derivatives by a One-pot Three-component (3+2) Cycloaddition Reactions

Manjunatha Narayanarao, Susmita Kamila*
Department of Chemistry, East Point College of Engineering and Technology, Bidarahalli, Bangalore-560049, India

ABSTRACT

Multicomponent reactions are potentially useful tools for the synthesis of library compounds. Herein the same strategy has been adopted to generate a library of stereospecific spiro compounds by reacting three-components such as ninhydrin/isatin, sarcosine/L-proline/thioproline with dipolarophile. A series of N-alkylated vinyl indoles, indazoles and acetylene derivatives of 7- azaindoles were prepared as dipolarophiles and treated with different dipoles. The synthesized compounds were characterized by LCMS and single-crystal X-ray analysis. The reaction was proceeded in a very short time and at a lower temperature with excellent yields.
Keywords : Vinyl Indole, Vinyl Indazole, 4-Ethynylazaindole, Ninhydrin, Sarcosine

I. INTRODUCTION

One strategy that potentially meets the goals of synthesis and its library production is the multicomponent reactions (MCRs), which is a very useful tool for the chemist where three or more starting materials are brought together to build up molecular structure and complexity.[1] For decades indole and its derivatives played a vital role in speciality chemicals, pharmaceutical applications and medicines. Many works of the literature suggest indole containing compounds with significant biological activities.[2-7] Both indoles and indazoles have captured the attention of synthetic organic chemists due to their significant effect in anti-cancer, anti-inflammatory, anti-viral and anti-bacterial.[8-9]
Also, the synthesis of spiro indoline/indene through its corresponding dipolarophile via multicomponent reaction strategy can be a useful tool to generate a highly functionalized library of compounds.

II. METHODS AND MATERIAL

General procedure for the preparation of spiro pyrrolidine derivatives compounds.

To the solution of **1** (Scheme 1) (1 mmol, 1 equiv) in dry methanol (5 mL) taken in a single-necked round-bottomed flask, ninhydrin (1.2 mmol, 1.2 equiv) and L-proline/sarcosine (1.2 mmol, 1.2 equiv) were added. The reaction mixture was heated to 60 °C for 30 min and the reaction progress was monitored by TLC (EtOAc/hexanes 1:1). After completion of the reaction, the organic solvent was evaporated to dryness. Water (10 mL) was added to the residue and extracted twice with ethyl acetate (2 × 10 mL) and the solvent was

removed under vacuum. The crude product obtained was purified by flash chromatography on silica gel (EtOAc/hexane 1:1) to get corresponding spiro pyrrolidine derivatives **5a-k** and **6a-k**.

General procedure for the preparation of spiro indoline/indene derivatives compounds.

To the solution of **4** (Scheme 2) (1 mmol, 1 equiv) in dry methanol (5 mL) taken in a single-necked round-bottomed flask, ninhydrin/isatin (1.2 mmol, 1.2 equiv) and L-proline/sarcosine/thioproline (1.2 mmol, 1.2 equiv) were added. The reaction mixture was heated to 60 °C for 30 min and the reaction progress was monitored by TLC (EtOAc/hexanes 1:1). After completion of the reaction, the organic solvent was evaporated to dryness. Water (10 mL) was added to the residue and extracted twice with ethyl acetate (2 × 10 mL) and the solvent was removed under vacuum. The crude product obtained was purified by flash chromatography on silica gel (EtOAc/hexane 1:1) to get corresponding spiro indoline/indene derivatives **7a-d, 9a-d, 10a-d, 12a-d, 13a-d** and **14a-d**.

III. RESULTS AND DISCUSSION

Chemistry

Herein we have synthesized a new series of N-alkylated vinyl derivatives of indole, azaindole and the acetylene derivatives of 7-azaindole by utilizing commercially available bromo intermediates as dipolarophiles. Further, the cyclization reaction was explored on these dipolarophiles by the in situ generations of azomethine ylides by the reaction of ninhydrin/isatin with amino acids such as sarcosine/L-proline/thioproline. The reaction proceeds in a very short time at 60° C in methanol solvent with excellent yields (Scheme 1 & 2). The synthesized compounds were confirmed by analytical techniques such as LCMS and single-crystal X-ray analysis.[10-11]

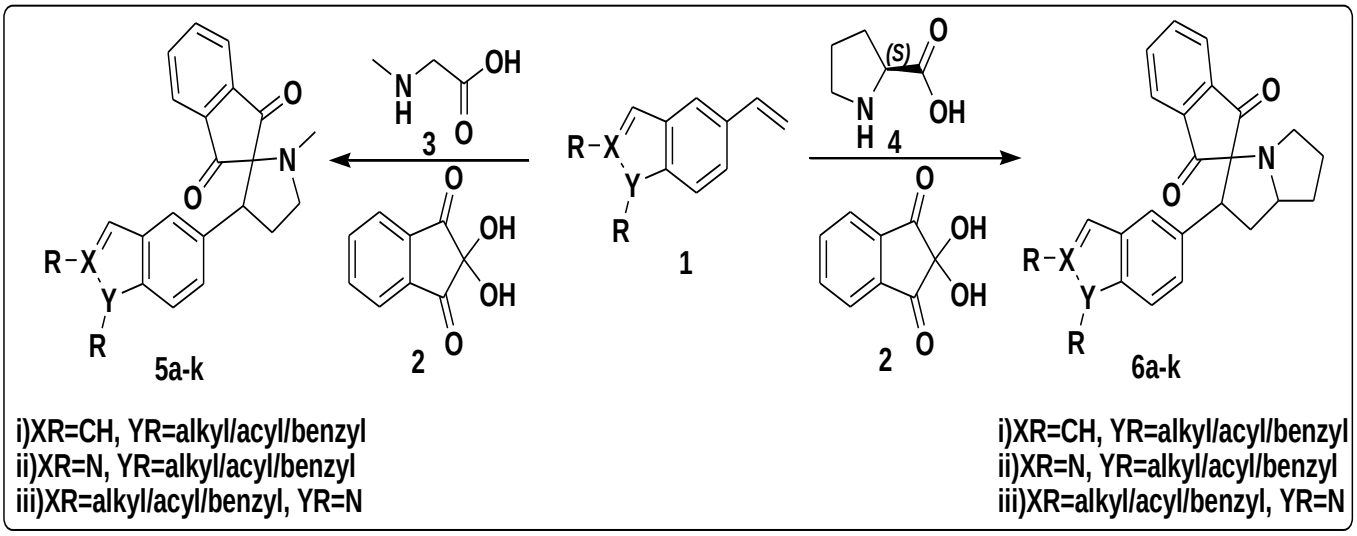

Scheme 1: Synthetic scheme for indole/indazole spiro compounds 5a-k and 6a-k

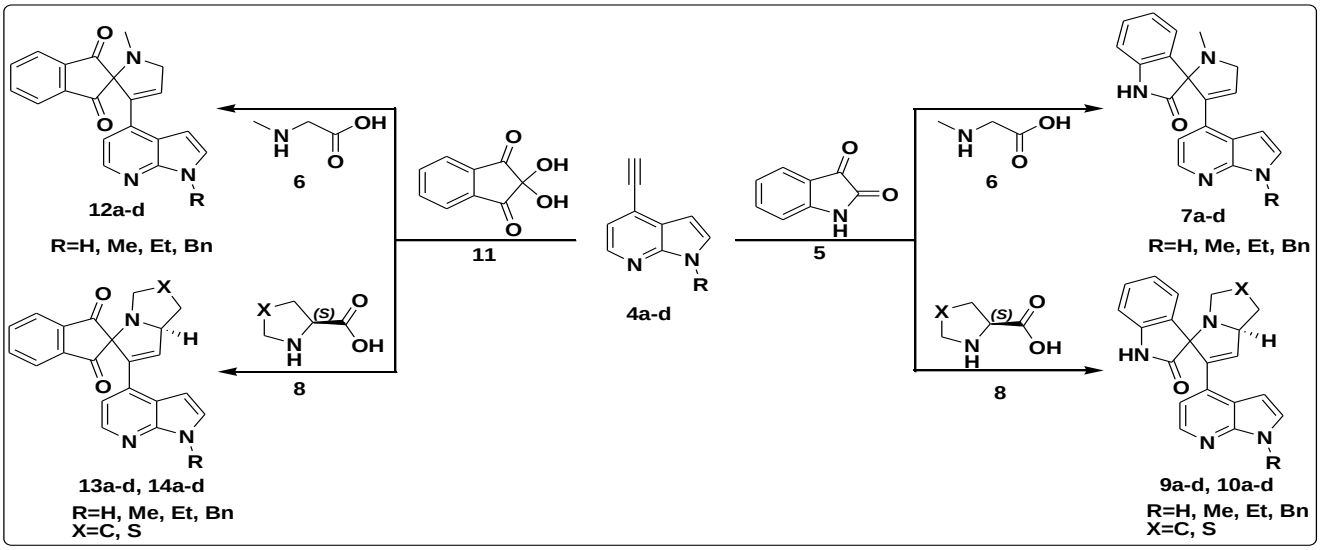

Scheme 2: Synthetic scheme for 7-azaindole spiro compounds **7a-d, 9a-d, 10a-d, 12a-d, 13a-d & 14a-d**

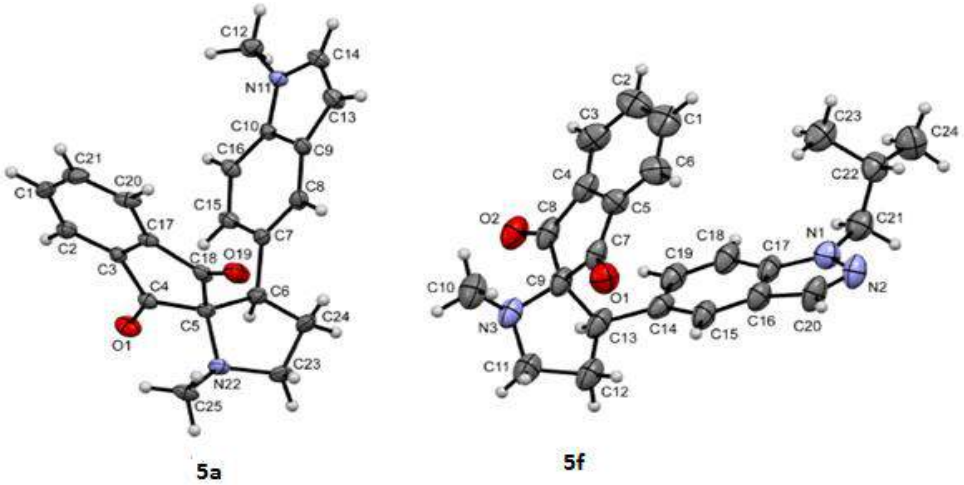

Fig 1: Crystallographic data for compound 5a & 5f

IV. CONCLUSION

The present work explores a range of spiro indoline/indene derivatives via vinyl and acetylene framework which gives an array of novel compounds that could find use in different areas of chemistry. The advantages of the synthesis described are its ease of execution, short reaction times and diversity of the products synthesized.

Analytical data for the compounds 5a and 5f

1'-Methyl-3'-(1-methyl-1*H*-indol-5-yl)spiro[indene-2,2'-pyrrolidine]-1, 3-dione (5a)

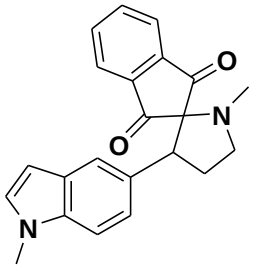

Yellow solid; yield 0.07g (0.20 mmol, 90%). LCMS: *m/z* (%): 345 [M+1]. Anal. Calcd for $C_{22}H_{20}N_2O_2$ (344.15): C, 76.72; H, 5.85; N, 8.13; O, 9.29. Found: C, 76.80; H, 5.89; N, 8.30.

3'-(1-Isobutyl-1*H*-indazol-5-yl)-1'-methylspiro[indene-2,2'-pyrrolidine]-1,3-dione (5f)

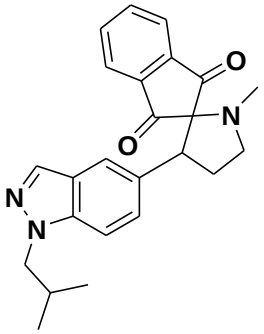

Pale yellow solid; yield 0.07g (0.18 mmol, 82%). LCMS: *m/z* (%): 389 [M+1]. Anal. Calcd for $C_{24}H_{25}N_3O_2$ (387.19): C, 74.39; H, 6.50; N, 10.84; O, 8.26. Found: C, 74.43; H, 6.59; N, 10.87.

2'-(1-methyl-1*H*-pyrrolo[2,3-b] pyridin-4-yl)-5',6',7',7a'-tetrahydrospiro[indene-2,3'-pyrrolizine]-1,3-dione (13b)

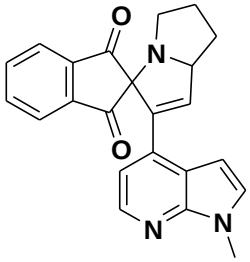

Pale yellow solid; yield 0.050g (0.13 mmol, 77%). LCMS *m/z* (%): 370.2 [M+1]. Anal. Calcd for $C_{23}H_{19}N_3O_2$ (369.42): C, 74.78; H, 5.18; N, 11.37; O, 8.66. Found: C, 74.93; H, 5.23; N, 11.32; O, 8.70.

Acknowledgments

Manjunatha Narayanarao is grateful to East Point College of Engineering & Technology, Bidarahalli, Bengaluru, Karnataka, for providing the opportunity to do Ph.D. programme. This work has not been supported by any funding sources.

V. REFERENCES

[1]. S. L. Schreiber, "Target-Oriented and Diversity-Oriented Organic Synthesis in Drug Discovery," Science, vol. 287, pp. 1964 – 1969, 2000.
[2]. N. K. Terrett, Combinatorial Chemistry: Oxford University Press: New York 1998.
[3]. R. W. Armstrong, "Multiple-Component Condensation Strategies for Combinatorial Library Synthesis," ACC. Chem. Res, vol. 29, pp. 123 – 131, 1996.

[4]. M. J. Plunkett, and J. A. Ellman, "Combinatorial Chemistry and New Drugs," Sci. Am, vol. 276, pp. 68 – 73, 1997.

[5]. L. Weber, "Drug Discovery Today," vol. 7, pp. 143 – 147, 2007

[6]. K. N. Houk, R. A. Firestone, L. L. Munchausen, P. H. Mueller, B. H. Arison, and L. A. Garcia, "Stereospecificity of 1,3-dipolar cycloadditions of p-nitrobenzonitrile oxide to cis- and trans-dideuterioethylene," J. Am. Chem .Soc ., vol. 107, pp. 7227-7228, 1985.

[7]. P. Shanmugam, B. Viswambharam, and S. Madhavan, "Synthesis of Novel Functionalized 3-Spiropyrrolizidine and 3-Spiropyrrolidine Oxindoles from Baylis–Hillman Adducts of Isatin and Heteroaldehydes with Azomethine Ylides via 3+2] Cycloaddition," Org. Letters, vol. 9, pp. 4095-4098, 2007.

[8]. N. K. Kaushik, and N. Kaushik, "Biomedical importance of Indoles," Molecules, vol. 18, pp. 6620-6662, 2013.

[9]. T. Yuan, P. Nahar, and M. Sharma, "Indazole-Type Alkaloids from Nigella sativa Seeds Exhibit Antihyperglycemic Effects via AMPK Activation in Vitro," J. Nat. Prod., vol. 77, pp. 2316–2320, 2014.

[10]. N. Manjunatha, K. Lokesh, G. R. Vijayakumar, G. Subramanya, and K. Susmita,"Multicomponent synthesis of spiro pyrrolidine analogues derived from vinylindole/indazole by a 1, 3-dipolar cycloaddition reaction," Beilstein. J. Org. Chem. vol. 12, pp. 2893-2897, 2016.

[11]. N. Manjunatha, K. Lokesh, G. R. Vijayakumar, G. Subramanya, Y. R. Suman, and K. Susmita, "A one-pot three-component synthesis of fused Spiro Indoline/Indene derivatives derived from ethynyl azaindole by 1, 3-dipolar cycloaddition reaction," Syn. Comm. vol. 48, pp. 2441-2451, 2018.

National Conference on Applied Sciences Synergising the Engineering and Technology
Print ISSN: 2395-6011 | Online ISSN: 2395-602X (www.ijsrst.com)
© 2021 IJSRST | Volume 8 | Issue 2

Application of Variational Homotopy Perturbation Method For Schrodinger Equation

Doreswamy H. S[1], Gayathri V[2]

[1]Professor, Department of Mathematics, East Point College of Engineering and Technology, Bengaluru, Karnataka, India

[2]Assitant Professor, Department of Mathematics, East Point College of Engineering and Technology, Bengaluru, Karnataka, India

ABSTRACT

In the present work, we apply the Variational Homotopy Perturbation Method to obtain the solution of linear and nonlinear Schrodinger equation. The Variational Homotopy Perturbation Method (VHPM) deforms a difficult problem into a simple problem which is easy to get the result. The method produces a solution in the form of a convergent series under conditions that are easy to calculate. Some examples are given to show that this method is easy to apply and the results are obtaining very fast.

Keywords : Linear, Nonlinear, Boundary Conditions, VHPM, Schrodinger Equations

I. INTRODUCTION

The Schrodinger equation has been widely used in various areas of physics including optics, mechanics, plasma physics and quantum mechanics. The Homotopy Perturbation Method (HPM) and the Variational iteration method (VIM) was introduced by Chinese mathematician J. Huan He [1-5]. In recent years, various methods have been proposed such as Adomian decomposition method [ADM], Laplace decomposition method [LDM], Finite difference technique [FDT], Variational method [VIM], but all these methods have some limitations.

The VHPM is a general analytic approach to get series solutions of various types of equations. The VHPM provides us a simple way to ensure the convergence of series solution by introducing a small parameter to ideal results. In this case, the parameter p takes the values from 0 to 1. Suppose, at $p=0$, the problem usually reduces to simplified form. As parameter p slowly increases to 1, the problem goes through a sequence of deformation. Suppose, at $p=1$, the problem takes the original form and the final stage of deformation gives the exact solution.

In the recent decade, several scholars in the fields of partial differential equations have paid attention in showing the existence and the solutions of linear and nonlinear Schrodinger equations were developed [6-10].

The main output of the present paper is details of VHPM in solving the linear and nonlinear Schrodinger equations to show the simplicity and straight forwardness are explained.

II. BASIC IDEA OF VARIATIONAL HOMOTOPY PERTURBATION METHOD

Consider a nonlinear Partial Differential Equations (PDE) with the initial conditions

$$L[u(x,t)]+N[u(x,t)]=g(t) \tag{1}$$

where $L=$ linear differential operator

N =general nonlinear differential operator

$g(t)=$ source term

According to Variational Iteration Method (VIM), we write a correctional functional as

$$u_{n+1}(x,t)=u_n(x,t)+\int_0^t \lambda(x,t)\left[Lu_n(x,t)+N\tilde{u}_n(x,t)-g(t)\right]dt \tag{2}$$

where λ represents the general Lagrangian multiplier which can be identified optimally,

$u_n=$ nth approximate solution,

$\tilde{u}_n=$ restricted variation, i.e., $\delta\tilde{u}_n=0.$

By Homotopy perturbation method (HPM), we can construct an equation is as follows

$$\sum_{i=0}^{\infty} p^i u_i = u_0(x)+p\int_0^t \lambda(x,t)\left[\sum_{i=o}^{\infty} L\left(p^i u_i(x,t)\right)+N\left(p^i\tilde{u}_i(x,t)\right)\right]dt-\int_0^t \lambda(x,t)g(t)dt \tag{3}$$

an approximation to the solution usually will be obtained by identical powers of p and taking the limit as $p\to 1$, we get

$$u(x,t)=\lim_{p\to 1}\sum_{i=0}^{\infty} p^i u_i(x,t)=u_0(x,t)+u_1(x,t)+u_2(x,t)+u_3(x,t)+..... \tag{4}$$

III. APPLICATIONS

3.1 The linear Schrodinger equation

Example 1: Consider the linear Schrodinger equation

$$u_t+iu_{xx}=0 \tag{5}$$

Initial condition is given by

$$u(x,0)=1+\cosh 2x$$

This is solved by VHPM.

Now, by exerting the VHPM, it is possible to obtain the equation as follows,

$$u_0+pu_1+p^2u_2+p^3u_3+.....=(1+\cosh 2x)-ip\int_0^t\left(u_0+pu_1+p^2u_2+p^3u_3+.....\right)_{xx}dt \tag{6}$$

Comparing the powers of p from both sides, we have

$$p^0: u_0(x,t)=1+\cosh 2x$$

$$p^1: u_1(x,t)=-4it\cosh 2x$$

$$p^2: u_2(x,t)=\frac{(-4it)^2}{2!}\cosh 2x$$

$$p^3 : u_3(x,t) = \frac{(-4it)^3}{3!}\cosh 2x$$

$$p^4 : u_4(x,t) = \frac{(-4it)^4}{4!}\cosh 2x$$

……

$$u(x,t) = 1 + \cosh 2x + (-4it)\cosh 2x + \frac{(-4it)^2}{2!}\cosh 2x + \frac{(-4it)^3}{3!}\cosh 2x + \frac{(-4it)^4}{4!}\cosh 2x + ...$$

$$= 1 + \cosh h2x\left[1 + (-4it) + \frac{(-4it)^2}{2!} + \frac{(-4it)^3}{3!} + \frac{(-4it)^4}{4!} + ...\right]$$

$$= 1 + \cosh 2xe^{-4it} \qquad (7)$$

This is the exact solution which is readily obtained upon using the Taylor's series expansion of e^{-4it}.

Example 2: Consider the linear Schrodinger equation

$$u_t + iu_{xx} = 0 \qquad (8)$$

Initial condition is given by

$$u(x,0) = e^{3ix}$$

This is solved by VHPM.

Now, by exerting the VHPM, it is possible to obtain the equation as follows,

$$u_0 + pu_1 + p^2u_2 + p^3u_3 + ... = e^{3ix} - ip\int_0^t \left(u_0 + pu_1 + p^2u_2 + p^3u_3 + ...\right)_{xx} dt \qquad (9)$$

Comparing the powers of p from both sides, we have

$$p^0 : u_0(x,t) = e^{3ix}$$

$$p^1 : u_1(x,t) = 9ite^{3ix}$$

$$p^2 : u_2(x,t) = \frac{(9it)^2}{2!}e^{3ix}$$

$$p^3 : u_3(x,t) = \frac{(9it)^3}{3!}e^{3ix}$$

……

Substituting this value in equation (4), we get

$$u(x,t) = e^{3ix} + 9ite^{3ix} + \frac{(9it)^2}{2!}e^{3ix} + \frac{(9it)^3}{3!}e^{3ix} + ...$$

$$= e^{3ix}\left[1 + 9it + \frac{(9it)^2}{2!} + \frac{(9it)^3}{3!}.....\right]$$

$$= e^{3ix}.e^{9it}$$

$$= e^{3i(x+3t)} \qquad (10)$$

This is the exact solution.

3.2 The Nonlinear Schrodinger equation

Example 3: Consider the nonlinear Schrodinger equation

$$iu_t + u_{xx} + m|u|^2 u = 0 \quad \text{or} \quad u_t = iu_{xx} + im|u|^2 u \tag{11}$$

Initial condition is given by

$$u(x,0) = e^{nix}$$

This is solved by VHPM.

Now, by exerting the VHPM, it is possible to obtain the equation as follows

$$u_0 + pu_1 + p^2u_2 + p^3u_3 + \ldots\ldots = e^{nix} + ip\int_0^t \left(u_0 + pu_1 + p^2u_2 + p^3u_3 + \ldots.\right)_{xx} dt + imp\int_0^t \left(u_0 + pu_1 + p^2u_2 + \ldots.\right) dt \tag{12}$$

Comparing the powers of p from both sides, we have

$$p^0 : u_0(x,t) = e^{nix}$$

$$p^1 : u_1(x,t) = i(m-n^2)te^{nix}$$

$$p^2 : u_2(x,t) = i^2(m-n^2)^2\frac{t^2}{2!}e^{nix}$$

$$p^3 : u_3(x,t) = i^3(m-n^2)^3\frac{t^3}{3!}e^{nix}$$

.....

Substituting this value in equation (4), we get

$$\begin{aligned} u(x,t) &= e^{nix} + i(m-n^2)te^{nix} + i^2(m-n^2)^2\frac{t^2}{2!}e^{nix} + i^3(m-n^2)^3\frac{t^3}{3!}e^{nix} + \ldots\ldots \\ &= e^{nix}\left[1 + i(m-n^2)t + i^2(m-n^2)^2\frac{t^2}{2!} + i^3(m-n^2)^3\frac{t^3}{3!} + \ldots\ldots\right] \\ &= e^{nix}.e^{i(m-n^2)t} \\ &= e^{i\left[nx+\left(m-n^2\right)t\right]} \end{aligned} \tag{13}$$

This is the exact solution.

Example 4: Consider the nonlinear Schrodinger equation

$$iu_t + u_{xx} + 2|u|^2 = 0 \tag{14}$$

or

$$u_t = iu_{xx} + 2i|u|^2$$

Initial condition is given by

$$u(x,0) = 2\,\mathrm{sech}(2x)$$

This is solved by VHPM.

Now, by exerting the VHPM, it is possible to obtain the equation as follows,

$$u_0 + pu_1 + p^2u_2 + p^3u_3 + \ldots\ldots = 2\,\mathrm{sech}(2x) + ip\int_0^t \left(u_0 + pu_1 + p^2u_2 + p^3u_3 + \ldots.\right)_{xx} dt \qquad (15)$$

Comparing the powers of p from both sides, we have

$$p^0 : u_0(x,t) = 2\,\mathrm{sech}\,2x$$

$$p^1 : u_1(x,t) = 8it\,\mathrm{sech}\,2x$$

$$p^2 : u_2(x,t) = 16i^2t^2\,\mathrm{sech}\,2x$$

$$p^3 : u_3(x,t) = \frac{64}{3}i^3t^3\,\mathrm{sech}\,2x$$

.....

Substituting this value in equation (4), we get

$$u(x,t) = 2\,\mathrm{sech}\,2x + 8it\,\mathrm{sech}\,2x + 16i^2t^2\,\mathrm{sech}\,2x + \frac{64}{3}i^3t^3\,\mathrm{sech}\,2x + \ldots\ldots$$

$$u(x,t) = 2\,\mathrm{sech}\,2x\left[1 + 4it + \frac{(4it)^2}{2!} + \frac{(4it)^3}{3!} + \ldots\ldots\right]$$

$$= 2\,\mathrm{sech}\,2x.e^{4it} \qquad (16)$$

This is the exact solution.

IV. CONCLUSION

In this paper, the Variational Homotopy Perturbation Method has been successfully applied to find the solution of the linear and nonlinear Schrodinger equations. The present method is easy and reliable to use. The outcomes show that VHPM is very powerful and efficient technique in finding analytical solutions for wider problems. The convergence accuracy of this method was examined in several examples. This method is capable of reducing the computational work.

Acknowledgements:

The authors would like to thank the reviewers for their valuable comments and suggestions to improve this paper. The authors would like to express their gratitude to chairman, principal and staff members of East Point College of Engineering and Technology, Bengaluru.

V. REFERENCES

[1]. J.H. He, Homotopy perturbation technique, computer methods in applied mechanics and engineering, 178, 257-262, 1999.

[2]. J.H. He, A review on some new recently developed nonlinear analytical techniques, International journal of nonlinear sciences and numerical simulation,1,51-70, 2000.

[3]. J. H. He, Homotopy perturbation method: a new nonlinear analytical technique, Applied Mathematics and Computation, 135, 73-79, 2003.

[4]. J.H. He, Homotopy perturbation method for solving boundary value problems, physics letters A 350:87-88, 2006.
[5]. J.H. He, Recent development of the homotopy perturbation method, Topological Methods in Nonlinear Analysis, vol.31,2,205-209,2008.
[6]. Sh. Sadigh Behzadi, Solving Schrodinger equation by using modified variational iteration and homotopy analysis methods, J. Appl. Anal. Compute, 1(4), 427-437,2011.
[7]. R Hao, Lu Li, Zhonghao Li, W Xue, G Zhou, A new approach to exact soliton solutions and soliton interaction for nonlinear Schrodinger equation for nonlinear Schrodinger equation with variable coefficients, Opt. Commun, 236 (1-3), 79-86, 2004.
[8]. Biao Li, Yong Chen, On exact solutions of the nonlinear Schrodinger equations in optical fiber, Chaos Solitons Fractals, 21(1), 241-247,2004.
[9]. S.Z. Rida, H.M. El-Sherbiny, A.A.M. Arafa, on the solution of the fractional nonlinear Schrodinger equation, Physical Letters, A, 372 (5),553-558, 2008
[10]. A M Wazwaz, Study on linear and nonlinear Schrodinger equations by the variational iteration method, Chaos Solitons Fractals, 37 (4), 1136-1142,2006.

National Conference on Applied Sciences Synergising the Engineering and Technology
Print ISSN: 2395-6011 | Online ISSN: 2395-602X (www.ijsrst.com)
© 2021 IJSRST | Volume 8 | Issue 2

The Onset of Magnetoelectrothermoconvection in a Dielectric Fluid Saturated Rotating Porous Medium

B. V. Rangaraju[1], M. S. Gayathri[2], P. A. Dinesh[3]

[1]Department of Mathematics, East point college of engineering and Technology, Bengaluru, Karnataka, India

[2]Department of Mathematics, B.M.S. College of Engineering, Bengaluru, Karnataka, India

[3]Department of Mathematics, Ramaiah Institute of Technology, Bengaluru, Karnataka, India

ABSTRACT

The purpose of this paper is to study the effects of magnetic field and rotation in the presence of uniform temperature and electric modulation field on the onset of magnetoelectrothermo convection in a horizontal layer with densely packed porous medium saturated by a dielectric fluid using linear stability analysis based on normal mode technique. The dielectric constant is assumed to be a linear function of temperature. Modified Darcy equation is used to describe the flow in porous medium and the resulting eigenvalue problem is solved using a regular perturbation method with small amplitude approximation by choosing free-free boundaries. The correction electric Rayleigh number is calculated as a function of Hartmann number, frequency of electric modulation, thermal Rayleigh number, Darcy number, Prandtl number and Taylor number and their effects on the stability of the system are discussed.

Keywords: Magnetoelectrothermoconvection, Modulated Electric Modulation, Porous Layer, Magnetic Field, Regular Perturbation Method

NOMENCLATURE

A	Specific heat ratio	t	Time (sec)
$\vec{B}$	Magnetic field (tesla)	**Greek symbols**	
D_a	Darcy number	α	Coefficient of thermal expansion
$\vec{E}$	Electric field	σ	Electric conductivity
$\vec{g}$	Acceleration due to Gravity	δ	Porosity
h	Thickness (m)	φ	Electric potential (volts)
$\vec{J}$	Electric current density (amp/m^2)	ε	Dielectric constant
		η	Amplitude of the electric potential
k	Wave number (m^{-1})	ν	Kinematic viscosity (m^2 /s)
K	Permeability (m^2)		(electric permittivity)
M_a	Hartmann number	χ	Thermal diffusivity (m^2 /s)
P	Pressure	Ω	Frequency of modulation
		ρ	Density of the fluid

P_r	Prandtl number	**Subscripts/Superscripts**	
$\vec{q}$	(u,v,w) Velocity vector (m/s)	b	Base state
R_a	Thermal Rayleigh number	c	Critical value
R_e	Electric Rayleigh number	0	Reference value
T_a	Taylor number	$'$	Perturbed quantity
T	Temperature (kelvin)	$*$	Non-dimensional quantity

I. INTRODUCTION

Magnetoelectroconvection is the study of the motion of electrically conducting liquids in the presence of magnetic field. It deals with the interaction of electromagnetic and hydrodynamic forces to yield the effects of electric field and magnetic field on the flow and the flow is based on the basic principles of Magneto Electro Hydro Dynamics. The Magnetoelectroconvective instability of a periodic states of mechanical systems has long been an object of study and is of considerable interest due to their numerous applications in various fields such as geothermal energy utilization, oil reservoir modeling, building of thermal insulations, plasma studies, the design of nuclear reactors, MHD power generator, particularly in the fields of biomechanics in designing the artificial organs like cartilages in synovial joints, coronary artery deceases etc. Dynamic stabilization or destabilization can lead to the dramatic modifications of their behavior depending on the proper tuning of the amplitude and frequency of the modulation. It is only in the recent past that attention has been focused on such possibilities in hydrodynamics. The interest lies not only with the mechanics of this new class of problems but also with the possibilities for other industrial and materials science processing applications. If an imposed modulation can destabilize the stable state, then there can be a major enhancement of heat / mass / momentum transport. If an imposed modulation can stabilize an unstable state, then higher efficiencies can attained in various processing techniques.

In the above mentioned applications rotation plays an important role. It is realized that earth's crust is essentially a porous medium consisting of different types of fluid like water, oil, gases, etc., the temperature of which increments as one dive deep inside. Likewise, steady angular velocities of the earth about its geological pivot offers ascend to Coriolis force. Subsequently any endeavor to examine convective streams in geothermal frameworks will prompt the issue of finding the impact of rotation on the stability of liquid dynamical system in a porous layer.

The stability of the flow of an electrically conducting fluid between two infinite parallel plates under a transverse magnetic field has been studied by Lock (1955). Whereas, Takashima (1994) have investigated the linear stability of natural convection of an electrically conducting fluid which is confined between two parallel vertical plates maintained at different constant temperature in the presence of a transverse magnetic field.

In geophysical and astrophysical applications, Coriolis force plays an important role in suppressing the oscillations caused by an external constraint of electric field. When the prandtl number is sufficiently small and the Taylor number not too low, on set of convection occurs in the form of an oscillatory mode in rotating systems. It was shown that Chandrashekar (1961), for Rayleigh-Benard convective instability, the effect of a uniform rotation is similar to the effect of a magnetic field in magnetoconvection by Rudraiah *et al.* (1985,

1986). These two factors have a stability role in natural convection. Rudraiah *et al.* (1986) have studied the effects of the Coriolis force and a non-uniform temperature gradient on the onset of Rayleigh-Benard and Marangoni convection and showed that combined effects of rotation and non-uniform temperature gradient is to control the convection

Onsets of natural convection in the presence of external fields such as a magnetic field or an electric field (Turnbull, 1968, 1969; Maekaw et al, 1992; char etal, 1994) have been examined by many researchers. In highly conducting fluids such as mercury or molten metals and semi-conductors, magnetic effects will be dominant. To the contrary, in Dielectric fluids with low values of the conductivity the electric effects will essentially govern the motion. The forces that are exerted by an electric field on free charges present in the liquid are transmitted by collision to the neutral molecules. These forces acting on particles are important in many applications of dielectric materials. It decisively affects the dynamical behavior of particles in high voltage insulating systems, where particles are often subjected to a non-uniform field. The particles may be either conducting or dielectric. Many works on the electric field and its force have already been published on charged conducting particles by Smorodin *et al.* (2000).

Takashima (1976) studied the effect of rotation under the action of temperature gradient and AC electric field on the onset of convective instability and analyzed that the coriolis force has an preventing outcome on the onset of instability even when the electrical effects are taken into account and as the speed of rotation rises the coupling among electrical and buoyancy force turns into tighter

Douiebe *et al.* (2001) discussed the influences of both rotation and AC electric field on the coupled thermocapillary and buoyancy instability in an electrically conducting fluid medium. Special attention was given at the occurrence of both stationary and oscillatory convection. Othman (2004) analyzed the linear stability of a rotating layer of a viscoelastic dielectric fluid under the action of a vertical temperature gradient and AC electric field. The eigen value problem is solved for various critical values by choosing free-free boundaries and was discussed in detail.
The stability on the onset of convection in a fluid saturated porous medium subject to both temperature modulation and rotation was investigated by Malashetty *et al.* (2007, 2008). Gaikwad *et al.* (2012) have investigated the combined effects of thermal modulation and rotation of small amplitude on the convection in Walter's B fluid saturated porous layer.

Bhadauria *et al.* (2011) have investigated the onset of natural convection in a rotating porous medium with internal heat generation. Combined effects of a vertical AC electric field and Coriolis force on the onset of electro convection in a dielectric fluid saturated Brinkman porous medium for a various types of velocity boundary conditions are carried out by Shiva kumara *et al.*(2011,2016) and Shiva kumara *et al.* (2013) studied the effects of rotation in couple stress dielectric fluid layer on the electro hydrodynamics instability.

The effect of thermal modulation on the onset of electrothermoconvection in a horizontal dielectric fluid saturated with densely packed porous medium has been studied by Rudraiah and Gayathri (2009). Onset of electro convection in a dielectric fluid saturated porous layer in a modulated electric field was carried out by Gayathri *et al.* (2015). Gayathri *et al.* (2018) have analyzed the effect of magnetic field on the onset of magnetoelectroconvection in a horizontal dielectric fluid layer saturated with densely packed porous medium in the presence of uniform electric field and modulated temperature. Also, Gayathri *et al.* (2018) continued

their work on the effects of thermal modulation and rotation on the convective instability in a dielectric fluid saturated porous medium in the presence of uniform magnetic field using modified Darcy equation by choosing free-free boundaries.

The literature pertaining to the effects of modulation electric field and rotation on the onset of magnetoelectroconvection in a dielectric fluid saturated porous medium with the effects of magnetic field and uniform temperature is missing regardless of its significance in understanding the control of convection in many scientific and technological problems.

Therefore, the main object of this paper is to study the effect of magnetic field on the magnetoelectroconvective instability of a dielectric horizontal fluid layer saturated with densely packed porous medium in the presence of modulated electric field, rotation and uniform temperature by choosing free-free boundaries.

II. MATHEMATICAL FORMULATION

Let us consider an infinite horizontal layer of incompressible dielectric fluid saturated porous medium bounded by the free plates at $z=0$ and $z=h$ with uniform applied magnetic field B_o is present in the horizontal direction (Fig.1). The fluid saturated porous layer is subjected to rotation with an angular velocity $\overline{\Omega}$. The axis of rotation is taken along the z-axis. Constant different temperatures $T_b = \pm\frac{\Delta T}{2}$ and the boundaries are maintained at a different modulated electric potential of the form $\phi_b = \pm U(\eta_1 + \eta_2 \cos\Omega t)$. Here U is the characteristic voltage applied between the embedded electrodes and Ω is its modulation frequency.

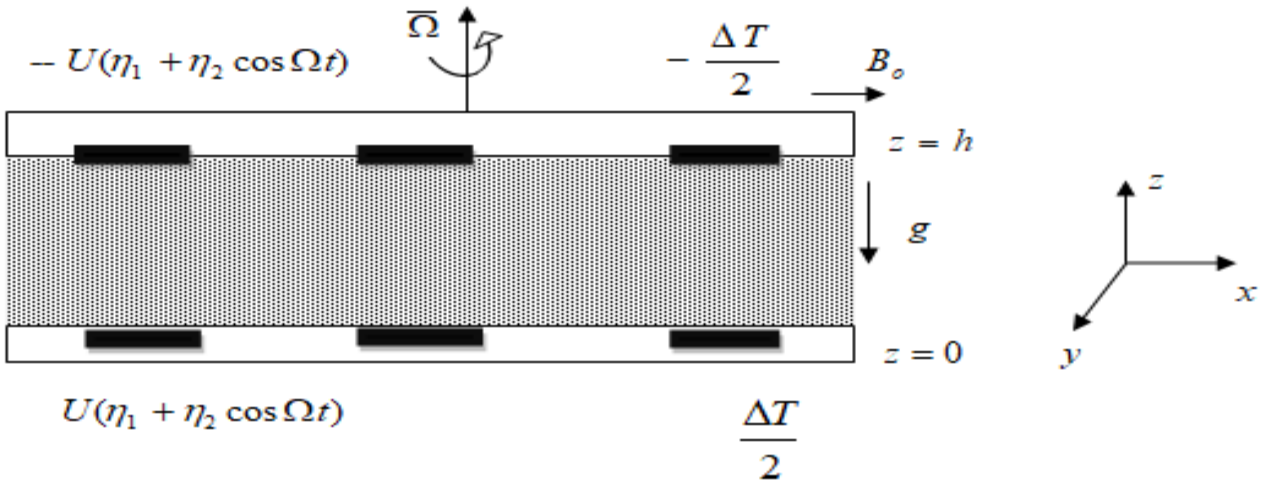

With the usual assumptions and approximations made in the convection problems, the basic governing and Maxwell equations of a Boussinesq incompressible fluid when the magnetic field is present are as follows

$$\nabla \circ \vec{q}, \qquad (1)$$

$$\delta^{-1}\frac{\partial \vec{q}}{\partial t}+\delta^{-2}(\vec{q}\circ\nabla)\vec{q}+2\delta^{-1}\overline{\Omega}\hat{k}\times\vec{q}=-\nabla P+\frac{\rho}{\rho_0}\vec{g}-\frac{\nu}{K}\vec{q}-\frac{\vec{E}^2}{2\rho_0}\nabla\varepsilon+\frac{(\vec{J}\times\vec{B})}{\rho_0}, \quad (2)$$

$$A\frac{\partial T}{\partial t}+(\vec{q}\circ\nabla)T=\chi\nabla^2 T. \quad (3)$$

$$\nabla\times\vec{E}=0 \quad \text{OR} \quad \vec{E}=-\nabla\varphi, \quad (4)$$

$$\nabla\circ(\varepsilon\vec{E})=0, \quad (5)$$

$$\varepsilon=\varepsilon_m(1+\eta T), \quad (6)$$

$$\rho=\rho_0(1-\alpha T). \quad (7)$$

The quantities at basic state of the system are described of the form

$$\vec{q}=\vec{q}_b=0,\ \varepsilon=\varepsilon_b(z),\ \vec{E}=\vec{E}_b(z,t),\ T=T_b(z),\ \varphi=\varphi_b(z,t), \quad (8)$$

Substituting eq. (8) into the above eqs, we obtain the quiescent state solutions from (1) – (7), are as follows

$$-\nabla P_b+\frac{\rho_b}{\rho_0}\vec{g}-\frac{E_b^{\,2}}{2\rho_0}\nabla\varepsilon_b=0, \quad (9)$$

$$\frac{d^2T_b}{dz^2}=0, \quad (10)$$

$$\nabla\circ(\varepsilon_b\vec{E}_b)=0, \quad (11)$$

$$\varepsilon_b=\varepsilon_m(1+\eta T_b). \quad (12)$$

Eq. (10) is solved by using the conditions at the boundaries, we obtain

$$T_b=\frac{\Delta T}{2h}(h-2z), \quad (13)$$

From eq. (12), we get

$$\varepsilon_b\approx\varepsilon_m\left(1-\frac{\Delta T}{h}\eta z\right), \quad (14)$$

$$\frac{d\varepsilon_b}{dz}=-\frac{\varepsilon_m\eta\Delta T}{h}. \quad (15)$$

Using $E_b=-\nabla\varphi_b$ in Eq. (10) and solving the resulting equation, we get the solution for φ_b in the form

$$\varphi_b=-\frac{2U(\eta_1+\eta_2\cos\Omega t)}{log(1-\eta\Delta T)}\log(1-\frac{\eta\Delta T}{h}z)+U(\eta_1+\eta_2\cos\Omega t), \quad (16)$$

$$\therefore\ E_b=\frac{2U(\eta_1+\eta_2\cos\Omega t)}{h}\left(1+\frac{\Delta T}{h}\eta z\right), \quad (17)$$

$$\frac{dE_b}{dz}=\frac{2U(\eta_1+\eta_2\cos\Omega t)\eta\Delta T}{h^2}. \quad (18)$$

We now introducing perturbations on the basic flow in the form

$$\vec{q} = \vec{q}' = (u', v', w'), \quad \varepsilon = \varepsilon_b + \varepsilon', \quad P = P_b + P', \quad \varphi = \varphi_b + \varphi', \quad \vec{E} = \vec{E} + \vec{E}', \quad T = T_b + T'. \tag{19}$$

Eq. (19) using in Eqs. (1)- (6) and also substituting the solutions given by Eqs. (9)- (18) and after linearizing, we obtain

$$\delta^{-1}\frac{\partial \vec{q}'}{\partial t} + 2\delta^{-1}\overline{\Omega}\hat{k}\times\vec{q}' = -\nabla\Pi + \alpha g T'\hat{k} - \frac{\nu}{K}\vec{q}' + Q'\hat{k} - \frac{\sigma}{\rho_0}B_0{}^2 w'\hat{k}\ , \tag{20}$$

$$\left(A\frac{\partial}{\partial t} - \chi\nabla^2\right)T' = \frac{\Delta T}{h}w', \tag{21}$$

$$\nabla^2\varphi' = \frac{2U(\eta_1 + \eta_2\cos\Omega t)}{\varepsilon_m h}\frac{\partial\varepsilon'}{\partial z} - \frac{1}{\varepsilon_m}\frac{d\varepsilon_m}{dz}\frac{\partial\varphi'}{\partial z}\ , \tag{22}$$

$$\varepsilon' = \varepsilon_m \eta T', \tag{23}$$

$$\text{Where } \Pi = P' + \frac{\varepsilon' E_b{}^2}{2\rho_0}, \tag{24}$$

$$Q' = \frac{\Delta T \eta E_b \varepsilon_m}{\rho_0 h}\left(\frac{2U(\eta_1 + \eta_2\cos\Omega t)}{h\varepsilon_m}\varepsilon' - \frac{\partial\varphi'}{\partial z}\right). \tag{25}$$

Following analysis of Roberts [3], we assume $\eta\Delta T << 1$. Under this approximation Eq. (22), using Eq. (23), becomes

$$\nabla^2\varphi' = \frac{2\eta U(\eta_1 + \eta_2\cos\Omega t)}{h}\frac{\partial T'}{\partial z}\ , \tag{26}$$

and Eq. (25) becomes

$$Q' = \frac{2\eta\varepsilon_m \Delta T U(\eta_1 + \eta_2\cos\Omega t)}{h^2\rho_0}\left(\frac{2\eta U(\eta_1 + \eta_2\cos\Omega t)}{h}T' - \frac{\partial\varphi}{\partial z}\right), \tag{27}$$

From Eq. (26), we get

$$\nabla^2 Q' = \frac{4\eta^2\varepsilon_m \Delta T U^2(\eta_1 + \eta_2\cos\Omega t)^2}{\rho_0 h^3}\nabla_H{}^2 T', \tag{28}$$

Where $\nabla_H{}^2 = \frac{\partial^2}{\partial x^2} + \frac{\partial^2}{\partial y^2}$.

Operating curl on both sides of Eq. (20), and taking its vertical component we get an equation for vertical component of vorticity ς in the form

$$\left(\frac{1}{\delta}\frac{\partial}{\partial t} + \frac{\nu}{K}\right)\varsigma = \frac{2\overline{\Omega}}{\delta}\frac{\partial w}{\partial z} \tag{29}$$

Eliminating the pressure form Eq. (20), we take curl twice on it and obtain

$$\left(\frac{1}{\delta}\frac{\partial}{\partial t} + \frac{\nu}{K}\right)\nabla^2 w' = \alpha g\nabla_H{}^2 T' + \nabla_H{}^2 Q' - \frac{2\overline{\Omega}}{\delta}\frac{\partial\varsigma}{\partial z} - \frac{\sigma}{\rho_0}B_0{}^2\nabla_H{}^2 w'. \tag{30}$$

We impose following conditions at the boundaries.

$$w' = \frac{\partial^2 w'}{\partial z^2} = T' = \varphi' = \varsigma = 0 \quad \text{at} \quad z = 0, h. \tag{31}$$

Substituting Eqs. (21), (28) and (29) in Eq. (30), we get the following expression for the temperature perturbation in the form:

$$\left[\begin{array}{l}\frac{h}{\Delta T}\left(\frac{1}{\delta}\frac{\partial}{\partial t}+\frac{\nu}{K}\right)^2\left(A\frac{\partial}{\partial t}-\chi\nabla^2\right)\nabla^2+\frac{h}{\Delta T}\frac{4\overline{\Omega}^2}{\delta^2}\frac{\partial^2}{\partial z^2}\left(A\frac{\partial}{\partial t}-\chi\nabla^2\right)\\ +\frac{h}{\Delta T}\frac{\sigma}{\rho_0}{B_0}^2\left(\frac{1}{\delta}\frac{\partial}{\partial t}+\frac{\nu}{K}\right)\left(A\frac{\partial}{\partial t}-\chi\nabla^2\right){\nabla_H}^2-\alpha g\left(\frac{1}{\delta}\frac{\partial}{\partial t}+\frac{\nu}{K}\right){\nabla_H}^2\end{array}\right]\nabla^2 T' \qquad (32)$$

$$=\frac{4\eta^2\varepsilon_m\Delta T U^2\ {\eta_1}^2(1+\eta_3\cos\Omega t)^2}{\rho_0 h^3}\left(\frac{1}{\delta}\frac{\partial}{\partial t}+\frac{\nu}{K}\right){\nabla_H}^4 T'.$$

Where $\eta_3=\eta_2/\eta_1$ is the relation between the modulated and steady amplitudes of electric potential. Non-dimensionalizing the above Eq. (32) by taking the accompanying relations.

$$\left(x^*,\ y^*,\ z^*\right)=\left(\frac{x}{h},\frac{y}{h},\frac{z}{h}\right),\ \ T^*=\frac{T}{\Delta T},\ \ t^*=\frac{t}{Ah^2/\chi},\ \ \omega=\frac{\Omega}{\chi/Ah^2}. \qquad (33)$$

Therefore, the resulting equation (after neglecting star-shaped character $*$)

$$\left[\begin{array}{l}\left(\frac{1}{\delta A P_r}\frac{\partial}{\partial t}+\frac{1}{Da}\right)^2\left(\frac{\partial}{\partial t}-\nabla^2\right)\nabla^2+T_a\ \frac{\partial^2}{\partial z^2}\left(\frac{\partial}{\partial t}-\nabla^2\right)\\ +M_a\left(\frac{1}{\delta A P_r}\frac{\partial}{\partial t}+\frac{1}{Da}\right)\left(\frac{\partial}{\partial t}-\nabla^2\right){\nabla_H}^2-R_a\left(\frac{1}{\delta A P_r}\frac{\partial}{\partial t}+\frac{1}{Da}\right){\nabla_H}^2\end{array}\right]\nabla^2 T' \qquad (34)$$

$$=R_e\left(1+\eta_3\cos\omega t\right)^2\left(\frac{1}{\delta A P_r}\frac{\partial}{\partial t}+\frac{1}{Da}\right){\nabla_H}^4 T'$$

The boundary conditions (31) can also be made dimensionless using the scales given by. Eq. (34) and using $\frac{\partial^4 T'}{\partial\ z^4}=0.$ If w', T', ς' and φ' are zero, we obtain

$$T'=\frac{\partial^2 T'}{\partial z^2}=\frac{\partial^4 T'}{\partial z^4}=0 \quad \text{at} \quad z=0,1. \qquad (35)$$

If the horizontal dependence of T' in Eq. (34) is assumed to be of the form $e^{i(k_x x+k_y y)}$, where k_x and k_y are the horizontal wave numbers, then T' takes the following form:

$$T'=T(z,t)\,e^{i(k_x x+k_y y)},$$

It follows that

$${\nabla_H}^2 T'=-\mathrm{k}^2 T',$$

Here $\mathrm{k}^2=\mathrm{k}_x{}^2+\mathrm{k}_y{}^2$. Also Eqs. (34) and (35), respectively become

$$\left[\begin{array}{l}\left(\frac{1}{\delta AP_r}\frac{\partial}{\partial t}+\frac{1}{Da}\right)^2\left(\frac{\partial}{\partial t}-\left(D^2-\mathrm{k}^2\right)\right)\left(D^2-\mathrm{k}^2\right)+T_a D^2\left(\frac{\partial}{\partial t}-\left(D^2-\mathrm{k}^2\right)\right) \\ -M_a k^2\left(\frac{1}{\delta AP_r}\frac{\partial}{\partial t}+\frac{1}{Da}\right)\left(\frac{\partial}{\partial t}-\left(D^2-\mathrm{k}^2\right)\right)+R_a \mathrm{k}^2\left(\frac{1}{\delta AP_r}\frac{\partial}{\partial t}+\frac{1}{Da}\right)\end{array}\right]\left(D^2-\mathrm{k}^2\right)T \quad (36)$$

$$= R_e \mathrm{k}^4 (1+\eta_3 \cos\omega t)^2\left(\frac{1}{\delta AP_r}\frac{\partial}{\partial t}+\frac{1}{Da}\right)T,$$

$$T = \frac{\partial^2 T'}{\partial z^2} = \frac{\partial^4 T'}{\partial z^4} = 0 \qquad \text{at} \quad z = 0,1. \quad (37)$$

We use the following regular perturbation procedure to get an equation for an eigenvalue R_e in Eq. (36)

III. REGULAR PERTURBATION METHOD WITH SMALL AMPLITUDE APPROXIMATION

We seek the eigenvalues R_e and eigenfunctions T of the Eq. (36) vary from those related with unmodulated system by the amounts of the order η_3. We therefore write the solution of Eq. (36) as an expansion of the form.

$$T = T_0 + \eta_3 T_1 + \eta_3^2 T_2 + \cdots\cdots \quad (38)$$

$$R_e = R_{e0} + \eta_3 R_{e1} + \eta_3^2 R_{e2} + \cdots\cdots$$

The expansions (38) are inserted in Eq. (36) and the coefficients of different powers of η_3 compared on the two sides of the subsequent condition. From these we get:

$$L T_0 = 0. \quad (39)$$

$$L T_1 = 2 R_{e0} \mathrm{k}^4 \cos\omega t\left(\frac{1}{\delta AP_r}\frac{\partial}{\partial t}+\frac{1}{Da}\right)T_0 + R_{e1}\mathrm{k}^4\left(\frac{1}{\delta AP_r}\frac{\partial}{\partial t}+\frac{1}{Da}\right)T_0 - \frac{2R_{e0}\mathrm{k}^4\omega}{\delta A p_r}\sin\omega t\, T_0. \quad (40)$$

$$\begin{aligned} L T_2 &= R_{e0}\mathrm{k}^4\frac{\cos^2\omega t}{Da}\cos^2\omega t\, T_0 + 2R_{e0}\mathrm{k}^4\cos\omega t\left(\frac{1}{\delta AP_r}\frac{\partial}{\partial t}+\frac{1}{Da}\right)T_1 \\ &+ R_{e2}\mathrm{k}^4\left(\frac{1}{\delta AP_r}\frac{\partial}{\partial t}+\frac{1}{Da}\right)T_0 - \frac{R_{e0}\mathrm{k}^4\omega}{\delta AP}\sin 2\omega t\, T_0 - \frac{2R_{e0}\mathrm{k}^4\omega}{\delta AP}\sin\omega t\, T_1. \end{aligned} \quad (41)$$

T_0 , T_1, T_2 and so on have to be determined using the boundary conditions given by Eq. (37). The function T_0 is a solution of the problem when $\eta_3 = 0$ and marginally stable solutions for (39) are by

$$T_0^{(n)} = \sin(n\pi z).$$

and corresponding to the eigenvalues are given by

$$R_{e0}^{(n)} = \frac{\left(n^2\pi^2+\mathrm{k}^2\right)^3}{Da\ \mathrm{k}^4} - \frac{R_a(n^2\pi^2+\mathrm{k}^2)}{\mathrm{k}^2} + \frac{M_a\left(n^2\pi^2+\mathrm{k}^2\right)^2}{\mathrm{k}^2} + \frac{Da\ T_a\, n^2\pi^2(n^2\pi^2+\mathrm{k}^2)^2}{\mathrm{k}^4}. \quad (42)$$

The least eigenvalue for a fixed wave number k , when $n = 1$, is obtained:

$$R_{e0} = \frac{\left(\pi^2+\mathrm{k}^2\right)^3}{Da\ \mathrm{k}^4} - \frac{R_a\left(\pi^2+\mathrm{k}^2\right)}{\mathrm{k}^2} + \frac{M_a\left(\pi^2+\mathrm{k}^2\right)^2}{\mathrm{k}^2} + \frac{Da\ T_a\,\pi^2(\pi^2+\mathrm{k}^2)^2}{\mathrm{k}^4} \quad (43)$$

Suppose the minimum value R_{e0} is R_{e0c}, when $\mathrm{k} = \mathrm{k}_c$ satisfies the equation

$$\left(k_c^{\,2}\right)^3 - \pi^2\left(3\pi^2 - R_a\,Da + M_a\,Da\,\pi^2 - 2(Da)^2\,T_a\,\pi^2\right)\mathrm{k}_c^{\,2} - 2\pi^6\left(1-(Da)^2\,T_a\right) + M_a\,Da\left(\mathrm{k}_c^{\,2}\right)^3 = 0. \tag{44}$$

Following studies of [1], R_e should be independent of the powers of η_3, i.e., $R_{e1} = R_{e3} = 0$ in Eq. (38).

The expression (40) becomes

$$L\,T_1 = 2\,R_{e0}\,\mathrm{k}^4\cos\omega t\left(\frac{1}{\delta A P_r}\frac{\partial}{\partial t} + \frac{1}{Da}\right)T_0 - \frac{2R_{e0}\,\mathrm{k}^4\,\omega}{\delta\,A\,p_r}\sin\omega t\,T_0. \tag{45}$$

Now from Eq. (45), we have

$$T_1 = 2R_{e0}\,\mathrm{k}^4\,\mathrm{Re}\left(\left(\frac{1}{\delta A P_r}\frac{\partial}{\partial t} + \frac{1}{Da}\right)\frac{\sin\pi z}{L(\omega,n)}e^{-i\omega t}\right), \tag{46}$$

It follows that

$$L\sin(n\pi z)e^{-i\omega t} = L(\omega,n)\sin(n\pi z)e^{-i\omega t}, \tag{47}$$

We now define $L(\omega,n) = D1 - i\omega D2$ (48)

Now, from Eq. (41), we have

$$L\,T_2 = R_{e0}\,\mathrm{k}^4\frac{\cos^2\omega t}{Da}\cos^2\omega t\;T_0 + 2\,R_{e0}\,\mathrm{k}^4\cos\omega t\left(\frac{1}{\delta A P_r}\frac{\partial}{\partial t} + \frac{1}{Da}\right)T_1 + R_{e2}\,\mathrm{k}^4\left(\frac{1}{\delta A P_r}\frac{\partial}{\partial t} + \frac{1}{Da}\right)T_0 - \frac{R_{e0}\,\mathrm{k}^4\,\omega}{\delta AP}\sin 2\omega t\,T_0 - \frac{2R_{e0}\,\mathrm{k}^4\,\omega}{\delta AP}\sin\omega t\,T_1. \tag{49}$$

The solubility condition requires that the steady part of the right hand side should be orthogonal to $\sin(\pi z)$. Hence

$$R_{e2} = -R_{e0}\left(\overline{\cos^2\omega t} + 4Da\int_0^1\overline{\left(\frac{1}{\delta A P_r}\frac{\partial}{\partial t} + \frac{1}{Da}\right)(\cos\omega t\,T_1)}\sin\pi z\,dz - \frac{\omega\,Da}{\delta AP}\,\overline{\sin 2\omega t}\right), \tag{50}$$

Where the bar denotes a time average of the quantities

Substituting Eqs. (45) and (46) in Eq. (50), we obtain

$$R_{e2} = -R_{e0}\left(\frac{1}{2} + R_{e0}\,Da\;\mathrm{k}^4\left(\frac{-\omega^2}{\delta^2A^2P_r^{\,2}} + \frac{1}{(Da)^2}\right)\frac{\left\{L(\omega,n) + L^{\otimes}(\omega,n)\right\}}{\left|L(\omega,n)\right|^2}\right). \tag{51}$$

where the superscript $^{\otimes}$ denotes the complex conjugate.

IV. RESULTS AND DISCUSSION

In this section, The Rayleigh number R_e is evaluated up to $\mathrm{O}\left(\eta_3^{\,2}\right)$ by the expression $R_e = R_{e0} + \eta_3^2 R_{e2}$, here we note that R_{e0} and R_{e2} are taken from the expressions (43) and (51) respectively and calculated at $\mathrm{k} = \mathrm{k}_c$. The correction electric Rayleigh number R_{e2} as a function of the frequency of electric modulation ω is

computed using MATHEMATICA for different physical parameters of Hartmann number M_a, Prandtl number P_r, Darcy number Da. Taylor number T_a. The effect of these parameters on the stability of the system is examined and is shown in the figures 2, 3 and 4.

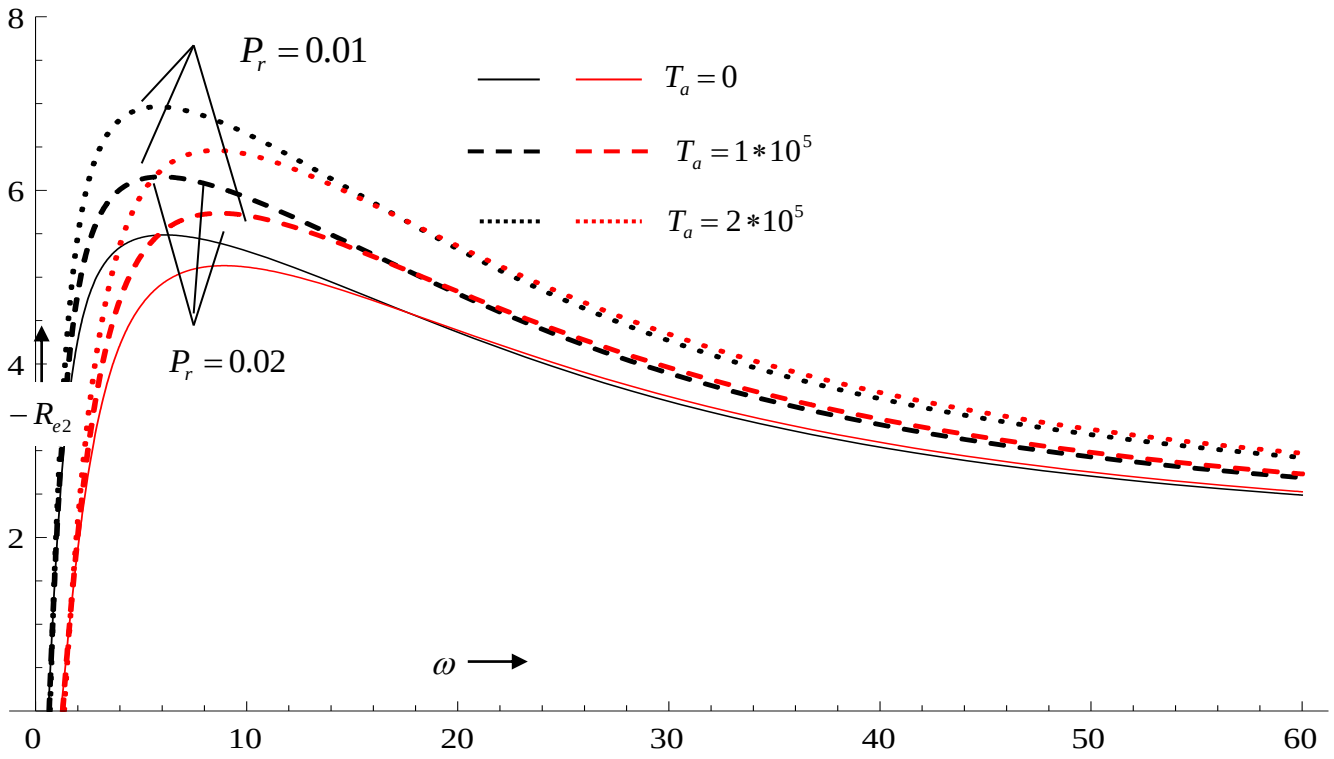

Fig. 2. R_{e2} **versus** ω **for various values of** T_a **and** P_r **with fixed values of** $D_a = 10^{-3}$, $M_a = 50$ **and** $R_a = 2*10^4$.

Fig. 2 is a plot of the correction $-R_{e2}$ with ω for various estimations of T_a and P_r while $D_a = 10^{-3}$, $M_a = 50$ and $R_a = 2*10^4$ are fixed, This figure demonstrates that $-R_{e2}$ increases as Taylor number T_a increases indicating that the effect of rotation is to stabilize the onset of Magnetoelectroconvection for the given frequency ω. However, the effect of T_a disappears for fairly large estimations of ω, in which $-R_{e2} \to 0$.

We can also observe form this figure that the value of $-R_{e2}$ decreases as P_r increases. Hence P_r reduces the destabilizing effect on the system of electric modulation for ω

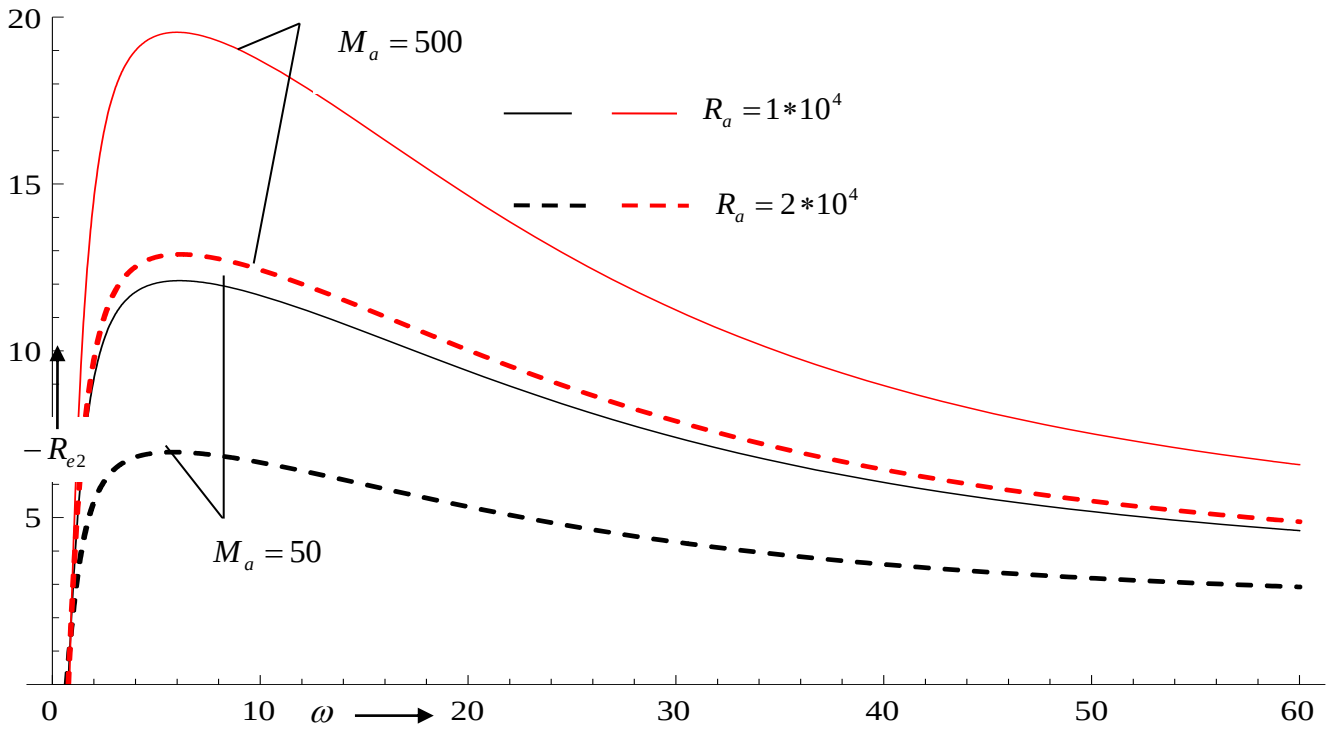

Fig. 3. R_{e2} **versus** ω **for various values of** M_a **and** R_a **with fixed values of** $D_a = 10^{-3}$, $T_a = 2*10^5$ **and** $P_r = 0.01$.

Fig. 3 is the plot of Rayleigh number R_{a2} with modulation frequency ω for several estimations of R_a and M_a with fixed $D_a = 10^{-3}$, $P_r = 0.01$ an $T_a = 2*10^5$. It is found that for the given frequency ω, $-R_{e2}$ decreases as thermal Rayleighnumber R_a increases. Thus the effect of R_a reduces the destabilizing system.

Further, it is also observed that for a given ω, $-R_{e2}$ increases as increases in the value of Hartmann number M_a. Hence the effect of magnetic field on the system is to augment Magnetoelectroconvection.

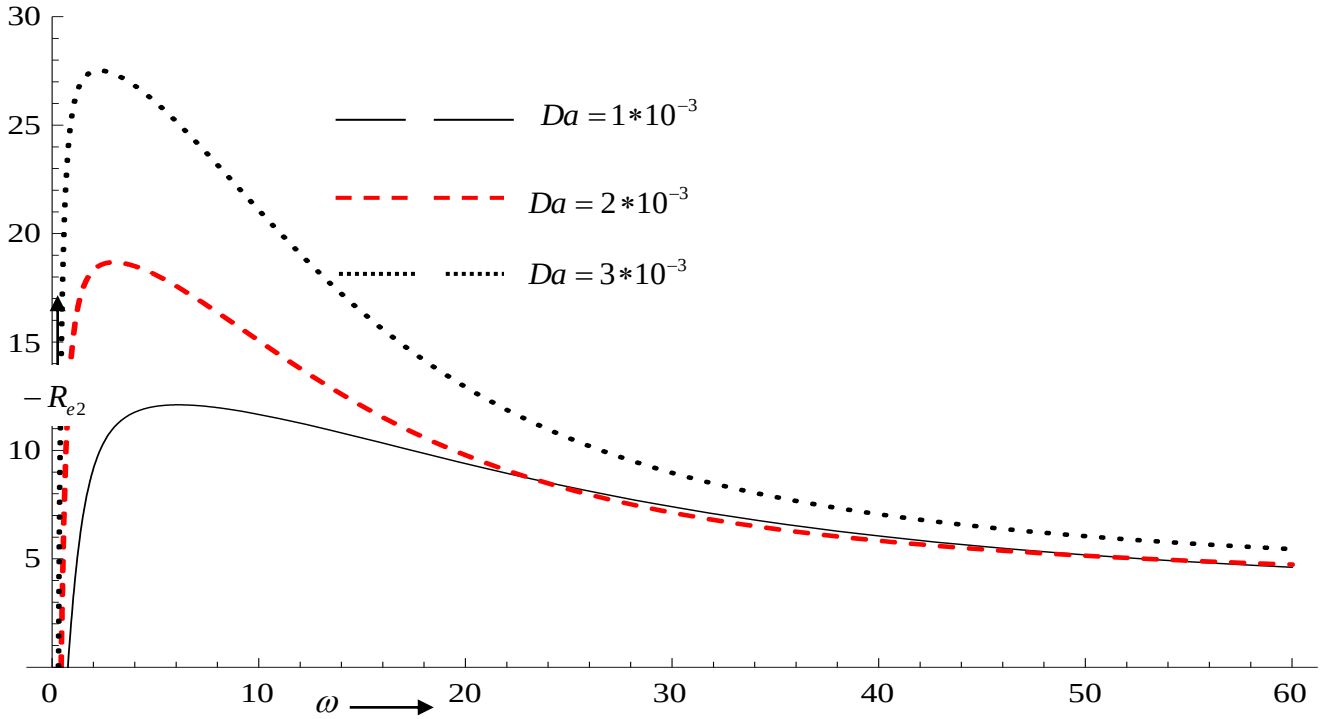

Fig. 4. R_{e2} **versus** ω **for various values of** Da **with fixed values of** $R_a = 1*10^4$, $T_a = 2*10^5$, $M_a = 50$ **and** $P_r = 0.01$.

Fig. 4 presents the effect of D_a on $-R_{e2}$, for fixed $P_r = 0.01$, $T_a = 2*10^5$, $R_a = 1*10^4$ and $M_a = 50$. From this figure for a given ω, $-R_{e2}$ increases as Darcy number D_a increases. Hence the effect of D_a is to advance the onset of Magnetoelectroconvection.

V. CONCLUSION

The effects on the Onset of Magnetoelectroconvection in a dielectric fluid saturated horizontal porous medium in the presence of magnetic field, uniform temperature, alternating electric field is studied in this paper. It is observed that the effect of T_a is to stabilize the system for the given value of frequency ω. It is also observed that the effect of Prandtl number P_r and thermal Rayleigh number R_a reduces the destabilizing effect on the system. The effect of Darcy number Da is to advance the onset of Magnetoelectroconvection the system. Further, we conclude that the effect of magnetic field M_a on the system is to augment Magnetoelectroconvection.

ACKNOWLEDGMENTS

The authors would like to acknowledge the BMS College of Engineering, Ramaiah Institute of Technology and East Point College of Engineering and Technology, Bengaluru, for giving their help to complete this exploration work.

Appendix

$$Da=\frac{K}{h^2},\ R_a=\frac{\alpha g\Delta T h^3}{\nu\chi},\ R_e=\frac{4\eta^2\varepsilon_m\Delta T^2U^2\eta_1^{\,2}}{\rho_0\nu\chi},\ P_r=\frac{\nu}{\chi},\ M_a=B_0h\sqrt{\frac{\sigma}{\rho_0\nu}}$$

$$T_a=\frac{4\overline{\Omega}^2h^4}{\delta^2\nu^2},\quad \mathrm{P}=\frac{p}{\rho_0}-E^2\frac{\partial\varepsilon}{\partial\rho},\quad A=\frac{(\rho C_p)_m}{(\rho C_p)_f},\quad \vec{J}=\sigma(\vec{q}\times\vec{B})$$

$$L=\begin{bmatrix}\left(\frac{1}{\delta AP_r}\frac{\partial}{\partial t}+\frac{1}{Da}\right)^2\left(\frac{\partial}{\partial t}-\left(D^2-\mathrm{k}^2\right)\right)\left(D^2-\mathrm{k}^2\right)^2+R_a\mathrm{k}^2\left(\frac{1}{\delta AP_r}\frac{\partial}{\partial t}+\frac{1}{Da}\right)\left(D^2-\mathrm{k}^2\right)\\ -R_{e0}\mathrm{k}^4\left(\frac{1}{\delta AP_r}\frac{\partial}{\partial t}+\frac{1}{Da}\right)-M_a\mathrm{k}^2\left(\frac{1}{\delta AP_r}\frac{\partial}{\partial t}+\frac{1}{Da}\right)\left(\frac{\partial}{\partial t}-\left(D^2-\mathrm{k}^2\right)\right)\left(D^2-\mathrm{k}^2\right)\\ +T_aD^2\left(\frac{\partial}{\partial t}-\left(D^2-\mathrm{k}^2\right)\right)\left(D^2-\mathrm{k}^2\right)\end{bmatrix}$$

$$D1=\begin{bmatrix}\left(\frac{-\omega^2}{\delta^2A^2P_r^{\,2}}+\frac{1}{(Da)^2}\right)\left(n^2\pi^2+\mathrm{k}^2\right)^3-\frac{2\omega^2\left(n^2\pi^2+\mathrm{k}^2\right)^2}{\delta AP_rD_a}+T_an^2\pi^2\left(n^2\pi^2+\mathrm{k}^2\right)^2\\ -\frac{R_a\mathrm{k}^2\left(n^2\pi^2+\mathrm{k}^2\right)}{D_a}+M_a\mathrm{k}^2\left(\frac{-\omega^2}{\delta AP_r}+\frac{\left(n^2\pi^2+\mathrm{k}^2\right)}{D_a}\right)\left(n^2\pi^2+\mathrm{k}^2\right)-\frac{R_{e0}\,\mathrm{k}^4}{D_a}\end{bmatrix}$$

$$D2=\begin{bmatrix}\left(\frac{-\omega^2}{\delta^2A^2P_r^{\,2}}+\frac{1}{(Da)^2}\right)\left(n^2\pi^2+\mathrm{k}^2\right)^2+\frac{2\left(n^2\pi^2+\mathrm{k}^2\right)^3}{\delta AP_rD_a}+T_an^2\pi^2\left(n^2\pi^2+\mathrm{k}^2\right)\\ -\frac{R_{e0}\,\mathrm{k}^4}{\delta AP_r}+M_a\mathrm{k}^2\left(\frac{\left(n^2\pi^2+\mathrm{k}^2\right)}{\delta AP_r}+\frac{1}{D_a}\right)\left(n^2\pi^2+\mathrm{k}^2\right)-\frac{R_a\,\mathrm{k}^2}{\delta AP_r}\left(n^2\pi^2+\mathrm{k}^2\right)\end{bmatrix}$$

VI. REFERENCES

[1]. G. Venezian, Effect of Modulation on the onset of Thermal Convection, J. Fluid Mech., 35, (1969) 243.

[2]. Lapwood E R. Convection of a Fluid in a Porous Medium. Pro. Cambridge philos. soc, 1948, 44: 508-521.

[3]. Roberts P H. Electrohydrodynamic Convection Q J Mech Appl Math, 1969, 22: 211-220

[4]. Chandrasekhar S. Hydrodynamic and hydromagnetic Stability. Oxford, Clarendon Press, 1961

[5]. Rudraiah N, Chandana O P. Effects of Coriolis force and Non-uniform Temperature Gradient on Rayleigh Benard Convection. Can J Phys, 1985, 64(11): 90

[6]. Rudraiah.N, Chandana O P. Surface tension driven convection subjected to rotation and Non-uniform Temperature Gradient. Mausam, 1986, 37(1): 39

[7]. Rudraiah N, Ramachandra murthy.: Effects of Coriolis force and Non-uniform Temperature Gradient on Benard-Marangoni instability. Acta Mechanics, 1986, 61

[8]. Char M I and Chiang K T. Boundary effects on the Benard –Marangoni instability under an electric field.Applied Sci. Res, 1994, 52(4): 331-354

[9]. R.J. Turnbull.:Electro convective instability with a stabilizing temperature gradient. I. Theory physics of Fluid, 1968, 11:2588-2596

[10]. R.J. Turnbull:Effect of dielectrophoretic forces on the Benard instability. Theory phys, of Fluid, 1969, 12:1809-1815

[11]. B.L. Smorodin and M.G. Velarde, Electric thermo-convective instability of an ohmic liquid layer under unsteady electric field, J. Electrostat.48 (2000) 261.

[12]. PalmE, TyvandP A.Thermal convection in a rotating porous layer. J. Appl Math and Phys (ZAMP), 1984, 35, 122-131.

[13]. Jou J J, Liaw J S. Thermal convection in a porous medium subject to transient heating and rotation. Int J Heat Mass Tranfer, (1987a,b), 30: 208

[14]. Qin Y, Kaloni P N. Non-linear stability problem of a rotating porous layer. quartely of Appl Math,1995, 53(1): 129

[15]. Veronis G.Motions at sub critical values of the Rayleigh number in a rotating fluid. J Fluid Mech., 1966, 24: 545

[16]. Chandrasekhar S. Hydrodynamic and hydromagnetic Stability, Dover. New York, 1981

[17]. MalashettyM S, Mahantesh Swamy.The combined effect of thermal modulation and rotation onset of stationary convection in a porous layer. Trans. Porous Medium, 2007, 69: 313-330

[18]. Malashetty M S, Mahantesh Swamy. Effect of thermal modulation on the onset of convection in a rotating fluid layer. Int J Heat and Mass Transfer, 2008, 51: 2814-2823

[19]. Gaikwad S N, Irfana Begum. Effect of thermal modulation and rotation on the onset of convection in a Walters B fluid saturated porous medium. International journal of mathematical Archive, 2012, 3(4): 1649-1659

[20]. Shivakumara I S,Akkanagamma, Chiu-on Ng. Effect of horizontal AC electric field on the stability of natural convection in a vertical dielectricfluid layer. Journal of applied fluidmehanics, 2016, 9(6): 3073-3086.

[21]. Shivakumara I S,Akkanagamma, Chiu-on Ng. The onset of electrothermoconvection in a rotating Brinkman porous layer. Int J of engineering science , 2011, 49: 646-663

[22]. Shivakumara I S,Akkanagamma, Chiu-on Ng. Electrodynamics instability of a rotating couple stress dielectricfluid layer. Int J Heat Mass Transfer , 2013, 62: 761-771

[23]. Rudraiah. N; Gayathri, M.S.: Effectof thermal modulation on the onset of electro Thermo convection in a dielectric fluid saturated porous medium, J. Heat Transfer. ASME, vol.131 (2009)101009(1-7)

[24]. Gayathri M. S., Chandra Shekara G and Sujatha N: Onset of electrothermoconvection in a Dielectric fluid saturated porous medium in a Modulated electric field, international conference on Computational Heat and Mass Transfer 127 (2015) 835-845.

[25]. Gayathri M.S, Dinesh P.A, Rangaraju B.V and Rushi kumar B. The onset of Magneto-electroconvection in a dielectric fluid saturated porous medium, International Journal of Special Topics and Reviews in porous Media, 2018, 9(2), 133-144.

[26]. Gayathri M.S, Dinesh P.A, Rangaraju B.V, Dooresway H. Effects of Thermal Modulation and rotation in a porous medium saturated by a dielectric fluid on the onset of Magneto-electrothermoconvection, International Research Journal of Bulletin of mathematic and Statistics Research, 2018, 6(4), 18-34, ISSN: 2348-0580.

[27]. Rana G C, Jamwal H S.:Effect of rotation on the onset of compressible viscoelastic fluid saturating a Darcy-Brinkman porous medium. Engineering mechanics, 2012, 19: 445-455

[28]. Rana.G C, Chand R. On the onset of thermal convection in rotating nanofluid layer saturating aDarcy-Brinkman porous medium. Int J Heat Mass Transfer, 2012, 55: 5417-5424

[29]. Rana G C, Kango S K, Kumar. Effect of rotation on the onset of convection in Walters B (model B) heated from below in a Brinkman porous medium. JPorous Media 2012, 15: 1149-1153

[30]. Rana G C, Chand R, Sharma: The effect of rotation on the onset electrodynamics instabilityof elastico-viscous di electric fluid layer. Bullpol Ac: Tech Sc, 2016, 64(1): 143-149

[31]. Ruo A C, Chang M H, Chen F.:Effect of rotation on the onset of electro hydrodynamic instability of a fluid layer with an electrical conductivity gradient. Physics of Fluids, 2010, 22:024102.1-024102.11

National Conference on Applied Sciences Synergising the Engineering and Technology
Print ISSN: 2395-6011 | Online ISSN: 2395-602X (www.ijsrst.com)
© 2021 IJSRST | Volume 8 | Issue 2

Forgotten Topological Index and Revan Indices of Cayley Tree, Silicate Layer and Molybdenum Disulphide

Raghu M Bankar[1], Manjula G J[2], M A Sriraj[3], Kavitha G N[4]

[1,2,4]Department of Mathematics, Siddaganaga Institute of Technology, Tumakuru, India

[3]Department of Mathematics, Vidyavardhaka College of Engineering, Mysuru, India

ABSTRACT

A topological index is a real number derived from a graph. In 2015, The forgotten topological index was introduced by Furtula and Gutman and in 2017, Kulli has introduced Revan indices. In this paper we compute the forgotten topological index, first, second and third Revan indices of Cayley tree, silicate layer and molybdenum disulfide nanostructure.

Keywords : Forgotten Topological Index, Revan Indices, Cayley Tree, Silicate Layer and Molybdenum Disulfide.

I. INTRODUCTION

In theoretical chemistry topological indices are used for studying the physical, biological properties of the chemical compounds and they are used to predict certain physicochemical properties like boiling point, stability, enthalpy of vaporization and so forth [2][3][4]. There are certain types of topological indices such as degree based topological indices, distance based topological indices and counting related topological indices etc. Consider a graph G which is a finite, simple and connected with vertex set V(G) and edge set E(G). The degree d_v of a vertex v is the number of vertices adjacent to v. For additional definitions and notations, the reader may refer to [1].

In 2015, Furtula and Gutman [5] introduced Forgotten topological index (or, F-index) which is stated as

$$F(G) = \sum_{v\in V(G)}(d_v)^3 = \sum_{uv\in E(G)}[(d_u)^2 + (d_v)^2] \qquad (1)$$

In 2017, Kulli [6] defined a novel degree concept in graph theory: The Revan vertex degree of a vertex v in G is defined as $r_G(v) = \Delta(G) + \delta(G) - d_v$. The first, second and third Revan indices were defined as

$$R_1(G) = \sum_{uv\in E(G)}[r_G(u) + r_G(v)] \qquad (2)$$
$$R_2(G) = \sum_{uv\in E(G)} r_G(u).r_G(v) \qquad (3)$$
$$R_3(G) = \sum_{uv\in E(G)}|r_G(u) - r_G(v)| \qquad (4)$$

To derive the topological index for a chemical compound first their topological representation called molecular graph must be derived. A molecular graph is a collection of points representing the atoms in the molecule and set of lines representing the covalent bonds. These points are named vertices and the lines are named edges in graph theory language. Once the molecular graph is defined the edge partition table of the graph (sometimes degree partition may also be required) should be computed. The edge partition is nothing, but the classification of the edges based on the degree of the vertices they connect. The edge partition table gives the number of edges corresponding to each type of edge. The index is then computed based on the formula defined for that particular index.

II. MATERIALS AND METHODS

The Cayley Tree Γ^k:

The Cayley tree Γ^k of order $k \geq 1$ is an infinite and symmetric regular tree, that is, a graph without cycles, from each vertex of which exactly k + 1 edges are issued. In this paper, we consider the Cayley tree $\Gamma_n^2 = (V, E, i)$ of order 2 and with n levels from the root x_0, where V is the set of vertices of Γ_n^2, E is the set of edges of Γ_n^2, and 'i' is the incidence function associating each edge $e \in E$ with its end vertices.

It is easy to compute the number of vertices reachable in step n or in level n starting from the root x_0, which is $|W_n| = 3.2^{(n-1)}$. The number of vertices of Γ_n^2 is $|V_n| = 1 + 3(2^n - 1)$, and the number of edges of Γ_n^2 is $|E_n| = 3(2^n - 1)$, as is shown in Figure 1 below.

Silicate Layer:

Silicates are obtained by fusing metal oxides or metal carbonates with sand. A silicate network in symbolized by SL_n where n is the number of hexagons between the centre and boundary of SL_n. A 2-dimensional silicate layer network is shown in Fig 2.

Molybdenum disulphide:

The MoS_2 (Molybdenum disulphide) is an inorganic compound with layered structure where a plane of Molybdenum atoms is sandwiched by planes of sulphide ions. As it has a low friction and robustness, it is used as a lubricant and it is also used as co-catalyst. Schematic representation of side view of a monolayer of is given in fig. 3. The layered structure makes it to be used as lubricant, capable of handling shear stress.

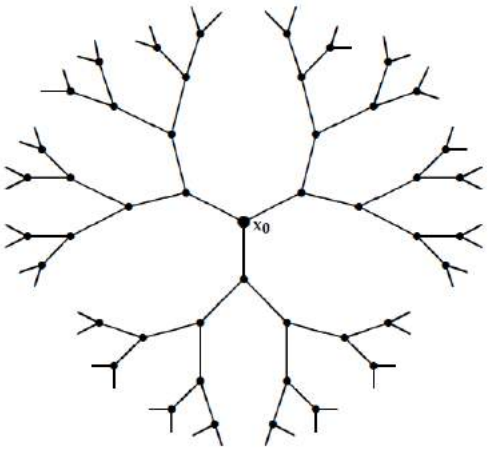

Fig 1: Cayley tree Γ_n^2 of order 2 with n levels, where $n \geq 1$.

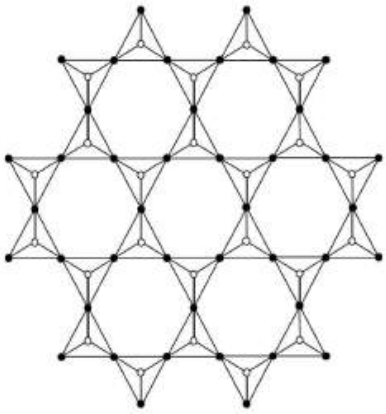

Fig 2: A two-dimensional silicate network.

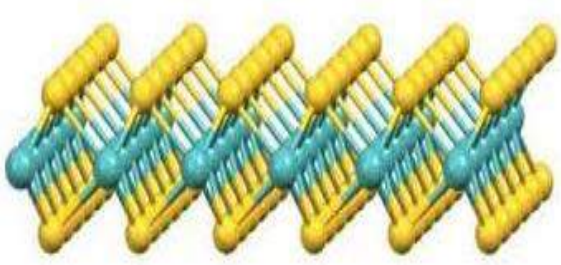

Fig 3: Schematic representation of side view of a monolayer of MoS_2

III. RESULTS AND DISCUSSION

Referring to Fig 1, there are two types of edges in Γ_n^2 on the basis of the degrees of the end vertices of each edge, as follows: the first type, for $e = uv \in E(\Gamma_n^2)$, is such that $d_u = 1$ and $d_v = 3$; the other type is, for $e = uv \in E(\Gamma_n^2)$, is such that $d_u = d_v = 3$. In the first type, there are 3.2^{n-1} edges, and in the other type, there are $3(2^{n-1} - 1)$ edges, as is shown in Table 1. The edge partition of Γ_n^2 on the basis of revan vertex degrees of end vertices is shown TABLE 2.

TABLE 1: Edge partition of Γ_n^2 on the basis of degrees of end vertices of each edge.

(d_u, d_v) where $uv \in E(\Gamma_n^2)$	Number of Edges
(1,3)	3.2^{n-1}
(3,3)	$3(2^{n-1}-1)$

TABLE 2: Edge partition of Γ_n^2 on the basis of revan vertex degrees of end vertices of each edge.

(d_u, d_v) where $uv \in E(\Gamma_n^2)$	$r_G(u)$	$r_G(u)$	Number of Edges
(1,3)	3	1	3.2^{n-1}
(3,3)	1	1	$3(2^{n-1}-1)$

TABLE 3: Edge partition of SL_n on the basis of degrees of end vertices of each edge.

(d_u, d_v) where $uv \in E(SL_n)$	Number of Edges
(3,3)	$6n$
(3,6)	$18n^2+6n$
(6,6)	$18n^2-12n$

TABLE 4: Edge partition of SL_n on the basis of revan vertex degrees of end vertices of each edge.

(d_u, d_v) where $uv \in E(SL_n)$	$r_G(u)$	$r_G(u)$	Number of Edges
(3,3)	6	6	$6n$
(3,6)	6	3	$18n^2+6n$
(6,6)	3	3	$18n^2-12n$

In SL_n, by algebraic method, there are three types of edges based on the degree of the vertices of each edge as follows: the first type, for $e = uv \in E(SL_n)$, is such that $d_u = d_v = 3$; the second type, for $e = uv \in E(SL_n)$, is such that $d_u = 3 \; and \; d_v = 6$; the third type, for $e = uv \in E(SL_n)$, is such that $d_u = d_v = 6$. In the first type, there are $6n$ edges, In the second type, there are $18n^2 + 6n$ edges and in the third type, there are $18n^2 - 12n$ edges as shown in TABLE 3. The Edge partition of SL_n on the basis of revan vertex degrees of end vertices is shown in TABLE 4.

There are three types of edges in MoS_2, one connecting vertex with degree two to another vertex with degree two, second type of edge connects vertex with degree two to vertex with degree four and the third type of vertex connects vertex with degree four to vertex with degree four. The number of edges for each type of edges for MoS_2 is given in the TABLE 5. The Edge partition of MoS_2 on the basis of revan vertex degrees of end vertices is shown in TABLE 6.

TABLE 5: Edge partition of MoS_2 on the basis of degrees of end vertices of each edge.

(d_u, d_v) where $uv \in E(MoS_2)$	Number of Edges
(2,2)	4
(2,4)	$4p + 4q - 8$
(4,4)	$4pq - 4p - 4q + 4$

TABLE 6: Edge partition of MoS_2 on the basis of revan vertex degrees of end vertices of each edge.

(d_u, d_v) where $uv \in E(MoS_2)$	$r_G(u)$	$r_G(u)$	Number of Edges
(2,2)	4	4	4
(2,4)	4	2	$4p + 4q - 8$
(4,4)	2	2	$4pq - 4p - 4q + 4$

Theorem 1: The Forgotten topological index of Cayley tree, Silicate layer network and molybdenum disulphide are: i. $F(\Gamma_n^2) = 21.2^{n+1} - 54$.

ii. $F(SL_n) = 2106n^2 - 486n$

iii. $F(MoS_2) = 128pq - 48(p + q)$

Proof:

i. Using (1) and TABLE 1, we get

$F(\Gamma_n^2) = 3.2^{n-1}(1^2 + 3^2) + 3(2^{n-1} - 1)(3^2 + 3^2)$ $F(\Gamma_n^2) = 21.2^{n+1} - 54$

ii. Using (1) and TABLE 3, we get

$$F(SL_n) = 6n(3^2 + 3^2) + (18n^2 + 6n)(3^2 + 6^2) + (18n^2 - 12n)(6^2 + 6^2)$$

$F(SL_n) = 2106n^2 - 486n$

iii. Using (1) and TABLE 5, we get

$$F(MoS_2) = 4(2^2 + 2^2) + (4p + 4q - 8)(2^2 + 4^2) + (4pq - 4p - 4q + 4)(4^2 + 4^2)$$

$F(MoS_2) = 128pq - 48(p + q)$

Theorem 2: The first, second and third revan indices of Cayley tree Γ_n^2 are:

i. $R_1(\Gamma_n^2) = 9.2^n - 6$

ii. $R_2(\Gamma_n^2) = 21.2^n - 3$

iii. $R_3(\Gamma_n^2) = 3.2^n$.

Proof:

i. Using (2) and TABLE 2 we get

$R_1(\Gamma_n^2) = 3.2^{n-1}(3 + 1) + 3(2^{n-1} - 1)(1 + 1)$

$R_1(\Gamma_n^2) = 9.2^n - 6$.

ii. Using (3) and TABLE 2 we get

$R_2(\Gamma_n^2) = 3.2^{n-1}(3.1) + 3(2^{n-1} - 1)(1.1)$

$R_2(\Gamma_n^2) = 21.2^{n-1} - 3.$

iii. Using (4) and TABLE 2 we get

$R_3(\Gamma_n^2) = 3.2^{n-1}|3 - 1| + 3(2^{n-1} - 1)|1 - 1|$

$R_3(\Gamma_n^2) = 3.2^{n+1}.$

Theorem 3: The first, second and third revan indices of Silicate layer network SL_n are:

i. $R_1(SL_n) = 270n^2 + 54n$

ii. $R_2(SL_n) = 486n^2 + 216n$

iii. $R_3(SL_n) = 54n^2 + 18n.$

Proof:

i. Using (2) and TABLE 4 we get

$R_1(SL_n) = 6n(6 + 6) + (18n^2 + 6n)(6 + 3) + (18n^2 - 12n)(3 + 3)$

$R_1(SL_n) = 270n^2 + 54n$.

ii. Using (3) and TABLE 4 we get

$R_2(SL_n) = 6n(6.6) + (18n^2 + 6n)(6.3) + (18n^2 - 12n)(3.3)$

$R_2(SL_n) = 486n^2 + 216n.$

iii. Using (4) and TABLE 4 we get

$R_3(SL_n) = 6n|6 - 6| + (18n^2 + 6n)|6 - 3| + (18n^2 - 12n)|3 - 3|$

$R_3(SL_n) = 54n^2 + 18n.$

Theorem 4: The first, second and third revan indices of Molybdenum disulphide MoS_2 are:

i. $R_1(MoS_2) = 16pq + 8p + 8q$

ii. $R_2(MoS_2) = 16pq + 16p + 16q + 16$

iii. $R_3(MoS_2) = 8p + 8q - 16.$

Proof:

i. Using (2) and TABLE 4 we get

$R_1(MoS_2) = 4(4 + 4) + (4p + 4q - 8)(4 + 2) + (4pq - 4p - 4q + 4)(2 + 2)$

$R_1(MoS_2) = 16pq + 8p + 8q$.

ii. Using (3) and TABLE 4 we get

$R_2(MoS_2) = 4(4.4) + (4p + 4q - 8)(4.2) + (4pq - 4p - 4q + 4)(2.2)$

$R_2(MoS_2) = 16pq + 16p + 16q + 16.$

iii. Using (4) and TABLE 4 we get

$R_3(MoS_2) = 4|4 - 4| + (4p + 4q - 8)|4 - 2| + (4pq - 4p - 4q + 4)|2 - 2|$

$$R_3(MoS_2) = 8p + 8q - 16.$$

IV. CONCLUSION

In this paper, certain degree-based topological indices, namely, the Forgotten topological index, first, second and third Revan indices are studied. We have determined and computed these indices for Cayley tree, Silicate layer network and molybdenum disulphide nano material. These results are novel and significant contributions in graph theory and network science, and they provide a good basis to understand the topology of these graphs and networks.

V. REFERENCES

[1] F. HARARY, "Graph Theory", Addison-Wesley, 1969.
[2] I.Gutman and N.Trinajstic, "Graph theory and molecular orbitals, Total -electron energy of alternant hydrocarbons" ,Chem. Phys. Lett., vol. 17, pp. 535-538, 1972.
[3] I.Gutman and O.E.Polansky, "Mathematical Concepts in Organic Chemistry", Springer, Berlin, 1986.
[4] R.Todeschini and V.Consonni, "Molecular Descriptors for Chemoinformatics", Wiley-VCH, Weinheim, 2009.
[5] B. Furtula, I. Gutman, "A forgotten topological index", Journal of Mathematical Chemistry, vol. 53(4), pp. 1184-1190, 2015.
[6] V.R. Kulli, "Revan Indices of Oxide and Honeycomb Networks", International Journal of Mathematics And its Applications, vol. 5, pp. 663–667, 2017.

National Conference on Applied Sciences Synergising the Engineering and Technology
Print ISSN: 2395-6011 | Online ISSN: 2395-602X (www.ijsrst.com)
© 2021 IJSRST | Volume 8 | Issue 2

Convection-Diffusion in Unsteady Non-Newtonian Fluid Flow in a Channel with Wall Absorption and Porous Boundaries

G J Manjula[1], M Sankar[2]

[1]Department of Mathematics, Siddaganga Institute of Technology, Tumkur, India

[2]Department of Mathematics School of Engineering, Presidency University, Itgalpura Rajanukunte, Yelahanka, India

ABSTRACT

Exact analysis of miscible dispersion of solute with interphase mass transfer in a couple stress fluid flowing through a rectangular channel bounded by porous beds is considered because of its application in many practical situations. Blood consists of a Newtonian fluid called plasma in which are suspended white blood cells, red blood cells, platelets and other micron sized suspensions. The suspensions spin relative to the plasma and thus necessitate the consideration of conservation of angular momentum in addition to the conservation of linear momentum. Therefore, it is appropriate to model blood as a couple stress fluid. Transport of dissolved gases like oxygen, carbon dioxide and nutrients in blood through walls of the capillaries involve a first order chemical reaction. In order to understand this, a first order chemical reaction at the walls is considered. The generalized dispersion model of Sankar Subramanian and Gill is used, which brings into focus the exchange coefficient, the convective coefficient and the dispersion coefficient. The exchange coefficient comes into picture due to the interphase mass transfer and independence of solvent fluid viscosity. It is observed that the convective coefficient increases with an increase in the porous parameter, while it decreases with an increase in the couple stress parameter. The dispersion coefficient is plotted against the wall reaction parameter for different values of porous parameter and couple stress parameter. It is noted that the dispersion coefficient decreases with an increase in the value of the couple stress parameter but increases with porous parameter.

Keywords : Couple Stress, Porous Parameter, Generalized Dispersion

I. INTRODUCTION

In this paper, we have discussed generalized unsteady dispersion of solute in the presence of interphase mass transfer. In many biomedical problems the interphase mass transfer plays a significant role because many physiological situations involve interphase mass transfer. Therefore, it is necessary to develop a technique to handle problems, which involve interphase mass transport. Early works on dispersion were mainly concerned with Taylor's (1953) dispersion, which is valid for large time. Physiological fluid flow problems have been mainly concerned with transient phenomena where Taylor's model is not valid. However, Sankarasubramanian and Gill (1973) have developed analytical method to analyze transient dispersion of non-uniform initial distribution called generalized dispersion in laminar flow in a tube with a first order chemical reaction occurs at the tube wall. This method can be applied to physiological problems where a first order chemical reaction occurs at the tube wall. One such situation is transport of oxygen and nutrients to tissue cells and removal of

metabolic waste products from tissue cells. Interphase mass transfer also takes place in pulmonary capillaries where the carbon dioxide is removed from the blood and oxygen is taken up by the blood.

Blood mainly consists of plasma in which are the suspended micron sized white blood cells, red blood cells and platelets. The suspension of these particles has spin relative to the plasma and this necessitates the consideration of conservation of angular momentum in addition to the conservation of linear momentum. Stokes (1963) introduced a special type of such fluid called couple stress fluid, in which the spin matches with the vorticity. Rudraiah et al., (1986) studied the dispersion in a Stokes's couple-stress fluid flow by using the generalized dispersion model of Gill and Sankarasubramanian (1970). Their work is silent about considering solute reaction at the channel walls in their all time analysis of dispersion. Reaction at the walls is of practical interest and in the simplest case, a first order chemical reaction at the walls is considered by them in carrying out an exact analysis of unsteady convection in couple stress fluid flows. The corresponding problems for plane-poiseuille flows of micropolar; casson and Ostwald- de- Waele fluids have been investigated by Siddheshwar and Manjunath (1998). The problem for Hagen- Poiseuille flows of micropolar, couple stress, casson and Ostwald-de-Waele fluids have been investigated by Siddheshwar and Sripad (1998).

In this paper we present an exact analysis of miscible dispersion of solute with interphase mass transfer in a couple stress fluid bounded by porous beds. The generalized dispersion model of Sankarasubramanian and Gill (1973) has been used which brings in to focus the exchange coefficient K_0, convective coefficient K_1 and dispersion coefficient K_2. Only the last two coefficients (K_1, K_2) are influenced by the couple stress parameter arising due to suspension in the fluid and porous parameter. The exchange coefficient arises mainly due to the interphase mass transfer and is independent of the solvent fluid velocity. The interphase mass transfer also influences the convection and dispersion coefficients. Asymptotically, the large time evaluations have been carried out for all the three coefficients to get a feel of the nature of these coefficients.

Mathematical formulation

The physical configuration considered is same as the one given in fig. 1.

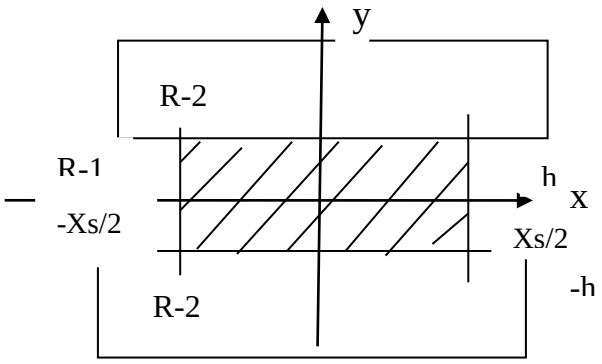

Fig. 1 Physical configuration

The governing basic equations are:

Region 1:

$$-\frac{\partial p}{\partial x}+\mu\frac{\partial^2 u}{\partial y^2}-\lambda\frac{\partial^4 u}{\partial y^4}=0, \tag{1.1}$$

$$-\frac{\partial p}{\partial y}=0\,. \tag{1.2}$$

Region 2:

$$-\frac{\partial p}{\partial x}-\frac{\mu}{k}(1+\beta_1)u_p=0 \tag{1.3}$$

$$-\frac{\partial p}{\partial y}=0 \tag{1.4}$$

In the above equations, u is the velocity in the x-direction, μ is the viscosity of the fluid, λ is the couple stress parameter, k is the permeability of the porous medium, u_p is the Darcy velocity and p is the pressure. Equation (1.3) is the modified Darcy equation and β_1 is the couple stress parameter. The boundary conditions on the velocity are given by

$$\frac{\partial u}{\partial y}=-\frac{\alpha}{\sqrt{k}}\left(u-u_p\right) \quad at\ y=h\,, \tag{1.5a}$$

$$\frac{\partial u}{\partial y}=\frac{\alpha}{\sqrt{k}}\left(u-u_p\right) \quad at\ y=-h\,, \tag{1.5b}$$

$$\frac{\partial^2 u}{\partial y^2}=0 \quad at\ y=\pm h\,, \tag{1.6}$$

where α is the slip parameter. Equations (1.5a, b) are the well-known Beavers and Joseph (1967) slip condition at the lower and upper permeable surfaces and (1.6) is the vanishing of the couple stress condition.
Non –dimensionalising these equations using $Y=\frac{y}{h}$ and rearranging, we get

Region -1:

$$\frac{d^4u}{dY^4}-a^2\frac{d^2u}{dY^2}=-\frac{h^2a^2}{\mu}\frac{dp}{dx}, \tag{1.7}$$

where $l=\sqrt{\lambda/\mu}$, $a=h/l$ is the couple stress parameter.

Region -2:

$$u_p=\frac{-k}{\mu\,(1+\beta_1)}\frac{\partial p}{\partial x}\,. \tag{1.8}$$

The boundary conditions now become

$$\frac{\partial U}{\partial \eta}=-\alpha\ \sigma\left(U-U_p\right) \quad at\ \ Y=1, \tag{1.9a}$$

$$\frac{\partial U}{\partial \eta}=\alpha\ \sigma\left(U-U_p\right) \quad at\ \ Y=-1, \tag{1.9b}$$

$$\frac{\partial^2 U}{\partial \eta^2}=0 \quad at\ \ Y=\pm 1. \tag{1.10}$$

where $\sigma=h/\sqrt{k}$ is the porous parameter. The solution of (1.7), satisfying the boundary conditions (1.9) and (1.10) is

$$u=\frac{-h^2}{2\mu}\frac{\partial p}{\partial x}\left(1-Y^2-\frac{2}{a^2}\left[1-\frac{cosh(aY)}{cosh\,a}\right]+A_0\right), \tag{1.11}$$

where

$$A_0=\frac{2}{\sigma^2(1+\beta_1)}-\frac{2}{\alpha\,\sigma}\left[\frac{\tanh a}{a}-1\right].$$

The average velocity $\bar{u}$ is given by

$$\bar{u} = \frac{1}{2}\int_{-1}^{1} u\, dY = \frac{-h^2}{2\mu}\frac{\partial p}{\partial x}\left[\frac{2}{3} - \frac{2}{a^2} + \frac{2}{a^2}\frac{\tanh a}{a} + A_0\right]. \tag{1.12}$$

II. DISPERSION MODEL

We consider the dispersion of reactive solute in the fully developed flow through a parallel channel bounded by porous beds. In to this flow is introduced a slug of concentration $C = C_0 f(x, y)$. The mass balance equation concerning the solute concentration C undergoing heterogeneous chemical reaction is

$$\frac{\partial C}{\partial t} + u\frac{\partial C}{\partial x} = D\left[\frac{\partial^2 C}{\partial x^2} + \frac{\partial^2 C}{\partial y^2}\right], \tag{2.1}$$

with the initial condition

$$C(0, x, y) = C_0 f(x, y), \tag{2.2a}$$

where C_0 is a reference concentration.

The heterogeneous reaction conditions are

$$-D\frac{\partial C}{\partial y}(t, x, h) = k_s C(t, x, h), \tag{2.2b}$$

$$D\frac{\partial C}{\partial y}(t, x, -h) = k_s C(t, x, -h), \tag{2.2c}$$

where k_s is the reaction rate constant catalyzed by the walls.

The away boundary conditions are

$$C(t, \infty, y) = \frac{\partial C}{\partial x}(t, \infty, y) = 0, \tag{2.2d}$$

and

$$C(t, x, y) = \text{finite}. \tag{2.2e}$$

We make (2.1) and (2.2) dimensionless using

$$U = \frac{u}{\bar{u}},\ Y = \frac{y}{h},\ X = \frac{x}{hPe},\ Pe = \frac{\bar{u}h}{D},\ \theta = \frac{C}{C_0},\ \tau = \frac{tD}{h^2} \text{ and } \beta = \frac{k_s h}{D}. \tag{2.3}$$

where Pe is the Peclet number and $\bar{u}$ is the average velocity. Substituting (2.3) in (2.1) and (2.2), we get

$$\frac{\partial \theta}{\partial \tau} + U\frac{\partial \theta}{\partial X} = \frac{1}{Pe^2}\frac{\partial^2 \theta}{\partial X^2} + \frac{\partial^2 \theta}{\partial Y^2} \tag{2.4}$$

and

$$\theta(0, X, Y) = \phi(X)\,\psi(Y), \tag{2.5a}$$

$$\frac{\partial \theta}{\partial Y}(\tau, X, 1) = -\beta\theta(\tau, X, 1), \tag{2.5b}$$

$$\frac{\partial \theta}{\partial Y}(\tau, X, -1) = \beta\theta(\tau, X, 1), \tag{2.5c}$$

$$\theta(\tau, \infty, Y) = \frac{\partial \theta}{\partial X}(\tau, \infty, Y) = 0, \tag{2.5d}$$

$$\theta(\tau, X, Y) = \text{finite}. \tag{2.5e}$$

Here the right-hand side of (2.5a) is the assumed form of the non-dimensional form of $f(x, y)$. The solution of (2.4), subject to the conditions (2.5), following Gill and Sankarasubramanian (1973), is

$$\theta(\tau,X,Y) = f_0(\tau,Y)\theta_m(\tau,X) + f_1(\tau,Y)\frac{\partial\theta_m}{\partial X}(\tau,X) + f_2(\tau,Y)\frac{\partial^2\theta_m}{\partial X^2}(\tau,X) + \ldots\ldots, \tag{2.6}$$

where θ_m is the dimensionless cross sectional average concentration and is given by

$$\theta_m(\tau,X) = \frac{1}{2}\int_{-1}^{1}\theta\, dY\,. \tag{2.7}$$

Equation (2.6) signifies that the difference between θ and its mean θ_m can be accounted by the convective and diffusive contributions. This is based on an observation by Taylor (1953).

Integrating (2.4) with respect to Y between -1 and 1 and using the definition of θ_m, we get

$$\frac{\partial\theta_m}{\partial\tau} = \frac{1}{Pe^2}\frac{\partial^2\theta_m}{\partial X^2} - \frac{1}{2}\frac{\partial f_0}{\partial y}\Big]_{-1}^{1} - \frac{\partial}{\partial X}\int_{-1}^{1}\frac{(1-Y^2-\frac{2}{a^2}(1-\frac{\cosh aY}{\cosh a})+A_0}{\left[\frac{2}{3}-\frac{2}{a^2}+\frac{2}{a^2}\frac{\tanh a}{a}+A_0\right]}\,\theta\, dY \tag{2.8}$$

On using (4.3.6) in (4.3.8), we get the dispersion model for θ_m as

$$\frac{\partial\theta_m}{\partial\tau} = K_0\theta_m + K_1\frac{\partial\theta_m}{\partial X} + K_2\frac{\partial^2\theta_m}{\partial X^2} + K_3\frac{\partial^3\theta_m}{\partial X^3} + \ldots., \tag{2.9}$$

where K_i's are given by

$$K_i(\tau) = \frac{\delta_{i2}}{Pe^2} - 2\frac{\partial f_i}{\partial Y}(\tau,1) - \frac{1}{2}\int_{-1}^{1}\frac{(1-Y^2-\frac{2}{a^2}(1-\frac{\cosh aY}{\cosh a})+A_0}{\left[\frac{2}{3}-\frac{2}{a^2}+\frac{2}{a^2}\frac{\tanh a}{a}+A_0\right]}\, f_{i-1}(\tau,Y)dY\,. \tag{2.10}$$

Here $f_{-1}= 0$ and δ_{i2} is the Kronecker delta.

The exchange coefficient $K_0(\tau)$ accounts for the non-zero solute flux at the channel wall and negative sign indicates the depletion of solute in the system with time caused by the irreversible reaction, which occurs at the channel wall. The presence of non-zero solute flux at the walls of the channel also affects the higher order K_i due to the explicit appearance of $\frac{\partial f_i}{\partial Y}(\tau,1)$ in (2.10). Equation (2.10) can be truncated after the terms involving K_2 without causing serious error because K_3, K_4 etc. become negligibly small compared to K_2. The resulting model for the mean concentration is

$$\frac{\partial\theta_m}{\partial\tau} = K_0(\tau)\theta_m + K_1(\tau)\frac{\partial\theta_m}{\partial X} + K_2(\tau)\frac{\partial^2\theta_m}{\partial X^2}\,. \tag{2.11}$$

Substituting (2.6) in (2.4) and using the generalized dispersion model of Shankarsubramanian and Gill (1973) in the resulting equation, we get the equation for f_0, f_1 and f_2 from the general equation of the form:

$$\frac{\partial f_k}{\partial\tau} = \frac{\partial^2 f_k}{\partial Y^2} - U\, f_{k-1} + \frac{1}{Pe^2}\, f_{k-2} - \sum_{i=0}^{k} K_i\, f_{k-i}, \quad (k = 0,1,2), \tag{2.12}$$

where $f_{-1}= f_{-2} = 0$.

We note that to evaluate K_i's we need to know the f_k's, which are obtained by solving (2.12) for f_k's subject to the boundary conditions

$$f_k(\tau,0) = \text{finite}, \tag{2.13a}$$

$$\frac{\partial f_k}{\partial Y}(\tau,1) = -\beta\, f_k(\tau,1), \tag{2.13b}$$

$$\frac{\partial f_k}{\partial Y}(\tau,0) = 0, \tag{2.13c}$$

$$\frac{1}{2}\int_{-1}^{1} f_k(\tau,Y)dY = \delta_{k0}, (k = 0, 1,2). \tag{2.13d}$$

The function f_0 and the exchange coefficient K_0 are independent of the velocity field and can be solved easily. It should be pointed out here that a simultaneous solution has to be obtained for these two quantities since K_0, which can be obtained from (2.10) as

$$K_0(\tau) = \frac{1}{2}\left.\frac{\partial f_0}{\partial y}\right]_{-1}^{1}. \tag{2.14}$$

Substituting $k = 0$ in (2.10) we get the differential equation for f_0 as

$$\frac{\partial f_0}{\partial \tau} = \frac{\partial^2 f_0}{\partial Y^2} - f_0 K_0. \tag{2.15}$$

We now derive an initial condition for f_0 using (2.7) by taking $\tau = 0$ in that equation to get

$$\theta_m(0, X) = \frac{1}{2}\int_{-1}^{1} \theta(0, X, Y)\, dY. \tag{2.16}$$

Substituting $\tau = 0$ in (2.6) and setting $f_k(y) = 0$ (k = 1, 2, 3,…) gives us the initial condition for f_0 as

$$f_0(0, Y) = \frac{\theta(0, X, Y)}{\theta_m(0, X)}. \tag{2.17}$$

We note that the left hand side of (2.17) is a function of Y only and the right hand side is a function of both X and Y. Thus clearly the initial concentration distribution must be a separable function of X and Y. This is the justification for the chosen form of $\theta(0, X, Y)$ in (2.17). Substituting (2.5) into (2.17), we get

$$f_0(0, Y) = \frac{\psi(Y)}{\frac{1}{2}\int_{-1}^{1} \psi(Y) dY}. \tag{2.18}$$

The solution of the reaction diffusion equation (2.15) with these conditions may be formulated as

$$f_0(\tau, y) = g_0(\tau, y)\ \exp[-\int_0^{\tau} K_0(\eta)\, d\eta] \tag{2.19}$$

from which it follows that $g_0(\tau, y)$ has to satisfy

$$\frac{\partial g_0}{\partial \tau} = \frac{\partial^2 g_0}{\partial y^2}, \tag{2.20}$$

along with the conditions

$$f_0(0, Y) = g_0(0, Y) = \frac{\psi(Y)}{\frac{1}{2}\int_{-1}^{1} \psi(Y) dY}, \tag{2.21a}$$

$$g_k(\tau, 0) = \textit{finite} \tag{2.21b}$$

$$\frac{\partial g_0}{\partial Y}(\tau, 1) = -\beta\, g_0(\tau, 1). \tag{2.21c}$$

The solution of (2.20) subject to conditions (2.21) is

$$g_0(\tau, Y) = \sum_{n=0}^{\infty} A_n \cos(\mu_n Y) \exp[-\mu_n{}^2 \tau] \tag{2.22}$$

where μ_n's are the roots of

$$\mu_n \tan \mu_n = \beta, \qquad \text{n} = 0,1,2,\ldots\ldots \tag{2.23}$$

and $A_n{}'s$ are given by

$$A_n = \frac{2\int_{-1}^{1} \psi(Y)\cos\mu_n Y dY}{\left(1+\frac{\sin 2\mu_n}{\sin 2\mu_n}\right)\int_{-1}^{1}\psi(Y)dY}. \tag{2.24}$$

Now from (2.19) it follows that

$$f_0(\tau,Y) = \frac{2g_0(\tau,Y)}{\int_{-1}^{1} g_0(\tau,Y)dY} = \frac{\sum_{n=0}^{9} A_n \exp[-\mu_n^2\tau]\cos\mu_n Y}{\sum_{n=0}^{9}\frac{A_n}{\mu_n}\exp[-\mu_n^2\tau]\sin\mu_n}. \tag{2.25}$$

The first ten roots of the transcendental equation (2.23) are obtained using Mathematica and are given in Table 1. We find that these ten roots ensured convergence of the series seen in the expansions for f_0 and K_0. Having obtained f_0, we get K_0 from (4.3.14) in the form

$$K_0(\tau) = -\frac{\sum_{n=0}^{9} A_n\ \mu_n \exp[-\mu_n^2\ \tau]\sin\mu_n}{\sum_{n=0}^{9}\frac{A_n}{\mu_n}\exp[-\mu_n^2\ \tau]\sin\mu_n}. \tag{2.26}$$

By considering the simplest case of the initial concentration occupying the entire cross section of the channel, we take $\psi(Y)=1$ and then $K_0(\tau)$ for this case becomes

$$K_0(\tau) = -\frac{\sum_{n=0}^{9}\frac{1}{(\mu_n^2+\beta^2+\beta)}\exp[-\mu_n^2\ \tau]}{\sum_{n=0}^{9}\frac{1}{\mu_n^2(\mu_n^2+\beta^2+\beta)}\exp[-\mu_n^2\tau]}, \quad n=0\ (1)\ 9. \tag{2.27}$$

We now proceed and do only long time analysis of K_0, K_1, K_2 …… As $\tau\to\infty$, we get the asymptotic solution for K_0 from (2.28) as

$$K_0(\infty) = -\mu_0^2, \tag{2.28}$$

where μ_0 is the first root of the equation (2.23). Physically this represents first order chemical reaction coefficient. Having obtained $K_0(\infty)$, we can now get $K_1(\infty)$ from (2.10) (with i = 1) knowing $f_0(\infty,Y)$ and $f_1(\infty, Y)$. Likewise, $K_2(\infty), K_3(\infty)\ldots$ require the knowledge of K_0, K_1, f_0, f_1 and f_2. Equation (2.25) in the limit $\tau\to\infty$ reduces to

$$f_0(\infty, Y) = \frac{\mu_0}{\sin\mu_0}\cos(\mu_0 Y). \tag{2.29}$$

We then find f_1, K_1, f_2 and K_2. For asymptotically long times, i.e., $\tau\to\infty$, (2.10) and (2.12) give us K_i's and f_k's as

$$K_i(\infty) = \frac{\delta_{i2}}{Pe^2} - \beta\, f_i(\infty,1) - \int_{-1}^{1} f_{i-1}(\infty, Y)\, dY, \ (i=1,2,3,). \tag{2.30}$$

$$\frac{d^2 f_k}{dY^2} + \mu_0^2 f_k = +K_1) f_{k-1} - (\frac{1}{Pe^2} - K_2) f_{k-2}, \ (k=1,2). \tag{2.31}$$

The f_k's must satisfy the conditions (2.7) and this permits the eigenfunction expansion in the form

$$f_k(\infty,Y) = \sum_{j=0}^{9} B_{j,k}\cos(\mu_j Y), \quad k=1,2,3 \tag{2.32}$$

Substituting (2.32) in (2.31) and multiplying the resulting equation by $\cos(\mu_j Y)$ and integrating with respect to Y from -1 to 1, we get after simplification

$$B_{j,k}=\frac{1}{(\mu_j^2-\mu_0^2)}\left[\frac{1}{Pe^2}B_{j,k-2}-\sum_{i=1}^{k}B_{j,k-i}K_i-\left(1+\frac{\sin 2\mu_j}{2\mu_j}\right)^{-1}\sum_{l=0}^{9}B_{l,k-1}I(j,l)\right],(k=1,2)$$

where

$$I(j,l)=\int_{-1}^{1}\cos\mu_l Y\cos\mu_j Y dY, \tag{2.34}$$

$$B_{j,-1}=0,\quad B_{j,0}=0 \text{ for } j=1(1)\,9. \tag{2.35}$$

(2.33)

The first expansion coefficient $B_{0,k}$ in (2.32) can be expressed in terms of $B_{j,k}$ (j = 1(1) 9) by using the conditions (2.13) as

$$B_{0,k}=-\left(\frac{\mu_0}{\sin\mu_0}\right)\sum_{j=1}^{9}B_{j,k}\frac{\sin\mu_j}{\mu_j},\quad (k=1,2,3,4\ldots.). \tag{2.36}$$

Further, from (2.32) and (2.29) we find that

$$B_{0,0}=\frac{\mu_0}{\sin\mu_0}. \tag{2.37}$$

Substituting i = 1 in (2.30) and using (2.34), (2.35) and (2.37) in the resulting equation, we get

$$K_1(\infty)=-\frac{I(0,0)}{\left[1+(\sin 2\mu_0/2\mu_0)\right]}. \tag{2.38}$$

Substituting i = 2 in (2.30) and using (2.33), (2.34) and (2.37) in the resulting equation, we get

$$K_2=\frac{1}{Pe^2}-\frac{\sin\mu_0}{\mu_0\left[1+(\sin 2\mu_0/2\mu_0)\right]}\sum_{l=1}^{9}B_{l,1}I(0,l). \tag{2.39}$$

Using the asymptotic coefficients $K_0(\infty)$, $K_1(\infty)$ and $K_2(\infty)$ in (2.11) one can determine the mean concentration distribution as a function of X, τ and the parameters of the problem a, Pe, σ and β. This distribution is valid only for long time and is a gross approximation at short and moderate times.

The initial conditions for solving (2.11) can be obtained from (2.5a) by taking the cross-sectional average. Since we are making long time evaluations of the coefficients, we note that the side effect is independent of θ_m on the initial concentration distribution. In view of this, the solution to (2.11) with asymptotic coefficients can be written as

$$\theta_m(\tau,X)=\frac{1}{2Pe\sqrt{\pi K_2(\infty)\,\tau}}\exp\left\{K_0(\infty)\tau-\frac{\left[X+K_1(\infty)\tau\right]^2}{4K_2(\infty)\tau}\right\}, \tag{2.40}$$

where

$$\theta_m(\tau,\infty)=0,\ \frac{\partial\theta_m}{\partial X}(\tau,\infty)=0. \tag{2.41}$$

Equation (2.41) is obtained from (2.5d) and $K_0(\infty)$, $K_1(\infty)$ and $K_2(\infty)$ are given by the (2.28), (2.38) and (2.39).

III. RESULTS AND DISCUSSIONS

In this paper, we have modeled the solvent as a couple-stress fluid and studied dispersion of solute in a couple-stress fluid bounded by porous beds considering heterogeneous chemical reaction. The walls of the channel act as catalysts to the reaction. The problem brings in to focus three important dispersion coefficients namely the

exchange coefficient $-K_0$ which arises essentially due to the wall reaction and the classical convective coefficient $-K_1$ and diffusive coefficient K_2. The asymptotic values of these three coefficients are plotted in Figures 3.1 to 3.5 for various value of couple stress parameter *a*, porous parameter σ and reaction rate parameter β. From these figures we predict the following.

From Figure 3.1, it is evident that $-K_0(\infty)$ increases with an increase in the value of the wall reaction parameter β but it is unaffected by the porous parameter and the couple stress parameter. The classical convective coefficient $-K_1$ is plotted in Figures 3.2 and 3.3 versus wall reaction parameter β for different values of porous parameter σ and couple stress parameter *a* respectively for a fixed value of slip parameter $\alpha = 0.1$. From these figures we conclude that increase in β and σ as well as decrease in *a* is to increase $-K_1$. This is advantageous in maintaining the laminar flow. The scaled dispersion coefficient $K_2 - Pe^{-2}$ is plotted versus β in Figure 3.4 for different values of σ and for fixed values of *a* =1 and α.= 0.1 and in Figure 3.5 for different values of *a* for fixed values of α=0.1 and σ=100. From these figures, it is clear that the increase in σ and *a* is to increase and decrease the effective dispersion coefficient respectively. These are useful in the control of dispersion of a solute.

The cross-sectional average concentration θ_m is plotted versus x in Figures 3.6 to 3.8 respectively for different values of σ, β, *a* and for fixed values of the other parameters given in these figures. It is clear that the increase in σ and β decreases θ_m, while an increase in *a* increases θ_m as expected on the physical grounds. This may be attributed to the fact that an increase in σ and β is to reduce the velocity and hence decreases θ_m. This θ_m is also plotted in Figures 3.9 to 3.11 respectively against the time τ for different values of σ, β and *a* for fixed values of the other parameters given in these figures. We note that the peak of θ_m decreases with an increase in β occurring at the lower interval of time τ. We also note that although the peak decreases with an increase in σ and increases with an increase in *a* but occurs at almost at the same interval of time τ. These information are useful to understand the transport of solute at different times.

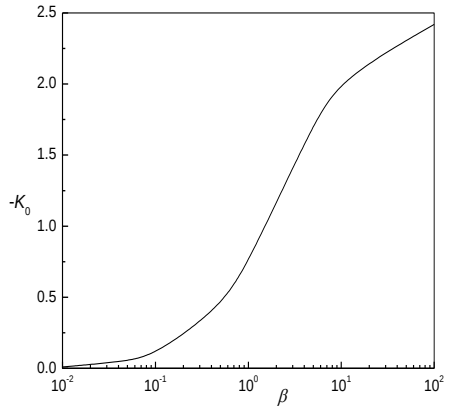

Fig.3.1: Plots of exchange coefficient versus reaction rate parameter β.

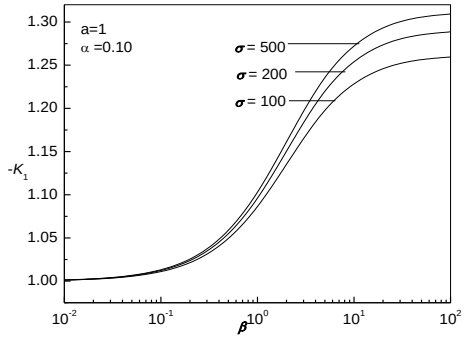

Fig. 3.2: Plots of the convective coefficient $-K_1$ versus wall reaction Parameter β for different values of σ

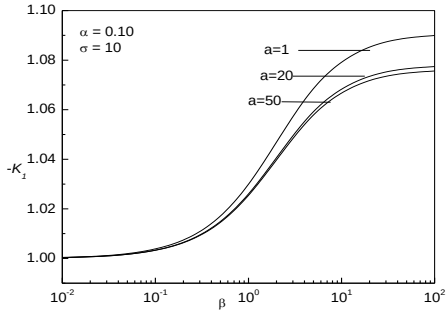

Fig. 3.3: Plots of the convective coefficient $-K_1$ versus wall reaction parameter β for different values of couple stress parameter a

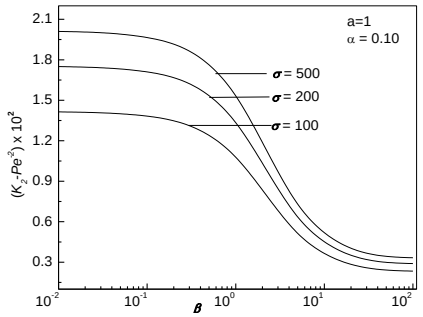

Fig. 3.4: Plots of scaled dispersion coefficient $K_2(\tau)-Pe^{-2}$ versus β for different values of σ

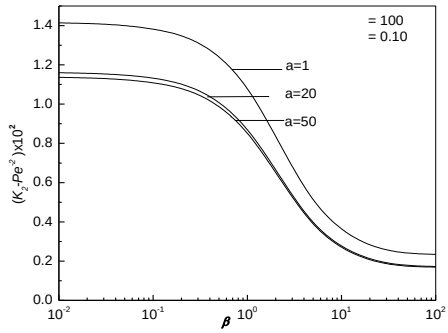

Fig. 3.5: Plots of scaled dispersion coefficient $K_2(\tau)-Pe^{-2}$ versus β for different values of *a*

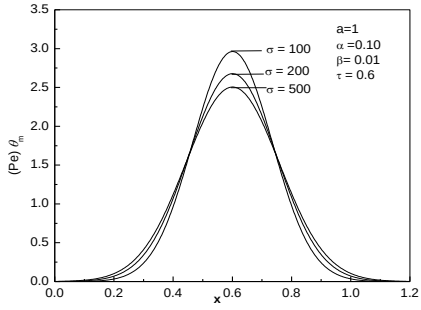

Fig. 3.6: Plots of mean concentration θ_m versus X for different values of porous parameter σ.

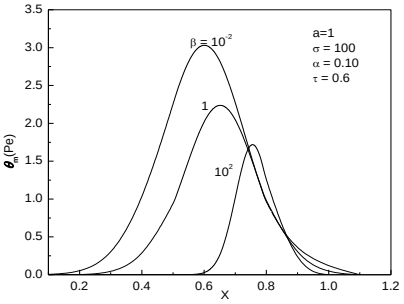

Fig. 3.7: Plots of mean concentration θ_m versus X for different values of reaction rate parameter at the wall

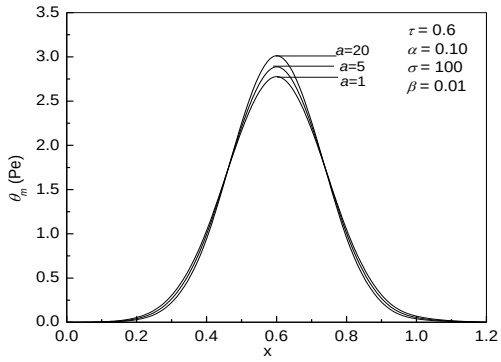

Fig. 3.8: Plots of mean concentration θ_m versus X for different values of couple stress parameter *a*.

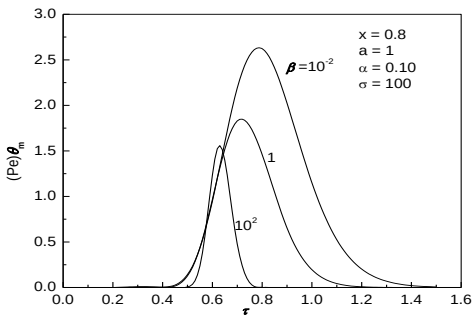

Fig. 3.9: Plots of mean concentration θ_m versus τ for different values of wall reaction parameter β.

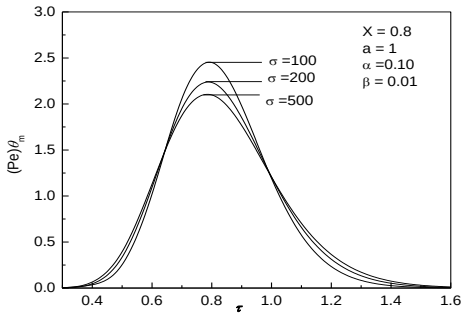

Fig. 3.10: Plots of mean concentration θ_m versus τ for different values of porous parameter σ

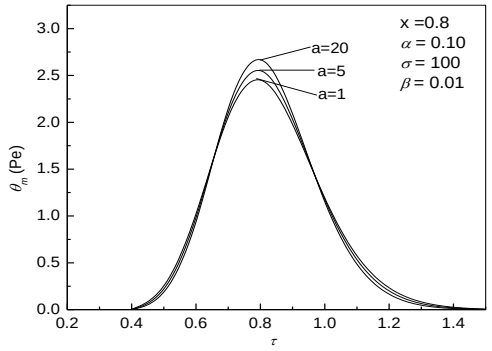

Fig. 3.11: Plots of mean concentration θ_m versus τ for different values couple stress parameter *a*

IV. REFERENCES

[1] Taylor, G. I. (1953). Dispersion of soluble matter in solvent flowing slowly through a tube, Proc. R. Soc. Lond. A, 219, 186–203.

[2] Aris, R. (1956). On the dispersion of a solute in a fluid flowing through a tube, Proc. R. Soc. Lond. A, 235,67–77.

[3] Barton, N. G. (1983). On method of moments for solute dispersion, J. Fluid Mech., 126, 205–218.

[4] Fan, L. T and W.S. Hwang (1965). Dispersion of Ostwald-de-waele fluid in laminar flow through a cylindrical tube, Proc. Roy. Soc. London, Vol.A283, pp576

[5] Ghoshal, S (1971) Dispersion of solute in non-Newtonian flows through a circular tube, Chem, Engg, Sci, vol26, pp.185.

[6] Gill, W. N. and Sankarasubramanian, R. (1970). Exact analysis of unsteady convective diffusion, Proc. R. Soc. Lond. A, 316, 341–350.

[7] Sankarasubramanian, R. and Gill, W. N. (1976). Unsteady convective diffusion in non-Newtonian flows, Can. J. Chem. Eng., 54, 121.

[8] Beavers, G.S. and Joseph, D.D., 1967, boundary conditions at a naturally permeable wall, J. Fluid Mech., vol. 30, pp197.

[9] Shah, S, N, and Cox H. F, 1974, Dispersion of solutes in non -Newtonian laminar flow through a circular tube, Eyring model fluid, Chem. Engg. Sci., Vol.29, pp1282.

National Conference on Applied Sciences Synergising the Engineering and Technology
Print ISSN: 2395-6011 | Online ISSN: 2395-602X (www.ijsrst.com)
© 2021 IJSRST | Volume 8 | Issue 2

Unsteady Convective Diffusion in Couple Stress Fluid with Porous Beds

G J Manjula[1], M Sankar[2], Kavitha G N[3], Raghu M Banakar[4]

[1,2,4]Department of Mathematics, Siddaganga Institute of Technology, Tumkur, India

[3]Department of Mathematics School of Engineering, Presidency University, Itgalpura Rajanukunte, Yelahanka, India

ABSTRACT

Unsteady convective diffusion in a couple stress fluid flow through a channel bounded by porous layers is investigated. The effect of wall permeability is taken into account by using the Beavers-Joseph slip condition at the fluid and porous interface. The unsteady dispersion coefficient and mean concentration distribution are obtained using the generalized dispersion model of Gill and Sankarasubramanian (1970). It is shown that the effect of a couple stress parameter and porous parameter (wall permeability) is to decrease the magnitude of dispersion and thereby increase the concentration distribution. The corresponding results for 'pure-convection' are also obtained as a particular case. The results obtained pave the way for understanding the mechanism of haemolysis caused by artificial organs either implanted or extracorporeal.

Keywords : Couple Stress, Porous Parameter, Generalized Dispersion

I. INTRODUCTION

The study of dispersion in a channel bounded by a porous medium is of considerable physiological importance. Experimental investigations have shown that the nature of flow of blood is different in different parts of the body. This necessitates one to consider different fluids in different physiological situations depending on the problems under investigation. In this Chapter, we study the unsteady dispersion in a couple stress fluids with the motivation of understanding haemolysis caused by artificial organs.

The artificial organs, either implanted or extracorporeal, designed using metals because various forms of blood damage due to lack of biocompatibility either due to rough surface or smooth surface. Both of them are dangerous because both of them produce stress leading to the force. This force drives erythrocytes (i.e. Red Blood Cells (RBC)) in to a particular region leading to bursting of RBCs and hemoglobin to be let loosed known as haemolysis. One of the most important blood damages is known as haemolysis, the loss of hemoglobin from erythrocytes (RBC) in the blood due to mechanical reasons. Haemolysis may also be due to physiological and chemical reasons.

In this paper, we concentrate on haemolysis caused by mechanical process due to lack of biocompatibility. This produces either high shear stresses or low stresses as explained above. In a healthy blood the erythrocytes are of irregular shape and hence do not spin as they move. The micron-sized erythrocytes are merely suspensions and for all practical purposes form an integral part of the continuum. The stress in this case is symmetric and its

effect is to disperse oxygen, proteins and other elements freely by hemoglobin in the erythrocytes without rupture. In the case of lack of bio-compatibility produced by artificial organs, the irregular shape of the erythrocytes deforms either due to high or low stress and become almost spherical producing a spin field due to their micro rotation. The experiments of Christopherson and Dowson (1959) using solid sphere model support this. This spin field sets up an antisymmetric stress. Fluids with antisymmetric stress are known as polar fluids. Couple stress fluids are specialized micropolar fluids wherein, unlike most micropolar fluids, there is a match between the spin of the suspension and the vorticity of the suspending fluid.

Rudraiah et al., (1986) have studied the effect of couple stress on the dispersion of erythrocytes in a channel bounded by rigid walls and showed that the couple stress augments haemolysis. Rudraiah et al., (1988) have shown that self-generated electric field reduces the concentration of erythrocytes and hence increases dispersion. In bioengineering problems, particularly in the mechanism of controlling haemolysis, the assumption of "capillary bounded by rigid walls" is unrealistic. This is because; there is transport of oxygen, proteins and other nutrients from capillaries to the permeable tissues. The blood flowing in the capillaries slips at the boundary of the permeable tissues. Therefore, in a study involving the control of haemolysis it is important that the combined effect of couple stress and slip at the porous layer have to be taken into account. The results so obtained are useful in the design of artificial organs. The objective of this chapter is therefore to consider these effects in the study of the unsteady convective diffusion of erythrocytes in the plasma flow by using the generalized dispersion model of Gill and Sankarasubramanian (1970). To achieve this objective, the required equations and the boundary and initial conditions are given in section 1. The solutions for velocity and concentration distribution are also given in this section. Generalized dispersion is discussed in section 2 using Gill and Sankarasubramanian (1970). Important results and discussion are given in section 3.

Mathematical formulation

The physical configuration shown in Figure 1.1 consists of a rectangular channel bounded by porous layers and separated by a distance 2h. A Cartesian coordinate system is chosen such that the origin is at the middle of the channel (i.e. R-1). As shown in the figure 1, under laminar and fully developed flow (unidirectional) conditions with a uniform axial pressure gradient and in the absence of gravity the governing equations are:

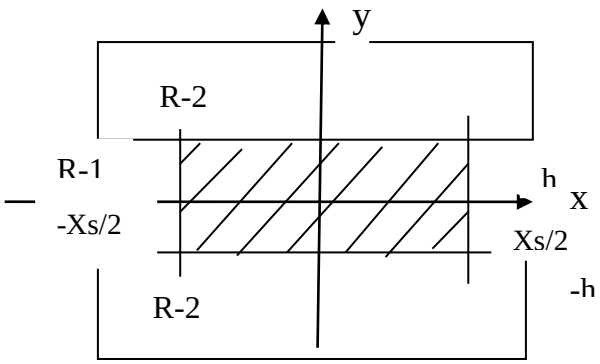

Fig: 1 Physical configuration

Region 1:

$$-\frac{\partial p}{\partial x}+\mu\frac{\partial^2 u}{\partial y^2}-\lambda\frac{\partial^4 u}{\partial y^4}=0, \tag{1.1}$$

$$-\frac{\partial p}{\partial y}=0. \tag{1.2}$$

Region 2:

$$-\frac{\partial p}{\partial x}-\frac{\mu}{k}(1+\beta_1)u_p=0 \quad , \tag{1.3}$$

$$-\frac{\partial p}{\partial y}=0, \tag{1.4}$$

where u is the velocity in the x-direction, μ is the viscosity of the fluid, λ is the couple stress parameter, k is the permeability of the porous medium, u_p is the Darcy velocity and p is the pressure. It may be noted that (1.3) is the modified Darcy equation, modified in the sense of incorporating couple stress parameter β_1 in to the Darcy equation. We consider dispersion of passive/ reactive solute in this fully developed flow through a parallel plate channel bounded by porous beds. In to this flow is introduced a slug of concentration C which is a function of time t and coordinates x and y. The concentration C satisfies the convective diffusion equation

$$\frac{\partial C}{\partial t}+u\frac{\partial C}{\partial x}=D\left(\frac{\partial^2 C}{\partial x^2}+\frac{\partial^2 C}{\partial y^2}\right). \tag{1.5}$$

where D is the molecular diffusivity. The initial and boundary conditions on the velocity and concentration are given as follow

1.1 Boundary Conditions on Velocity

The boundary conditions on velocity are:

$$\frac{\partial u}{\partial y}=-\frac{\alpha}{\sqrt{k}}\left(u-u_p\right) \quad at\ y=h, \tag{1.6a}$$

$$\frac{\partial u}{\partial y}=\frac{\alpha}{\sqrt{k}}\left(u-u_p\right) \quad at\ y=-h, \tag{1.6b}$$

$$\frac{\partial^2 u}{\partial y^2}=0 \quad at\ y=\pm h, \tag{1.7}$$

where α is the slip parameter. Equations (1.6a, b) are the well-known Beavers and Joseph (1967) (BJ) slip conditions at the lower and upper permeable surfaces and (1.7) specifies the vanishing of the couple stress. We note that the BJ-slip conditions (1.6 a, b) are valid only when the thickness of the bounding porous layer is large compared to film thickness. This is because conditions (1.6 a, b) are independent of their thickness. If one wants to consider the thickness of the porous layer in the slip condition then one has to use the slip condition proposed by Rudraiah (1985).

1.2 Initial and Boundary Conditions on Concentration

The initial conditions are

$$C(0, x, y)=C_0 \quad \text{for} \quad |x|\le\frac{1}{2}x_s, \tag{1.8a}$$

$$C(0, x, y) = 0 \qquad \text{for} \quad |x| > \frac{1}{2} x_s . \tag{1.8b}$$

where C_0 is the concentration of the initial slug input of length x_s.

The boundary conditions are:

$$\frac{\partial C}{\partial y}(t, x, h) = 0 , \tag{1.8c}$$

$$\frac{\partial C}{\partial y}(t, x, -h) = 0 , \tag{1.8d}$$

$$C(t, \infty, y) = \frac{\partial C}{\partial y}(t, \infty, y) = 0 , \tag{1.8e}$$

$$C(t, x, y) = \text{finite.} \tag{1.8f}$$

The condition (1.8e) specifies that the concentration does not reach points far away downstream and (1.8 c, d) specifies that there is no transfer of mass flux at the walls.

We make (1.1) (1.3) and (1.5) dimensionless using the variables

$$U = \frac{u}{\bar{u}}, \ \eta = \frac{y}{h}, \ X = \frac{x}{hPe}, \ \theta = \frac{C}{C_0}, \ \tau = \frac{tD}{h^2} \tag{1.9}$$

where $\bar{u}$ is the average velocity of the flow and $\text{Pe} = \bar{u}\, h / D$ is the Peclet number. Equations (1.1) and (1.5) in non-dimensional form can be written as

$$\frac{d^4 U}{d\eta^4} - a^2 \frac{d^2 U}{d\eta^2} = -\frac{h^2 a^2}{\mu} \frac{dp}{dx}, \tag{1.10}$$

$$\frac{\partial \theta}{\partial \tau} + U^* \frac{\partial \theta}{\partial \xi} = \frac{1}{Pe^2} \frac{\partial^2 \theta}{\partial \xi^2} + \frac{\partial^2 \theta}{\partial \eta^2} \tag{1.11}$$

where $l = \sqrt{\lambda/\mu}$, $a = h/l$ is the couple stress parameter, $\mathrm{U}^* = (\mathrm{U} - \bar{\mathrm{U}}) / \overline{U}$ (non- dimensional velocity in a moving coordinate system) and $\xi = X - \tau$ is the dimensionless axial coordinate moving with the average velocity $\overline{U}$. The dimensionless boundary conditions on velocity are

$$\frac{\partial U}{\partial \eta} = -\alpha\, \sigma (U - U_p) \quad at \quad \eta = 1, \tag{1.12a}$$

$$\frac{\partial U}{\partial \eta} = \alpha\, \sigma (U - U_p) \quad at \quad \eta = -1, \tag{1.12b}$$

$$\frac{\partial^2 U}{\partial \eta^2} = 0 \qquad at \quad \eta = \pm 1. \tag{1.13}$$

where $\sigma = h/\sqrt{k}$ is the porous parameter. The non-dimensional initial and boundary conditions on concentration from (1.8a) to (1.8f) take the form

$$\theta(0, X, \eta) = 1 \ \text{ for } \ |X| \le \frac{1}{2} X_s ,$$

$$\theta(0, X, \eta) = 0 \ \text{ for } \ |X| > \frac{1}{2} X_s , \tag{1.14a}$$

$$\frac{\partial \theta}{\partial \eta}(\tau, X, 1) = 0 , \tag{1.14b}$$

$$\frac{\partial \theta}{\partial \eta}(\tau, X, -1) = 0 , \tag{1.14c}$$

$$\theta(\tau,\infty,\eta)=\frac{\partial\theta}{\partial\eta}(\tau,\infty,\eta)=0\,, \tag{1.14d}$$

$\theta(\tau, X, \eta)=$ finite.

The solution of (1.10) satisfying the conditions (1.12), (1.13) is

$$U=-\frac{h^2}{2\mu}\frac{dp}{dx}\left[1-\eta^2\ -\frac{2}{a^2}\left(1-\frac{\cosh a\eta}{\cosh a}\right)+A_0\right] \tag{1.15}$$

Where $A_0=\dfrac{2}{\sigma^2(1+\beta_1)}-\dfrac{2}{\sigma\,\alpha}\left(\dfrac{\tanh a}{a}-1\right)$.

The solution of (1.11), following Gill and Sankarasubramanian (1970), can be written as a series expansion in the form

$$\theta(\tau,\xi,\eta)=f_0(\tau,\eta)\,\theta_m(\tau,\xi)+f_1(\tau,\eta)\frac{\partial\theta_m}{\partial\xi}(\tau,\xi)+f_2(\tau,\eta)\frac{\partial^2\theta_m}{\partial\xi^2}(\tau,\xi)+\ldots\ldots, \tag{1.16}$$

where $\theta_m=\dfrac{1}{2}\int_{-1}^{1}\theta\,d\eta$, is the dimensionless cross-sectional average concentration.

Integrating (1.11) with respect to η in [-1,1] and using the definition of θ_m we get

$$\frac{\partial\theta_m}{\partial\tau}=\frac{1}{Pe^2}\frac{\partial^2\theta_m}{\partial\xi^2}-\frac{1}{2}\frac{\partial}{\partial\xi}\int_{-1}^{1}U^*\theta\,d\eta\,. \tag{1.17}$$

II. DISPERSION MODEL

In the study of dispersion, the following approaches are mainly used.

Following Rudraiah et al., (1986) we determine in this section the effect of permeability, slip and couple stress on the generalized dispersion coefficient of Gill and Sankarasubramanian (1970), which is valid for all time.

We now assume that the process of distributing θ is diffusive in nature right from time zero (unlike the models of Taylor 1953, Aris, 1956 and Lighthill, 1969). One can introduce, following Gill and Sankarasubramanian (1970), the generalized dispersion model with time-dependent dispersion coefficient as

$$\frac{\partial\theta_m}{\partial\tau}=K_1\frac{\partial\theta_m}{\partial\xi}+K_2\frac{\partial^2\theta_m}{\partial\xi^2}+K_3\frac{\partial^3\theta_m}{\partial\xi^3}+\ldots., \tag{2.1}$$

where K_i's are given by

$$K_i(\tau)=\frac{\delta_{i2}}{Pe^2}-\frac{1}{2}\int_{-1}^{1}U\ f_{i-1}(\tau,\eta)d\eta\,,\ (i=1,2,3) \tag{2.2}$$

Here $f_{-1}=0$ and δ_{i2} is the Kronecker delta.

Equation (2.1) is solved subject to the conditions

$$\theta_m(0,\xi)=1 \qquad |\xi|\le\frac{1}{2}X_s\,,$$

$$\theta_m(0,\xi)=0 \qquad |\xi|\ge\frac{1}{2}X_s\,, \tag{2.3}$$

$$\theta_m(\tau,\infty)=0.$$

Introducing (1.17) in to (1.16), rearranging terms and also observing that

$$\frac{\partial^{k+1}\theta_m}{\partial\tau\,\partial\xi^k}=\sum_{k=1}^{\infty}K_i(\tau)\frac{\partial^{i+k}\theta_m}{\partial\xi^{i+1}}, \tag{2.4}$$

we obtain

$$\left[\frac{\partial f_1}{\partial\tau}-\frac{\partial^2 f_1}{\partial\eta^2}+U^*+K_1(\tau)\right]\frac{\partial\theta_m}{\partial\xi}+\left[\frac{\partial f_2}{\partial\tau}-\frac{\partial^2 f_2}{\partial\eta^2}+U^*f_1+K_1(\tau)f_1+K_2(\tau)-\frac{1}{Pe^2}\right]\frac{\partial^2\theta_m}{\partial\xi^2}$$
$$+\sum_{k=1}^{\infty}\left[\begin{array}{l}\dfrac{\partial f_{k+2}}{\partial\tau}-\dfrac{\partial^2 f_{k+2}}{\partial\eta^2}+U^*f_{k+1}+K_1(\tau)f_{k+1}\\ +\left(K_2(\tau)-\dfrac{1}{Pe^2}\right)f_k\ +\sum_{i=3}^{k+2}K_i f_{k+2-1}\end{array}\right]=0$$

$$\text{with } f_0=1 \tag{2.5}$$

and

$$U^*=\frac{1}{2}\frac{\left(1-3\eta^2+\dfrac{6}{a^2\cosh a}(\cosh a\eta-\dfrac{\sinh a}{a})\right)}{1+\dfrac{3}{a^2}\left(\dfrac{\tanh a}{a}-1\right)+\dfrac{3}{2}A_0}. \tag{2.6}$$

Equating the coefficients of $\frac{\partial^k\theta_m}{\partial\xi^k}$ (k = 1, 2, 3…) in (2.5) to zero, we obtain the following infinite set of non-homogenous, parabolic partial differential equations:

$$\frac{\partial f_1}{\partial\tau}=\frac{\partial^2 f_1}{\partial\eta^2}-U^*f_0-K_1(\tau)f_0, \tag{2.7}$$

$$\frac{\partial f_2}{\partial\tau}=\frac{\partial^2 f_2}{\partial\eta^2}--U^*f_1-K_1(\tau)f_1-K_2(\tau)+\frac{1}{Pe^2} \tag{2.8}$$

$$\frac{\partial f_{k+2}}{\partial\tau}=\frac{\partial^2 f_{k+2}}{\partial\eta^2}-U^*f_{k+1}-K_1(\tau)f_{k+1}-\left(K_2(\tau)-\frac{1}{Pe^2}\right)f_k-\sum_{i=3}^{k+2}kf_{k+2-i}. \tag{2.9}$$

Since θ has to satisfy the conditions (1.14), we should have

$$f_k(0,\eta)=\delta_{k0}\quad k=0,1,2,3..... \tag{2.10a}$$

$$\frac{\partial f_k}{\partial\eta}(\tau,-1)=0,\frac{\partial f_k}{\partial\eta}(\tau,1)=0,k=1,2,3..... \tag{2.10b}$$

Further

$$\int_{-1}^{1}f_k(\tau,\eta)d\eta=0\qquad k=1,2,3..... \tag{2.10c}$$

From (2.2) for i = 1, using f_0 =1, we get K_1 as

$$K_1(\tau)=0. \tag{2.11}$$

From (2.2) and (2.6), we get

$$K_2(\tau)=\frac{1}{Pe^2}-\frac{1}{4\left(1+\frac{3}{a^2}\left(\frac{\tanh a}{a}-1\right)+\frac{3}{2}A_0\right)}$$

$$\{\int_{-1}^{1}\left(1-3\eta^2+\frac{6}{a^2\cosh a}(\cosh a\eta-\frac{\sinh a}{a})\right)f_1 d\eta\}. \qquad (2.12)$$

First we have to solve (2.7) for f_1 satisfying the conditions (2.10), because (2.8) and (2.9) require f_1 to find f_2 and $K_2(\tau)$, respectively. For this, we write

$$f_1 = f_{10}(\eta)+ f_{11}(\tau,\eta), \qquad (2.13)$$

where f_{10} corresponds to an infinitely wide slug which is independent of τ satisfying

$$\frac{df_{10}}{d\eta}=0 \qquad at\ \eta=\pm1, \qquad (2.14a)$$

$$\text{and}\ \int_{-1}^{1} f_{10}\, d\eta = 0. \qquad (2.14b)$$

Also, f_{11} is τ-dependent. Then (2.7) using (2.13), becomes

$$\frac{d^2 f_{10}}{d\eta^2}=\frac{1}{2}\frac{\left(1-3\eta^2+\frac{6}{a^2\cosh a}(\cosh a\eta-\frac{\sinh a}{a})\right)}{1+\frac{3}{a^2}\left(\frac{\tanh a}{a}-1\right)+\frac{3}{2}A_0}, \qquad (2.15)$$

$$\frac{\partial f_{11}}{\partial\tau}=\frac{\partial^2 f_{11}}{\partial\eta^2}. \qquad (2.16)$$

Solution of (2.15) satisfying (2.14) is

$$f_{10}=\frac{1}{2(1+\frac{3}{a^2}(\frac{\tanh a}{a}-1)+\frac{3}{2}A_0)}\left(\frac{\eta^2}{2}-\frac{\eta^4}{4}+\frac{6}{a^2}(\frac{\cosh a\eta}{a^2\cosh a}-\frac{\tanh a}{a}\frac{\eta^2}{2}+F)\right), \qquad (2.17)$$

$$F=-\left(\frac{7}{60}+\frac{6\tanh a}{a^5}-\frac{\tanh a}{a^3}\right). \qquad (2.18)$$

Equation (2.16) is of the well-known heat conduction type and its solution satisfying (2.10) is of the form

$$f_{11}=\sum_{n=1}^{\infty}A_n e^{-\lambda_n^2\tau}\cos\lambda_n\eta, \qquad (2.19)$$

where

$$A_n=\frac{1}{(1+\frac{3}{a^2}(\frac{\tanh a}{a}-1)+\frac{3}{2}A_0)}\left(\frac{6\cos\lambda_n}{\lambda_n^2}\left\{\frac{1}{\lambda_n^2}-\frac{\tanh a}{a(\lambda_n^2+a^2)}\right\}\right), \qquad (2.20)$$

$$\lambda_n=n\pi,$$

$$f_1(\eta)=\frac{1}{2(1+\frac{3}{a^2}(\frac{\tanh a}{a}-1)+\frac{3}{2}A_0)}\{\left(\frac{\eta^2}{2}-\frac{\eta^4}{4}+\frac{6}{a^2}(\frac{\cosh a\eta}{a^2\cosh a}-\frac{\tanh a}{a}\frac{\eta^2}{2}+F)\right) \qquad (2.21)$$

$$-12\sum_{n=1}^{\infty}e^{-\lambda_n^2\tau}\cos\lambda_n\eta\frac{\cos\lambda_n}{\lambda_n^2}\left\{\frac{1}{\lambda_n^2}-\frac{\tanh a}{a(\lambda_n^2+a^2)}\right\}\}$$

Substituting (2.21) in to (2.12) and integrating we get

$$K_2(\tau)=\frac{1}{Pe^2}+\frac{1}{8\left(\frac{1}{3}+\frac{1}{a^2}\left(\frac{\tanh a}{a}-1\right)+\frac{A_0}{2}\right)^2}(\frac{16}{945}-\frac{4}{135}\frac{\tanh a}{a^7}(12a^4-180a^2-135)$$

$$-\frac{20}{a^6}+\frac{4}{3a^6}\left(\frac{\tanh a}{a}\right)^2(5a^2+12)-\frac{16e^{-\lambda_n^2\tau}}{\lambda_n^2}\sum_{n=1}^{\infty}\left(\frac{1}{\lambda_n^2}-\frac{\tanh a}{a(\lambda_n^2+a^2)}\right)^2). \qquad (2.22)$$

We note that (2.1) has no physical meaning as it stands. We, however, found that $k_3(\tau)$, $k_4(\tau)$ and so on i.e. $k_i(\tau)$ $(i \geq 3)$ obtained using the procedure explained above are negligibly small compared to $k_2(\tau)$. Hence (2.1) now leads to

$$\frac{\partial \theta_m}{\partial \tau} = K_2 \frac{\partial^2 \theta_m}{\partial X^2}, \tag{2.23}$$

which is the usual diffusion equation.

This form, though similar to the Taylor's (1953) model, differs from it due to the fact that the most dominant dispersion coefficient $k_2(\tau)$ is time dependent. It will be useful if we have an estimate of the separate contributions of diffusion and pure convection on dispersion coefficient. To that end we now evaluate the contribution of pure convection, the result of which cannot be obtained from the above general case. Following the earlier procedure $k_2(\tau)$ for pure convection (i.e. neglecting the diffusion terms in (1.11), is given by

$$K_2(\tau) = \frac{\tau}{8\left(1+\frac{3}{a^2}\left(\frac{\tanh a}{a}-1\right)+\frac{A_0}{2}\right)^2}\left(\frac{36}{a^4\cosh^2 a}-\frac{\left(48a^2+108\right)}{a^5}\tanh a-\frac{72}{a^6}\tanh^2 a+\frac{8}{5a^4}(a^4+90)\right) \tag{2.24}$$

The exact solution of (2.23) subject to (2.3) is given by

$$\theta_m(\xi,\tau) = \frac{1}{2}\left[erf\left(\frac{\frac{X_S}{2}+\xi}{2\sqrt{T}}\right) + erf\left(\frac{\frac{X_S}{2}-\xi}{2\sqrt{T}}\right)\right],$$

$$T = \int_0^\tau K_2(z)dz \text{ and } erf(x) = \frac{1}{\pi}\int_0^x e^{-z^2}dz.$$

In what follows θ_{mcd} refers to θ_{mcd} based on (2.22) (i.e. convection +diffusion) and θ_{mc} refers to θ_{mc} based on (2.24) (i.e. pure convection).

III. RESULTS AND DISCUSSIONS

The axial dispersion of a solute in a couple stress fluid bounded by permeable boundaries is studied using generalized dispersion model of Gill and Sankarasubramanian (1970). The dominant dispersion coefficient given by (2.22) is computed for different values of couple stress parameter '*a*', slip coefficient α, porous parameter σ and the dimensionless time τ. The results are graphically represented in Figure 3.1. In this figure, the result $\sigma \to \infty$ corresponds to those given by Rudraiah et al., (1986) for impermeable boundaries. It is clear that the increase in '*a*' and σ(wall permeability) decreases the axial dispersion coefficient. This result is useful in understanding one of the causes for haemolysis, which in turn useful in the design of an artificial organ.

The transport of major metabolisis (such as sugars and amino acids) is rather slow and convective transport plays a major role in accelerating them. Therefore, we have plotted the variation of mean concentration θ_m with axial distance x for a fixed τ in Figures 3.2 and 3.3. These figures reveal a marked variation of θ_m with time and the effect of σ (wall permeability) is to increase the concentration distribution, a result that is true for combined convection plus diffusion and pure convection.

Figures 3.4 and 3.5 represent the variation of concentration of a tracer with τ along the pressure gradient, at a given point, for different values of σ and for a fixed '*a*'. In Figure 3.4, the observation point is inside the concentration slug whereas in Figure 3.5 it is outside. In Figure 3.4, the observation point is close to

the entrance and the influence of σ on θ_m is neglectable, also pure convection has a major contribution to θ_m. From Figure 3.5, it is clear that the effect of pure convection is decreased by the same magnitude when the observation point gets farther and farther away from the entrance. We see that the dispersion (molecular diffusion and convection) is faster, i.e., the parabolic nature of θ_m with τ at a fixed *x/h* if the observation point is far away from the entrance. In these figures we note that θ_m for convection and diffusion and θ_m for pure convection increases with decrease in σ and for small values ofτ, θ_{mcd} curve is above θ_{mc}. In other words, the porous parameter significantly influences θ_m. This information is also useful in understanding the cause for hemolysis.

Apart from the above biomechanical applications of this study, certain general conclusions of a mathematical nature can also be made. They are:

i) The couple stresses are operative only for small values of '*a*' and the present results reduce to Newtonian fluids in the limit of $a \to \infty$.

ii) Taylor's dispersion model forms a particular case of the generalized dispersion model for asymptotic values of τ. In ot her words, the generalized dispersion model reduces to Taylor's dispersion model asymptotically.

iii) For large values of σ, the results of present study reduce to those of Rudraiah et al., (1986).

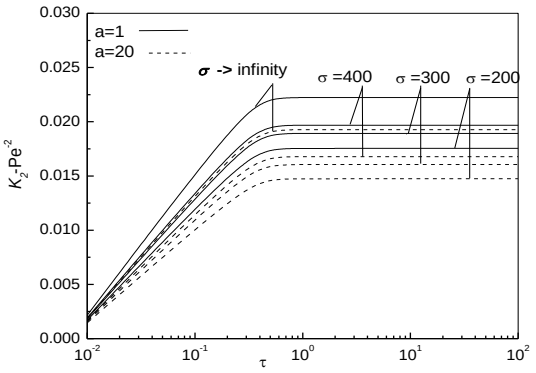

Fig. 3.1: Effect of couple stress parameter a and porous parameter σ on dispersion coefficient K_2

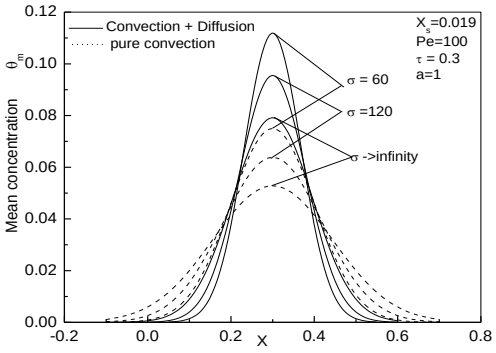

Fig. 3.3: Comparison of results of convective diffusion for the θ_m distribution with that of pure convection for different values of σ.

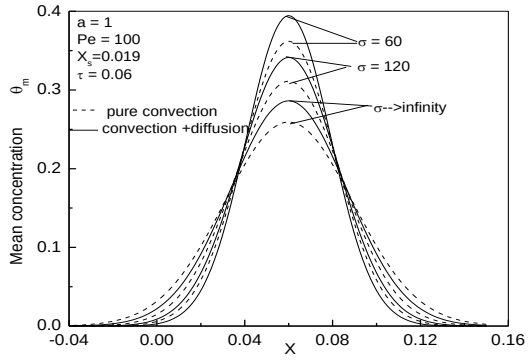

Fig. 3.2: Comparison of results of convective diffusion for the θ_m distribution with that of pure convection for different values of σ.

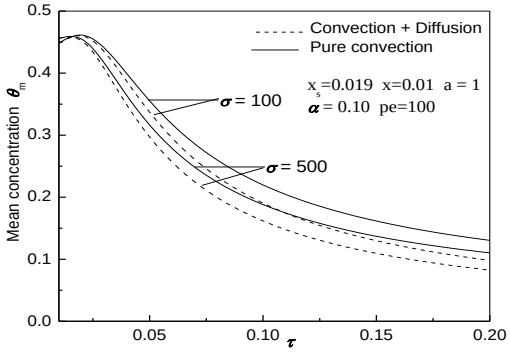

Fig. 3.4: Plots of mean concentration θ_m versus dimensionless time τ

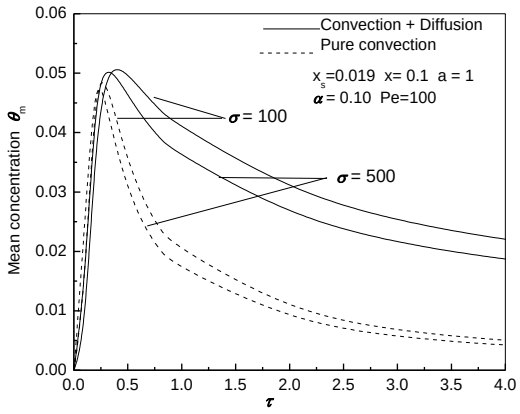

Fig. 3.5: Plots of mean concentration θ_m versus dimensionless time τ

IV. REFERENCES

[1] Taylor, G. I. (1953). Dispersion of soluble matter in solvent flowing slowly through a tube, Proc. R. Soc. Lond. A, 219, 186–203.

[2] Aris, R. (1956). On the dispersion of a solute in a fluid flowing through a tube, Proc. R. Soc. Lond. A, 235,67–77.

[3] Barton, N. G. (1983). On method of moments for solute dispersion, J. Fluid Mech., 126, 205–218.

[4] Fan, L. T and W.S. Hwang (1965). Dispersion of Ostwald-de-waele fluid in laminar flow through a cylindrical tube, Proc. Roy. Soc. London, Vol.A283, pp576

[5] Ghoshal, S (1971) Dispersion of solute in non-Newtonian flows through a circular tube, Chem, Engg, Sci, vol26, pp.185.

[6] Gill, W. N. and Sankarasubramanian, R. (1970). Exact analysis of unsteady convective diffusion, Proc. R. Soc. Lond. A, 316, 341–350.

[7] Sankarasubramanian, R. and Gill, W. N. (1976). Unsteady convective diffusion in non-Newtonian flows, Can. J. Chem. Eng., 54, 121.

[8] Beavers, G.S. and Joseph, D.D., 1967, boundary conditions at a naturally permeable wall, J. Fluid Mech., vol. 30, pp197.

[9] Shah, S, N, and Cox H. F, 1974, Dispersion of solutes in non -Newtonian laminar flow through a circular tube, Eyring model fluid, Chem. Engg. Sci., Vol.29, pp1282.

National Conference on Applied Sciences Synergising the Engineering and Technology
Print ISSN: 2395-6011 | Online ISSN: 2395-602X (www.ijsrst.com)
© 2021 IJSRST | Volume 8 | Issue 2

Mathematical Analysis of Reactive Transport with Physical and Chemical Heterogeneity, Dissipation Coefficient and Sorption

Ramesh T[1], Rangaraju BV[2], Shobhankuma DM[3]

[1]Department of Mathematics, Cambridge Institute of Technology, Bengaluru, Karnataka, India
[2]Department of Mathematics, East point college of engineering and Technology, Bengaluru, Karnataka, India
[3]Department of Mathematics, Maharani's, Science College, Bengaluru, Karnataka, India

ABSTRACT

The purpose of this paper is to study the analytical solutions for one-dimensional advection-dispersion equations in the unsaturated permeable medium infinite area. The transform technique tied with the general integral transform method is used to achieve analytical solutions. Solutions are received for both 1st and 3rd type inlet boundary situations. The established analytical solutions for the finite areas related to solutions for the semi-infinite area to make clear how the exit boundary impacts one-dimensional transportation in a permeable medium system.

Keywords: Porous Medium, Sorption, Heterogeneity, Dissipation, Laplace Transform.

I. INTRODUCTION

The effect of spatially variable hydraulic parameters on transport and spreading of conservative, non-reacting solutes in natural subsurface has been the point of interest of many latest studies. Gelhar et. al. (1979), Sudheendra (2010, 2011). Aral et.al (1996) and others have provided methodologies for enhancing the outline and prediction of non-reacting solute transport is complicated based formations, in comparison with the prediction based on the ADE with constant coefficients. Then again, the delivery of sorbing solutes in geochemically in addition to hydraulically heterogeneous porous media has received little attention.

For the important case of delivery of sorbing solutes in geochemically homogeneous porous media, the effects of sorption are generally accounted for by means of a dimensionless retardation factor, which may be defined as the ratio of the average fluid pore velocity to the propagation speed of the solute. Aside from the possibilities of mass delivery limitations and solute transformation or decay, any determined fluctuations at the retardation thing are attributed totally to the variability of the distribution coefficient, which is an experimentally received degree of sorption or solute retention by way of the solid formation.

Sorption methods can be complex and depend upon many variables, including temperature, strain, ionic energy and solution PH, sorbent floor charge, sorbent sorptive capability, and the presence of species that whole for

sorption sites. Spatial or temporal fluctuations in any of these variables, for this reason, have an effect on the distribution coefficient and, consequently, the movement of sorbing solutes in subsurface porous media.

For example, the distribution coefficient of non-polar natural solutes (synthetic organic chemicals, essential materials of floor water toxic pollution) is correlated with the natural carbon content material of the sorbent (Karckhoff (1984) and Sudheendra (2014)). Even though any such correlation isn't always fully reliable for every solute-sorbent system (Curtis and Roberts, 1985), it could provide an explanation for to a degree the variable retardation located in field experiments (Roberts et.al 1986).

Garabedian (1987) & Sudheendra (2012) employed spectral techniques to analyze reactive solute macro-dispersion under the belief that the log-hydraulic conductivity is linearly associated with each the porosity and the distribution coefficient. His end result implies that solute spreading is superior while there's a negative correlation between the log-hydraulic conductivity and the distribution coefficient.

The current work is centered at the transport of pollutants but in any other case non-reacting solutes under local equilibrium conditions in a one-dimensional unsaturated porous medium. Analytical solutions are hired to resolve the one-dimensional advection-dispersion equation with uniform, constant fluid flow conditions and spatially variable retardation component, for a semi-infinite medium and flux-type inlet boundary situation.

An analytical first-order solution to the one-dimensional advection-dispersion equation with spatially variable retardation factor is derived using a generalized integral transform technique to analyze the transport of sorbing, but otherwise non-reacting solutes in hydraulic homogenous though geochemically heterogeneous porous formations.

The solution is derived under situations of steady-state flow and arbitrary initial and inlet BCs. The outcomes acquired by using this solution agree well with the results acquired with the aid of numerically inverting Laplace transform-generated solutions previously published in the literature. The solution is advanced for a 3rd or flux kind inlet boundary condition that is relevant while thinking about resident solute concentrations and a semi-infinite permeable medium.

II. MATHEMATICAL MODEL

The A D E along with ICs and BCs is of the form

$$\frac{\partial C}{\partial t}+\frac{(1-n)}{n}\frac{\partial S}{\partial t}=D\frac{\partial^2 C}{\partial z^2}-w\frac{\partial C}{\partial z}-\lambda C$$

The adsorbed phase is given by

$$\frac{\partial S}{\partial t}=K_d\frac{\partial C}{\partial t},$$

K_d is the distribution coefficient.

$$\frac{\partial C}{\partial t}+\frac{(1-n)}{n}K_d\frac{\partial C}{\partial t}=D\frac{\partial^2 C}{\partial z^2}-w\frac{\partial C}{\partial z}-\lambda C$$

$$\left[1+\frac{(1-n)}{n}K_d\right]\frac{\partial C}{\partial t}=D\frac{\partial^2 C}{\partial z^2}-w\frac{\partial C}{\partial z}-\lambda C$$

$$R\frac{\partial C}{\partial t}=D\frac{\partial^2 C}{\partial z^2}-w\frac{\partial C}{\partial z}-\lambda C$$

Let us take D_1 = D/R, w_1 = w/R, [illegible]= [illegible]R. Firstly, saturated flow of fluid of concentration, $C = 0$, in the permeable media.

$$\frac{\partial C}{\partial t} = D_1 \frac{\partial^2 C}{\partial z^2} - w_1 \frac{\partial C}{\partial z} - \lambda_1 C \qquad .1)$$

Thus, the appropriate BC for the given model

$$\left.\begin{aligned} C(z, 0) &= 0 \qquad z \geq 0 \\ C(0, t) &= C_0 e^{-\gamma t} \qquad t \geq 0 \\ C(\infty, t) &= 0 \qquad t \geq 0 \end{aligned}\right\}. \qquad (2)$$

The problem then is to describe the absorption as a function of z and *t*, where the i/p state is supposed at the origin and a 2nd type state has been assumed. C_0 is an initial concentration. To moderate equation (5.1) to a simple form, we assume

$$C(z,\ t) = \Gamma(z,\ t)\, Exp\left[\frac{w_1 z}{2D_1} - \frac{w_1^2 t}{4D_1} - \lambda_1 t\right] \qquad (3)$$

Substituting equation (5.3) into equation (5.1) gives

$$\frac{\partial \Gamma}{\partial t} = D_1 \frac{\partial^2 \Gamma}{\partial z^2} \qquad (4)$$

The ICs and BCs (5.2) transform to

$$\left.\begin{aligned} \Gamma(0, t) &= C_0\ Exp\left[\frac{w_1^2 t}{4D_1} + (\lambda_1 - \gamma)t\right] \qquad t \geq 0 \\ \Gamma(z, 0) &= 0 \qquad z \geq 0 \\ \Gamma(\infty,\ t) &= 0 \qquad t \geq 0 \end{aligned}\right\} \qquad (5)$$

Equation (5.4) may be resolved for a time dependent influx of the fluid at $z = 0$. The solution of equation (5.4) is gained by Duhamel's theorem. If $C = F(x, y, z, t)$ is the solution of the conduction equation for semi-infinite media in which the initial concentration C_0 is zero and its surface is sustained at concentration unity, then the solution of the problem in which the surface is sustained at temperature $\phi(t)$ is

$$C = \int_0^t \phi(\tau) \frac{\partial}{\partial t} F(x, y, z, t - \tau)\, d\tau$$

This theorem is used for conduction problems, but the above to fit this precise case of interest. Let us think about, the problem in which C_0 is zero and the boundary is preserved at concentration unity. The BCs are

$$\left.\begin{aligned} \Gamma(0, t) &= 0 \qquad t \geq 0 \\ \Gamma(z, 0) &= 1 \qquad z \geq 0 \\ \Gamma(\infty, t) &= 0 \qquad t \geq 0 \end{aligned}\right\}$$

The LT of equation (5.4) is

$$L\left[\frac{\partial \Gamma}{\partial t}\right] = D_1 \frac{\partial^2 \Gamma}{\partial z^2}$$

Hence, it is reduced to an O D E

$$\frac{\partial^2 \overline{\Gamma}}{\partial z^2} = \frac{p}{D_1}\overline{\Gamma} \qquad (6)$$

The solution of the equation is $\overline{\Gamma} = Ae^{-qz} + Be^{qz}$ where, $q = \pm\sqrt{\frac{p}{D_1}}$.

The BC as $z \to \infty$ requires that $B = 0$ and boundary condition at $z = 0$ requires that $A = \frac{1}{p}$, then the solution of the equation using Laplace transform is

$$\overline{\Gamma} = \frac{1}{p}e^{-qz}$$

The inverse Laplace transform of the above function is given in any table. The result is

$$\Gamma = 1 - erf\left(\frac{z}{2\sqrt{D_1 t}}\right) = \frac{2}{\sqrt{\pi}} \int_{\frac{z}{2\sqrt{Dt}}}^{\infty} e^{-\eta^2} d\eta$$

Using Duhamel's theorem, the solution of the problem with C_0 zero and the time dependent surface condition at $z = 0$ is

$$\Gamma = \int_0^t \phi(\tau) \frac{\partial}{\partial t}\left[\frac{2}{\sqrt{\pi}} \int_{\frac{z}{2\sqrt{D(t-\tau)}}}^{\infty} e^{-\eta^2} d\eta\right] d\tau$$

Since $e^{-\eta^2}$ is a continuous function, it is possible to differentiate under the integral, which gives

$$\frac{2}{\sqrt{\pi}}\frac{\partial}{\partial t} \int_{\frac{z}{2\sqrt{D_1(t-\tau)}}}^{\infty} e^{-\eta^2} d\eta = \frac{z}{2\sqrt{\pi D_1}(t-\tau)^{3/2}} Exp\left[\frac{-z^2}{4D_1(t-\tau)}\right]$$

The solution to the problem is

$$\Gamma = \frac{z}{2\sqrt{\pi D_1}} \int_0^t \phi(\tau) Exp\left[\frac{-z^2}{4D_1(t-\tau)}\right] \frac{d\tau}{(t-\tau)^{3/2}} \qquad (7)$$

Putting $\mu = \frac{z}{2\sqrt{D_1(t-\tau)}}$ then the equation (5.7) can be written as

$$\Gamma = \frac{2}{\sqrt{\pi}} \int_{\frac{z}{2\sqrt{D_1 t}}}^{\infty} \phi\left(t - \frac{z^2}{4D_1\mu^2}\right) e^{-\mu^2} d\mu \quad . \qquad (8)$$

Since $\phi(t) = C_0\, Exp\left(\frac{w_1^2 t}{4D_1} + (\lambda_1 - \gamma)t\right)$ the solution of the problem can be written as

$$\Gamma(z,t) = \frac{2C_0}{\sqrt{\pi}} Exp\left(\frac{w_1^2 t}{4D_1} + (\lambda_1 - \gamma)t\right)\left\{\int_0^{\infty} Exp\left(-\mu^2 - \frac{\varepsilon^2}{\mu^2}\right) d\mu - \int_0^{\alpha} Exp\left(-\mu^2 - \frac{\varepsilon^2}{\mu^2}\right) d\mu\right\} \qquad (9)$$

where,

$$\alpha = \frac{z}{2\sqrt{D_1 t}} \text{ and } \varepsilon = \sqrt{\left(\frac{w_1^2}{4D_1} + \lambda_1 - \gamma\right)} \left(\frac{z}{2\sqrt{D_1}}\right).$$

Evaluation of the integral solution

The integration of the 1st term of equation (5.9) gives

$$\int_0^\infty Exp\left(-\mu^2 - \frac{\varepsilon^2}{\mu^2}\right) d\mu = \frac{\sqrt{\pi}}{2} e^{-2\varepsilon}. \qquad (10)$$

For suitability the 2nd integral may be specified in terms of the error function (Horen Stein, 1945), because of the function was well tabulated.

Noticing that

$$-\mu^2 - \frac{\varepsilon^2}{\mu^2} = -\left(\mu + \frac{\varepsilon}{\mu}\right)^2 + 2\varepsilon = -\left(\mu - \frac{\varepsilon}{\mu}\right)^2 - 2\varepsilon.$$

The 2nd integral of equation (5.9) may be written as

$$I = \int_0^\alpha Exp\left(-\mu^2 - \frac{\varepsilon^2}{\mu^2}\right) d\mu = \frac{1}{2}\left\{e^{2\varepsilon} \int_0^\alpha Exp\left[-\left(\mu + \frac{\varepsilon}{\mu}\right)^2\right] d\mu + e^{-2\varepsilon} \int_0^\alpha Exp\left[-\left(\mu - \frac{\varepsilon}{\mu}\right)^2\right] d\mu\right\} \qquad (11)$$

Meanwhile, the process of reducing integral to a tabulated function is the same for both integrals in the right side of equation (5.11), only the first term is considered. Let $a = \varepsilon/\mu$ and the integral might be expressed as

$$I_1 = e^{2\varepsilon} \int_0^\alpha Exp\left[-\left(\mu + \frac{\varepsilon}{\mu}\right)^2\right] d\mu$$

$$= -e^{2\varepsilon} \int_{\varepsilon/\alpha}^\infty \left(1 - \frac{\varepsilon}{a^2}\right) Exp\left[-\left(\frac{\varepsilon}{a} + a\right)^2\right] da + e^{2\varepsilon} \int_{\varepsilon/\alpha}^\infty Exp\left[-\left(\frac{\varepsilon}{a} + a\right)^2\right] da. \qquad (12)$$

Further, let, $\beta = \left(\frac{\varepsilon}{a} + a\right)$

In the $\beta = \frac{\varepsilon}{a} + a$ 1st term of the above equation, then

$$I_1 = -e^{2\varepsilon} \int_{\alpha + \frac{\varepsilon}{\alpha}}^\infty e^{-\beta^2} d\beta + e^{2\varepsilon} \int_{\frac{\varepsilon}{\alpha}}^\infty Exp\left[-\left(\frac{\varepsilon}{a} + a\right)^2\right] da. \qquad (13)$$

Similar evaluation of the 2nd integral of equation (5.11) gives

$$I_2 = e^{-2\varepsilon} \int_{\varepsilon/\alpha}^\infty Exp\left[-\left(\frac{\varepsilon}{a} - a\right)^2\right] da - e^{-2\varepsilon} \int_{\varepsilon/\alpha}^\infty Exp\left[-\left(\frac{\varepsilon}{a} - a\right)^2\right] da.$$

Again substituting $-\beta = \frac{\varepsilon}{a} - a$ into the 1st term, the result is

$$I_2 = e^{-2\varepsilon} \int_{\frac{\varepsilon}{\alpha} - \alpha}^\infty e^{-\beta^2} d\beta - e^{-2\varepsilon} \int_{\varepsilon/\alpha}^\infty Exp\left[-\left(\frac{\varepsilon}{a} - a\right)^2\right] da.$$

Noting that

$$\int_{\varepsilon/\alpha}^{\infty} Exp\left[-\left(a+\frac{\varepsilon}{a}\right)^2+2\varepsilon\right]da=\int_{\varepsilon/\alpha}^{\infty} Exp\left[-\left(\frac{\varepsilon}{a}-a\right)^2-2\varepsilon\right]da$$

Substitution into equation (5.11) gives

$$I=\frac{1}{2}\left(e^{-2\varepsilon}\int_{\frac{\varepsilon}{\alpha}-\alpha}^{\infty}e^{-\beta^2}d\beta-e^{2\varepsilon}\int_{\alpha+\frac{\varepsilon}{\alpha}}^{\infty}e^{-\beta^2}d\beta\right). \qquad (14)$$

Thus, equation (5.9) may be expressed as

$$\Gamma(z,t)=\frac{2C_0}{\sqrt{\pi}}Exp\left(\frac{w_1^2t}{4D_1}+(\lambda_1-\gamma)t\right)\left\{\frac{\sqrt{\pi}}{2}e^{-2\varepsilon}-\frac{1}{2}\left[e^{-2\varepsilon}\int_{\frac{\varepsilon}{\alpha}-\alpha}^{\infty}e^{-\beta^2}d\beta-e^{2\varepsilon}\int_{\alpha+\frac{\varepsilon}{\alpha}}^{\infty}e^{-\beta^2}d\beta\right]\right\} \qquad (15)$$

However, by definition,

$$e^{2\varepsilon}\int_{\alpha+\frac{\varepsilon}{\alpha}}^{\infty}e^{-\beta^2}d\beta=\frac{\sqrt{\pi}}{2}e^{2\varepsilon}\ erfc\left(\alpha+\frac{\varepsilon}{\alpha}\right)$$

also, $$e^{-2\varepsilon}\int_{\frac{\varepsilon}{\alpha}-\alpha}^{\infty}e^{-\beta^2}d\beta=\frac{\sqrt{\pi}}{2}e^{-2\varepsilon}\left(1+erf\left(\alpha-\frac{\varepsilon}{\alpha}\right)\right) \quad .$$

Writing equation (5.15) in terms of error functions, we get

$$\Gamma(z,t)=\frac{C_0}{2}Exp\left(\frac{w_1^2t}{4D_1}+(\lambda_1-\gamma)t\right)\left[e^{2\varepsilon}erfc\left(\alpha+\frac{\varepsilon}{\alpha}\right)+e^{-2\varepsilon}erfc\left(\alpha-\frac{\varepsilon}{\alpha}\right)\right] \qquad (16)$$

Thus, Substitution into equation (5.3) the solution is

$$\frac{C}{C_0}=\frac{1}{2}Exp\left[\frac{w_1z}{2D_1}-\gamma t\right]\left[e^{-2\varepsilon}erfc\left(\alpha-\frac{\varepsilon}{\alpha}\right)+e^{2\varepsilon}erfc\left(\alpha+\frac{\varepsilon}{\alpha}\right)\right]$$

Re-substituting for ε and α gives

$$\frac{C}{C_0}=\frac{1}{2}Exp\left[\frac{w_1z}{2D_1}-\gamma t\right]\left[Exp\left[\frac{\sqrt{w_1^2+4D_1(\lambda_1-\gamma)}}{2D_1}z\right]\cdot erfc\left[\frac{z+\sqrt{w_1^2+4D_1(\lambda_1-\gamma)}}{2\sqrt{D_1t}}t\right]+\right.$$

$$\left.\left[Exp\left[-\frac{\sqrt{w_1^2+4D_1(\lambda_1-\gamma)}}{2D_1}z\right]\cdot erfc\left[\frac{z-\sqrt{w_1^2+4D_1(\lambda_1-\gamma)}}{2\sqrt{D_1t}}t\right]\right. \qquad (17)$$

III. RESULTS AND DISCUSSION

This observation gives analytical solutions for one-dimensional advection-dispersion equations in the unsaturated permeable medium infinite area. The transform technique tied with the general integral transform method is used to achieve analytical solutions. Solutions are received for both 1st and 3rd type inlet boundary situations. The established analytical solutions for the finite areas related to solutions for the semi-infinite area to make clear how the exit boundary impacts one-dimensional transportation in a permeable medium system.

The primary barriers of the analytical techniques are that the applicability is for comparatively simple problems. The geometry of the problem must be normal. The houses of the soil in the vicinity taken into consideration need to be homogeneous inside the sub area. The analytical technique is stretchier than the normal form of other techniques for one-dimensional transference model. Fig (5.2) to (5.5) denotes the concentration contours v/s time with in the adsorbing media for depth z = 10m and Retardation factor R=1. it's seen that for a rigid velocity w, dispersion coefficient D and distribution coefficient K_d, C/C_0 decreases with intensity as permeability n decreases because of the distributive coefficient Kd and if time will increase the concentration decreases for exclusive time and decay chain.

The primary barriers to the analytical techniques are that the applicability is for comparatively simple problems. The geometry of the problem must be normal. The houses of the soil in the vicinity taken into consideration need to be homogeneous inside the sub-area. The analytical technique is stretchier than the normal form of other techniques for a one-dimensional transference model. Fig (5.2) to (5.5) denotes the concentration contours v/s time within the adsorbing media for depth z = 10m and Retardation factor R=1. it's seen that for a rigid velocity w, dispersion coefficient D and distribution coefficient K_d, C/C_0 decreases with intensity as permeability n decreases because of the distributive coefficient Kd and if time will increase the concentration decreases for exclusive time and decay chain.

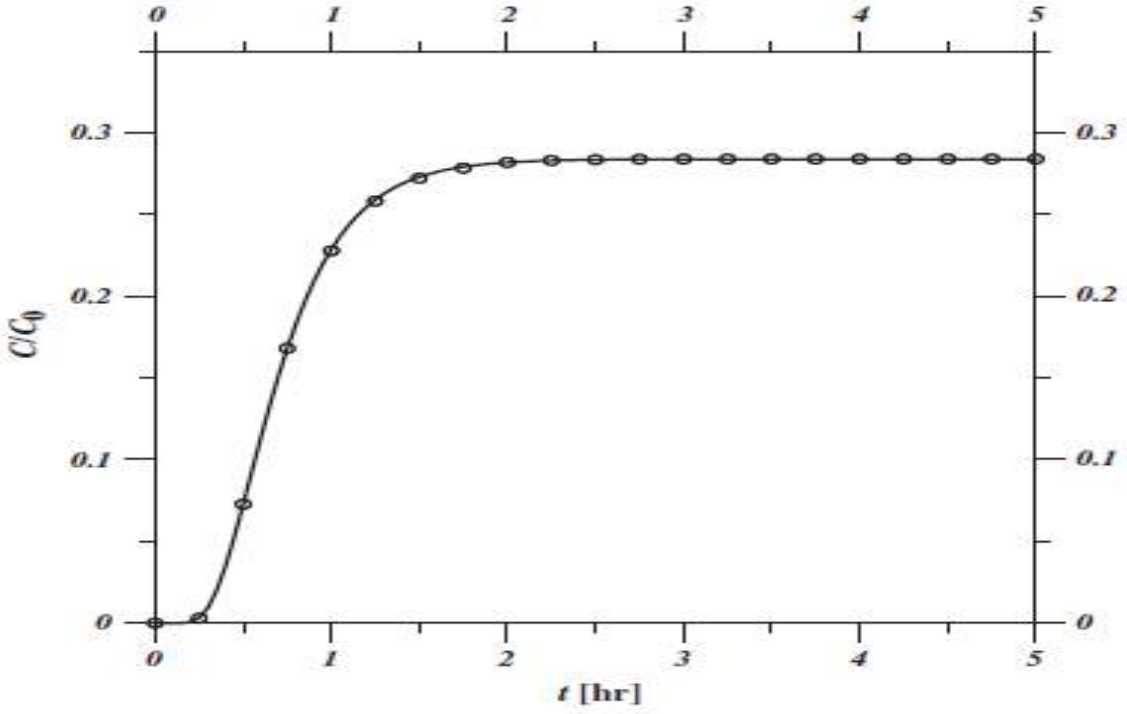

Figure 5.2: Break-through-curve for C/C_0 v/s time for z=10m, R=1.0, λ=0.5 & γ = 0

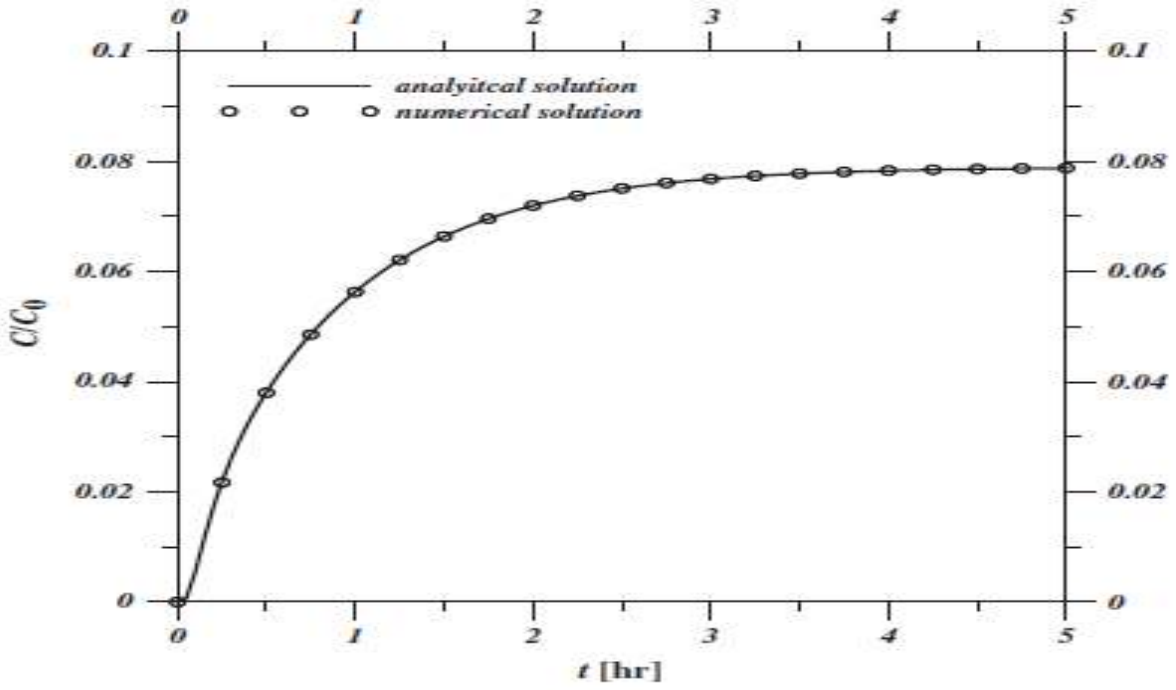

Figure 5.3: Break-through-curve for C/C_0 v/s time for z=10m, R=1.0, λ=0.5 & γ = 0.25

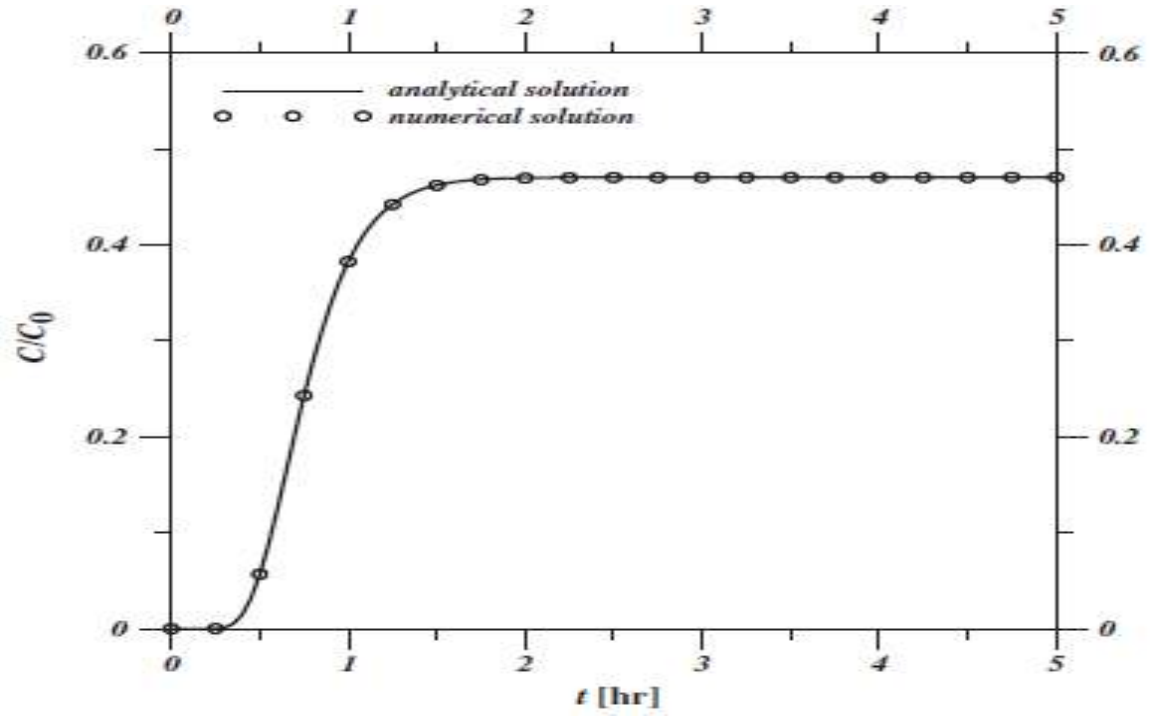

Figure 5.4: Break-through-curve for C/C_0 v/s time for z=10m, R=1.0, λ=0.5 & γ = 0.5

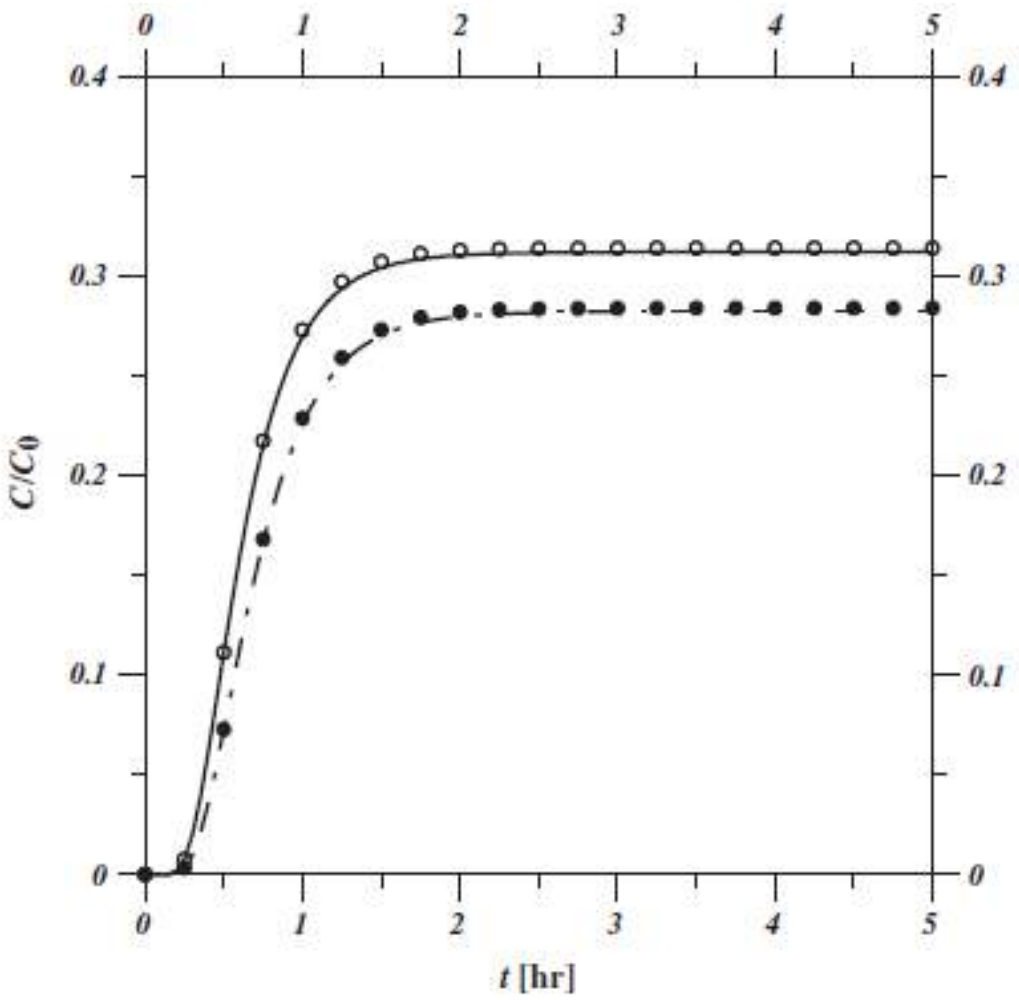

Figure 5.5: Break-through-curve for C/C_0 v/s time for z=10m, R=1.0, λ=0.5, γ = 0.75 & 1.0

IV. REFERENCES

[1]. Eaton, A.D., Cleseeri, L.S., and A.E. Greenberg (1995): Standard Methods. 19th Edition, APHD, AWWA and WEF, USA.

[2]. Feddes, R.A., Kabat, P., van Bakel, P.J.T., Bronswijk, J.J.B., and J. Halbertsma (1988): Modelling soil water dynamics in the unsaturated zone – State of the art. J. Hydrology. 100: 69-111.

[3]. Foussereau, X., Graham, W.D., G., AshieAkpoji, Destouni, G. and P.S.C. Rao (2000b): Stochastic analysis of transient flow in unsaturated heterogeneous soils under transient flow regimes. Water Resour. Res., 36(4) 911-921.

[4]. Foussereau, x., Grahan, W.D., and P.S.C. Rao (2000a): Stochastic analysis of transient flow in unsaturated heterogeneous soils. Water Resour. Res. 36 (4): 891-910.

[5]. Fowler, A.C. (1997): Mathematical Models in the Applied Sciences. Cambridge University Press. U.K.

[6]. Freeze, R.A., and J.A. Cherry (1979): Groundwater, Prantice Hall, Inc., New Jersey, USA
[7]. Fried, J.J., and M.A. Combarnous (1971): Dispersion in porous media. Advances in Hydro science (EDT: V.T. Chow). No. 7, pp. 170-282.
[8]. Gelhar, L.W., and M.A. Collins (1971): General analysis of longitudinal dispersion in nonuniform flow. Water Res. Res., 7(5): 1511-1521
[9]. Green, W.H., and G.A. Ampt, (1911): Studies on Soil Physics – I. Flow of air and water through soils. J. Agri. Res., 4: 1-24.
[10]. Grisak, G.E., and Pickens, J.F. Cherry (1980): Solute transport through fractured media, @ common study of fractured till. Water Resour. 16 (4): 731-739.
[11]. Haleman, D.R.F., and R.R., Rumer, Jr (1963): Longitudinal and lateral dispersion in an isotropic porous medium. J. Fluid Mech., 16: 1-12.
[12]. Hanks, R.J., Klute A., and E.Bresler (1969): A numerical methods for estimating infiltration, Redistribution drainage, and evaporation of water from soil. Water Resour. Res., 5(5): 1064-1069.
[13]. Hantush, M.M., Marino, M.A., and M.R. Islam (2000): Models for leaching of pesticides in soils and groundwater. J. of Hydrology, 227: 66-83.
[14]. Hillel, D.E. and Baker R.S. 1988: A descriptive theory of fingering during infiltration in to layered soils. Soil. Sci. 146: 51-56.
[15]. Horton, R.E. 1939: Analysis of run off-plot experiments with varying infiltration capacity. Trans. Amer. Geophys. Union 20: 693-711.
[16]. Horton, R.E., (1939): Approach towards a physical interpretation of infiltration capacity. Soil Sci. Soc. Of Am. Proc. 5: 399-395.
[17]. Hubbert, M. K (1956): Darcy's law and the field equations of the flow of underground fluids. Trans. Am. Inst. Mining Met. Engrs. 207, 222-239.
[18]. Hunt, B. (1998): Contaminant source solutions with scale-dependent dispersivities. J. Hydrologic Engg. 3 (4), 268-275.
[19]. Hutson, J.L., and A. Cass (1987): A retentively functions for use in soil-water simulation models. J. Soil Sci. 38; 105-113.

National Conference on Applied Sciences Synergising the Engineering and Technology
Print ISSN: 2395-6011 | Online ISSN: 2395-602X (www.ijsrst.com)
 | Volume 8 | Issue 2

Hirshfeld Surface Analysis and DFT Calculations of 2-Amino-N-(2-Fluorophenyl)-4,5,6,7-Tetrahydro-1-Benzothiophene-3-Carboxamide

Madhura TK[1], Rajesh BM[2], Chandra Kumar K[3], Shubha S[2], Chandra[4]

[1]Department of Physics, Mount Carmel College, Autonomous, Bengaluru, Karnataka, India

[2]Department of Physics, RV College of Engineering, Bengaluru, Karnataka, India

[3]Department of Engineering, Physics HKBK College of Engineering, Bengaluru, Karnataka, India

[4]Department of Physics, The National Institute of Engineering, Mysore, Karnataka, India

ABSTRACT

Thiophene nucleus has been established as a potential entity in the heterocyclic compounds possessing promising pharmacological characteristics such as anti-HIV PR inhibitors and anti-breast cancer activities. Importantly, benzothiophene derivative shows significant antimicrobial and anti-inflammatory activities. The title compound, $C_{15}H_{15}FN_2OS$ was characterized by single-crystal X-ray diffraction studies. The molecular conformation is consolidated by intramolecular N-H···F and N-H···O hydrogen bonds. The Hirshfeld surface analysis revealed that H···H and C···H contacts contribute significantly to the intermolecular interactions. Further, their structures were optimized by density functional theory (DFT) calculations using B3LYP hybrid functionals with 6-31G(d,p) level basis set. The transitions among the molecular orbital's were investigated using time-dependent density functional theory (TD-DFT) and the UV–Vis spectra showed the absorption peak at 306 nm. In addition, natural bond orbital (NBO) analysis was carried out to explore inter/intra molecular electron delocalization and hyperconjugative interactions responsible for the molecular structure stability.

Keywords - Hirshfeld, DFT and Thiophene

I. INTRODUCTION

Thiophene and its substituted derivatives are very important entity in the heterocyclic compounds shows a promising pharmacological characteristics. It possess various biological activities such as anti-bacterial, anti-inflammatory, anti-depressive, analgesic, anti-allergic, anti-fungal, antibacterial, anti-microbial and anti-cancer activities [1]. Due to its importance, the 2-amino-N-(2-fluorophenyl)- 4,5,6,7-tetrahydro-1-benzothiophene-3-carboxamide was synthesized and the molecular structure was studied using a X-ray diffraction method. The single crystal XRD analysis reveals that the title compound $C_{15}H_{15}FN_2OS$ crystallizes in the monoclinic system in Cc space group with the unit cell parameter a= 11.213 Å, b= 14.231 Å, c= 09.582 Å, $\alpha = 90°$, $\beta = 116.76°$ and $\gamma = 90°$, Z=4, V = 1365 $Å^3$ [2]. In addition, the combination between benzothiophene and other ring molecule was used in different pharmaceutical applications and the theoretical study on molecular geometry, vibrational,

pharmaceutical and electronic properties were carried out using DFT B3LYP hybrid functional [3]. Hirshfeld surface analysis was used to study intermolecular interactions in the heterocyclic compound [4].

II. COMPUTATIONAL METHOD

A. Hirshfeld SurfaceAnalysis

The Crystal Explorer 17.5 tool is used to perform Hirshfeld surface (HS) analysis to understand the intermolecular interactions and packing modes of the title compound $C_{15}H_{15}FN_2OS$ [5]. The CIF file data (CCDC No-1045467) obtained from the XRD measurements was used for performing the calculations. To quantify the intermolecular contacts present within the crystal structure of the compound, the HS and fingerprint plots were generated and analyzed. The contact distances d_{norm} is based on d_e and d_i, where d_e represents the distance between a point on the surface to the nearest nucleus outside the surface and d_i the distance between a point on the surface to the nearest nucleus inside the surface and it is calculated using the formula,

$$d_{norm} = \frac{d_i - r_i^{vdW}}{r_i^{vdW}} + \frac{d_e - r_e^{vdW}}{r_e^{vdW}}$$

Where, r_e^{vdW} and r_i^{vdW} are the vander Waal radii of the nearest nucleus outside and inside the surface.

B. DFT calculations

To understand the frontier molecular orbital energies of the compound $C_{15}H_{15}FN_2OS$, the structure is optimized by the Gaussian 16 package using the density functional theory (DFT) method with the basis set of B3LYP/6-31G(d,p) based on the single-crystal X-ray diffraction structure data (CCDC reference: 1045467) [6]. Comparative analysis of theoretically computed data with experimental data of the studied compound is obtained for better description. In addition, vibrational frequency calculations were conducted to get IR frequencies. Electronic properties such as energy of highest occupied molecular orbital (E_{HOMO}), lowest unoccupied molecular orbital (E_{LUMO}) and (E_{gap}) energy gap between HOMO and LUMO is measured with the visual representation is shown in fig. 8.

III. RESULTS AND DISCUSSION

A. Hirshfeld surface analysis

Hirshfeld Surface indicating d_{norm}, Shape index, Fragment patch and Curvdness of title compound $C_{15}H_{15}FN_2OS$ is as shown in the fig.1. The red spots indicate the strong intermolecular interactions with negative d_{norm} value where as light red spots shows the weak interactions. The blue regions correspond to longer contacts with positive d_{norm} value. A white region represents the distance of contact exactly equal to Van der Waal separation with a d_{norm} value of zero. The shape of electron density and surface around the molecular interactions is represented by shape index. The curvedness is a measure of the shape of the surface area of the molecule.

The 2D fingerprint plots of the title compound is as shown in fig. 2, highlighting the H...H contributing 47.3% of the overall crystal packing which has large hydrogen content of the molecule with the tip at 1.18Å, H...S contributing 10.8% having pair of spikes with tips at d_e+d_i =~2.9Å, H...C contributing 16.3% having pair of wings with one edge at d_e+d_i =~ 2.8Å and another at d_e+d_i =~ 23.42Å. These interactions are the primary contributors to the intermolecular stabilization in the crystal as shown in the fig.3 [7]. From the total contributions the H···H contacts has maximum and F···S has minimum contributions. Similarly the H-S, H-F, H-O, H-N, H-C, O-C, C-C, C-N, C-F, C-S and N-F contacts also contribute to the total area of the surface. The red and blue triangular patches on the same region of the shape index shows the π-π stacking [8]. Curvedness is a function of the root-mean-square curvature of the surface showing the flat areas having lower curvedness and sharp curvature having high curvedness. The calculated volume inside the Hirshfeld surface is 334.99 Å3 in the area of 307.19 Å2 with globularity (G) 0.759 as well as asphericity (U) 0.202. The overall calculation is performed with the Gaussian 16 integrated with Crystal Explorer.

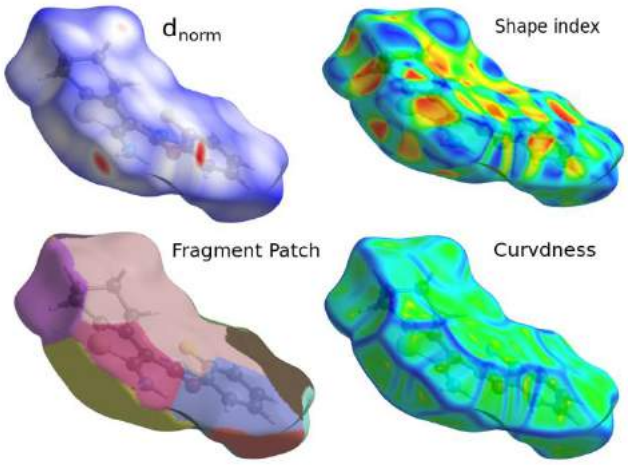

Fig. 1. Hirshfeld Surface d_{norm}, Shape index, Fragment patch and Curvdness of $C_{15}H_{15}FN_2OS$

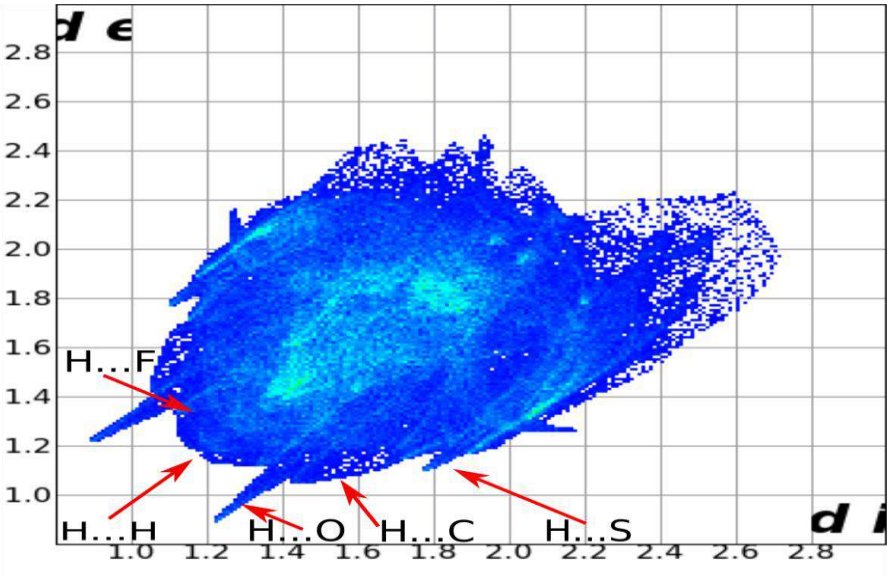

Fig. 2. The 2D fingerprint plot showing overall crystal packing.

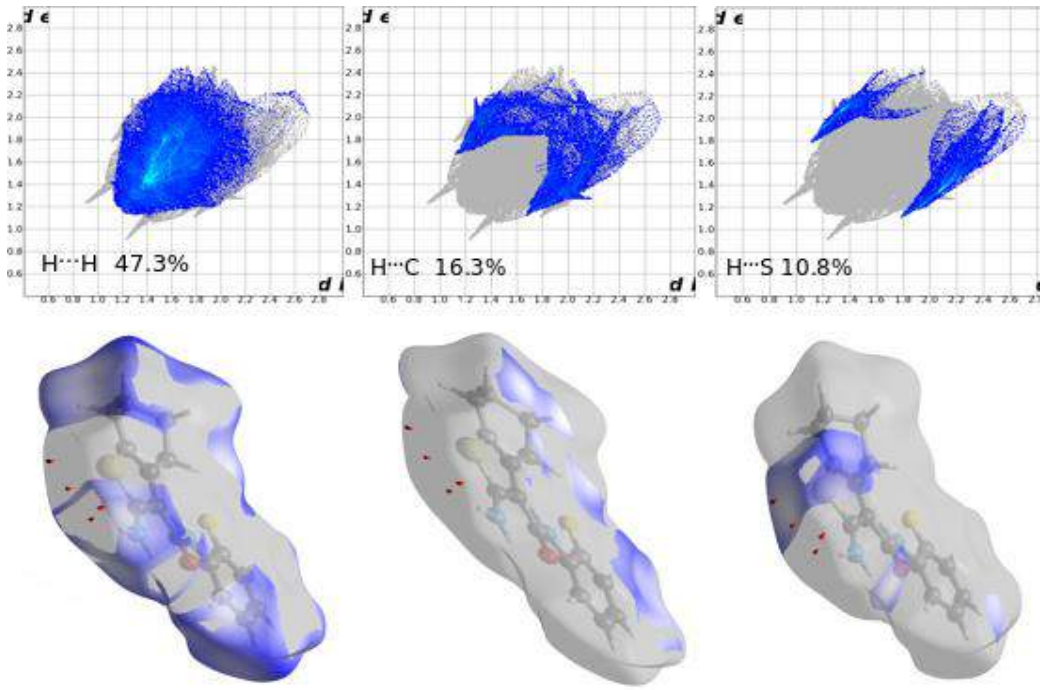

Fig. 3. The 2D fingerprint plots of H…H, H…C and H…S interactions with Hirshfeld surface.

Molecular electrostatic potential is used to visualize the active sites and the relative polarity of the molecule as shown in the fig. 4. The negative potential, red region is located over the terminal oxygen of the molecule.

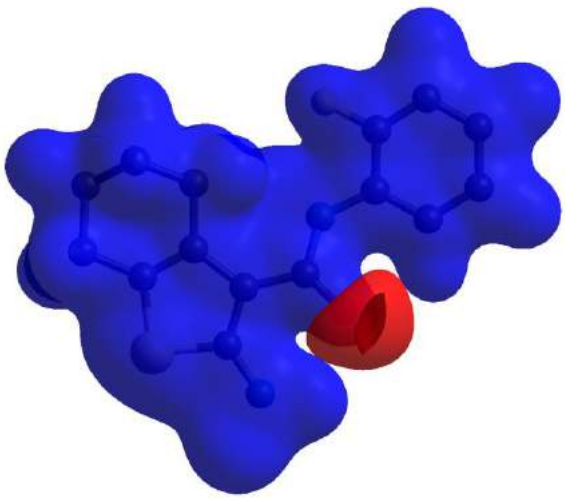

Fig. 4. Electrostatic Potential map of the molecule range 0.0500 to 0.0500 a.u. using the B3LYP/6-31G(d,p) Gaussian basis set at the DFT level of theory.

Interaction energy calculations:

The intermolecular interaction energies were calculated using the B3LYP/6–31G(d,p) basis set energy model in Crystal Explorer 17.5 [9], where a cluster of molecules is generated by applying crystallographic symmetry operations with respect to a selected central molecule within a default radius of 3.8 Å is as shown in fig. 5 [10]. The total intermolecular energy (E_{tot}) is the sum of electrostatic (E_{ele}), polarization (E_{pol}), dispersion (E_{dis}) and exchange-repulsion (E_{rep}) energies [11] with scale factors of 1.057, 0.740, 0.871 and 0.618, respectively.

Hydrogen bonding interaction energies (in kJ mol^{-1}) were calculated as -9.8(E_{ele}), -3.1 (E_{pol}), -64.2 (E_{dis}), 34.1 (E_{rep}) and -47.5 (E_{tot}) is tabulated in table 1.

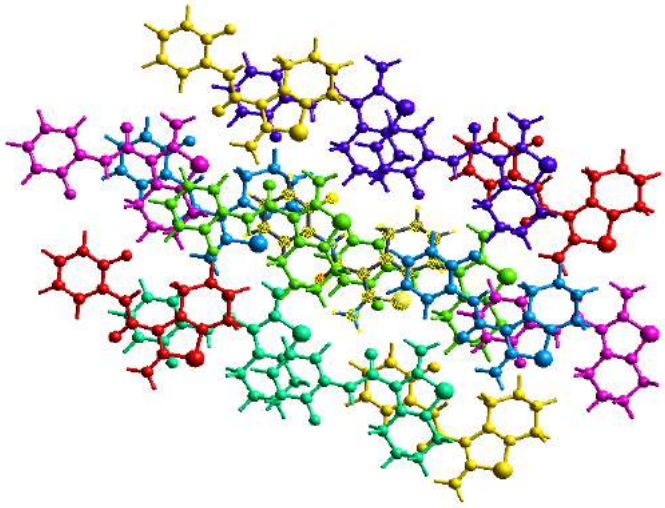

Fig. 5. Interaction energies for a 3.8Å cluster around the selected fragment.

TABLE 1: ENERGY FRAMEWORK DETAIL OF INTERACTION WITH COLOUR-CODED SYMMETRY OPERATIONS (SYMMOP) AND DISTANCES BETWEEN MOLECULAR CENTROIDS (R) IN Å.

	N	Symmop	R	Electron Density	E_{ele}	E_{pol}	E_{dis}	E_{rep}	E_{tot}
	2	x+1/2, y+1/2, z	11.20	B3LYP/6-31G(d,p)	-0.8	-0.1	-6.1	1.4	-5.4
	2	x+1/2, y+1/2, z	11.20	B3LYP/6-31G(d,p)	-2.7	-1.3	-10.5	6.8	-8.7
	2	x+1/2, -y+1/2, z+1/2	5.50	B3LYP/6-31G(d,p)	-9.8	-3.1	-64.2	34.1	-47.5
	2	x, -y, z+1/2	8.69	B3LYP/6-31G(d,p)	-24.9	-4.9	-17.7	26.4	-29.0
	2	x, y, z	9.58	B3LYP/6-31G(d,p)	-2.5	-0.9	-22.2	11.0	-15.8
	2	x, -y, z+1/2	8.47	B3LYP/6-31G(d,p)	-3.4	-0.5	-24.1	12.5	-17.2
	2	x+1/2, -y+1/2, z+1/2	12.86	B3LYP/6-31G(d,p)	-1.6	-0.2	-11.3	7.7	-6.9

B. DFT calculations

Geometry optimization of the compound

The optimized structure and its atoms numbering with Milliken charges are displayed in Fig. 6. The optimized geometry is correlated with the crystallographic data of the title compound and the correlation coefficient of 0.969 and 0.952 for bond length and the bond angles respectively is tabulated in the table 2 and 3. The overall energy minimum of 2-amino-N-(2-fluorophenyl)-4,5,6,7-tetrahydro-1-benzothiophene-3-carboxamide is -1263.44 Hartree with Dipole moment (μ)1.6989 Debye as calculated with B3LYP/6-31G(d,p) basis set. The optimization studies shows that the molecule be appropriate to C_1 symmetry point group.

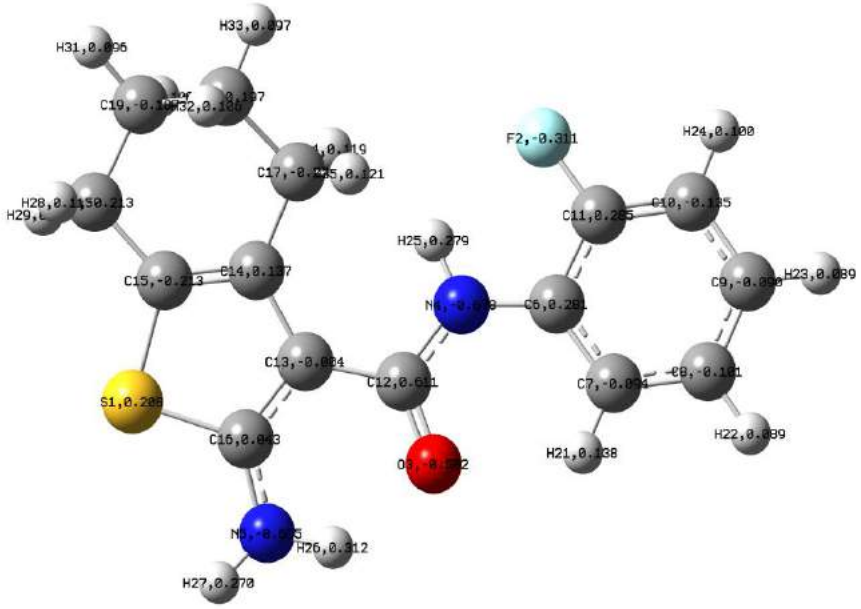

Fig. 6. Optimized structure with Mulliken charges.

Spectroscopic measurement

UV-visible spectrum analysis

Theoretical UV-visible spectrum calculation has been carried out to have better understanding of charge delocalization pattern, electron densities of the atoms, electron transition and stability of the title molecule [12]. In the present study, the maximum absorption wavelengths (λ_{max}), excitation energies (ΔE) and oscillator strengths (f) of the title molecule in the gaseous phase are computed using the TD DFT/B3YLP/6-31G(d,p) basis set level. The simulated UV-visible spectrum of the title molecule is shown in fig. 7 and the molecule have three maximum absorption peaks at 263.4, 284.9 and 306.9 nm with oscillator strengths 0.0288, 0.0038 and 0.2292 a.u respectively. The observed peaks in the spectrum are due to one electron excitation from HOMO-LUMO (ΔE=0.164 eV) is shown in fig. 8, HOMO-1-LUMO (ΔE=0.194 eV) and HOMO-2-LUMO (ΔE=0.221 eV).

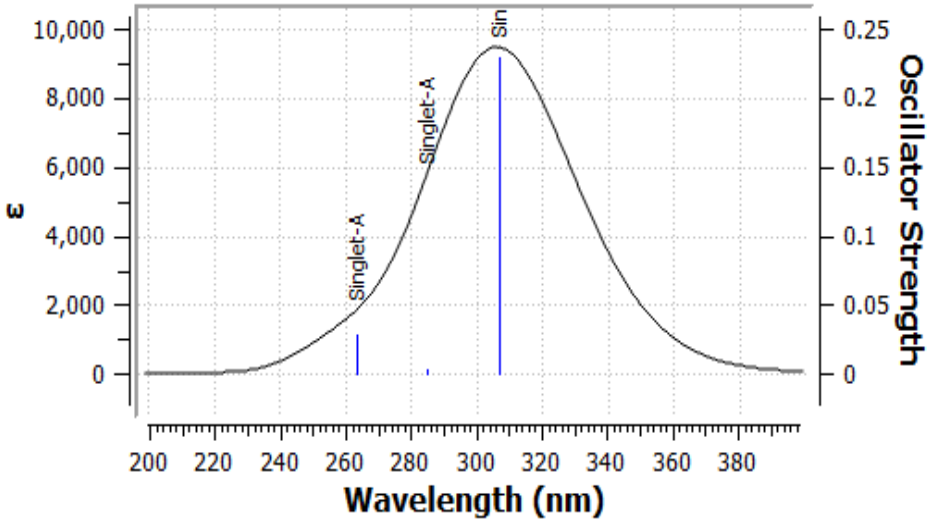

Fig. 7. UV-visible spectrum

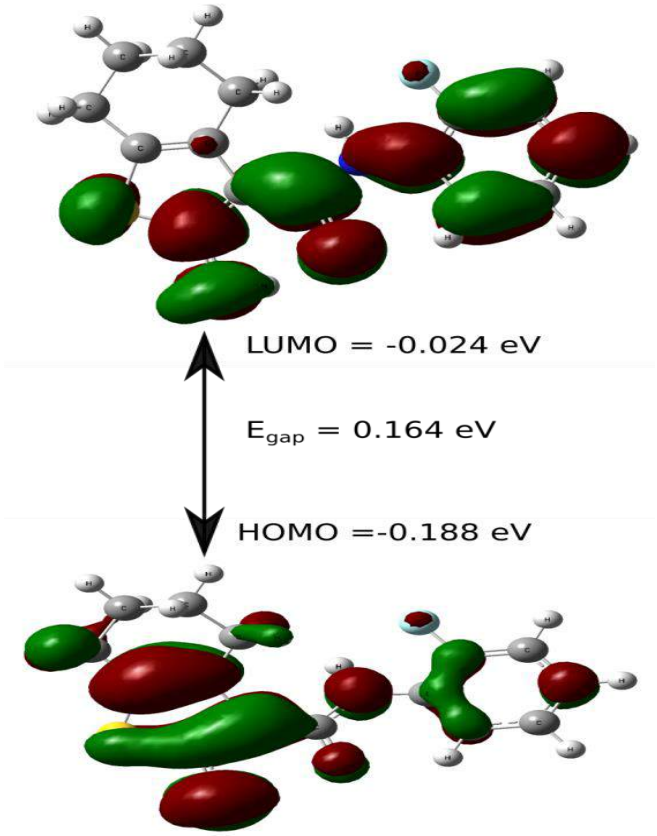

Fig. 8. HOMO, LUMO and E_{gap} of the title molecule.

IR Spectrum analysis

Theoretically calculated IR spectrum is as shown in fi. 9. In the IR spectrum the strong absorption band at 3478 cm^{-1} indicates the presence of amide NH and two peaks at 3666, 3690 cm^{-1} for the presence of amide NH^2 group. Peak at 1635 cm^{-1} shows the C=O stretching.

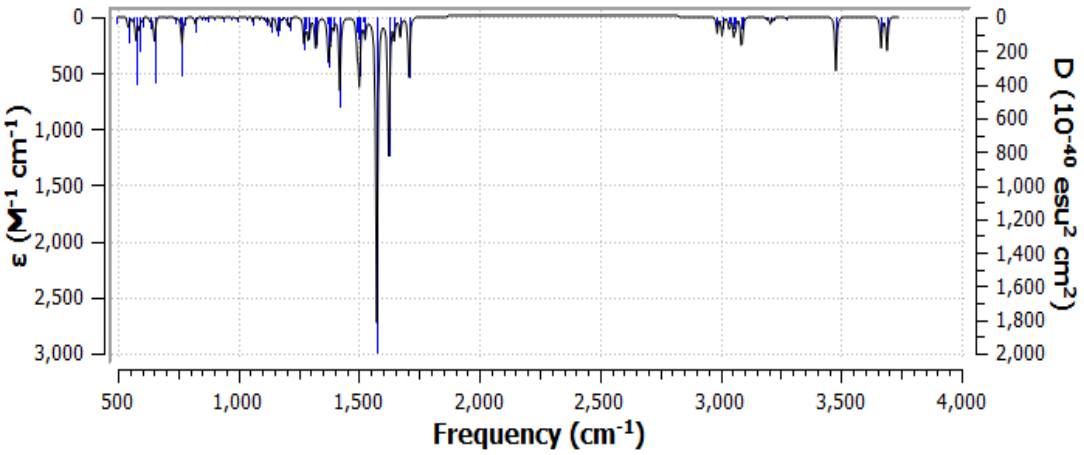

Fig. 9. IR spectrum

The electrostatic potential of the crystal can be analysed by obtaining the positive and negative charge distribution. This Molecular Electrostatic potential (MEP) from -4.68×10^{-2} to 4.68×10^{-2} is obtained using B3LYP/6-31G(d,p). In fig.10 the red colour indicates is the maximum negative region providing the site for electrophilic attack and the blue colour indicates maximum positive region providing the site for nucleophilic

attack. This MEP map shows that there is electrophilic site localised at O(3) atom and nucleophilic site located at H(27). This shows that the most reactive site of the molecule is the site containing the oxygen [13].

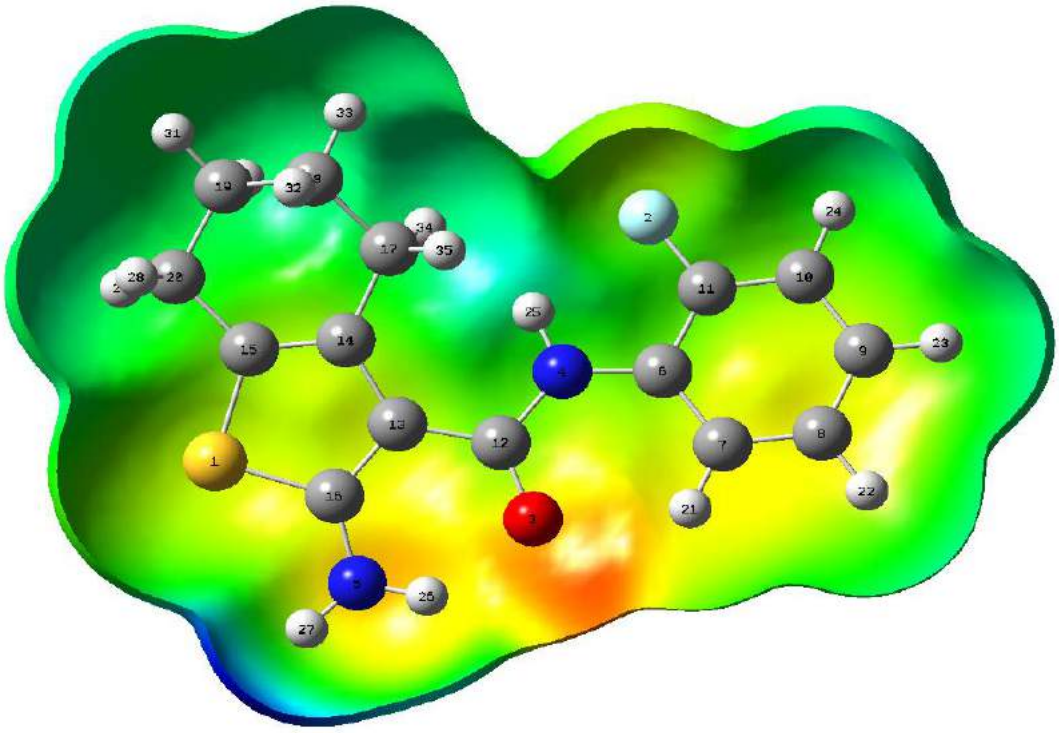

Fig. 10. 3D-representation of the electrostatic potential around the molecule using the Density Functional Theory at B3LYP level of theory at 6-31G(d,p).

Natural Bond Orbital Analysis

The most possible accurate "natural Lewis structure" is obtained by natural bond orbital (NBO) analysis. It gives the information about interactions in both filled and virtual orbital spaces enhancing the possible intra and intermolecular hydrogen bond. With the help of NBO, shifting of charges from the filled bonding molecular orbital to empty non bonding molecular orbital can easily be indicated. The following equation gives stabilization energy (electronic delocalization). In the given equation, q_i is orbital occupancy, ε_i and ε_j are diagonal NBO Fock matrix elements and f_{ij} is off diagonal NBO Fock matrix element respectively [14].

$$E^2 = q_i \frac{f_{ij}^2}{\varepsilon_j - \varepsilon_i}$$

IV. REFERENCES

[1]. B. Pramodh, K. C. Prathap, M. Hema, I. Warad, and N. Lokanath, "Synthesis, structure, quantum computational and biological studies of novel thiophene derivatives," Journal of Molecular Structure, p. 129587, 2020.

[2]. K. Chandra Kumar, V. Umesh, T. Madhura, B. Rajesh, and Chandra, "Crystal structure of 2-amino-N-(2-fluorophenyl)-4, 5, 6, 7-tetrahydro-1-benzothiophene-3-carboxamide," Acta Crystallographica Section E: Crystallographic Communications, vol. 71, pp. o807-o808, 2015.

[3]. A. Sagaama and N. Issaoui, "Design, molecular docking analysis of an anti-inflammatory drug, computational analysis and intermolecular interactions energy studies of 1-benzothiophene-2-carboxylic acid," Computational biology and chemistry, vol. 88, p. 107348, 2020.

[4]. A. V. Ivachtchenko, O. D. Mitkin, D. V. Kravchenko, S. M. Kovalenko, S. V. Shishkina, N. D. Bunyatyan, I. S. Konovalova, I. G. Dmitrieva, V. V. Ivanov, and T. Langer, "Synthesis, X-ray crystal structure, Hirshfeld surface analysis, and molecular docking study of novel inhibitor of hepatitis B: Methyl 4-fluoro-3-(morpholinosulfonyl) benzo b] thiophene-2-carboxylate," Heliyon, vol. 5, p. e02738, 2019.

[5]. M. A. Spackman and D. Jayatilaka, "Hirshfeld surface analysis," CrystEngComm, vol. 11, pp. 19-32, 2009.

[6]. M. Frisch, "Gaussian 09 Revision D. 01; b) MJ Frisch, GW Trucks, HB Schlegel, GE Scuseria, MA Robb, JR Cheeseman, G. Scalmani, V. Barone, GA Petersson, H. Nakatsuji et al," Gaussian 16 Revision A, vol. 3, 2016.

[7]. L. H. Al-Wahaibi, J. Joubert, O. Blacque, N. H. Al-Shaalan, and A. A. El-Emam, "Crystal structure, Hirshfeld surface analysis and DFT studies of 5-(adamantan-1-yl)-3-(4-chlorobenzyl) sulfanyl]-4-methyl-4 H-1, 2, 4-triazole, a potential 11β-HSD1 inhibitor," Scientific reports, vol. 9, pp. 1-11, 2019.

[8]. K. Azouzi, B. Hamdi, R. Zouari, and A. B. Salah, "Synthesis, structure and Hirshfeld surface analysis, vibrational and DFT investigation of (4-pyridine carboxylic acid) tetrachlorocuprate (II) monohydrate," Bulletin of Materials Science, vol. 40, pp. 289-299, 2017.

[9]. M. Turner, J. McKinnon, S. Wolff, D. Grimwood, P. Spackman, D. Jayatilaka, and M. Spackman, "CrystalExplorer17; University of Western Australia: Crawley, Australia, 2017," Google Scholar There is no corresponding record for this reference, 2017.

[10]. M. J. Turner, S. Grabowsky, D. Jayatilaka, and M. A. Spackman, "Accurate and efficient model energies for exploring intermolecular interactions in molecular crystals," The journal of physical chemistry letters, vol. 5, pp. 4249-4255, 2014.

[11]. M. J. Turner, S. P. Thomas, M. W. Shi, D. Jayatilaka, and M. A. Spackman, "Energy frameworks: insights into interaction anisotropy and the mechanical properties of molecular crystals," Chemical Communications, vol. 51, pp. 3735-3738, 2015.

[12]. V. Balachandran, T. Karthick, S. Perumal, and A. Nataraj, "Comparative theoretical studies on natural atomic orbitals, natural bond orbitals and simulated UV-visible spectra of N-(methyl) phthalimide and N-(2 bromoethyl) phthalimide," 2013.

[13]. R. Rahmani, N. Boukabcha, A. Chouaih, F. Hamzaoui, and S. Goumri-Said, "On the molecular structure, vibrational spectra, HOMO-LUMO, molecular electrostatic potential, UV–Vis, first order hyperpolarizability, and thermodynamic investigations of 3-(4-chlorophenyl)-1-(1yridine-3-yl) prop-2-en-1-one by quantum chemistry calculations," Journal of Molecular Structure, vol. 1155, pp. 484-495, 2018.

[14]. M. Khalid, M. N. Arshad, M. N. Tahir, A. M. Asiri, M. M. Naseer, M. Ishaq, M. U. Khan, and Z. Shafiq, "An efficient synthesis, structural (SC-XRD) and spectroscopic (FTIR, 1HNMR, MS spectroscopic) characterization of novel benzofuran-based hydrazones: An experimental and theoretical studies," Journal of Molecular Structure, vol. 1216, p. 128318, 2020.

TABLE 2: BOND ANGLES FROM X-RAY CRYSTALLOGRAPHY AND USING B3LYP/6-31G(D,P) BASIS SET

Atom1	Exp (X-ray)	B3LYP	Atom	Exp (X-ray)	B3LYP
C15-S1-C16	91.9(1)	91.5	C11-C12-C17	127.1(2)	126.75
C1-N8-C9	129.3(2)	128.49	C13-C12-C17	119.3(3)	119.78
C1-N8-H9A	115.3	113.74	S14-C13-C12	111.6(2)	111.73
C9-N8-H9A	115.4	117.67	S14-C13-C20	120.3(2)	120.95
C15-N16-H15C	120	113.12	C12-C13-C20	128.1(3)	127.3
C15-N16-H15D	120.1	119.1	S14-C15-N16	118.8(2)	120.52
H15C-N16-H15D	119.9	119.31	S14-C15-C11	111.5(2)	111.8
N8-C1-C2	125.8(2)	126.4	N16-C15-C11	129.6(3)	127.6
N8-C1-C6	117.1(2)	116.27	C12-C17-C18	111.9(2)	112.44
C2-C1-C6	117.1(3)	117.33	C12-C17-H22A	109.2	110.11
C1-C2-C3	119.9(3)	119.86	C12-C17-H22B	109.2	110.31
C1-C2-H2A	120	118.66	C18-C17-H22A	109.3	108.62
C3-C2-H2A	120.1	121.47	C18-C17-H22B	109.3	108.63
C2-C3-C4	121.0(3)	121.42	H22A-C17-H22B	107.9	106.54
C2-C3-H3A	119.5	118.74	C17-C18-C19	111.7(2)	111.68
C4-C3-H3A	119.5	119.84	C17-C18-H21A	109.3	109.1
C3-C4-C5	119.8(3)	119.45	C17-C18-H21B	109.3	109.32
C3-C4-H4A	120.1	120.69	C19-C18-H21A	109.3	109.13
C5-C4-H4A	120.1	119.86	C19-C18-H21B	109.3	110.71
C4-C5-C6	118.6(3)	118.57	H21A-C18-H21B	107.9	106.78
C4-C5-H5A	120.6	122.33	C18-C19-C20	112.1(3)	110.52
C6-C5-H5A	120.8	119.1	C18-C19-H20A	109.1	109.43
F7-C6-C1	117.0(2)	117.14	C18-C19-H20B	109.1	110.63
F7-C6-C5	119.4(3)	119.5	C20-C19-H20A	109.2	109.43
C1-C6-C5	123.6(3)	123.36	C20-C19-H20B	109.2	109.8
O10-C9-N8	120.4(3)	120.77	H20A-C19-H20B	107.9	106.96
O10-C9-C11	122.8(3)	122.12	C13-C20-C19	109.8(2)	109.99
N8-C9-C11	116.8(2)	117.11	C13-C20-H18A	109.7	110.28
C9-C11-C12	129.8(2)	130.31	C13-C20-H18B	109.8	110.65
C9-C11-C15	118.7(2)	118.18	C19-C20-H18A	109.7	109.68
C12-C11-C15	111.5(2)	111.5	C19-C20-H18B	109.7	110.1
C11-C12-C13	113.5(3)	113.44	H18A-C20-H18B	108.2	106.07

TABLE 3: BOND LENGTHS FROM CALCULATIONS USING X-RAY CRYSTALLOGRAPHY AND B3LYP/6-31G(D,P) BASIS SET

Atom	Exp (X-ray)	B3LYP	Atom	Exp (X-ray)	B3LYP	Atom	Exp (X-ray)	B3LYP
S14-C13	1.749(3)	1.7631	C2-C3	1.387(5)	1.3966	C13-C20	1.497(4)	1.503
S14-C15	1.734(4)	1.7495	C2-H2A	0.93	1.0797	C17-C18	1.530(4)	1.539
F7-C6	1.357(3)	1.3643	C3-C4	1.382(6)	1.3943	C17-H22A	0.97	1.102
O10-C9	1.238(3)	1.2428	C3-H3A	0.93	1.0857	C17-H22B	0.969	1.0964
N8-C1	1.400(4)	1.4014	C4-C5	1.370(5)	1.3974	C18-C19	1.505(6)	1.5321
N8-C9	1.377(3)	1.3809	C4-H4A	0.93	1.0851	C18-H21A	0.97	1.0976
N8-H9A	0.859	1.0073	C5-H5A	0.929	1.0845	C18-H21B	0.97	1.0953
N16-C15	1.350(4)	1.3587	C9-C11	1.449(4)	1.4723	C19-C20	1.525(4)	1.5372
N16-H15C	0.861	1.0178	C11-C12	1.460(4)	1.461	C19-H20A	0.97	1.0976
N16-H15D	0.86	1.0076	C11-C15	1.387(4)	1.3977	C19-H20B	0.97	1.0954
C1-C2	1.386(4)	1.4034	C12-C13	1.346(4)	1.3624	C20-H18A	0.971	1.1002
C1-C6	1.388(4)	1.4041	C12-C17	1.516(4)	1.5169	C20-H18B	0.97	1.0972

National Conference on Applied Sciences Synergising the Engineering and Technology
Print ISSN: 2395-6011 | Online ISSN: 2395-602X (www.ijsrst.com)
© 2021 IJSRST | Volume 8 | Issue 2

Electrochemical Properties of Cobalt Doped $GdAlO_3$

P.K. Jisha[1], Sumitha. K.S[2], S.C. Prashantha[3]

[1]Department of Physics, New Horizon College of Engineering, New Horizon College of Engineering Bangalore, Karnataka, India

[2]Department of Physics, East Point College of Engineering & Technology, East Point College of Engineering & Technology, Bangaluru, Karnataka, India

[3]Department of Science, East West Institute of Technology East West Institute of Technology Bangaluru, Karnataka, India

ABSTRACT

Nanocrystalline (GAG) $GdAlO_3:CO^{2+}$is prepaid by combustion process. The morphology, structure and particle size of the prepared $GdAlO_3:CO^{2+}$sample characterized by transmission electron microscope (TEM) image. The cyclic voltammetry (CV) and electrochemical impedance spectroscopy (EIS) studies clearly indicate that Co^{2+} dopant was successful doping material due to increasing the reversibility by reducing the E_O-E_R value of the electrode reaction. The R_{Ct} and double layer capacitance of the electrodes were recognized by fitting the equivalent circuit for EIS spectrum. $GdAlO_3:Co^{2+}$composite material could be a promising electrode material for the fabrication of super capacitors.

Keywords : Perovskite, GAG, TEM, Cyclic Voltammetry (CV) , Electrochemical Impedance Spectroscopy(EIS)

I. INTRODUCTION

Nanomaterials have attracted attention due to their interesting properties and potential application in many important areas such as: microelectronics, sensing, environmental remediation, biomedicine etc. Generally, the properties of these materials are due to their high quantum yield, high molar extinction coefficient, broad absorption spectra ranging from ultraviolet to near-infrared with narrow fluorescence emission in the visible region [1]. which generate interest in the synthesis of nanoparticles .Study of $GdAlO_3$ nanoparticles are attractive for nanoscience as well as for nanotechnology applications on photoluminescence, semiconductors, photocatalysists, gas sensors, UV photodetector, light emitting diodes (LEDs), solar cells etc [2,3].

In 21st century energy is a fundamental worldwide issue for the human society .Energy we needed is provided by fossil fules.But it is not renewable and also it emits pollutants while burning which degrade the environment and greenhouse gases lead to global warming problem[4,5]. Such frameworks require the advantages of compactness and energy effectiveness while being environmental friendly [6]. The technology and systems of an external thermal interface or that of an external electrical interface embrace by Energy

conversion and storage systems [7] .Based on amount of energy and power available for the load they are categorised into groups which includes batteries, fuel cells, capacitors and supercapacitors [8].

In order to study the effect of cation dopant on the structure , Cyclic Voltammetry and ac impedence of perovskite $GdAlO_3$, In this paper $GdAlO_3:CO^{2+}$ prepaired by solution combustion method [17]and observed its characteristics and study of cyclic voltammetry (CV), electrochemical impedance spectroscopy (EIS)[9] in presence and absence of Paracetamol in1MKOH electrolyte.

II. EXPERIMENTAL

2.1 Preparation of sample

$GdAlO3:CO^{2+}$ (15mol) synthesised using the solution combustion method by using stoichiometric quantities of gadolinium nitrate [Gd $(NO_3)_3$], aluminium nitrate (Al $(NO_3)_2$**,** cobalt nitrate CO $(NO_3)_2$, laboratory prepared Oxalyl dihydrazide (ODH:$C_2H_6N_4O_2$) fuel were dissolved in doubled distilled water. A homogeneous solution obtained after stirring 15min. The resultant solution was placed in a furnace pre heated at 400^oC for, until surplus free water evaporated and natural ignition occurred ensuing in a fine powder product obtained after grinding. Finally, the as prepared powders were calcined at 1000^oC for 3 h. The resulting $GdAlO_3:CO^{2+}$powder were cooled down to room temperature and mixed well by using a pestle and mortar.

2.2 Preparation of the modified electrode

The sample, graphite powder and silicone oil ratio was 15:70:15 % by weight and were mixed in an agate mortar for about 40 min. the carbon paste was packed in to the of homemade carbon paste electrode and then smoothened on a tissue paper till the surface become uniform.

III. RESULTS AND DISCUSSION

3.1 Transmission Electron Microscope (TEM)

In order to determine the morphology of the sample, typical transmission electron microscopy (TEM) measurements were carried out and are presented in Fig. 1. represent the TEM micrograph of $GdAlO_3$ containing 15mol % of CO^{2+} It is clear from Figure 1 that irregular to round shaped, nanophosphors with particle size 100nm were formed

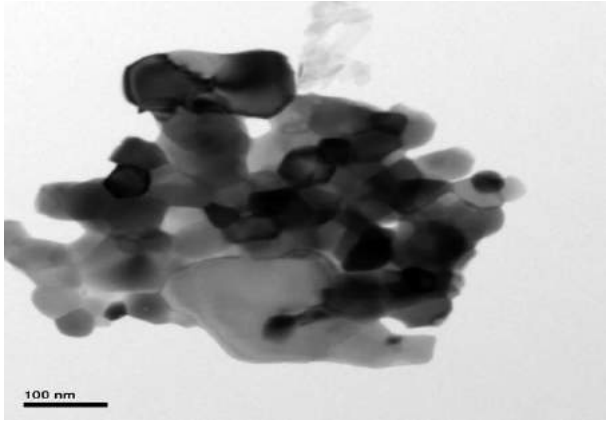

Fig 1. TEM images CO^{2+}doped $GdAlO_3$.

3.2 CYCLIC VOLTAMMETRY

Cyclic voltammograms (CVs) analysis used for understand the electrochemical performance of the Cobalt doped $GdAlO_3$ electrode for super capacitor during charging and discharging processes. In order to understand the effect of various mol concentrations on the electrochemical performance of $GdAlO_3:CO^{2+}$ nanoporous carbon electrodes, the CV experiments were conducted for the electrodes with different mol concentration. Fig.2 successively represents the CV cures for $GdAlO_3:CO^{2+}$ (15mol%) electrodes at different scan rates (10, 20, 30, 40 and 50 mVs^{-1})in 1 M KOH electrolyte and with 2 ml of Paracetamol electrolyte concentration using a platinum wire as counter electrode and Ag/AgCl as a reference electrode in the potential window between –0.1 and 0.6 V[10]. Here, the capacitance was mainly based on the redox reaction because the shapes of the CVs were distinguished from the shape of the electric double-layer capacitance, which is normally close to an ideal rectangle [11,12].

The quantification of charge efficiency, charge-discharge of electrodes and the reversibility of the electrode reaction were carried out using cyclic voltammetry. The reversibility of the electrode reaction was measured by taking into account the difference between the oxidation potential (E_O) and the reduction potential (E_R) [13] at 20 mV/s scan rate. Smaller the value of E_O-E_R, more reversible was the electrode reaction. This result shows the prepared electrode material is used for sensor applications.

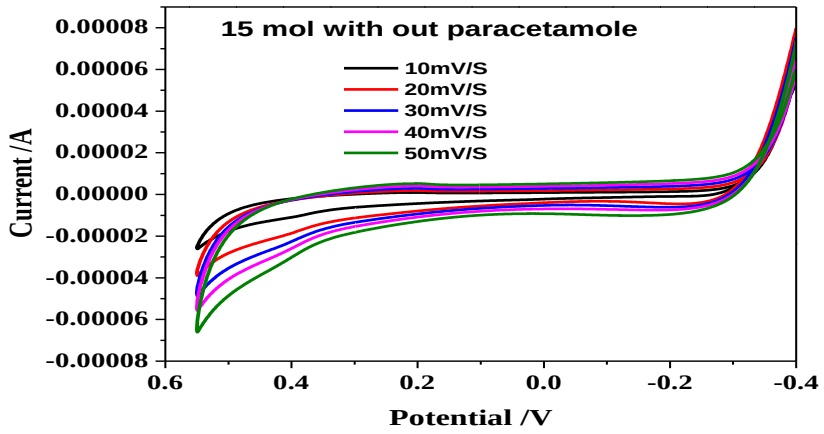

Fig.2. a) Cyclic voltammogram of Cobalt doped $GlAlO_3$ in 1M KOH electrolyte.

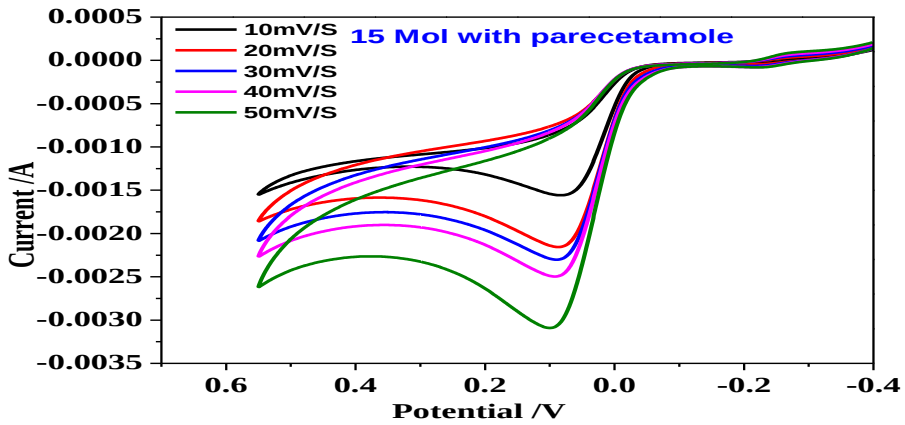

Fig.2 b) Cyclic voltammogram of Cobalt doped $GlAlO_3$ in 1M KOH electrolyte with 2 ml of Paracetamol

3.3 AC IMPEDENCE

Electrochemical impedance spectroscopy (EIS) measurements are very essential in assessing the resistive characteristics of the electrode. It shows the response of components performance in the frequency domain [14]. EIS were carried out with ac amplitude of 5 mv and frequency range of 1hz to 1Mhz in order to evaluate the frequency response of $GdAlO_3:CO^{2+}$(15mol%) electrode in 1 M KOH electrolyte and with 2 ml of Paracetamol. The Nyquist plots for the electrodes are depicted in Fig. 3The EIS data was analysed using Nyquist plots and each data point is at a different frequency. The Nyquist plots consists of two frequency regions, a high frequency region denoted by a semicircle which represents the transfer of charges occurring at the electrode/ electrolyte interface and the low frequency region signified by a straight line representing the diffusion of ions in the electrolyte. The equivalent series resistance (ESR) can be obtained from the x- intercept of the Nyquist plot and the charge transfer resistance Rct can be directly measured as the diameter of the semicircle arc on the real axis [15]. The ESR and Rct values of the electrochemical is indirectly proportional to results of the specific capacitance, specifically, the higher the Rct value, the lower the specific capacitance of the electrochemical capacitor . specific capacitance get affected due to the presence of paracetamol in the electrolyte

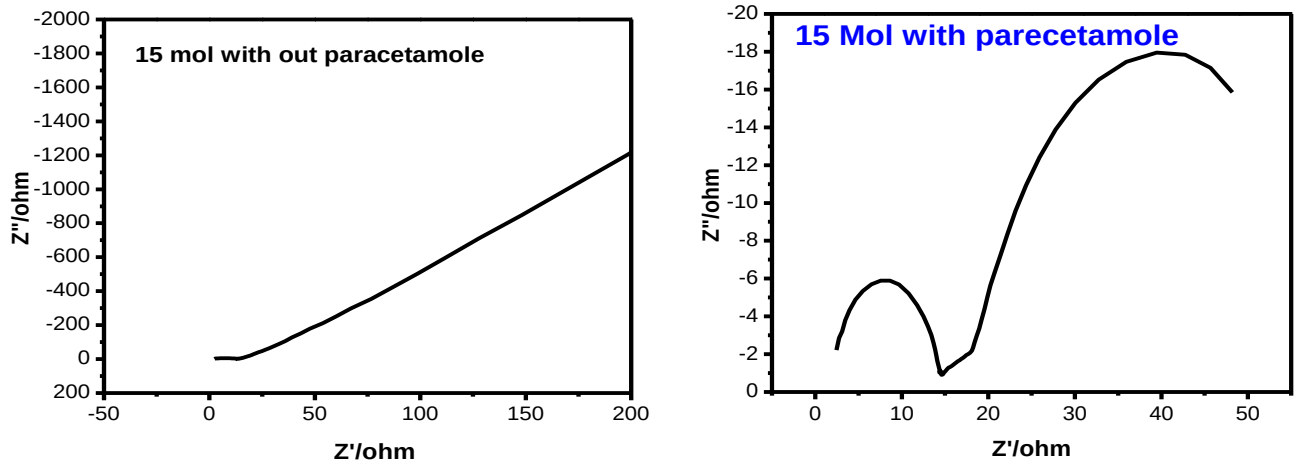

Fig.3.a) Nyquist plot with simulation of Cobalt doped $GdAlO_3$ in 1M KOH electrolyte .

b) Nyquist plot with simulation of Cobalt doped $GdAlO_3$ in 1M KOH electrolyte with 2 ml of Paracetamol

Table 1 Impedance parameters of $GdAlO_3:CO^{2+}$ and Oxidation potential (E_O), reduction potential (E_R), the difference between E_O and E_R

CO^{2+}mol%	ESR(Ω)	R_{ct}(Ω)	E_O(V)	E_R(V)	E_O-E_R(V)
15	15	13	-0.2	-0.300	-0.1
15 with parecetamol	14	11	0.08	-0.02	0.06

IV. CONCLUSION

Cobalt doped $GdAlO_3$ compositions were prepared by solution combustion method. The structure were analysed by TEM. The CV studies clearly indicate that Paracetamol additive were successful in increasing the reversibility by reducing the E_O-E_R value of the electrode reaction. Paracetamol additive enhances the

performance of the positive electrode by reducing the resistance of the $GdAlO_3:CO^{2+}$electrode. As a future perspective, we believe that $GdAlO_3:CO^{2+}$ composite material could be a promising electrode material for the fabrication of various sensors, super capacitors and solar cells .

V. REFERENCES

[1]. Jisha, P.K., Prashantha, S.C. and Nagabhushana, H., 20172(4), pp.437-444.
[2]. Hsu, C.L., Chen, K.C., Tsai, T.Y. and Hsueh, T.J., 2013182, pp.190-196.
[3]. Cao, T., Yang, Y., Gao, Y., Zhou, J., Li, Z. and Li, F., 2011. Biomaterials,32(11), pp.2959-2968
[4]. J. B. Goodenough,Y. Kim, Chem.Mater. 22 (2010) 587-603.
[5]. H. Li, Z. Wang, L. Chen, X. Huang, Adv. Mater. 21 (2009) 4593-4607.
[6]. L. Dong, R. R. S. Gari, Z. Li, M. M. Craig, S. Hou, Carbon 48 (2010) 781–787.
[7]. J. Baker, Energy Policy 36 (2008) 4368–4373.
[8]. T. Christen, M. W. Carlen, J. Power Sources 91 (2000) 210–216.
[9]. A. H. Zimmerman , P. K. Effa, J Electrochem Soc .131(1984)709-713
[10]. X. Cao, J. Wei, Y. Luo, Z. Zhou, Y. Zhang, Int. J. Hydrogen Energy 25 (2000) 643– 647
[11]. I. Krejci, P. Vanysek, J. Power Sources 47 (1994) 79–88.
[12]. C. R. Ravi kumara, P. Kotteeswaran, V. Bheema Raju, A. Murugan, M. S. Santosh, H. P. Nagaswarupa, S. C. Prashantha, M. R. Anil Kumar, M. S. Shivakumar, Journal ofEnergy Storage 9 (2017) 12–24
[13]. J. Wang, Z. Gao, Z. Li, B. Wang, Y. Yan, Q. Liu, T. Mann, M. Zhang, Z. Jiang, J. Solid State Chem. 184 (2011) 1421–1427.
[14]. Y. Wu, S. Liu, H. Wang, X. Wang, X. Zhang, G. Jin, Electrochim. Acta 90 (2013) 210–218.
[15]. L. Deng, Z. Hao, J. Wang, G. Zhu, L. Kang, Z.-H. Liu, Z. Yang, Z. Wang, Electrochim. Acta 89 (2013) 191–198.

National Conference on Applied Sciences Synergising the Engineering and Technology
Print ISSN: 2395-6011 | Online ISSN: 2395-602X (www.ijsrst.com)
© 2021 IJSRST | Volume 8 | Issue 2

Investigations on Non Linear Optical Crystal ADP Doped With Inorganic Compounds

G. Maruthi[1], R. Ananda Kumari[2], R. Chandramani[3]

[1]Department of Physics, Jawaharlal Nehru Technological University, Anantapur, Andhra Pradesh, India

[2]Department of Physics, Sree Siddaganga College for Women, Tumkur, Karnataka, India

[3]Department of Physics, Dayananda sagar college of Engineering, Bangalore, Karnataka, India

ABSTRACT

Ammonium dihydrogen phosphate well known as ADP is a non-linear optical material having wide applications in non-linear and integrated optics. With appropriate dopants, the ADP crystals exhibit several properties. The behavior of these crystals in radiation fields is also of importance, for technology of the radiation induced formation of the optical wave guide (in these crystals). In the present work pure ADP and ADP doped with inorganic compounds like ferrous sulphate, Nickel chloride and Cuprium chloride have been investigated. Crystals were grown from supersaturated solution at room temperature by natural evaporation process. Grown crystals were characterized using X-ray diffraction and EDAX. The grown crystals were subjected to hardness studies to know the mechanical properties of NLO crystals which is essential for understanding the origin of laser induced damage in them. Hardness is calculated by Vicker's method. It has been observed that hardness increases in these crystals with load and the cracking has developed around 50gm. Dielectric constant and Dielectric loss is measured as a function of frequency. Study confirms the contribution of space charge polarization.

Keywords: - NLO crystals, Microhardness, Dielectric constant, Dielectric loss, Polarization, SHG efficiency.

I. INTRODUCTION

In the last few decades, significant advances have been made in the field of non-linear optics and optical computing. Since the invention of the first laser, the frequency conversion of laser radiation in nonlinear optical (NLO) crystals has become an important technique widely used in quantum electronics and laser physics for solving various scientific and engineering problems. Use of NLO materials makes it possible to extend the optical frequency range from ultraviolet to infrared. Non linear optical crystal ammonium dihydrogen orthophosphate (ADP) has gained considerable importance in recent years because of its non-linear, ferroelectric, piezoelectric and electro-optic properties.

We have made an attempt to modify ADP crystals by adding inorganic compounds like ferrous sulphate, Nickel chloride and Cuprium chloride in definite ratios with the aim of discovering new useful materials for

academic and industrial use. Present paper reports the studies of Vickers microhardness and dielectric constant of solution grown ADP crystals containing $FeSO_4$, $NiCl_2$ and $CuCl_2$.

II. METHODS AND MATERIAL

2.1 CRYSTAL GROWTH

Single crystals were grown from supersaturated solution at room temperature by natural evaporation process using AR grade samples of ADP, $FeSO_4$, $NiCL_2$ and $CuCl_2$.

ADP was added with $FeSO_4$, $NiCl_2$ and $CuCl_2$. Separately, each in definite molecular ratio, viz. ADP: X (X represents dopants added in one molar weight i.e. in 10:1 ratio).

Grown crystals were found to be transparent and exhibited **scalenohedral** (twelve sided polyhedron) morphology. Crystals with high transparency were used for microhardness and dielectric measurements.

The Grown crystals were characterized using X-ray diffraction and energy dispersive X-ray spectroscopy (EDAX). Data confirms that the impurities have entered into the lattice of the ADP

2.2 DIELECTRIC MEASUREMENTS

The extended portions of the crystals were removed completely and the samples were ground to proper thickness and polished. The final dimensions of the samples were about 1.5 to 2 sq.cm and 0.1 to 0.3 cm in thickness. Each sample was electroded on either side with air-drying silver paste so that it behaved like a parallel plate capacitor. A 4275A, Multi frequency LCR meter (Hewlett-Packard) was used to measure capacitance (C) and dissipation factor (D) of the sample as a function of frequency. The dielectric constant (ε_r) and dielectric loss ($\tan\delta$) were calculated from C and D using the relations,

$$\varepsilon_r = \frac{Cd}{A\varepsilon o} \quad \text{and} \quad \tan\delta = D\,\varepsilon_r$$

Where,

C is the capacitance of the sample, **d** the thickness of the sample,

A area of the face in contact with the electrode and ε_o the permittivity of free space.

2.3 Microhardness studies

Microhardness measurements were carried out using Zwick 3212 hardness tester fitted with a Vicker's diamond pyramidal indenter. All the indentation measurements were carried out on the freshly cleaved samples. The indentation was made varying a load from 5 to 25 gm and the time of indentation was kept at 10 sec. The indented impressions were approximately square. The crystal surfaces were indented at different sites. Diagonal lengths of the indented impression were measured during calibrated micrometer attached to the eyepiece of the microscope. Several indentations were made on each sample. The average value of the diagonal lengths of the indentation mark was used to calculate the hardness. The Microhardness is calculated using the expression [1]

$H = 1.8544\ P/d^2$ Kg mm^{-2}

Where, **P** is the applied load in **Kg** and **d** the average diagonal length of the Vickers impression in **mm** after unloading.

2.4 SHG EFFICIENCY

The grown crystals of pure ADP and doped ADP were subjected to Kurtz second harmonic generation (SHG) test. A Q-switched Nd: YAG laser whose output was filtered through 1064nm narrow pass filter was used for the purpose. To measure the SHG efficiency, the powder of the samples were derived from the crystals grown with full morphology, which ensure homogeneity of the material. The input power of the laser beam was measured to be 6.6 mJ/pulse. Pure ADP was used as reference sample. Both the reference and test samples had uniform particle size of 30-50μm.

III. RESULTS AND DISCUSSION

The variation of dielectric constant(ε_r) and dielectric loss (tanδ) at room temperature for ADP and ADP containing $FeSO_4$, $NiCL_2$ and $CuCl_2$.are shown in Figs 1 and 2. It is observed that the dielectric constant (ε_r) decreases with the increase in the frequency. Values of dielectric constant and dielectric loss at 100 kHz and 1 MHz frequency for pure ADP and ADP crystals containing $FeSO_4$, $NiCL_2$ and $CuCl_2$ are given in Table 1. The dielectric constant of a material is generally composed of four types of contributions, viz ionic, electronic, orientational and space charge polarizations. At low frequencies all polarizabilities are operative hence and are high. As frequency increases one polarization mechanism after another is frozen out. The first to stop contribution to and is orientational compound, then the ionic and the lastly the electronic [2, 3].The dielectric loss (tanδ) is due to the resistive component that makes them loose, so that they dissipate some of the applied ac energy. tanδ in the present study was found initially to decrease with frequency and later almost a constant over a range of frequency for all the three dopants.

Fig.3 shows the variation of microhardness with indenter load. The microhardness increases with increase of indenter load (from 5 to 25g). With gradual increase of the applied stress, the elastic limit of the material can be exceeded and the specimen will not restore its original shape on removal of the stress.

Presence of Fe^{3+}, Cu^{+} and Ni^{2+} ions has resulted in decreased microhardness value.

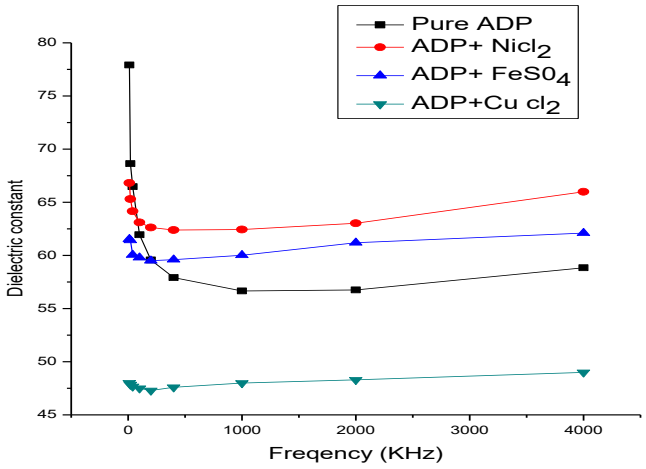

Fig1. Variation of dielectric constant with Frequency in pure and doped ADP crystals

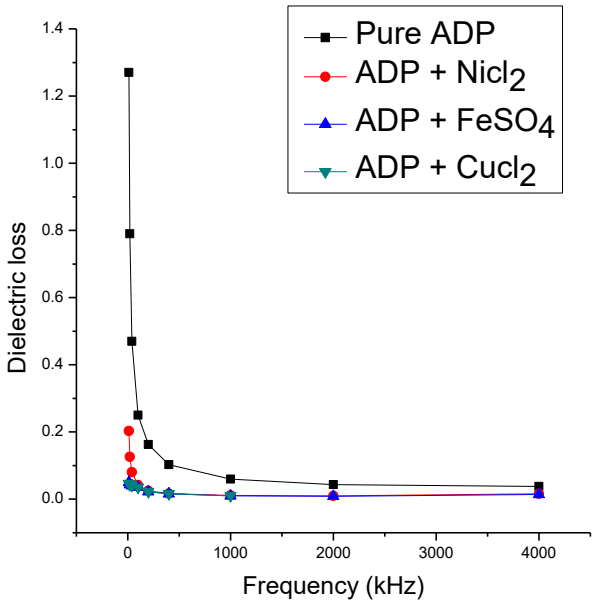

Fig2. Variation of dielectric loss with Frequency in pure and doped ADP crystals

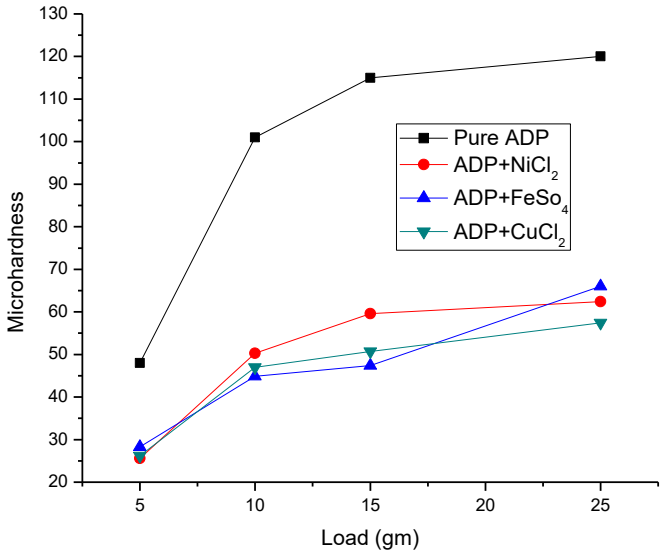

Fig3. Variation of microhardness with load in pure and doped ADP crystals

The hardness or softness of the material can be determined by using Meyer's equation, $P=ad^n$ where P is load in kg, d is diagonal length in mm and n is work hardening number. The n value tells us about the hardness or softness of the material [6]. A graph of **log p** versus **log d** has been plotted for pure ADP and doped ADP crystals. The slope gives the **n** value and the same are shown in the table2. The increase in **n** values of the doped ADP crystals confirms that, the material become soft on doping.

The SHG efficiency of ADP containing Cuprium chloride is found higher than pure ADP. It is surprising that the other metal additives $FeSO_4$, $NiCl_2$ are acting aspoison, not favoring SHG efficiency. In the present study

the additives and host are in the molar ratio of 1:9.It is interesting to carry out the work at lower ratios to know exactly at what molar ratio the materials start nullifying the SHG efficiency and making the host crystal lose the NLO property. Definite conclusion regarding the result requires further work on phase matched efficiency of single crystals. The measured SHG efficiency of the crystal is as shown in the table.3

IV. CONCLUSION

In summary, the ADP is turned out to be useful NLO device material for several reasons. It can be grown easily with suitable habit faces. It is transparent, so that phase matching for second harmonic and frequency mixing processes can be achieved well into the visible region. So higher efficiencies could be achieved by increasing the intensity of input signal. From the study of indentation hardness measurement in pure ADP and ADP containing FeSO4, NiCl2 single crystals, crystals have answered for different hardness values. Presence of Fe^{3+}, Cu^{+} and Ni^{2+} ions has resulted in decreased microhardness value. The hardness measurements may be useful in indicating the order of magnitude to be expected for the elastic constant in a new material. Dielectric constant and Dielectric loss decreases with frequency. Large value of dielectric constant at low frequencies in the present study confirms the purity of the sample, secondly, as due to the space charge polarization [4]. Values of hardness and dielectric constant in doped ADP crystals prove to be a useful candidature for many applications.

Table1. Values of dielectric constant (ε_r) and dielectric loss (tan δ) of pure and doped ADP crystals

Sample	At 100 kHz		At 1 MHz	
	ε_r	tan δ	ε_r	tan δ
Pure ADP	61.94	0.25	56.66	0.06
ADP+$FeSO_4$	60.074	0.0047	60.125	0.0044
ADP+$CuCl_2$	47.169	0.0069	47.169	0.0042
ADP+NiCl2	63.1	0.042	62.44	0.011

Table2.Work hardening number of ADP and ADP doped crystals

Sample	Work hardening number (n)
Pure ADP	**0.995**
ADP+ $CuCl_2$	**6.429**
ADP+ $FeSO_4$	**6.43**
ADP+ $NiCl_2$	**6.41**

Table3.SHG efficiency of pure ADP and doped ADP crystals.

Sample	SHG efficiency with respect to ADP
Pure ADP	**1.000**
ADP+ $CuCl_2$	**2.158**
ADP+ $FeSO_4$	**0.928**
ADP+ $NiCl_2$	**0.916**

V. REFERENCES

[1]. Hari Babu, U.V. Subba Rao and K. Venkata Ramaiah, Phys. Stat. Sol (a), 1975, 28, 269.
[2]. P. Suryanarayana, H.N. Acharya and K. Roa, J. Mater. Sci. Lett, 1984, 3, 21.
[3]. S. Sankara Narayanan Potty and M. Abdul Khadhar, Bull. Mater. Sci., 2002,23, 361.
[4]. Milton Ohring, Engineering materials science, Academic press 1995.
[5]. R.Ananda kumari and R.Chandramani, Bull.mater Sci., 2003, 26, 2
[6]. B.Schwartz,The Electrochemical Society, Princeton 1969

National Conference on Applied Sciences Synergising the Engineering and Technology
Print ISSN: 2395-6011 | Online ISSN: 2395-602X (www.ijsrst.com)
© 2021 IJSRST | Volume 8 | Issue 2

A Study On R-Super Mean Graphs

K R Ekambaram[1], M. Umapathi[2]

[1]Guest Lecturer, Department of Mathematics, Sri Subramaniya Swamy Govt Arts College, Tiruttani, Thiruvallur, Tamil Nadu, India

[2]Research Scholar, Department of Mathematics, SPIHER, Avadi, Chennai, Tamil Nadu, India

ABSTRACT

In this paper, first we define a Rounded Super mean labeling and a Rounded super graph. We proved that the cycle, kite, complete bipartite of $k_{2,n}$ and the ladder are R-super mean graphs.

Keywords : Rounded Super Mean Labeling, R-Super Mean Graph.

I. INTRODUCTION

In this chapter, we introduced a new concept, known as rounded super mean graph. Formally, we define a rounded super mean graph or R – super mean graph.

Basic Definitions and Notations Definition

Let G be the (p, q) graph and let $f: V \to \{1, 2, 3, \ldots\ldots, p + q\}$ be an injection function. For a vertex labeling f, the induced edge labeling $f(e = uv)$ is defined by $f(e) = \lceil [f(u) + f(v)] / 2 \rceil$(or) $\lfloor [f(u) + f(v)] / 2 \rfloor$. Then f is called a rounded super mean labelling if $f(V(G)) \cup \{f(e): e \in E(G)\} = \{1, 2, 3, \ldots\ldots, p + q\}$. A graph that admits rounded super mean labeling is called rounded super mean graph. It is denoted by R – super mean graph.

Definition

The chord of cycle C_4 adjoined by a path P_n. It is denoted by C_4 A P_n and is shown in Figure 1

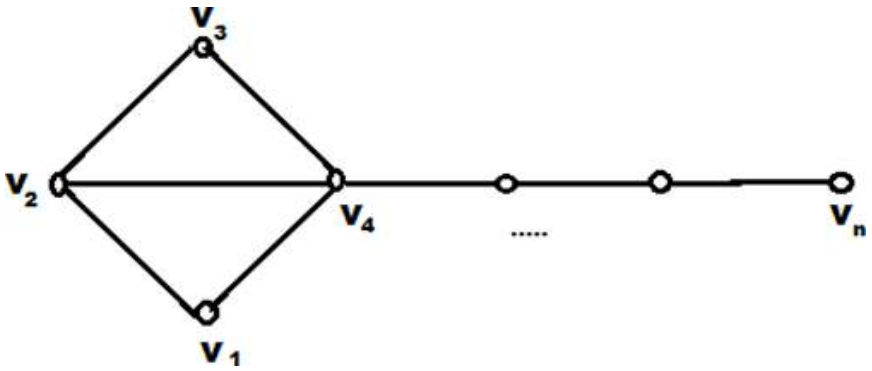

Figure 1

Theorem.

The cycle C_n. is a R-super mean graph

Proof.
Let be the vertices of the cycle C_n $v_1, v_2, v_3, \ldots, v_n$
In the cycle C_n, $p = n$ and $q = n$ To consider the vertex labeling of f, we consider the following two cases

Case(1). When n is odd

We define $f: V(Cn) \rightarrow \{1, 2, 3, \ldots, 2n\}$ by

$$= \begin{cases} 2i - 1 & \text{for} \quad 1 \leq i \leq (n+1)/2 \\ 2i & \text{for} \quad (n+1)/2 < i \leq n. \end{cases} \qquad f(v_i)$$

By the definition of R-super mean labeling, we

obtain

$$f(v(C_n)) = \{1, 3, 5, \ldots, n, n+3, n+5, \ldots, 2n\}$$

and

$$f(E(C_n)) = \{2, 4, 6, \ldots, n-1, n+1, n+2, n+4, \ldots, 2n-1\}.$$

Then f is R-super mean labeling.

$$f(E(C_n)) = \{2, 4, \ldots, n-2, n+1, \ldots, 2n-1\}$$

Then f is R-super mean labeling.

Thus the cycle C_n is a R-super mean graph.

Example

The R-super mean labeling of the cycle $C_7$is shown in Figure 2.

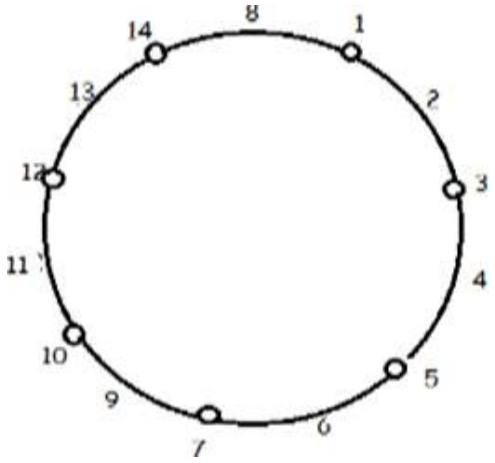

Figure 2

The R-super mean labeling of the cycle C_8 is shown in Figure 3

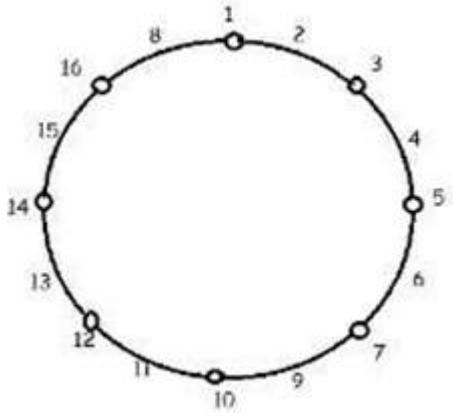

Figure 3

Theorem

The kite $k(4,n)$ is a R-super mean graph.

Proof

In the kite $k(4,n), p = n + 3$ and $q = n + 3$. Let $v_1, v_2, v_3, \ldots, v_{n+3}$ be the vertices of the kite

We define $f: V(K) \rightarrow \{1, 2, 3, \ldots., 2n + 6\}$ by

$$f(v_i) = \begin{cases} 2i - 1 & \text{for } 1 \leq i \leq 2 \\ 2i & \text{for } 3 < i \leq (n+3). \end{cases}$$

By the definition of R-super mean labeling, we obtain $f(V(K)) = \{1, 3, 6, 8, 10, \ldots., 2n + 6\}$ and

$f(E(K)) = \{2, 4, 5, 7, 9, 11, \ldots, 2n + 5\}$. Hence f is R-super mean labeling

Thus the kite $K(4,n)$ is a super mean graph

Example

The R-super mean labeling of the kite $K(4,5)$ is given in Figure 4

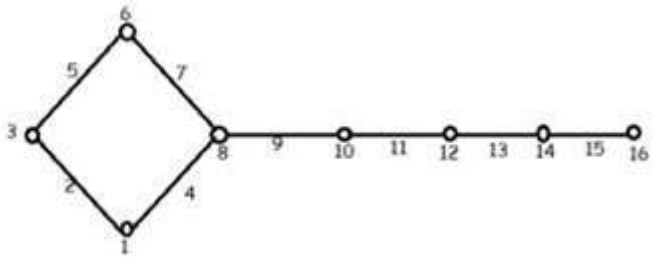

Figure 4

Theorem

The graph C_4A P_n is a R-super mean graph

Proof

Let $v_1, v_2, v_3, \ldots, v_{n+3}$ be the vertices of C_4A P_n. In this graph $p = n + 3$ and $q = n + 4$.

We define $f: V(C_4\, AP_n\, .) \rightarrow \{1, 2, 3, \ldots\ldots, 2n + 7\}$

By

$$f(v_i) = \begin{cases} 2i & \text{for} \quad 1 \leq i \leq 2 \\ 2i + 1 & \text{for} \quad 3 < i \leq n + 3. \end{cases}$$

By the definition of R-super mean labeling, we obtain

$f(V(C_4\, A\, P_n)) = \{1, 3, 7, 8, 9, 11, \ldots, 2n + 7\}$

And

$f(E(C_4\, A\, P_n)) = \{2, 4, 6, 10, 12, \ldots, 2n + 6\}$.

Then f is R-super mean labeling.

Hence the graph $C_4\, A\, P_n$ is a R- super mean graph

II. CONCLUSION

In this paper, we introduced a new concept named as rounded super mean graph or R-super mean graph. First that the cycle, kite, complete bipartite graph K2,n and the ladder are R- super mean graphs.

III. REFERENCES

[1]. Jeyanthi. P, Ramya. D and Thangavelu. P, "On Super Mean Labeling Of Graphs", AKCE Int. J. Graphs. Combin., 6(1) (2009), 103-112.

[2]. Jeyanthi. P, Ramya. D and Thangavelu. P, "On Super Mean Labeling Of Some Graphs", SUT Journal of Mathematics,46(1) (2010), 53-66.

[3]. Gallian. J.A, "A Dynamic Survey of Graph Labeling", The Electronic Journal of Combinotorics 6 (2001)

[4]. Ponraj. R and Ramya.D, "On Super Mean Graphs Of Order 5", Bulletin of pure and Applied Sciences, 25 (1) (2006), 143-148.

[5]. Ramya. D, Ponraj. R, and Jeyanthi. P "Super mean graphs", Ars Combin., 112 (2013), 65-72.

National Conference on Applied Sciences Synergising the Engineering and Technology
Print ISSN: 2395-6011 | Online ISSN: 2395-602X (www.ijsrst.com)
© 2021 IJSRST | Volume 8 | Issue 2

Effect of Nd+ Ion Addition on Gas Sensing Properties of Mg-Cd Ferrite Thick Films System

Shedam Rakesh M[1], Mathad Shdhar N[2], Shedam Mahadev R[3], Gadkari Ashok B[4]

[1]Department of Physics (Research Scholar) The New College, Kolhapur, Maharashtra, India

[2]Department of Physics (Associate Professor) KLE Institute of Technology, Huballi, Maharashtra, India.

[3]Department of Physics (HOD and Associate Professor) The New College, Kolhapur Kolhapur, Maharashtra, India

[4]Department of Physics (HOD And Associate Professor) G.K.G. College, Kolhapur, Maharashtra, India

ABSTRACT

Nd3+ added nanocrystallite ferrite samples with general formula CdxMg1-xFe2O4 (x = 0.5) were prepared by oxalate Co-precipitation method from high purity sulphates. The XRD, SEM and FT-IR Techniques were used for characterization of the samples. The XRD confirms cubic spinal structure with orthoferrite secondary phase. The XRD confirms cubic spinel structure with orthoferrite (NdFe2O3) secondary phase. The crystallite size is 57.67 nm. The surface morphology SEM study shows highly pours in nature and located in loosely algglomeate state particles. The FT-IR spectra show two strong absorption bands in the range of 350- 800 cm-1. The response and recovery time of Nd3+ added Mg-Cd ferrite studies for two gases (Acetone and LPG) Acetone gas shows good sensitivity as compare to LPG gas. The respond depends on the composition, test gas and grain size of the material.

Keywords : Nanocrystallite, Chemical Synthesis, Response, Selectivit,Y Response Time.

I. INTRODUCTION

Nano particles of spinel ferrite draw significant consideration due to their lower density and higher specific surface area and distinct optical, catalytic and magnetic properties [1]. Study of spinel ferrite MFe2O4 (Where M= metal ion) nano particles has significant application in modern technologies such as contrast enhacement of magnetic resonance imaging, high density data storage and magnetic carries for site specific drug delivery[2]. Spinel ferrites have the general molecular formula MFe2O4 where M2+ and Fe3+ are the divalent and trivalent cations occupying tetrahedral (A) and Octahedral (B) interstitial positons of the FCC lattice formed by O2- ions. Among the spinel ferrites, MFe2O4 nanoparticles finds extensive applications in magnetic based diagnosis and treatment devices [3], potential magnetorheological fluids[4]. Gas sensor [5], catalysts [6] and lithium ion batteries [7]. Magnesium ferrites is a soft magnetic n-type semiconducting material [8,9]. Recent increasing attention to nanostructures of magnetic materials has been due to their unique material

properties that are significantly different from those their bulk counter parts [10,11]. Physical, chemically and structural properties of oxide powders depend during preparation. A wide variety of methods are being used to synthesize spinel ferrite nano particles including citric acid combustion [12]. Sol-gel auto combustion[13] , hydrothermal [14] , co- precipitation methods [15,16]. In addition thermolysis [17]. Wet chemical co-precipitation technique[18]. Self propagating and microemulsion[19,20] are also used. The nano crystallite material provides absorption sites for test gases. The existence of large surface to volume ratio in nanostructured material facilities better response towards specific gases thermophogy and particle size is this material depends on method preparation and sintering temperature.

This communication reports the effect of Nd3+ion addition on gas sensing properties of nano crystallite Mg-Cd ferrites prepared by Oxalate Co- precipitation method for liquid petroleum gas(LPG), clorine(Cl2) and ethnol.

II. EXPERIMENTAL DETAILS

Nd3+ ions added spinel ferrites with general formula $Mg_{0.5}Cd_{0.5}Nd_{0.01}Fe_{1.99}SO_4$ The starting materials namely AR grade $MgSO_4{\cdot}6H^2O$ (Thomas baker), $CdSO_4{\cdot}6H_2O$ (Thomas Baker).

$FeSO_4{\cdot}7H_2O$ (Thomas Baker) and $Nd_2(SO_4)_3{\cdot}\ 8H_2O$ (purity 99.9%, alfa Asar) weighed in the required proportion. These matters are dissolve in double distill water. The pH of prepared solution was maintained by solution H_2SO_4 (Sd fine chem. Ltd.) drop by drop. The solution was heated for 1h so as to optimize the complete ionization of metal stirring until the complete precipitation was formed. The precipitate of ammonium oxalate was sulphate. Then AR grade ammonia oxalate (Thomas baker) was added slowly in the solution with constant heating on hot plate till precipitate settle down. The precipitant was filtered and washed several time with distill water using what man filter paper number 41. The Barium chloride test was used to confirm the removal of sulphate ions. The precipitates were dried and pre sintered for 1h at 200°C. The pre sintered powders were milled in an agate motor the powder was finally sintered for 5h at 500°C. By using various binders such as 4 wt % ethyl cellulose, 5 wt % 2-(2- butoxy ethoxy) ethyl acetate, 1 wt% ethyl acetate in addition to 90 wt % were used. The thick films were prepared by screen printing technique.

The test gases acetone and LPG were obtained in the form of gas cylinder available in the market.

III. RESULTS AND DISCUSSION

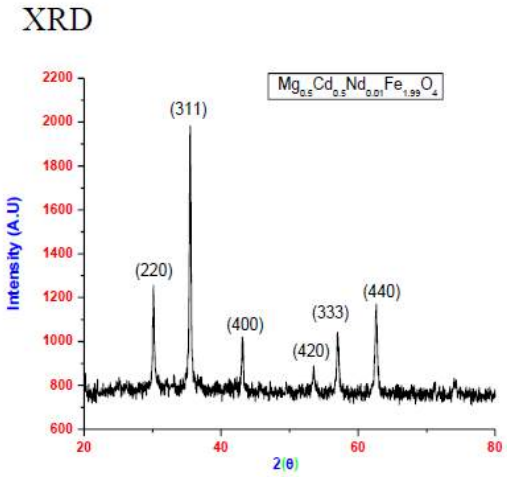

Fig.2. XRD of $Mg_{0.5}\,Cd_{0.5}\,Nd_{0.01}\,Fe_{1.99}\,O_4$

The structural analysis (XRD, SEM and FT-IR) of Nd^{3+} ion added Mg-Cd ferrites under investigation are already reported [21]. The typical XRD pattern of Nd^{3+} ion added MgFe2O4 presented in Fig. 2. The X- ray analysis confirms cubic spinel structure with ortho ferrite (Nd^{3+} FeO3) secondary phase of all the samples under investigation.

$$a = d_{hkl}\sqrt{h^2 + k^2 + l^2} \tag{2}$$

The average crystallite size of the samples is in the range of 8.3731 nm. The average grain size in the samples calculated by linear intercept method is presented in Table 1. The addition of Nd^{3+} ions reduces the grain growth probably due to deposition of Nd^{3+} on the grain boundaries which in turn hampers its motion [21]. Fig. 4 presents the typical FT-IR of Mg0.5Cd0.5Nd0.01 Fe2O4. It shows two absorption bands in the range of (ν1 and ν2) 437.11and 523.14 respectively. These two bands show well formation of ferrites.

The crystalline size for (311) plane was determined with the help of Debye Scherriter formula

$$D = \frac{0.94\lambda}{\beta\cos\theta} \tag{3}$$

Where 'λ' is the wavelength of X-ray, β is the full width at half maxima, and θ is the Bragg's diffraction angle. The average crystalline size 'D' of the samples lies in the nano particle range (57.67 nm) as shown in table1. X-ray density (ρ_x) for all compositions of Mg-Cd ferrites changes with increasing cadmium content as shown in table 1. The X-ray density of the sample is calculated by using Standley (1962) relation

$$\rho_x = \frac{8M}{Na^3} \tag{4}$$

Where, N is the Avogadro's number, a is lattice constant and M is the molecular weight. This may be due to the larger ionic radii of Cd_{2+} which replaces Mg_{2+} and Fe_{3+} of smaller ionic radii at octahedral site [21]. The bond lengths (A–O, B–O) and ionic radii (rA, rB), on tetrahedral (A) and octahedral (B) sites of cubic spinel structure are calculated by using the following equations suggested by Standely

$$A - O = \left(u - \frac{1}{4}\right)a\sqrt{3} \tag{5}$$

$$B - O = \left(\frac{5}{8} - u\right)a \tag{6}$$

$$r_a = \left(u - \frac{1}{4}\right)a\sqrt{3} - r(O^{2-}) \tag{7}$$

$$r_b = \left(\frac{5}{8} - u\right)a - r(O^{2}) \tag{8}$$

FTIR

The FTIR spectra present in fig. 3 are found to exhibit two major bands in the range 352-800 cm-1. The higher and lower frequency bands are in respective ranges of 437.11 - 523.14 cm-1 are they common characteristic of spinal structure. Waldron has detected the vibration of unit cell of the cubic spinel can be constructed in the tetrahedral (A) site and octahedral (B) site. Accordingly the absorption band (V1) caused by stretching vibration of tetrahedral metal–oxygen bond and absorption band (V2) by metal- oxygen vibration in octahedral sites.

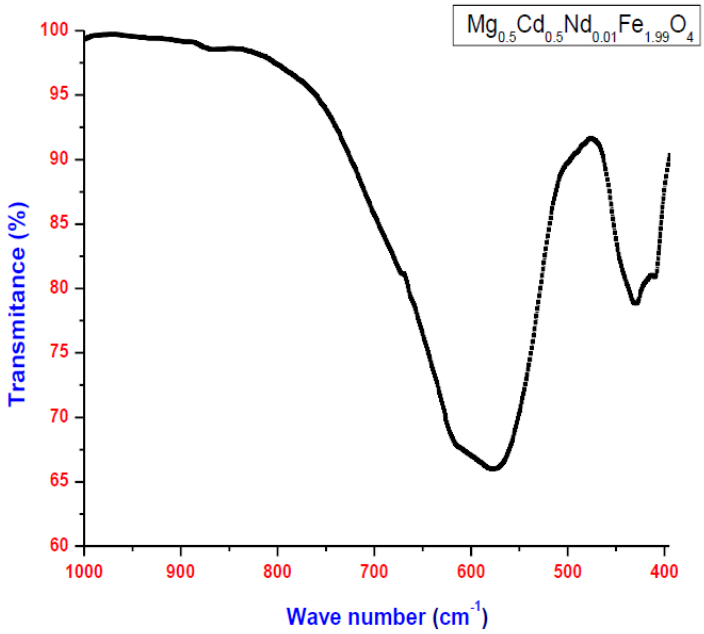

Fig. 2 FTIR of $Mg_{0.5}Cd_{0.5}Nd_{0.01}Fe_{1.99}O_4$

SEM

The scanning electron microscopy (SEM) micrographs are Mg0.5Cd0.5 Nd0.01 Fe1.99O4 system (shown in fig. 4) are highly porous in nature and located in loosely packed agglomerate state spherical particles. So it cannot identify shape and size of the indusial particle. The FE-SEM of Mg-Cd ferrites thick film at 100K magnification (shown in fig. 5) are nano- grained structure with uniform granular morphology. It is evident from fig. 4 that morphology of cadmium added sample deviated from fine structure of pure ferrite. The addition of Nd3+ results in to formation of the MFeO3 crystalline phase conformed by XRD studies. The formation of crystalline phase shows a very good densification of cadmium containing ferrites. The average grain size was calculated from SEM micrograph surface using the equation [e-14].

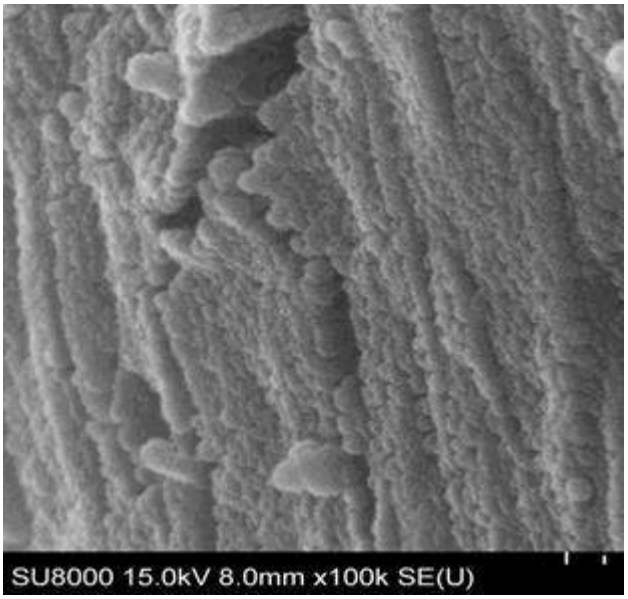

Fig.5. SEM Mg0.5 Cd0.5 Nd0.01 Fe1.99 O4

Gas sensing properties In case of ferrite sensor the gas sensing mechanism is mainly a surface controlled mechanism the change in resistance is a result of amount of chemi absorbed oxygen on the surface and the species [19]

The oxygen absorbed chemically on the surface of Mg-Cd ferrite sensor undergoes the reaction

$$O_{2gas} \leftrightarrow O_{2ads} \leftrightarrow 2O^{-}_{ads} \leftrightarrow 2O^{2-}_{ads} \quad (10)$$

This depicts how Mg-Cd ferrites are influenced by Oxygen absorption on the surface.

With increases in temperature, the equilibrium shifts to the right which results in the decreases in conductance. The conductance decreases significantly shown of that the effect of equilibrium is significant at higher temperatures. The oxygen from Mg-Cd ferrite sensors capture electrons leading to decreased concentration of electron and hence increased resistance of the sensors [13].

However when Mg-Cd sensor is exposed to the reducing gases such as LPG, and acetone is found that the resistance of the sensor decreases. This may explained as the result of reaction of the reducing gases with chemi adsorbed oxygen resulting in the release of electrons back to the conduction band. The general reaction of reducing gases with oxygen species O- and O2- on the surface of the ferrite are given below [22-24].

$$R_{(gas)} \leftrightarrow R_{(ads)} \quad (11)$$

$$R_{(ads)} + O^{-}_{(ads)} \leftrightarrow RO_{(ads)} + e^{-} \quad (12)$$

i) When ferrite sensor is exposed to LPG, the LPG reacts with chemisorbed oxygen. The absorbed oxygen is removed as a consequence of interactions of hydrocarbons (C_nH_{2n+2}) of LPG to from gases species and water vapor. The reaction, in general, may be represented as follows [25]

$$2C_nH_{2n+2} + 2O_2^{-} \rightarrow 2C_nH_{2n}O + 2H_2O + 2e^{-}$$

Where 2CnH2n+2 represents various hydrocarbons of LPG.

This reaction shows that the concentration of conduction band electron increases their by resistance of ferrite senor decrease [22, 26].

ii) The reaction show that the absorbed acetone interacts with oxygen ions (O) which release carbon dioxide, water vapor and electrons to the conduction band [18].

$$C_2H_6O + 8O^- \rightarrow 3CO_2 + 8H_2O + 8e$$

So it may be conclude that, the sensor with lower operating temperature is favored than higher operating temperature.

We can explain the conduction mechanism of gas sensor at different operating temperature depending on the reaction mechanism of surface observed oxygen O^{-2} ions and sensor resistance is high sensor resistance decreases reaches minimum value at particular temperature (6a to 7a) this shows that conduction electron generated due to transformation of ferrite sample in surface absorbed O^{-2} ions . As the temperature increases the conversion of O^{-2} ions to O-ion in the following reaction $O_2 \rightarrow 2O \rightarrow e^-$. The generated electron increases their concentration over up ferrite sample. Thus there is increase of conductivity (decreases of resistance).

The variation of sensor resistance with operating of temperature is shown in Fig 6a and 7a. Sensor resistance decreases becomes minimum and increases with operating temperature. Where Ra and Rg are resistance of sensor at air and gas. The minimum temperature range for acetone and LPG are 275 ^{0}C and 290 ^{0}C Respectively. This shows that different gases show different operating temperature which depends on nature of gases. The sensor sample x=0.5 shows good sensitivity for three gases.

The variation sensor resistance with time as shown in fig 6b and 7b. The sensor response for composition x=0.5 studies for the two gases the response time is defined as the require to from 90% of the conductivity of equilibrium value of the conductivity of equilibrium value of the applying the test gas. The recovery time is the time needed for initial conductivity in air to be established in the sensor. The LPG gas 500 ppm at their optimum temp 300°C and 290 as shown in Fig 6b and 7b. While the gas input is for LPG the value found to be 25s and relaxation time is found 80 sec. for LPG for the acetone input gas value found to be 43 sec. and relaxation time is found to 62 sec. Above observation was found that acetone gas good time sensitivity than LPG.

The variation of sensor response with gas concentration for different gases is shown in Fig. 6a to 7c. The maximum value of sensor response is 1.8 for acetone, 1.5 for LPG at x= 0.5 respectively. The value of response decreases.

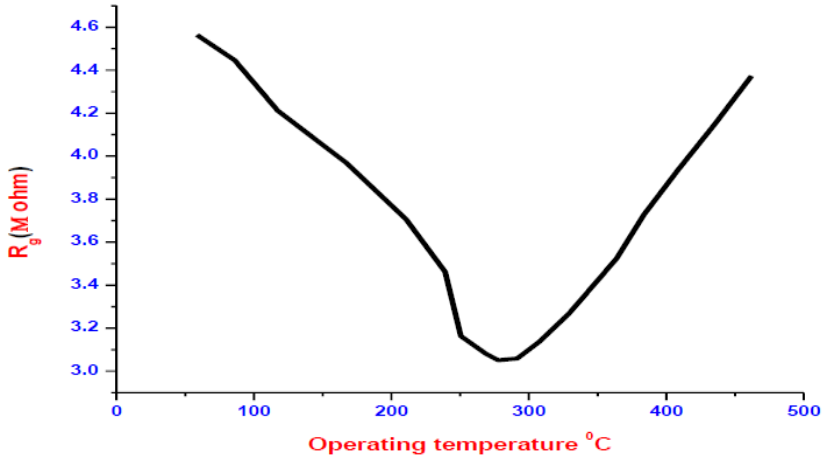

Fig.6.a. LPG variation of sensor resistance with operating temperature

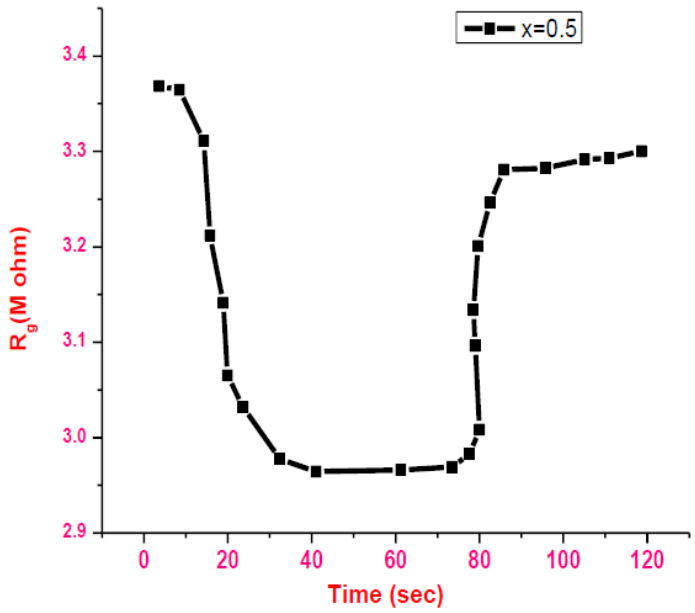

Fig.6.b. LPG variation of sensor resistance with transient time

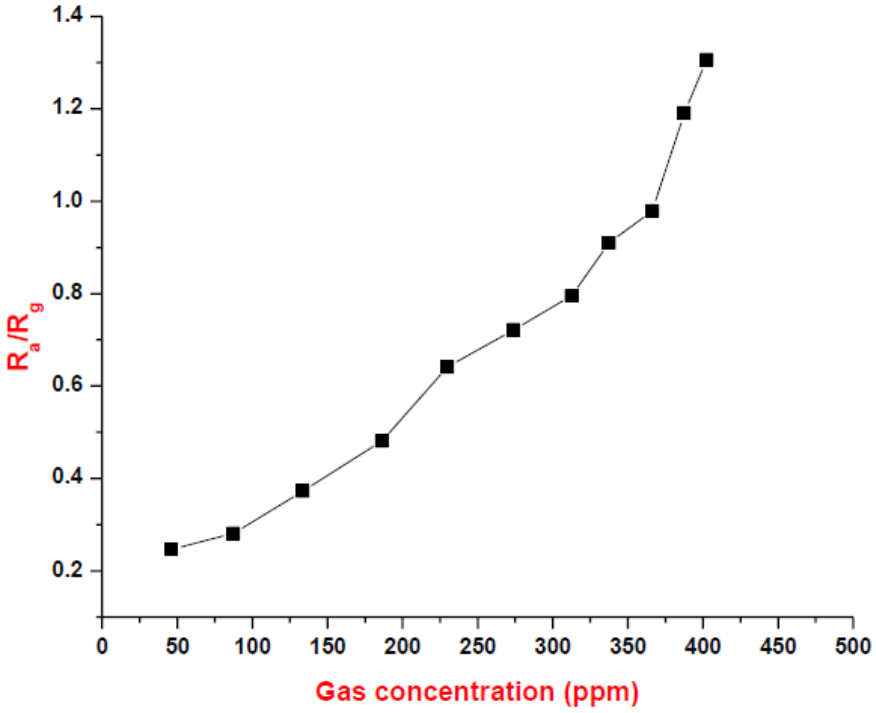

Fig.6.c. LPG variation of sensor response with gas concentration

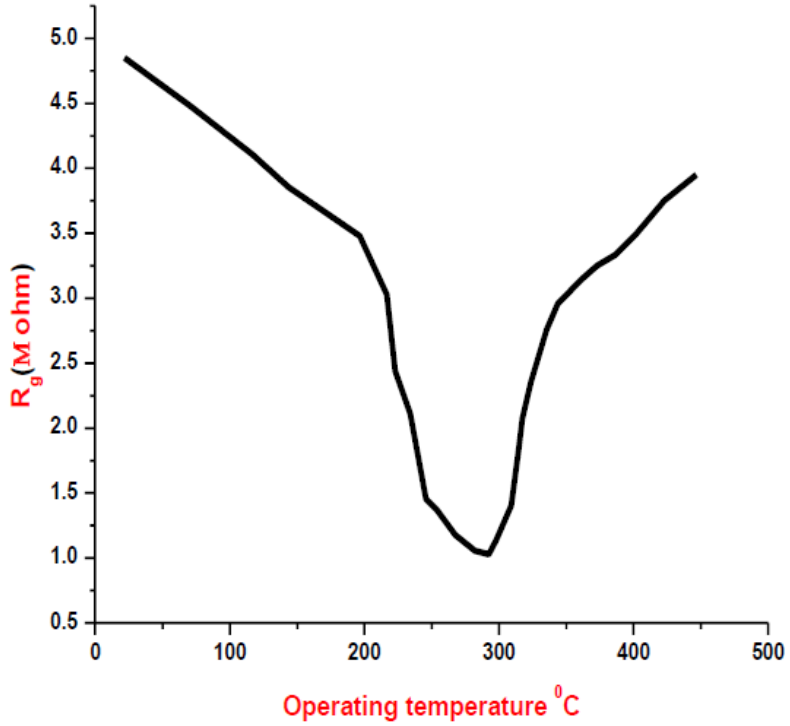

Fig.7.a. Acetone variation of sensor resistance with operating temperature

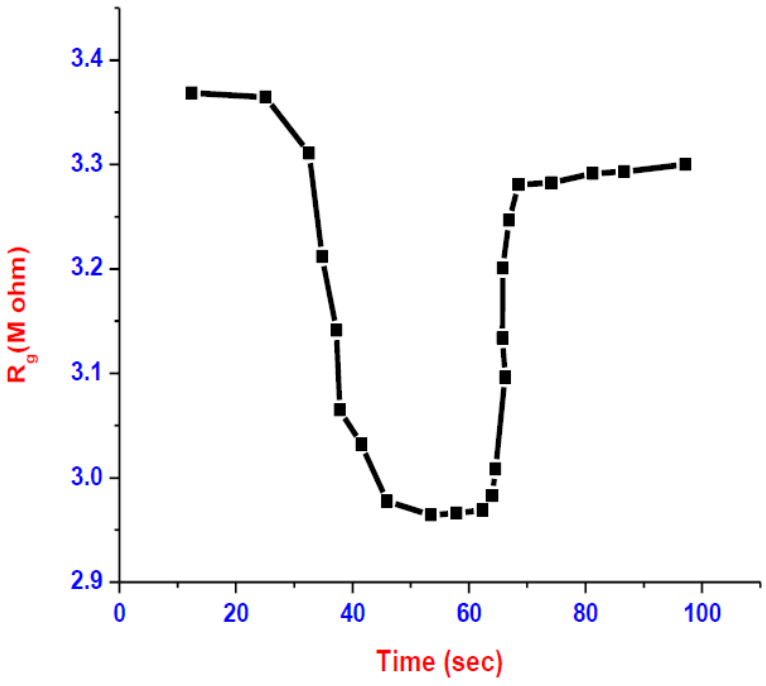

Fig.7.b. Acetone variation of sensor resistance with transient time

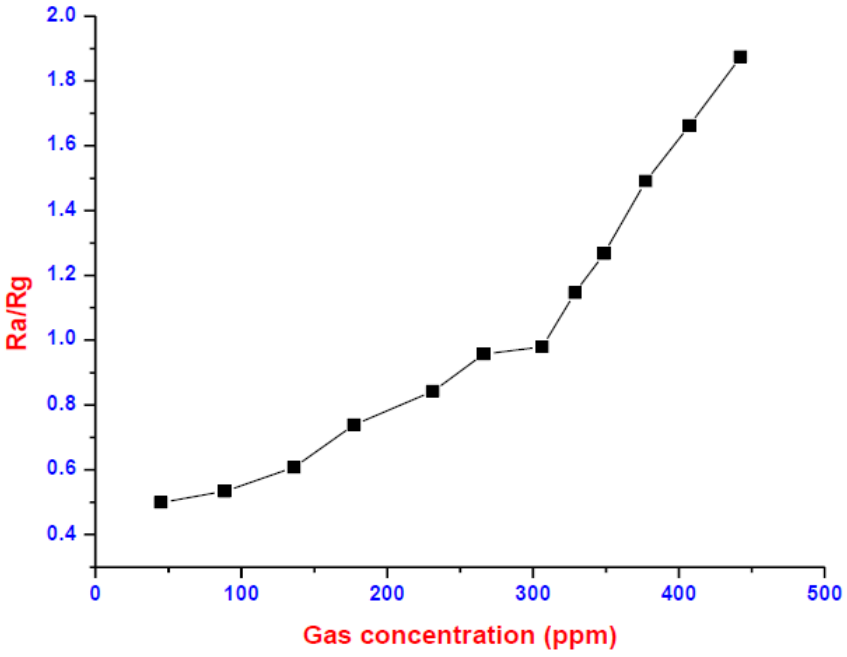

Fig.7.c. Acetone variation of sensor response with gas concentration

Content	Crystal Size (D) nm	Lattice constant (A^0)	X-Ray density	Bond length(A^0)		Ionic radia		Abortion Band	
				A-O site	B-O site	r_A	r_B	γ_1	γ_2
0.5	57.67	8.3731	8.773	1.6406	1.7703	0.2906	0.3937	437.11	523.14

IV. CONCLUSION

The preparation of Mg-Cd ferrites was carried out using oxalate co-precipitation method at sintering temperature of 500°C for 5 h. It is found that the average crystalline size lies in the nano particle range 57.67nm. With increase in Nd2+ content the lattice constant as well as the grain size increase. The band boarding is also observed which suggests the occurrence of octahedral B site. . The samples show increase in sensitivity with the operating temperature. The operating temp of thick film Nd doped ferrite found to be 300°C and 275°C for acetone and LPG gases. The thick film of ferrite shows good sensitivity for acetone gas.

V. REFERENCES

[1]. Lisjak D, Mertelj A (2018) Anisotropic magnetic nanoparticles: a review of their properties syntheses and potential applications. Prog Mater Sci 95:286– 328.

[2]. Wang ZL, Liu Y, Zhang Z (2002) Handbook of nanophase and nanostructured materials, vol 3. Kluwer Academic/Plenum, New York.

[3]. Nonkumwong J, Pakawanit P, Wipatanawin A, Jantaratana P, Ananta S, Srisombat L (2016) Synthesis and cytotoxicity study of magnesium ferrite-gold core-shell nanoparticles. Mater Sci Eng C 61:123–132

[4]. Wang G, Ma Y, Li M, Cui G, Che H, Mu J, Zhang X, Tong Y, Dong X (2017) Magnesium ferrite nanocrystal clusters for magnetorheological fluid with enhanced sedimentation stability. Solid State Sci 63:70–75.

[5]. Liu YL, Liu ZM, Yang Y, Yang HF, Shen GL, Yu RQ (2005) Simple synthesis of MgFe2O4 nanoparticles as gas sensing materials. Sensors Actuators B 107:600–604.

[6]. Kim HG, Borse PH, Jang JS, Jeong ED, Jung OS, Suhd YJ, Lee JS (2009) Fabrication of CaFe2O4/MgFe2O4 bulk heterojunction for enhanced visible light photocatalysis. Chem Commun 39:5889– 5891.

[7]. Pan Y, Zhang Y, Wei X, Yuan C, Yin J, Cao D, Wang G (2013) MgFe2O4 nanoparticles as anode materials for lithium-ion batteries. Electrochim Acta 109:89–94.

[8]. Willey RJ, Noirclerc P, Busca G (1993) Preparation and characterization of magnesium chromite and magnesium ferrite aero gels. Chem Eng Commun 123:1–16.

[9]. Sivakumar N, Narayanasamy A, Greneche JM, Murugaraj R, Lee YS (2010) Electrical and magnetic behavior of nanostructured MgFe2O4 spinel ferrite. J Alloys Compd 504:395–402.

[10]. Hyeon T (2003) Chemical synthesis of magnetic nanoparticles. Chem Commun 9:927–934 11. Jana NR, Chen Y, Peng X (2004) Size and shape controlled magnetic (Cr, Mn, Fe Co, Ni) oxide nanocrystals via a simple and general approach. Chem Mater 16:3931–3935

[11]. Raghasudha M, Ravinder D, Veerasomaiah P (2013) Characterization of chromium substituted cobalt nano ferrites synthesized by citrate-gel auto combustion method. Adv Mater Phys Chem 3(2):89– 99

[12]. Dalavi SB, Mishra PP, Cherian T, Raja MM, Panda RN (2020) Magnetic and Mössbauer studies on nanostructured CoCrxFe2-xO4 ($0 \le x \le 1$) spinel ferrites prepared by sol–gel auto-combustion method. J Nanosci Nanotec 20(8):983–990

[13]. Chien YT, Yi CC, Chien ML (2018) Hydrothermally synthesized Mg-based spinel nanoferrites: phase formation and study on magnetic features and microwave characteristics. Adv Funct Nanomater Appl 11(11):2274.

[14]. Joshi S, Kumar M, Chhoker S, Srivastava G, Jewariya M, Singh VN (2014) Structural magnetic dielectric and optical properties of nickel ferrite nanoparticles synthesized by co-precipitation method. J Mol Struct 1076:55–62

[15]. Rashad MM, Rayan DA, Turky AO, Hessien MM (2015) Effect of Co and Y ions insertion on the microstructure development and magnetic propertiesof Ni0.5Zn0.5Fe2O4 powders synthesized using Co-precipitation method. J Magn Magn Mater 374:359–366

[16]. Ningzhong B, Liming S, Yuhsiang W, Prahallad P, Arunava G (2007) A facile thermolysis route to monodisperse ferrite nanocrystals. J Am Chem 129(41):12374–12375

[17]. Iqbal T, Hassan A, Ghazal S (2017) Wet chemical co-precipitation synthesis of nickel ferrite nanoparticles and their characterization. J Inorg Organomet Poly Mater 27:1430–1438 .

[18]. Bennet J, Tholkappiyan R, Vishista K, Victor JN, Hamed F (2016) Attestation in self-propagating combustion approach of spinel AFe2O4 (A = Co, Mg and Mn) complexes bearing mixed oxidation states: Magnetostructural properties. Appl Surf Sci 383:113– 125

[19]. Rashad MM, Soltan S, Ramadan AA, Bekheet MF, Rayan DA (2015) Investigation of the structural, optical and magnetic properties of CuO/CuFe2O4 nanocomposites synthesized via simple microemulsion method. Cer Int 41(9):12237–12245.

[20]. A.B. Gadkari, T.J. Shinde, P.N. Vasambekar, Structural analysis of Sm3+ doped nanocrystalline Mg–Cd ferrites prepared by oxalate co-precipitation method, Materials Characterization 60 (11) (2009) 1328–1333.

[21]. T.G. Nenov, S.P. Yordanov, Ceramic Sensors, Technology and Applications, Technomic Publication, Lancaster, 1996, pp. 137–138.

National Conference on Applied Sciences Synergising the Engineering and Technology
Print ISSN: 2395-6011 | Online ISSN: 2395-602X (www.ijsrst.com)
 | Volume 8 | Issue 2

Numerical Graph Invariants : Its Scenery and Shared Associations

V. Lokesha
Professor of Mathematics, Vijayanagara Sri Krishnadevaraya University, Ballari, Karnataka, India

ABSTRACT

For the past three decades, a hefty number of numerical graph invariants (topological indices) encompass are defined and worn for correlation analysis in theoretical chemistry, pharmacology, toxicology, and environmental chemistry. The TIS are numerical measure based on various invariants or characteristics of molecules graphs. For the convenience of the discussion these indices are classified according to their logical derivation form TIs, rather than according to their sequential growth. Structural compassion is one of the most important and the least investigated property of the topological molecular descriptors. Here, I plan to present some works and avenues allied to the Topological indices.

2020 AMS Classification: 05C90, 05C35, 05C12

National Conference on Applied Sciences Synergising the Engineering and Technology
Print ISSN: 2395-6011 | Online ISSN: 2395-602X (www.ijsrst.com)

Zn_2SnO_4/ZnO Nanocomposite : Hydrothermal Synthesis and Photocatalytic Studies

Preethi G[1,2], Ramdas Balan[3], Nagaswarupa H P[4]

[1]Department of Chemistry, MVJ College of Engineering, Bangalore, India

[2] Research and Development Centre, Bharatiar University, Coimbatore, India

[3] Centre of Excellence - Materials Science, Department of Physics, CMR Institute of Technology, Bangalore, India

[4]Department of Chemistry, Davangere University, Davangere, India

ABSTRACT

Nanocomposite Zn_2SnO_4/ZnO was prepared by facile hydrothermal method with the support of $NaHCO_3$ mineralizer. Characterization techniques such as powder - X-ray diffraction, Raman spectroscopy and Scanning electron microscopy were used to analyze the phase purity and morphology. XRD study revealed that Zn_2SnO_4/ZnO composite phase with the crystallite size of 20 - 25 nm range, which was calculated using Scherrer expression. SEM analysis shown agglomerated particles of spherical shape morphology. Photocatalytic degradation studies of Methylene Blue dye under UV irradiation shown superior degradation activity by the prepared product, which suggested the formation of type II heterojunction nanocomposite.

Keywords : Nanocomposite, Hydrothermal Method, Photocatalyst

National Conference on Applied Sciences Synergising the Engineering and Technology
Print ISSN: 2395-6011 | Online ISSN: 2395-602X (www.ijsrst.com)

Characterisation of novel Quaternized Epoxy Ionomers for application in Anion Exchange Membrane Fuel Cells

Ashok Kumar Shukla

Professor, Chemistry Department, East Point College of Engineering and Technology, Bangalore.

Corresponding author's email: ashok.shukla@eastpoint.ac.in

ABSTRACT

The paper describes the key characteristics of novel Anion Exchange Membranes (AEM) derived from a commercial bifunctional epoxy resin. AEMs have been under intense study in recent years [1,2] due to their intrinsic advantages like low cost, ease of synthesis, enabling use of non-noble metal (Ni, Co, Fe) electrocatalysts [3] significantly lowering the overall cost of fuel cell over the conventional Proton Exchange Membranes (PEMs) which require noble metal (Pt, Ru, Pd) based electrocatalysts, besides being very expensive. However, the limitations of AEMs include lower ionic conductivity due to poor mobility of bulkier hydroxyl ion responsible for lower performance of the fuel cell.

The author presents the typical characteristics of anion exchange membranes (AEMs) prepared from Quaternized Epoxy Ionomer (QEI) and their Composite Ionomer (QECI) made by incorporating montmorillonite (MMT) nano-clay in proportions from 1 to 8% by weight of the polymer (QEI). Addition of MMT has shown significant improvement in mechanical properties like tensile strength and elongation at break, alkaline stability, and increase in thermal stability in air from 170°C to 180°C according to thermogravimetric analysis (TGA), as compared to those for the pristine QEI. Results show marginal reduction in Water Absorption (WA) by about 10% and the Swelling Ratio (SR) by about 15%. However, there is improvement in Ion Exchange Capacity (IEC) and Hydroxyl Conductivity of QECI membrane, however small, as compared to that of the pristine QEI. These results indicate good potential of these anion exchange membranes for application in Alkaline Polyelectrolyte Fuel Cells.

Keywords : Anion-exchange, Epoxy, Fuel Cells, Ionomers, Membranes; Quaternary

REFERENCES

1. L.G. Cruz, C. C. Coterillo, et. al., Journal of Carbon Research (MDPI), C (2016),2, 10; doi:10.3390/c2020010; www.mdpi.com/journal/carbon.
2. K.F.L. Hagesteijn , S.Jiang & B.P. Ladewig, J. Mat. Sci. (SpringerLink), 53 (2018), 11131-11150.
3. T. Palaniselvam, V. Kashyap, et. al., Adv. Funct. Mater., 26 (2016), 2150: doi: 10.1002/adfm.201504765

National Conference on Applied Sciences Synergising the Engineering and Technology
Print ISSN: 2395-6011 | Online ISSN: 2395-602X (www.ijsrst.com)

Studies on Acoustic Behaviour and Molecular Interactions of MgSO4 in Galactose-Water Mixed Solvent Systems

D. N. Ganesh and Susmita Kamila*

Department of Chemistry, Rajiv Gandhi institute of Technology, Bangalore, India

ABSTRACT

Acoustic studies in liquid and their mixtures are of great importance in different fields of research. Presently, the ultrasonic velocity, viscosity and density measurement have been carried out for MgSO4 in aqueous galactose mixed solvent systems at 303.15K temperature and atmospheric pressure. From the measured data, different acoustic parameters such as isentropic compressibility, βs, intermolecular free length, Lf, acoustic impedance, Z were calculated. The results were interpreted in terms of molecular interactions. It has been observed the presence of inter-molecular interactions among the component molecules in the mixed solvent systems.

National Conference on Applied Sciences Synergising the Engineering and Technology
Print ISSN: 2395-6011 | Online ISSN: 2395-602X (www.ijsrst.com)

Effect of Discrete Heating on Natural Convection in an Inclined Parallelogrammic Enclosure

Ravindra P[1], Pandurangappa C[2] and M. Sankar[3]

[1]Department of Mathematics, East Point College of Engineering and Technology, Bangalore, India

[2]Department of Mathematics, UBDT College, Davanagere, India

[3]Department of Mathematics, Presidency University, Bangalore, India

ABSTRACT

In many heat transfer applications, the physical configuration of equipment may not be of regular shape and one or more geometrical parameters in such non-regular shaped enclosure significantly influence the convective flow and associated thermal transport processes. Therefore, in this paper, numerical simulations are presented to understand the influence of inclination angle of a tilted parallelogrammic enclosure as well as partial heating and cooling of side walls. The upper and lower boundaries of the enclosure are treated as thermally insulated; side walls are considered to be single thermal source-sink pairs of two different lengths located at various locations. Using Darcy law, the momentum equations are modeled and unsteady energy equation is considered. The model equations are numerically solved using finite difference method, in particular, using ADI and SLOR methods. Based on standard coordinate transformations, the governing equations are transformed to rectangular shaped enclosure computational domain. In this analysis, due to large number parameters, the side wall inclination angle of the enclosure is fixed. The flow and thermal processes are depicted through streamlines and isotherms, while the thermal transport rates are illustrated through Nusselt number profiles. Numerical simulations capture the effects of side wall inclination angle and the effect of discrete heating on the flow and thermal patterns, heat transport rates for various parametric ranges of the problem.

REFERENCES

1) S. Ostrach, Natural convection in enclosures, Advances in Heat Transfer, J.P. Hartnett and T. F. Irvine Jr., ed., 8 (1972)161-227.
2) I. Catton, Natural convection in enclosures, Heat Transfer, 6 (1978)13-43.
3) T. Maekawa, I. Tanasawa, Natural convection heat transfer in parallelogrammic enclosures. Proc. 7th Int. Heat Transfer Conf., Munchen, vol.2. Hemisphere, Washington, D.C., (1982) 227-232.
4) A. Bairi, J.M. Garcia de Maria, I. Bairi, N. Laraqi, E. Zarco-Pernia, N. Alilat, 2D transient natural convection in diode cavities containing an electronic equipment with discrete active bands under constant heat flux, Int. J. Heat Mass Transfer, 55 (2012) 4970–4980.
5) A.J. Chamkha, H. Al-Naser, Double-diffusive convection in an inclined porous enclosure with opposing temperature and concentration gradients. Int. J. Therm. Sci., 40(2001) 227-244.

National Conference on Applied Sciences Synergising the Engineering and Technology
Print ISSN: 2395-6011 | Online ISSN: 2395-602X (www.ijsrst.com)

Semi Graph and its Associated Topological Space

Bhuvaneshwari. R. H[1], Satymurthi. P[2]

[1]K. L. E. Institute of Technology, Hubli, Karnataka, India

[2]Jain Institute of Technology Belagum, Karnataka, India

ABSTRACT

In this paper, definition of semi graph, some properties of degrees of vertices of a semi graph have been discussed. Definition the Topological space and Define the semi graph is associated with topological space.

Keywords : Semi graph; Adjacency and Degrees in Semi graph; Associated Topological space.

References

1. F. Harary, "Graph Theory," Addition Wesley, Reading Mass, 1972.
2. S. P. Subbaih, "A Study of Graph Theory: Topology, Steiner Domination and Semigraph Concepts," Ph.D Thesis, Madurai Kamaraj University, 2007.
3. N. Murugesan, D. Narmatha, "Some Properties of Semigraph and its Associated Graphs ," (IJERT), Vol. 3 Issue 5, May – 2014.

National Conference on Applied Sciences Synergising the Engineering and Technology
Print ISSN: 2395-6011 | Online ISSN: 2395-602X (www.ijsrst.com)

Dispersion of Tracer Particles in a Channel Bounded by Porous Media using Residual Shear Slip Condition

Dr. N. G. Siddagangamma

Assistant professor, Department of Mathematics, Siddaganga Institute of Technology, Tumkur, Karnataka, India

ABSTRACT

In the present paper an attempt is made do study the flow of a steady fluid through a channel under the influence of residual shear slip condition at the fluid deformable porous wall interface on steady arterial blood flow. The porous wall is modelled as a continuous binary mixture of solid and fluid phases. These equations are linear and are amenable to Fourier analysis. Analytical expressions for the velocities of fluid and dust particles are obtained by using Fourier series analysis technique. Results have been discussed with the help of graphs.

Keywords : Channel Flow, Two-Phase Flow, , Incompressible Flow, Volume Fraction

REFERENCES

1. HOLMES, M.H. & MOW, V.C., Holmes, 1990: The non-linear characteristics of soft gels and hydrated connective tissues in ultra filtration, J. Biomechanics, 23, 1145-1156
2. RUDRAIAH, N., 2001: Significant contribution of 2oth Century boundary conditions in Fluid Mechanics-selected topics in Applied Mathematics, IIT-Kharagpur Golden Jubilee Celebration
3. RUDRAIAH, N., 1984: Modified Beavers and Joseph slip condition for flow past a porous medium, Proc. Fluid Mech. And Fluid power, REC Tiruchinapalli, Inida, 19

National Conference on Applied Sciences Synergising the Engineering and Technology
Print ISSN: 2395-6011 | Online ISSN: 2395-602X (www.ijsrst.com)

Testing BNBRU Ageing Class of Life-Time Distribution Based on Moment Inequality

A. Touseef Ahmed and U. Rizwan

Department of Mathematics, Islamiah College(Autonomous), Vaniyambadi, Tirupattur Dt, Tamilnadu, India

ABSTRACT

In this paper, new moment inequality is derived for Bivariate New Better than Renewal Used (BNBRU) ageing class of life-time distribution. This inequality demonstrates that if the mean life is finite, then all higher order moments exist. Based on the Moment inequality, new testing procedures for testing bivariate exponentiality against BNBRU ageing class of life-time distribution is introduced. The asymptotic normality of the test statistic and its consistency are studied. Using Monte Carlo Method, critical values of the proposed test are calculated for n = 5(5)100 and tabulated. Finally, the theoretical results are applied to analyze real-life data sets.

AMS Subject Classification: 60K10

Keywords : Classes of life-time distribution, BNBRU, Moment inequality, U-statistic, Life testing

Certain classes of life-time distributions and their variations have been introduced in reliability theory, the applications of these classes of life-time distributions can be seen in engineering, biological science, maintenance and biometrics. The main aim of constructing new tests is to gain higher efficiencies.

Testing bivariate exponentiality against some bivariate ageing classes of life-time distributions has seen a good deal of attention. The moment inequality for the Bivariate New Better than Renewal Used (BNBRU) Ageing Class of life-time distribution can be found in the work of Sathiyaraj and Rizwan (2019). Now we propose a test statistic testing Bivariate Exponentiality Against Bivariate New Better than Renewal Used (BRNBU) Ageing Class of life-time distribution, based on the moment inequality.

National Conference on Applied Sciences Synergising the Engineering and Technology
Print ISSN: 2395-6011 | Online ISSN: 2395-602X (www.ijsrst.com)
© 2021 IJSRST | Volume 8 | Issue 2

Combined Effect of Surface Roughness and Micropolar Fluids on Squeeze Film Lubrication between Porous Rough Curved Annular Plates

Hanumagowda B N [1] and Chaithra N [2]

[1]REVA University, Bangalore, India

[2]Department of Mathematics, East Point College of Engineering and Technology, Bangalor, India

ABSTRACT

In this present article discuss the combined impacts of surface roughness and micropolar fluids on the squeeze film lubrication between porous curved annular plates. Two forms of one dimensional surface roughness patterns (radial and azimuthal) are used on the basis of Christensen stochastic theory of surface roughness. The stochastic modified Reynolds equation is derived and the closed form expressions are obtained for the mean squeeze film pressure, mean load carrying capacity and squeeze film time. It was observed that the radial (azimuthal) roughness decreases (increases) the squeeze film characteristics

Keywords : Porous, Curved Annular Plates, Squeeze films, Micropolar fluids, Surface Roughness.

References

[1] Ting L L "Engagement behaviour of lubricated porous annular disks Part I: Squeeze film phase-Surface roughness and elastic deformation effects," Wear, Vol. 34, pp 159-182, 1975.

[2] Bujurke N M and Naduvinamani N B, “A note on squeeze film between rough anisotropic porous rectangular plates", Wear, Vol. 217, pp 225-230, 1998.

[3] Gururajan K and Prakash J , “Surface roughness effects in infinitely long porous journal bearings”, Journal of Tribology , Vol. 121, pp 139-147, 1999.

[4] Gururajan K and Prakash J , “Effect of surface roughness in a narrow porous journal bearing”, Journal of Tribology, Vol. 122, pp 472-477, 2000.

[5] Naduvinamani N B, Santosh S and Siddanagouda A, “On the squeeze film lubrication of rough short porous partial journal bearings with micropolar fluids”, Engineering Tribology, Vol. 224, pp 249-257, 2009.

[6] Naduvinamania N B, Hiremath P S and Gurubasavaraja G, “Surface roughness effects in a porous journal bearing with a couple stress fluid”, Fluid Dynamics Research, Vol. 31, pp 333–354, 2002.

National Conference on Applied Sciences Synergising the Engineering and Technology
Print ISSN: 2395-6011 | Online ISSN: 2395-602X (www.ijsrst.com)

A Study on The Combined Effect of Couple Stress and MHD on Sine Slider Bearing Having Rough Surface

Hanumagowda B N[1], Tesymol Cyriac[2*]

[1]REVA University, Bangalore, Karnataka, India

[2]Muthoot Institute of Technology and Science, Varikoli PO, Ernakulam, Kerala, India

ABSTRACT

The present study is aimed for analyzing steady and dynamic characteristics of a sine slider bearing whose surface is assumed to have transverse or longitudinal roughness pattern. The stochastic model of Christensen theory is applied to analyze the roughness effect. Apart from this, the influence of couple stress parameter and magnetic field is also analyzed. It is observed that steady state pressure, steady state load carrying capacity, dynamic stiffness and damping coefficient increase with the increase in couple stress parameter and magnetic field. Also, the bearing characteristics are found to increase with the increase in the roughness parameter accounted for transverse roughness and decrease with the increase in the roughness parameter accounted for longitudinal roughness.

National Conference on Applied Sciences Synergising the Engineering and Technology
Print ISSN: 2395-6011 | Online ISSN: 2395-602X (www.ijsrst.com)
© 2021 IJSRST | Volume 8 | Issue 2

Analysis of Squeeze Film Lubrication Between Curved Circular Plate and Porous Flat Plate – A micropolar fluid model

Hanumagowda B. N.

School of Applied Sciences, Department of Mathematics, REVA University, Bangalore, Karnataka, India

ABSTRACT

The study of the effect of micropolar fluid between the circular plate and the porous flat plate is presented in this paper. The generalized Reynolds equation is derived for the curved circular plate and porous flat plate. Squeeze film characteristics are derived using the Reynolds equation. From the outcomes it is found that the influence of micropolar fluid enhances the pressure, the load carrying capacity and lengthen the squeezing time. Pressure, load carrying capacity and squeeze film time decreases with increasing values of porosity parameter.

Keywords : Micropolar Fluids, Porous, Curved Circular Plates

National Conference on Applied Sciences Synergising the Engineering and Technology
Print ISSN: 2395-6011 | Online ISSN: 2395-602X (www.ijsrst.com)
© 2021 IJSRST | Volume 8 | Issue 2

Combined Effect of Micropolar Fluid and Roughness on Curved Circular Plate and Rough Porous Flat Plate

Hanumagowda B. N.

School of Applied Sciences, Department of Mathematics, REVA University, Bangalore, Karnataka, India

ABSTRACT

This paper describes a theoretical analysis of the effect of surface roughness on the squeeze film lubrication between curved circular plate and flat plate with micropolar fluids. On the basis of Christensen stochastic theory modified Reynolds equation is derived for the study of impact of surface roughness on squeeze film characteristics of curved circular plate and flat plate with micropolar fluid. The expressions for the mean squeeze film pressure, mean load carrying capacity and squeeze film time are obtained. It is found that the squeeze film characteristics are increasing (decreasing) for the azimuthal (radial) roughness pattern. The effect of porosity decreases the squeeze film characteristics.

Keywords: Micropolar fluids, Surface roughness, Porous, curved circular plates.

National Conference on Applied Sciences Synergising the Engineering and Technology
Print ISSN: 2395-6011 | Online ISSN: 2395-602X (www.ijsrst.com)

Mixed Convection of Couple Stress Fluid in a Vertical Porous Stratum in the Presence of heat source or Sink and Thermal Radiation Effect

Kavitha L[1], Hanumagowda B N[2]

[1, 2] Department of Mathematics, School of Applied Sciences, REVA University, Bangalore.

Corresponding author : l.kavitha@reva.edu.in

ABSTRACT

The fully developed mixed convection of couple stress fluid in a vertical porous channel in the presence of heat source or sink and thermal radiation effect is analyzed. The two boundaries of the channel are considered as isothermal-isothermal, isothermal-isoflux and isoflux-isothermal for the left and right walls respectively. The governing momentum and energy equations are coupled and nonlinear due to the viscous effects. The results are represented graphically for different values of buoyancy parameter λ, couple stress parameter 'a', porous parameter 'K' and radiation parameter F on velocity and temperature profiles. We observe that for purely viscous fluid for $\lambda = -500$ the flow reversal was at the hot wall whereas for couple stress fluid through porous channel, there is a flow reversal both at left and right walls. The effect of ε on the flow for couple stress fluid is dominating compared to viscous fluid both on velocity and temperature. The profiles of temperature are significant for couple stress fluid for different values of ε whereas the profiles were not sensible for different values of ε for viscous fluid.

National Conference on Applied Sciences Synergising the Engineering and Technology
Print ISSN: 2395-6011 | Online ISSN: 2395-602X (www.ijsrst.com)
© 2021 IJSRST | Volume 8 | Issue 2

Study of Non Linear Optical Properties of Inorganic Compound Doped ADP Crystals

G. Maruthi

Department of Physics, East Point college of Engineering and Technology, Bangalore, Karnataka, India

ABSTRACT

Ammonium dihydrogen phosphate well known as ADP is a non-linear optical material having wide applications in non-linear and integrated optics. With appropriate dopants, the ADP crystals exhibit several properties. The behavior of these crystals in radiation fields is also of importance, for technology of the radiation induced formation of the optical wave guide (in these crystals). In the present work pure ADP and ADP doped with inorganic compounds like ferrous sulphate, Nickel chloride and Cuprium chloride have been investigated. Crystals were grown from supersaturated solution at room temperature by natural evaporation process. Grown crystals were characterized using X-ray diffraction and EDAX. The grown crystals were subjected to hardness studies to know the mechanical properties of NLO crystals which is essential for understanding the origin of laser induced damage in them. Hardness is calculated by Vicker's method. It has been observed that hardness increases in these crystals with load and the cracking has developed around 50gm. Dielectric constant and Dielectric loss is measured as a function of frequency. Study confirms the contribution of space charge polarization.

Keywords : NLO, ADP, Dielectric, EDAX, Inorganic

REFERENCES:

1. Hari Babu, U.V. Subba Rao and K. Venkata Ramaiah, Phys. Stat. Sol (a), 1975, 28, 269.
2. P. Suryanarayana, H.N. Acharya and K. Roa, J. Mater. Sci. Lett, 1984, 3, 21.
3. S. Sankara Narayanan Potty and M. Abdul Khadhar, Bull. Mater. Sci., 2002, 23, 361.
4. Milton Ohring, Engineering materials science, Academic press 1995.
5. R.Ananda kumari and R.Chandramani, Bull.mater Sci., 2003, 26, 2
6. B.Schwartz,The Electrochemical Society, Princeton 1969

National Conference on Applied Sciences Synergising the Engineering and Technology
Print ISSN: 2395-6011 | Online ISSN: 2395-602X (www.ijsrst.com)
 | Volume 8 | Issue 2

Decolorization studies of $La_{10}Si_6O_{27}:RE^{3+}$ (RE= Eu, Sm, Tb, Dy) Nanopowders for Textile Effluents

A. Naveen Kumar[1,2*], D.M. Jnaneshwara[1*], S.C. Prashantha[2], M.R. Anil Kumar[2], C.R. Ravikumar[2], Y. C Srinivas Gowda[3]

[1]Department of Physics, SJB Institute of Technology, VTU, Bangalore, Karnataka, India

[2]Research Center, Department of Science, East West Institute of Technology, VTU, Bangalore, Karnataka, India

[3]Department of Physics, East point college of Engineering and Technology, VTU, Bangalore, Karnataka, India

ABSTRACT

For the first time nanoparticles of RE3+(Eu, Sm, Tb, Dy) doped (7 mol %) La10Si6O27 have been prepared using low temperature (450oC) solution combustion technique. The photocatalytic degradation of Congo Red (CR) dye was evaluated under UV light irradiation by using synthesized photocatalyst. The catalyst showed an excellent photocatalytic activity (PCA) for the decoloraization of CR dye due to reduction of photo generated electron-hole pair recombination. The high excellent catalytic activity of La10Si6O27: RE3+ make it promising for multifunctional applications.

Keywords : La10Si6O27: Eu3+; Sm3+; Tb3+; Dy3+; Photocatalytic

Conference Proceedings
Abstracts Book

National Conference on Applied Sciences Synergising The Engineering And Technology ASSET-2021

Organised by

Department Basic Sciences
East Point College of Engineering And Technology, Avalahalli, Bengaluru, Karnataka, India

Publisher

Technoscience Academy

Website : www.technoscienceacademy.com
Email: info@technoscienceacademy.com